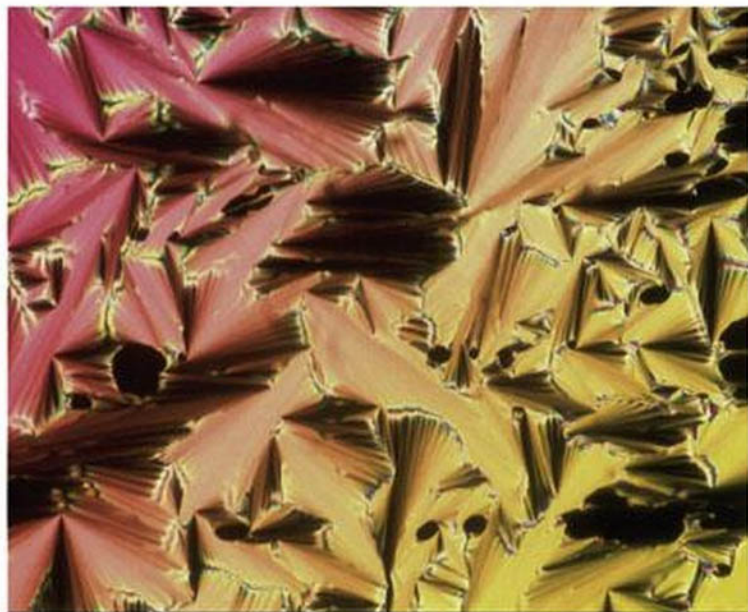


Ingo Dierking

WILEY-VCH

Textures of Liquid Crystals



Ingo Dierking

Textures of Liquid Crystals



WILEY-
VCH

WILEY-VCH Verlag GmbH & Co. KGaA

Ingo Dierking

Textures of Liquid Crystals

Further titles of interest

Demus, D., Goodby, J. W., Gray, G. W., Spiess, H. W., Vill, V.

Handbook of Liquid Crystals

4 Volumes

1998

ISBN 3-527-29502-X

Lagerwall, S. T.

Ferroelectric and Antiferroelectric Liquid Crystals

1999

ISBN 3-527-29831-2

Gray, G. W., Vill, V., Spiess, H. W., Demus, D., Goodby, J. W.

Physical Properties of Liquid Crystals

1999

ISBN 3-527-29747-2

Ingo Dierking

Textures of Liquid Crystals



WILEY-
VCH

WILEY-VCH Verlag GmbH & Co. KGaA

Dr. Ingo Dierking

Department of Physics and Astronomy
University of Manchester
Schuster Laboratory
Oxford Road
Manchester M13 9PL
UK

This book was carefully produced. Nevertheless, author and publisher do not warrant the information contained therein to be free of errors. Readers are advised to keep in mind that statements, data, illustrations, procedural details or other items may inadvertently be inaccurate.

Library of Congress Card No.:

Applied for.

British Library Cataloguing-in-Publication Data:

A catalogue record for this book is available from the British Library.

Bibliographic information published by

Die Deutsche Bibliothek

Die Deutsche Bibliothek lists this publication in the Deutsche Nationalbibliografie; detailed bibliographic data is available in the Internet at <<http://dnb.ddb.de>>.

© 2003 WILEY-VCH Verlag
GmbH & Co. KGaA, Weinheim

All rights reserved (including those of translation in other languages). No part of this book may be reproduced in any form – by photoprinting, microfilm, or any other means – nor transmitted or translated into machine language without written permission from the publishers. Registered names, trademarks, etc. used in this book, even when not specifically marked as such, are not to be considered unprotected by law.

Printed in the Federal Republic of Germany.

Printed on acid-free paper.

Composition Hagedorn Kommunikation,
Viernheim

Printing Druckhaus Darmstadt GmbH, Darmstadt

Bookbinding Litges & Dopf Buchbinderei GmbH,
Heppenheim

ISBN 3-527-30725-7

Preface

Liquid crystals were discovered well over 100 years ago, and since that time texture analysis by polarizing microscopy has been employed as a primary tool for the characterization of different liquid crystalline phases. More than 20 years have passed since the first monograph on liquid crystal textures by Dietrich Demus and Lothar Richter was published (*Textures of Liquid Crystals*, Verlag Chemie, Weinheim, 1979), with its emphasis on nematic, cholesteric, and fluid smectic phases, as many other phases were still to be discovered. Some years later, George W. Gray and John W. Goodby published their monograph on smectic liquid crystal textures (*Smectic Liquid Crystals – Textures and Structures*, Leonard Hill, Glasgow, 1986), with its obvious emphasis, as indicated by the title, on phases with positional order. These two books have served the liquid crystal community and generations of students extremely well in their efforts to identify and characterize the liquid crystalline phases of newly synthesized mesogenic compounds. The past decade, give or take a few years, has seen the discovery of a number of novel liquid crystalline phases, many of them inherently connected to the chirality of the constituent molecules. The time thus seems to be right, not to revise, but rather to complement, the existing range of literature on the textures of liquid crystals, especially when considering the fact that both of the above monographs have long been out of print.

The present publication does not claim to cover all of the different possible aspects of liquid crystal texture appearance, and it is not a text about the wealth of topological defects exhibited by these materials. Rather, I have tried to present a collection of the most commonly observed textures, placing a clear emphasis on chiral materials and especially on those phases which have raised increasing scientific, but also to some extent applicational, interest over the past decade. These are namely the frustrated twist grain boundary (TGB) phases, the chiral tilted smectic phases (ferroelectric liquid crystals), including the variety of SmC* subphases, and the so-called “banana phases”. As experimental investigations on many of these novel liquid crystalline phases are still in progress, and some of their structures and textures are still the subject of intense discussion, obviously it cannot be excluded that some of the remarks made in the present text may be subject to revision in years to come. The textures of lyotropic as well as polymer liquid crystals are generally quite similar to those of the calamitic mesogens, although often

much less pronounced and characteristic. For this reason, they were neglected in the present text. Obviously, I could not include all of the references that might have been relevant to cover certain subjects exhaustively, but I hope to have provided a representative overview and guide to further literature. I apologize to all those who are not mentioned, but who nevertheless have greatly contributed to the understanding of liquid crystals and their textures.

During years of teaching liquid crystal physics, in both lectures and the laboratory, I have gained the impression that, to many students, the textures of liquid crystals are very interesting and appealing on an aesthetic level, while at the same time they find it quite hard to relate the observed optic appearance to respective phases. On the other hand, graduate students and post-doctoral fellows are really the ones who spend numerous hours in the laboratory, performing much of the actually published research. For this reason, the present collection of liquid crystalline textures, their basic explanation, as well as short discussions of some related electrooptic effects, is designed for graduate students, post-doctoral fellows, and scientists who are generally new to the field of liquid crystal research, to be used in everyday laboratory work for the characterization of novel materials. The coverage of textures is presented as a tour through the polarizing microscopic world of a virtual liquid crystal on cooling all the way from the isotropic to the crystalline state. Although this text is primarily written for students and younger researchers, not for specialists in liquid crystal textures and their defects, I sincerely hope that it will also attract the interest of those members of the liquid crystal community who are familiar with the topic.

Completion of this texture collection would not have been possible without contributions from a number of colleagues, who provided their beautiful photographs and whom I would like to thank sincerely for their ready cooperation: G. Andersson, D. Demus, H. F. Gleeson, E. Grelet, W. Kuczynski, M. H. Li, J. G. Meier, H. T. Nguyen, B. Pansu, G. Pelzl, S. K. Prasad, P. Rudquist, and H. Stegemeyer. Most of all I would like to thank Dietrich Demus and Helen Gleeson for taking on the burden of carefully and critically reading the manuscript prior to publication, as well as D. Ganzke for his comments on parts of the manuscript. Finally, I am indebted to Jörn Ritterbusch and the staff at Wiley-VCH, Weinheim, for their continuous support and guidance throughout this project.

Ingo Dierking

Manchester, April 2003

Foreword

In the past 40 years, liquid crystal research has developed from a scientific curiosity to a topic of great scientific and technical importance. In the course of this development, more than 80,000 chemical compounds have been synthesized. The first characterization of newly synthesized materials is generally done by investigation with a polarizing microscope equipped with a hot stage, in order to observe the textures of liquid crystalline phases. Because of the number of different textures, in certain cases even for the same phase type, an extensive atlas showing and explaining the most important examples is urgently needed, even for experienced researchers.

In the more recent period of liquid crystal research, only two attempts have been undertaken to provide comprehensive collections of textures of thermotropic liquid crystals: *Textures of Liquid Crystals* by D. Demus and L. Richter in 1979, and *Smectic Liquid Crystals* by G. W. Gray and J. W. Goodby in 1986. In the meantime, several types of novel liquid crystals have been developed, e. g. discotic compounds, ferroelectric and antiferroelectric phases, twist grain boundary (TGB) phases, and banana-shaped compounds, showing characteristic textures with many unexpected features. Therefore, I warmly welcome the present up-to-date approach by Ingo Dierking, who is an active and experienced scientist in the field of chiral materials with their stimulating and complicated textural features.

In addition to the scientific and practical value of a collection of texture photographs, I would point out the aesthetic side of this study. The beauty of liquid crystal textures has excited not only researchers in this field, but also professional and amateur artists, who use photographs of special features or design motifs derived from textural studies.

I wish Ingo Dierking and his book deserved success. May this beautifully equipped volume help to inspire the scientific community in continuing research on liquid crystals.

Dietrich Demus

Halle, April 2003

Contents

	Preface	V
	Foreword	VII
1	Introduction	1
1.1	States of Matter	1
1.2	Liquid Crystal Nomenclature	3
1.3	General Structure of Liquid Crystal Phases	7
1.3.1	The Nematic Phase	7
1.3.2	The Fluid Smectic Phases	9
1.3.2.1	The Smectic A Phase	9
1.3.2.2	The Smectic C Phase	10
1.3.3	The Hexatic Smectic Phases (SmB, SmI, SmF)	13
1.3.4	The Soft Crystal Phases (B, J, G, E, K, H)	14
1.4	Chirality	16
2	Surface Anchoring and Elasticity	21
2.1	Surface Anchoring and Preparation Techniques	21
2.1.1	Planar Alignment of Nematics	22
2.1.2	Homeotropic Alignment of Nematics	24
2.1.3	Alignment of Smectic Phases	26
2.2	Bulk Elasticity	27
2.2.1	The Nematic and Cholesteric Phase	27
2.2.2	The Fluid Smectic Phases	29
3	Polarizing Microscopy	33
3.1	The Polarizing Microscope	33
3.2	Basic Liquid Crystal Optics	35
3.2.1	Uniaxial Phases	35
3.2.2	Biaxiality	38
3.2.3	Optical Activity	38
3.3	Conoscopy	39

4	The Blue Phases	43
4.1	Structure and Textures of Blue Phases	44
4.2	Kossel Diagrams	47
5	The Nematic and Cholesteric Phases	51
5.1	The Nematic Phase	51
5.1.1	Nematic Textures Under Planar Boundary Conditions	51
5.1.1.1	The Nematic Schlieren Texture	51
5.1.1.2	The Thread-like Texture	52
5.1.1.3	The Marble Texture	53
5.1.1.4	Uniform Planar Nematic Samples	53
5.1.2	The Pseudo-Isotropic Texture Under Homeotropic Boundary Conditions	54
5.2	The Cholesteric Phase	54
5.2.1	Natural Textures of the N* Phase	56
5.2.2	Short Pitch Cholesterics	57
5.2.2.1	Planar Boundary Conditions and Selective Reflection	59
5.2.2.2	Homeotropic Boundary Conditions and the Flexoelectric Effect	61
5.2.3	Long Pitch Cholesterics	64
5.2.3.1	Planar Boundary Conditions	64
5.2.3.2	Homeotropic Boundary Conditions	70
6	Twist Grain Boundary Phases	75
6.1	The TGBA* Phase	77
6.1.1	Natural Textures	79
6.1.2	Textures for Planar Anchoring Conditions	79
6.1.3	Textures for Homeotropic Anchoring Conditions	80
6.1.4	Wedge Cell Preparations	81
6.1.5	Droplet Preparation	83
6.1.6	Suppression of the TGBA* Structure	84
6.2	The TGBC* Phases	84
6.3	The TGBC _A * Phase	87
7	The Fluid Smectic Phases	91
7.1	The SmA/SmA* Phase	91
7.1.1	Natural Textures	91
7.1.2	Planar Anchoring Conditions and the Electroclinic Effect	93
7.1.3	Homeotropic Anchoring Conditions	96
7.1.4	Electric Field Induced Striped Domain Textures	96
7.2	The SmC/SmC* Phase	97
7.2.1	The Achiral SmC Phase	98
7.2.1.1	Natural Textures of SmC	98
7.2.1.2	SmC Under Planar Anchoring Conditions	99
7.2.1.3	SmC Under Homeotropic Anchoring Conditions	100

7.2.2	The Chiral SmC* Phase	100
7.2.2.1	Natural Textures	101
7.2.2.2	SmC* Under Planar Anchoring Conditions	103
7.2.2.3	SmC* Under Homeotropic Anchoring Conditions	104
7.2.2.4	Surface Stabilized Ferroelectric Liquid Crystals	105
8	The SmC* Subphases	123
8.1	General Introduction and Structural Models	123
8.2	Textures of the SmC* Subphases	131
9	The Hexatic Phases	135
9.1	The SmB ^(*) Phase	135
9.2	The SmI ^(*) and SmF ^(*) Phases	136
9.2.1	Natural Textures and Planar Anchoring Conditions	137
9.2.2	Homeotropic Boundary Conditions	138
10	Soft Crystal Phases and Crystallization	141
10.1	The Orthogonal Soft Crystal Phases	141
10.2	The Tilted Soft Crystal Phases	142
10.3	Crystallization of Calamitic Mesogenic Compounds	143
11	Other Liquid Crystal Phases	145
11.1	The Cubic D (CubD) Phase	145
11.2	The SmQ* Phase	146
11.3	Discotic Liquid Crystals	147
11.4	Bent-core Mesogens, “Banana” Liquid Crystal Phases	148
Appendix A		155
Appendix B		163
Color Plates		167
Index		213

1

Introduction

1.1

States of Matter

Liquid crystals are partially ordered, anisotropic fluids, thermodynamically located between the three dimensionally ordered solid state crystal and the isotropic liquid. Their discovery is generally dated back to the year 1888, when the Austrian botanist Friedrich Reinitzer reported on the observation of compounds (cholesteryl benzoate and cholesteryl acetate) with apparently two melting points [1]. In his publication, originally written in German, he wrote reluctantly: *“Es fiel mir jedoch auf, dass die Substanz dabei nicht zu einer klaren, durchsichtigen, sondern stets zu einer trüben, nur durchscheinenden Flüssigkeit schmolz ... [bis] beim Erwärmen auf höhere Temperaturen plötzlich die Trübung verschwindet ... Diese merkwürdige Erscheinung des Vorhandenseins von zwei Schmelzpunkten, wenn man sich so ausdrücken darf, und das Auftreten der Farberscheinungen war es hauptsächlich, welche mich auf den Gedanken brachte, dass hier und beim Acetat physikalische Isomerie vorliegen müsse ...”* (“I noticed, however, that the compound did not melt to a clear, transparent, but always to a muddy, only translucent, liquid ... [until] by further temperature increase suddenly this muddiness disappears ... This strange phenomenon of the existence of two melting points, if one may say so, and the occurrence of coloring was the main reason to conclude that here, and for the acetate, physical isomerism should be present ...”). Friedrich Reinitzer had observed the typical light scattering of a liquid crystal and the phenomenon of selective reflection of the helical cholesteric phase. Without really being able to explain the impact of his discovery, Reinitzer nevertheless realized that for the compounds he had investigated the observed behavior was different from the generally accepted view on the states of matter at his time. This should not detract from the fact that liquid crystalline phases had (possibly) been observed before [2–6], but the fundamental realization of a novel behavior of matter was missing from those reports. For further characterization, Reinitzer sent samples to Otto Lehmann, the successor of Heinrich Hertz in Karlsruhe, an accepted specialist in polarizing microscopy, who only one year later coined the term *“flüssiger Kristall”* (liquid crystal) [7], not without receiving massive resistance from his colleagues.

Liquid crystalline materials are generally divided into two categories (Fig. 1.1), the *thermotropic* and the *lyotropic* mesophases. The term “mesophase” originates

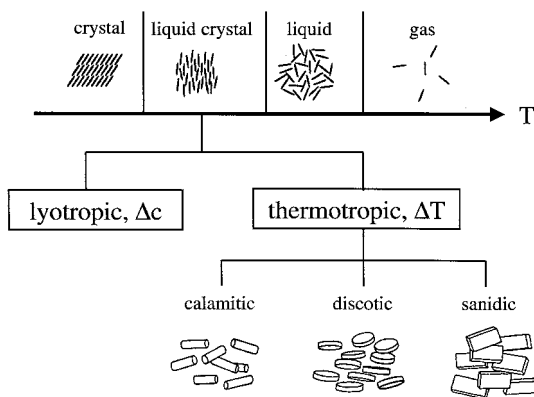


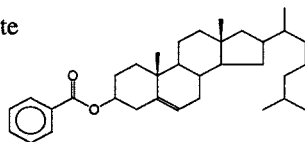
Fig. 1.1. Placement of the liquid crystal phases within the general scheme of the common states of matter. Two basic groups of liquid crystals are distinguished: *lyotropic* phases, which form as a function of concentration c in the presence of an isotropic solvent; and *thermotropic* phases, which are observed by variation of temperature T . Thermotropic phases are further classified according to their basic molecular shapes: rod-like (calamitic), disk-like (discotic), and lath-like (sanidic).

from the Greek word *meso*, meaning “in between” (the crystal and the liquid phases). Thermotropic liquid crystal phases are observed by a change of temperature, while lyotropic phases form in the presence of a suitable (isotropic) solvent. An additional variable of state in the latter case is the concentration. Thus lyotropic mesophases are always mixtures, whereas many of the reported thermotropic liquid crystals are single compounds. Some mesogens may exhibit both lyotropic and thermotropic phases; these materials are named *amphotropic*. To date, some 80000 different compounds, low molecular mass as well as polymeric materials, exhibiting liquid crystal properties have been reported. Most of these are collected in the database LiqCryst [8], together with their phase behavior, some physical properties and literature references. For an introductory text on the chemistry and physical properties of thermotropics, one may refer to books by Stegemeyer [9] and Collings and Hird [10]. An example of a more advanced text is that by Chandrasekhar [11], while the theoretical aspects are covered in the classic book by de Gennes and Prost [12]. Recently, a four volume compendium, summarizing the state of liquid crystal research up to approximately 1998, has been published as the *Handbook of Liquid Crystals* [13]. As lyotropic liquid crystals will not be covered within the scope of this book, we refer the reader to the monograph of Petrov [14].

Thermotropic liquid crystals are generally further distinguished with respect to the molecular shape of the constituent molecules, being called *calamitic* for rod-like, *discotic* for disk-like, and *sanidic* for brick- or lath-like molecules. In Fig. 1.2 a small selection of typical calamitic and discotic mesogens is shown. A common structural feature of calamitic mesogens is a relatively rigid core, often incorporating phenyl and biphenyl groups, and two flexible endgroups, often alkyl or alkoxy chains. In discotic mesogens six flexible endgroups are commonly attached to a rigid, disk-like core. Obviously, numerous variations to these general molecular structures may be implemented, leading to the large variety of mesogenic compounds we know today.

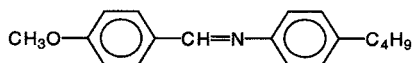
Calamitic mesogens:

Cholesteryl benzoate



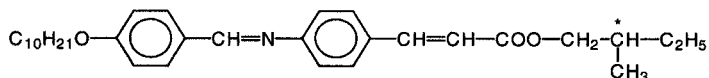
Cr* 145 N* 178 BP* 179 Iso*

4-butyl-N-[methoxy-benzylidene]-aniline (MBBA)



Cr 22 N 47 Iso

D-2-methylbutyl 4-[4-n-decyloxybenzylideneamino]-cinnamate (DOBAMBC)



Cr* 76 SmC* 95 SmA* 117 Iso*

Discotic mesogens:

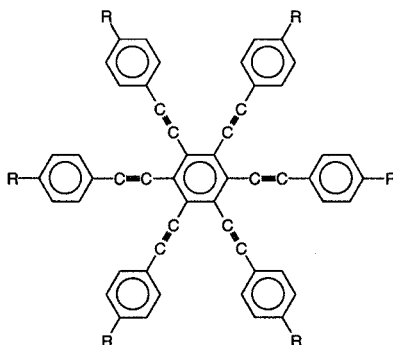
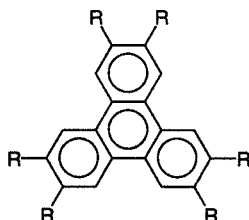


Fig. 1.2. A small selection of typical calamitic and discotic mesogens. Cholesteryl benzoate was the first liquid crystal reported by Friedrich Reinitzer in 1888, DOBAMBC the first mesogenic material where ferroelectric properties were demonstrated in the SmC* phase.

1.2

Liquid Crystal Nomenclature

The nomenclature of liquid crystals is probably a field of research in itself. As in any field of active research, the terminology of liquid crystal (LC) phases is subject to more or less continual change. It started with the classification of phases into

nematic, cholesteric, and smectic, as introduced by Friedel [15] in 1922. At that time not very many mesogenic compounds were known and the classification was meaningful, referring to systems with only long range orientational order (nematic), the helical nematic phase observed for compounds derived from cholesterol (cholesteric), and systems with additional positional order, thus phases with a layered structure (smectic). Already at that time those phases were distinguished by their typical textures in polarizing microscopy. It is also worth noting at this point that the nematic and the cholesteric phases are essentially equivalent from the thermodynamic point of view. The latter is simply a nematic phase composed of chiral molecules, which exhibits a helical superstructure.

During the decades following the classification by Friedel, especially in the 1950s and 1960s, a variety of different smectic phases were discovered, many of them by the liquid crystal group at Halle University, which has a very long tradition in liquid crystal research, dating back to the days of Daniel Vorländer. It was here that the nomenclature of assigning letters to different phases was first introduced [16], although their scheme does not follow any systematic classification as is the case for solid state crystal structures, but instead the phases were basically named alphabetically in the order of their discovery. While offering an unequivocal scheme of classification, this procedure had led to some confusion in the early days, as different groups named different phases with the same letter, or the same phases with different letters, which should have been assigned to an already known phase type. Many of these problems were resolved when Sackmann and Demus proposed their rule of miscibility [17] for the identification of liquid crystal phases: if an unknown phase is continuously miscible with a reference phase over the entire concentration range, then they are equivalent. On the other hand, if they are not miscible, no conclusion can be drawn. This implies that the complete phase diagram between the unknown and the reference compound has to be determined, as is exemplified in Fig. 1.3 (data after Ref. [18]), taken from an investigation of the Halle group. This procedure involves the preparation of a number of mixtures, which is quite time consuming. A less work intensive, but at the same time only qualitative, method is a contact preparation. The compound A with the higher crystallization temperature is melted on a hot stage and drawn between a glass substrate and a microscope coverslip by capillary action. Then the sample is cooled to recrystallize it and the procedure repeated with the other, lower melting, compound B. This yields a sample with a contact region between both compounds, varying their concentration between 100% A and 100% B (Fig. 1.4). Variation of temperature then simulates the whole phase diagram, although without knowledge of the absolute concentration of both compounds. An illustrative example is given in Plate 1, where the unidentified highly ordered phase of a compound at the bottom left is in contact with an extensively investigated reference compound at the upper right. For elevated temperatures a clear phase boundary is observed, but within the temperature region of interest, that of the highly ordered phase to be identified, the texture of the reference and the unidentified compound are the same, without any phase boundary. This indicates that the low temperature phase of the two materials are equivalent and we have thus identified the low tempera-

Fig. 1.3. Typical phase diagram of two (very similar) compounds A (left) and B (right). (Data after Ref. [18].) Considering A to be the reference compound and B the one to be identified, application of the miscibility rule allows one to identify the nematic phase of compound B, as this is miscible for all concentrations with the nematic phase of compound A.

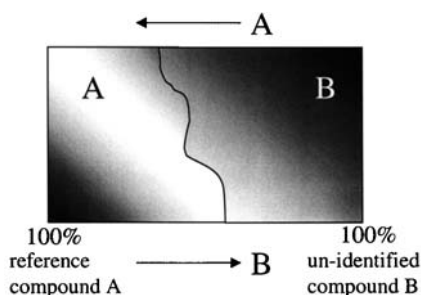
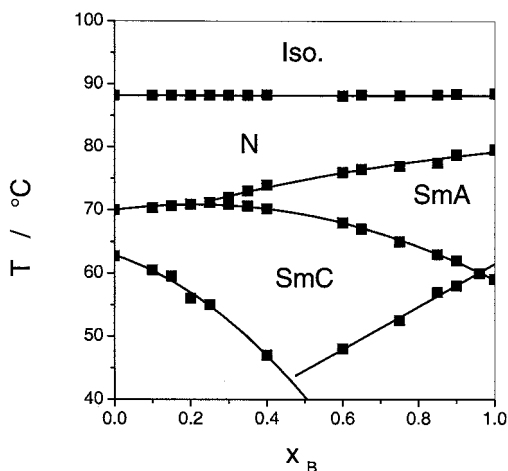


Fig. 1.4. Schematic illustration of a contact preparation to “simulate” the phase diagram of a binary system of compounds A and B. For an experimental example, see Plate 1.

ture phase of the novel compound by comparison with that of the known reference material.

Additional confusion about the nomenclature of phases arose with the discovery of several classes of novel chiral LCs, namely the *twist grain boundary* (TGB) phases and the smectic C* subphases. In several early papers the TGBA* phase was named SmA*, with the asterisk (*) denoting a helical superstructure. This was somewhat misleading, because we should already make a distinction between SmA, the phase composed of achiral molecules, and SmA*, a smectic A phase composed of chiral molecules, but without any helical superstructure. The reason for this distinction lies in the different properties of the two phases. SmA* exhibits effects that are simply absent in SmA, like molecular optical activity or the electroclinic effect [19], somewhat analogous to piezoelectricity in solid state materials. Here we will follow the recommendation of Lagerwall [20] and use the asterisk to denote a phase composed of chiral molecules, regardless of any possible helical superstructure. This means that we will not use the often found notation “Ch.” for cholesteric, but rather N*. Nevertheless, we will for historic reasons still refer to the “cholesteric” phase, when talking about the “chiral nematic” phase. Again, the notation N* will be used regardless of a helical superstructure, a situation that can be observed for twist in-

version compounds, which show a temperature interval where a nematic director configuration is observed with infinite pitch, even though the structure is composed of chiral molecules. To indicate this situation the notation N_{∞}^* will be used. Consistency requires that also phases which appear only in chiral materials, like the Blue Phases, should be denoted with an asterisk, BP*. Even the isotropic phase of chiral molecules should be abbreviated as Iso* to distinguish it from the isotropic phase of achiral mesogens, because the former shows optical activity, while the latter does not. (The notation “Iso” instead of “I” will be used to avoid confusion with the SmI phase, which is sometimes simply called “I” in the literature.)

Summarizing, we will mainly follow the nomenclature recommendations for thermotropic liquid crystals of the International Liquid Crystal Society (ILCS) and the International Union of Pure and Applied Chemistry (IUPAC) [21]:

- Crystalline phases
 - Cr for the crystalline phase (Cr₁, Cr₂, ... if several crystal modifications are observed).
 - Cr* for crystalline phases composed of chiral molecules.
- Soft crystals (with long range positional order)
 - B, E, G, H, J, K instead of the formerly used notation SmB^{cryst}, SmE, SmG, ...
 - B*, E*, G*, H*, J*, K* for the soft crystal phases composed of chiral molecules.
- Smectic liquid crystals
 - SmA, SmB, SmC, SmI, SmF for the achiral smectic phases.
 - SmA*, SmB*, SmC*, SmI*, SmF* for the chiral smectic phases.
- Smectic C* “subphases” (which appear only in chiral materials)
 - SmC_α* for a still controversially discussed, but presumably incommensurate, phase appearing just below the SmA* phase of some materials.
 - SmC* for the ordinary helielectric chiral smectic C phase, which is often referred to as “ferroelectric”.
 - SmC_{1/3}* and SmC_{1/4}* for the intermediate, often misleadingly termed “ferrielectric” phases Sm_{F11}* and Sm_{F12}*.
 - SmC_A* for the antiferroelectric chiral smectic C phase.
- Other antiferroelectric phases
 - SmI_A* for the antiferroelectric chiral smectic I phase, etc.
- Twist grain boundary phases (which appear only in chiral materials)
 - TGBA* for the twist grain boundary smectic A phase.
 - TGBC* for the ferroelectric twist grain boundary smectic C phase.
 - TGBC_A* for the antiferroelectric twist grain boundary smectic C phase.

Already here, we face problems with the nomenclature, as there are apparently different TGBC* phases. At this point it seems to be too early to define a notation, and we refer to the structural models shown in Chapter 6.
- Nematic phase

The nematic phase will be denoted as N, its chiral version as N*, also being referred to as the cholesteric phase.
- Blue Phases (which appear only in chiral materials)
 - BPI*, BPII*, BPIII* for the blue phases.

- Isotropic phase

The isotropic phase will be denoted as Iso for achiral and Iso* for chiral constituent molecules.

- Other phases

There are also some phases that will not play a great role in our further discussion, although some texture illustrations will be given. Their nomenclature will follow the ordinary scheme: SmQ* etc. Also the cubic D phase (CubD) and the recently discovered “banana phases” fall into this category and will be covered briefly in this context.

1.3

General Structure of Liquid Crystal Phases

1.3.1

The Nematic Phase

From the general liquid crystal phases, leaving the chiral ones aside to be treated individually in later chapters, the nematic phase is the one with the least order and the highest symmetry. It exhibits solely orientational order of the long molecular axis, i. e. an angular distribution of the long molecular axis around a particular direction, the director \mathbf{n} , while the molecules' centers of mass are isotropically distributed in all three dimensions, as schematically depicted in Fig. 1.5. The director \mathbf{n} is the average local direction of the long molecular axis and represents the direction of the optic axis of the system. Orientational order is generally described by a second rank symmetric traceless tensor with elements

$$Q_{\alpha\beta} = \langle a_\alpha a_\beta \rangle - \frac{1}{3} \delta_{\alpha\beta} \quad (1.1)$$

where \mathbf{a} is a unit vector along the long axis of a molecule at position \mathbf{r} , $\alpha, \beta = x, y, z$ is the fixed laboratory coordinate frame, and $\delta_{\alpha\beta}$ is the Kronecker tensor, which is equal to one when $\alpha = \beta$ and zero for $\alpha \neq \beta$. Brackets $\langle \rangle$ denote the temporal and spatial average. For an isotropic director distribution the average $\langle a_\alpha^2 \rangle$ is equal to 1/3, and therefore $Q_{\alpha\beta} = 0$ in the isotropic phase. The order parameter tensor can be diagonalized by a suitable choice of the coordinate system, so that the five different ten-

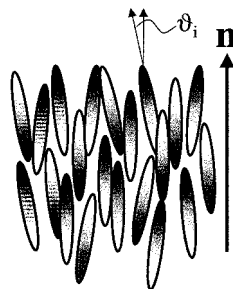


Fig. 1.5. Model structure of the nematic (N) phase. The spatial and temporal average of the long molecular axis is called the director \mathbf{n} . The angle ϑ_i denotes the deviation of the long molecular axis of an individual mesogen i from the director.

tor elements are reduced to the three diagonal elements. These are all different in the case of a biaxial phase, while any two of them are equal in the case of a uniaxial phase, like the nematic. In the latter case, we rewrite Eq. (1.1) for cylindrical molecules with rotational freedom around their long molecular axis as

$$Q_{\alpha\beta} = S_2 (n_\alpha n_\beta - \frac{1}{3} \delta_{\alpha\beta}) \quad (1.2)$$

with

$$S_2 = \frac{1}{2} \langle 3 \cos^2 \vartheta_i - 1 \rangle \quad (1.3)$$

the often used Hermans orientational order parameter [22], which was introduced as a scalar order parameter for liquid crystals by Tsvetkov [23]. If we choose the director \mathbf{n} along the z direction of the coordinate system, the diagonal elements of the tensor order parameter become $S_{xx} = S_{yy} = -\frac{1}{3}S_2$ and $S_{zz} = \frac{2}{3}S_2$. The brackets of Eq. (1.3) denote a statistical (spatial and temporal) average over an ensemble of molecules with their individual long molecular axis deviating from the director \mathbf{n} by an angle ϑ_i . S_2 is equal to the average of the second Legendre polynomial, $S_2 = \langle P_2 \rangle$, the first non-trivial term in a Legendre expansion of the order distribution function $f(\vartheta)$, which is itself generally not accessible from experiments. The scalar order parameter S_2 describes the phase transition from the isotropic to the liquid crystalline nematic phase: $S_2 = 0$ for random orientational order (the isotropic phase) and $S_2 = 1$ for perfectly aligned molecules. Experimentally, it is found that $S_2 \approx 0.3$ at the clearing point T_C (N–Iso transition), increasing to values of $S_2 \approx 0.6$ far below T_C (Fig. 1.6, data after Ref. [24]), with a temperature dependence that is described by the famous Maier–Saupe theory [25–27]. Note that these values for S_2 imply average values of $\langle \vartheta_i \rangle$ in the order of 30° , which means that the deviation of the long molecular axis from perfect orientational order, as would be expected for a solid state crystal, is considerable.

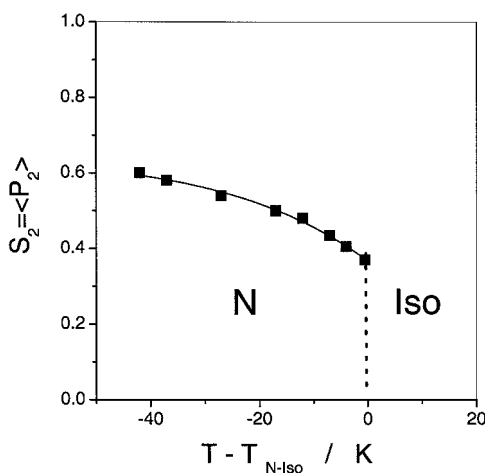


Fig. 1.6. Typical illustration of the temperature dependence of the scalar nematic order parameter S_2 for PAA (*p*-azoxyanisole). (Data after Ref. [24].)

1.3.2

The Fluid Smectic Phases

On lowering the temperature of a nematic material, additional features of order may appear, namely positional order of the molecules' centers of mass. This can at the least be one dimensional, leading to the layered structure of the SmA and SmC phases, which can in fact be regarded as two dimensional liquids. In addition to the orientational order of the long molecular axis, the molecules' centers of mass arrange in layers. Looking at their projection onto the smectic layer plane, the molecules' centers of mass are isotropically oriented, with no positional correlation being observed within or across the layer planes.

1.3.2.1 **The Smectic A Phase**

In the SmA phase the director \mathbf{n} and thus the optic axis are perpendicular to the smectic layer plane, as shown schematically in Fig. 1.7. At the same time, orientational order is far from being perfect. From a discussion with Woiteck Kuczyński some years back I remember his pointed description of the SmA phase: “... *it's more like a field of wheat in the wind*”. The degree of translational order with periodicity d , equal to the smectic layer spacing, i. e. the length L of a mesogen, is described by a smectic order parameter

$$\sigma = \left\langle \frac{3 \cos^2 \vartheta_i - 1}{2} \cos \left(\frac{2\pi}{d} z_i \right) \right\rangle \quad (1.4)$$

with the positions of individual molecule's centers of mass at z_i , if the smectic layer normal is chosen in the z direction. The smectic order parameter σ was first introduced by Kobayashi and McMillan [28–30]. It contains the orientational order term S_2 multiplied by the positional order term, which represents the first term of a Fourier expansion of the positional order distribution function. Equation (1.4) is directly related to x-ray experiments on respective phases. The smectic layer spac-

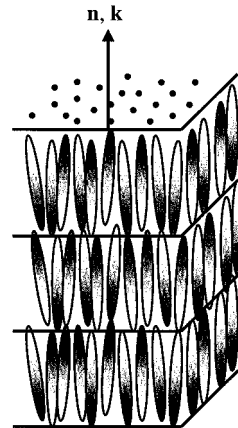


Fig. 1.7. Model structure of the smectic A (SmA) phase. The director \mathbf{n} is oriented parallel to the smectic layer normal \mathbf{k} , while within a smectic layer the molecules' centers of mass are isotropically distributed.

ing can be evaluated by small angle x-ray scattering (SAXS), for example with a Kratky camera, according to the Bragg equation

$$n\lambda = 2d \sin \alpha \quad (1.5)$$

where n is the diffraction order, λ is the x-ray wavelength (often $\lambda = 1.54 \text{ \AA}$, Cu $K_{\alpha 1}$ radiation), d is the periodicity, and α is the diffraction angle. For most fluid smectic liquid crystals, except amphiphilic molecules, mesogenic sugars, etc., generally only the first order diffraction peak is observed. As the x-ray diffraction pattern is in principle proportional to the Fourier transform of the electron density, we can readily deduce that in reality the fluid smectic structure is not perfectly layered (this would lead to reflections of higher diffraction order), but rather a sinusoidal distribution of the molecules' centers of mass. Thus, a more realistic view of the SmA phase is schematically given by Fig. 1.8 (after Ref. [11], p. 321). Some materials also form a double layer structure with the identity period $d = 2L$, or that of interdigitated molecules with $L < d < 2L$ (Fig. 1.9).

1.3.2.2 The Smectic C Phase

Another smectic phase with one dimensional positional order is the SmC phase, which looks similar to SmA, only with the director being tilted by an angle with respect to the smectic layer normal. The tilt of an individual molecule can be described by a vector with amplitude θ_i and azimuthal tilt direction φ_i . The average molecular tilt over an ensemble of molecules is given by

$$\theta = \left\langle \theta_i \begin{pmatrix} \cos \varphi_i \\ \sin \varphi_i \end{pmatrix} \right\rangle \quad (1.6)$$

While the amplitude of the tilt θ is determined by thermodynamic variables (temperature, pressure), the tilt direction is not predetermined at all. As we will discuss later in greater detail, the director tilt will have a tremendous impact on not only the physical properties but also the textures, if the constituent molecules are chiral. Nevertheless, the general structure of the SmC phase is schematically depicted in Fig. 1.10. With a uniform tilt direction the director tilt angle $\theta = \langle \theta_i \rangle$ is considered to be the order parameter for the SmA to SmC transition and is a function of temperature T , with increasing tilt for decreasing temperature. In the low temperature range of the SmC phase the majority of single component materials exhibit values for the director tilt in the order of $\theta \approx 25^\circ - 35^\circ$. Commercial SmC* mixtures are generally optimized to $\theta \approx 22.5^\circ$ at room temperature, due to applicational aspects. The interesting case of $\theta > 45^\circ$ has not yet seemed to be observed.

Two general groups of SmC materials may be distinguished: those with a high temperature SmA phase, and those with a high temperature nematic or isotropic phase. In the first case, the transition is (most often) of second order and can be described by a Landau theory, an expansion of the free energy density F at the phase transition temperature T_C with respect to the order parameter θ :

Fig. 1.8. A more realistic view of the SmA phase is a sinusoidal density modulation. (a) A horizontal line perpendicular to the director of the nematic phase (along the z direction) cuts the same number of molecules for all positions of z . (b) In the SmA phase the number of cut molecules (mostly) varies according to a sine function along the z direction with the period being the smectic layer spacing d , approximately equal to the length L of the extended conformation of the molecule.

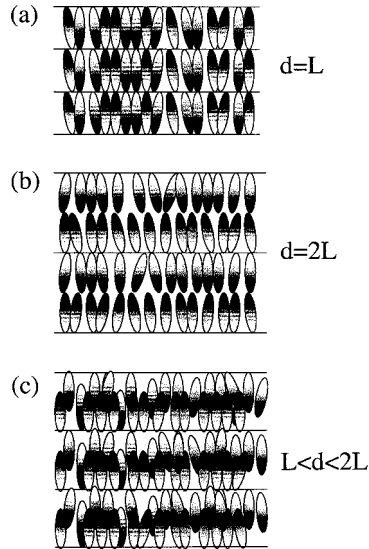
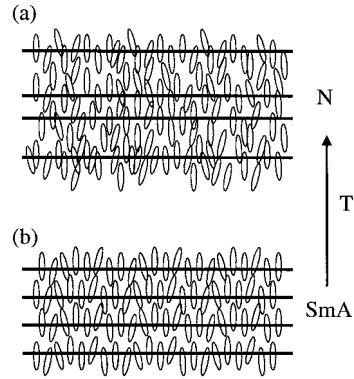


Fig. 1.9. Possible SmA layer arrangements: (a) simple monolayers, where the smectic layer spacing d is approximately equal to the molecular length L ; (b) double layers, where $d \approx 2L$; and (c) an interdigitated molecular arrangement with $L < d < 2L$.

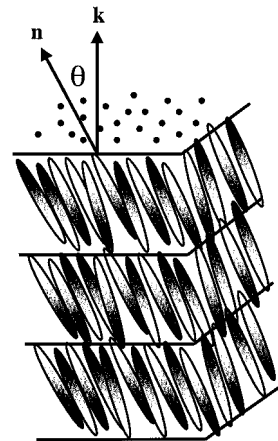


Fig. 1.10. Model structure of the smectic C (SmC) phase. The director \mathbf{n} is tilted with respect to the smectic layer normal \mathbf{k} by an angle θ , the director tilt angle, which is a temperature dependent quantity. The molecules' centers of mass within a smectic layer are isotropically distributed.

$$F - F_0 = \frac{1}{2} \alpha (T - T_C) \theta^2 + \frac{1}{4} b \theta^4 + \frac{1}{6} c \theta^6 + \dots \quad (1.7)$$

where F_0 is the free energy density of the SmA phase, and α , b , c are the so-called Landau coefficients. A crude first approximation, ending the expansion after the second term ($b > 0$) and with $(dF/d\theta)_{T,p} = 0$ (thermodynamic equilibrium), predicts a square root dependence of the tilt angle on reduced temperature $T_C - T$:

$$\theta = \sqrt{\frac{a}{b}} (T_C - T)^{\frac{1}{2}} \quad (1.8)$$

The order parameter θ decreases continuously with increasing temperature and is $\theta = 0$ in the SmA phase. Note that this description is not valid within the direct vicinity of the transition, where fluctuations have to be taken into account that cannot be treated by a mean field theory. Also for a tricritical transition ($b = 0$, $c \neq 0$), the above description is not valid, as the stability criterion is not fulfilled.

In the second case, generally a first order transition is observed, where θ decreases only slightly with increasing temperature and vanishes discontinuously at the transition temperature. An experimental example for both cases is given in Fig. 1.11, obtained from chiral materials by electrooptic methods, with closed symbols representing a second order SmC*–SmA* transition and open symbols referring to a first order SmC*–N* transition.

As the tilt angle increases from $\theta = 0$ in the SmA phase to $\theta > 0$ in the SmC phase, the smectic layer spacing $d = L$ decreases for decreasing temperature, as can be followed by SAXS experiments (Fig. 1.12, a second order transition). From x-ray measurements one can thus obtain the tilt angle by comparison of the layer spacing in SmA and SmC by

$$\theta = \arctan\left(\frac{d_{SmC}}{d_{SmA}}\right) \quad (1.9)$$

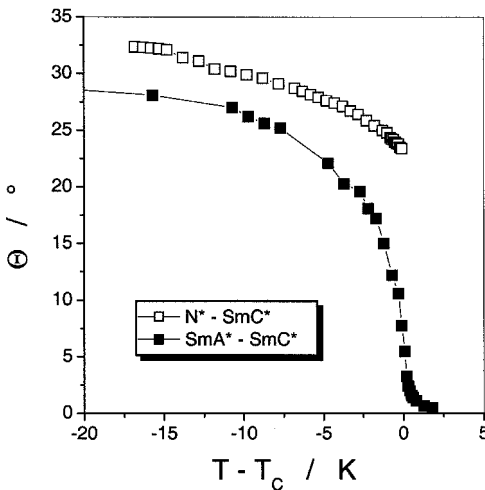
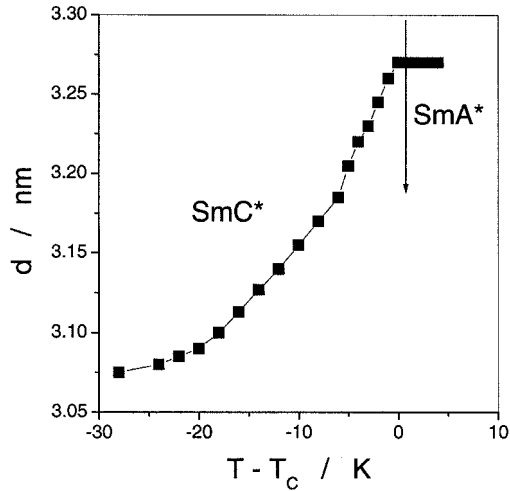


Fig. 1.11. Typical dependence of the director tilt angle θ on reduced temperature $T - T_C$ for a second order SmC*–SmA* (closed symbols) and a first order SmC*–N* phase transition (open symbols). The “tail” in the SmA* phase is due to the electroclinic effect observed for chiral materials.

Fig. 1.12. Dependence of the smectic layer spacing d on reduced temperature $T - T_c$ across the $\text{SmA}^* - \text{SmC}^*$ transition, obtained from small angle x-ray scattering (SAXS) experiments. From the data the SmC^* tilt angle can be evaluated according to Eq. (1.9).



At this point, attention should be drawn to the fact that tilt angles obtained by optical methods and by x-ray experiments may differ considerably [31, 32].

As for the SmA phase, also the SmC phase generally only exhibits the first order reflection, implying that the smectic layering is rather a density modulation than perfect one dimensional positional ordering. Also for SmC we may observe the respective structures of double layers or interdigitated layers.

1.3.3

The Hexatic Smectic Phases (SmB , SmI , SmF)

A next element of order that we can introduce on our long way to the crystalline state is long range orientational, but short range positional ordering of the molecules within a smectic layer. This is called *bond-orientational order* [33, 34], with “bonds” describing lines that join the centers of mass of nearest neighbor molecules. The molecules’ centers of mass within a smectic layer are arranged on an oriented hexagonal net (open circles in Fig. 1.13). Insertion of defects (closed circles) destroys the long range positional order, while orientational order of the centers of mass is preserved across the defect [35, 36]. Thus we have a structure with long range orientational order of the hexagons but only short range positional

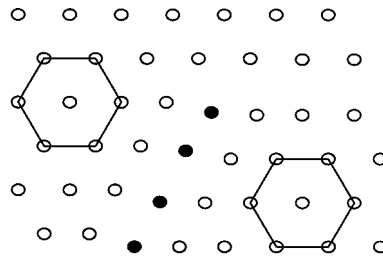


Fig. 1.13. Schematic illustration of *bond-orientational order* in hexatic smectic phases. The orientational order on the hexatic net is preserved across the defect, while positional order is not, leading to long range orientational order and short range positional order for the SmB , SmI , and SmF phases.

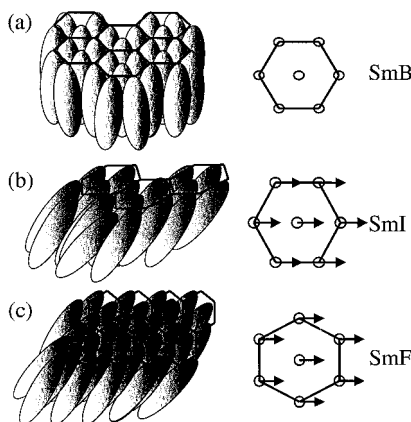


Fig. 1.14. Model structure of (a) the orthogonal SmB phase, (b) the SmI phase being tilted towards the apex of the hexagon, and (c) the SmF phase being tilted towards the side of the hexagon. (The soft crystal B, J, and K phases have a similar structure, only with positional order being long range.)

order within the smectic layer and no interlayer positional correlation. Experimental evidence on the existence of phases with bond-orientational order was given by Leadbetter et al. [37], conclusively being established by the high resolution x-ray experiments of Pindak and coworkers [38].

Three different phases have to be distinguished. The orthogonal hexatic smectic phase, comparable to SmA plus bond-orientational order, is called SmB and has the director pointing along the smectic layer normal. Its structure is schematically depicted in Fig. 1.14(a). For the tilted versions of hexatic smectic phases, we have to distinguish between two phases differing in their tilt direction: in the SmI phase the molecules are tilted towards the apex of the hexagon (Fig. 1.14(b)), while in the SmF phase the molecules are tilted towards its side (Fig. 1.14(c)).

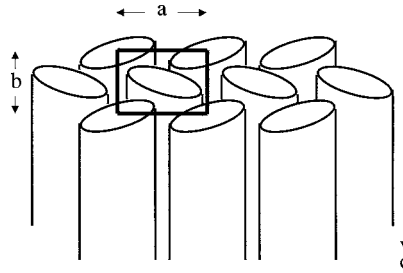
It should also be noted that there have been reports [39–42] on a smectic phase occurring below SmC or SmC* which does not exhibit positional order, but presumably belongs to the class of hexatic phases, while not being miscible with either SmI or SmF. The definite structure of this phase, denoted as SmM^(*), has not yet been conclusively determined, but theoretical investigations [43] predict four possible tilted hexatic phases: SmI and SmF as discussed above, a phase with a locked tilt direction at an arbitrary angle between those of SmI and SmF, and a fourth phase with an unlocked tilt direction. At this point it is not clear whether SmM corresponds to any of the later two predicted phases. The occurrence of the smectic M phase, which has only been observed for a few compounds so far, is independent of chirality, but its chiral version shows properties very similar to those of SmC* or SmI* [40]. Some texture examples of this phase can be found in Ref. [39].

1.3.4

The Soft Crystal Phases (B, J, G, E, K, H)

The structures of the soft crystal phases B, J, and K are very similar to the respective hexatic phase SmB, SmI, and SmF (Fig. 1.14), but they additionally exhibit a long range positional order, which is only short range for the hexatic phases. The

Fig. 1.15. Model structure of the orthorhombic soft crystal E phase with the “herringbone” arrangement of molecules. The respective tilted phases are K, being tilted towards side a , and H, being tilted towards side b .



B phase exhibits an orthogonal orientation of the molecules (long molecular axis parallel to the layer normal). The J phase is tilted towards the apex of the hexagon, while the G phase is tilted to the side. Note that especially in the older literature the soft crystal B phase is also called SmB^{cyst} , sometimes also SmL , while the J phase is sometimes referred to as SmG' .

Further soft crystal phases are characterized by a strong hindrance of the molecular rotation around the long axis. They exhibit the so-called “herringbone” structure. The E phase has an orthorhombic unit cell and is the orthogonal phase, whose structure is schematically depicted in Fig. 1.15. The respective tilted phases are called K, with the molecules being tilted to side a , and H, being tilted to side b . Both have a monoclinic unit cell. Note that the soft crystal K phase is sometimes also referred to as SmH' . A detailed review of the smectic state, its structures, and defects can be found in Refs. [44, 45].

The structural features of the different (achiral) smectic and soft crystal phases are summarized in Tab. 1.1. As a crude rule of thumb we may deduce a hypothe-

Tab. 1.1. General characteristic structural features of achiral smectic and soft crystal phases.

<i>Phase</i>	<i>Range of orientational order</i>	<i>Range of positional order</i>	<i>Orientation of long molecular axis</i>	<i>Distribution of molecular centers of mass</i>
SmA	short	short	orthogonal	isotropic
SmC	short	short	tilted	isotropic
SmB	long	short	orthogonal	hexagonal
SmI	long	short	tilted (to apex)	hexagonal
SmF	long	short	tilted (to side)	hexagonal
B	long	long	orthogonal	hexagonal
J	long	long	tilted (to apex)	hexagonal
G	long	long	tilted (to side)	hexagonal
E	long	long	orthogonal	orthorhombic
K	long	long	tilted (to side a)	monoclinic
H	long	long	tilted (to side b)	monoclinic

tical phase sequence on cooling from the isotropic melt (still disregarding various chiral phases):



Obviously, no single compound exhibits the whole range of the above phases, but investigations on numerous materials have shown that their individual phase sequences mostly follow this hypothetical sequence with the omission of those phases that do not appear. We should not forget that, as for every rule of thumb, there are also exceptions to the above mentioned general phase sequence. For a rare number of substances a reappearance of the high temperature phase, with higher symmetry, has been observed on cooling below a thermodynamically stable phase of lower symmetry. This phenomenon is called “re-entrant” behavior and was first reported for a cyano compound with the phase sequence Iso-N-SmA-N_{re}-Cr [46]. Several other reports followed over the years [47], also with different phases being involved. Nevertheless, there seems to be no universal explanation of the re-entrant phenomenon. Causes that are discussed include frustration, complex steric factors, and competing fluctuations [48]. From the above hypothetical phase sequence we have also omitted the relatively rarely observed cubic D phase, because it may in fact appear at different locations in the sequence [49].

1.4 Chirality

Chirality is an inherent property of many systems in nature [50], ranging from the well known molecular asymmetry (resulting from carbon atoms being substituted by four different ligands), helical biomolecules (such as natural polypeptides, enzymes or DNA), shells, snails, and plants growing in a one-handed fashion, all the way to the parity violation of the weak interaction in the β -decay of ^{60}Co . Chirality defines itself by the lack of mirror symmetry, or in the words of W. H. Thomson (Lord Kelvin): “I call any geometrical figure or group of points ‘chiral’ and say it has ‘chirality’, if its image in a plane mirror, ideally realized, cannot be brought into coincidence with itself” [51]. This definition is not specifically related to molecules, but universally valid for geometrical objects, although, from a historical point of view, stereochemistry has played a dominant role in the understanding of chirality since the groundbreaking discoveries of Louis Pasteur [52] on a salt of tartaric acid, which forms two types of crystals, being mirror images of each other. An object is chiral if symmetry elements of the second kind, such as mirror planes and mirror rotation axes, are absent. Symmetry elements of the first kind, such as translation and rotation axes, are allowed. The symmetry of all chiral objects is described by the point groups C_1 (no mirror planes, no rotation axis), C_n (one or more n -fold rotation axes), and D_n (one n -fold rotation axis and n two-fold rotation axes perpendicular to it).

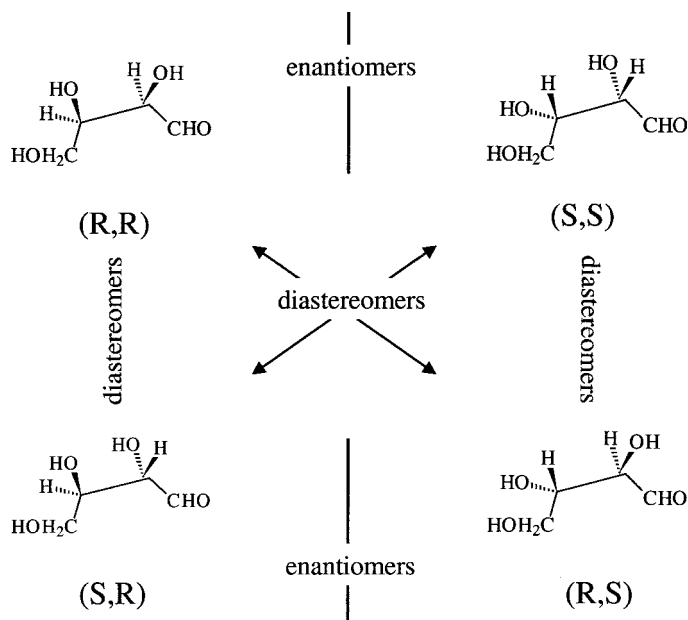


Fig. 1.16. Illustration of *enantiomers* of the $(R,R)/(S,S)$ and the $(S,R)/(R,S)$ configured (non-mesogenic) molecule 2,3,4-trihydroxybutanal and its *diastereomers* $(R,R)/(R,S)$, $(S,S)/(S,R)$, $(R,R)/(S,R)$, and $(S,S)/(R,S)$.

Coming back to molecules, its *constitution* describes the topology of the respective molecule. If the molecule is identical to its mirror image, it is called *achiral*. All molecules of equal constitution, which differ in their *configuration*, i.e. their spatial arrangement of atoms, are named *stereoisomers*. Two stereoisomers that behave like image and mirror image are *enantiomers*. These exhibit identical scalar physical properties such as melting points and have equal values of their chirality related properties (for example, optical rotation), but with an opposite sign. All other stereoisomers are named *diastereomers*. An illustrative example is given in Fig. 1.16 for the non-mesogenic molecule 2,3,4-trihydroxybutanal. Diastereomers have different physical properties. Note that for the formation of diastereomers the molecule has to contain at least two *chiral elements*. These do not necessarily have to be chiral centers, but may also be chiral axes or chiral planes [53]. Some representative examples are given in Fig. 1.17. A detailed overview of nomenclature and definitions on how to determine the absolute configuration of molecules was given by Cahn, Ingold, and Prelog [54].

In liquid crystals chirality can be introduced in several different ways. Chirality can directly be introduced within the molecule by incorporation of chiral elements, mostly chiral centers. These are then single component chiral systems. Another popular way, especially for materials used in applications, is the addition of a small amount (generally less than 5%) of a chiral dopant molecule to an achiral host phase. Chiral dopants can themselves be mesogenic or non-mesogenic and

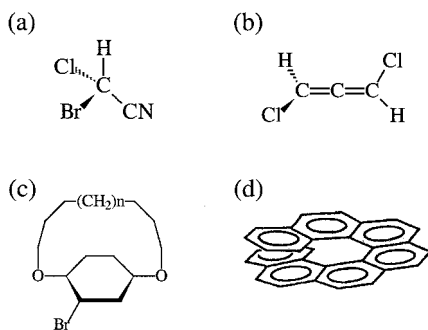


Fig. 1.17. Illustration of possible molecular chiral elements, here for non-mesogenic compounds: (a) a chiral center in chlorobromoacetonitrile, (b) a chiral axis in dichloroallene, (c) a chiral plane in an *ansa*-compound, and (d) a helical molecule like heptahelicene.

we speak of *induced chirality*. Further, mixtures of two mesogenic materials, one being chiral, the other achiral, can be prepared. We speak of chiral liquid crystal mixtures when the concentration of the chiral component is clearly larger than 5%. Obviously, there is no clear borderline between the use of chiral dopants and mixtures – it is just a case of the terminology used in the literature. We will see at a later point (Chapter 11) that phase chirality can also be introduced as a consequence of steric interactions, as in the case of the so-called “banana” phases.

The introduction of chirality into mesogenic systems has a tremendous impact on the respective liquid crystalline behavior. Novel structures, like the helical superstructure of the cholesteric and the SmC^* phase, appear. Whole new classes of phases, the so-called frustrated phases of the Blue Phase (BP^*) and the twist grain boundary phase (TGB^*), are observed. Also the physical properties of LC phases are modified by the loss of mirror symmetry. Tilted chiral smectic phases can exhibit a spontaneous polarization, and they are thus pyroelectric [55]. For several phases, namely SmC^* , SmI^* , and SmF^* , this spontaneous polarization is switchable between two stable states by an applied electric field. With the LC subjected to suitable geometry and boundary conditions, (improper) ferroelectricity is observed [56]. Orthogonal chiral smectic phases (SmA^* , SmB^*) likewise show what is called the electroclinic effect [19], in some sense the liquid crystal analogy to piezoelectricity. The properties of ferroelectric and antiferroelectric liquid crystals are discussed in great detail in the recent monographs by Lagerwall [57] and Mušević et al. [58]. An extensive overview on the effects of chirality in liquid crystals has just been published by Kitzerow and Bahr [59].

References

- [1] F. Reinitzer, *Monatsh. Chem.*, **9**, (1888), 421.
- [2] R. Virchow, *Arch. Pathol. Anat. Physiol. Klin. Med.*, **6**, (1854), 572.
- [3] C. Mettenheimer, *Corresp. Ver. Gem. Arb. Förd. Wiss. Heilkd.*, **24**, (1857), 331.
- [4] Planer, *Ann. Chem.*, **118**, (1861), 25.
- [5] W. Loebisch, *Ber. Deutsch. Chem. Ges.*, **5**, (1872), 510.
- [6] M. B. Rayman, *Bull. Soc. Chim. Paris*, **47**, (1887), 898.
- [7] O. Lehmann, *Z. Phys. Chem.*, **4**, (1889), 462.
- [8] V. Vill, LiqCryst database (www.lci-publisher.com/liqcryst.html).
- [9] H. Stegemeyer (ed.), *Liquid Crystals*, Steinkopff, Darmstadt, 1994.
- [10] P. J. Collings, M. Hird, *Introduction to Liquid Crystals: Chemistry and Physics*, Taylor & Francis, London, 1997.
- [11] S. Chandrasekhar, *Liquid Crystals*, 2nd edn., Cambridge University Press, Cambridge, 1992.
- [12] P. G. de Gennes, J. Prost, *The Physics of Liquid Crystals*, 2nd edn., Clarendon Press, Oxford, 1993.
- [13] D. Demus, J. Goodby, G. W. Gray, H.-W. Spiess, V. Vill (eds.), *Handbook of Liquid Crystals*, Wiley-VCH, Weinheim, 1998.
- [14] A. G. Petrov, *The Lyotropic State of Matter*, Gordon & Breach, New York, 1999.
- [15] G. Friedel, *Ann. Phys. (Fr.)*, **18**, (1922), 272.
- [16] H. Arnold, H. Sackmann, *Z. Elektrochem. Angew. Phys. Chem.*, **63**, (1959), 1171.
- [17] H. Sackmann, D. Demus, *Mol. Cryst. Liq. Cryst.*, **2**, (1966), 81.
- [18] K. H. Smalla, Thesis, Halle, Germany, 1983.
- [19] S. Garoff, R. B. Meyer, *Phys. Rev. Lett.*, **38**, (1977), 848.
- [20] S. T. Lagerwall, *Ferroelectrics*, **85**, (1988), 497.
- [21] M. Barón, *Pure Appl. Chem.*, **73**, (2001), 845.
- [22] P. H. Hermans, P. Platzeck, *Kolloid Z.*, **88**, (1939), 68.
- [23] V. Tsvetkov, *Acta Physicochim. (USSR)*, **16**, (1942), 132.
- [24] S. Chandrasekhar, N. V. Madhusudana, *Appl. Spectrosc. Rev.*, **6**, (1972), 189.
- [25] W. Maier, A. Saupe, *Z. Naturforsch.*, **13a**, (1958), 564.
- [26] W. Maier, A. Saupe, *Z. Naturforsch.*, **14a**, (1959), 882.
- [27] W. Maier, A. Saupe, *Z. Naturforsch.*, **15a**, (1960), 287.
- [28] K. K. Kobayashi, *J. Phys. Soc. Jpn.*, **29**, (1970), 101.
- [29] K. K. Kobayashi, *Mol. Cryst. Liq. Cryst.*, **13**, (1971), 137.
- [30] W. L. McMillan, *Phys. Rev. A*, **4**, (1971), 1238.
- [31] B. I. Ostrovskii, *Sov. Sci. Rev. (Sect. A, Phys. Rev.)*, **12(2)**, 85; reproduced in L. M. Blinov, V. G. Chigrinov, *Electro-optic Effects in Liquid Crystal Materials*, Springer-Verlag, Berlin, 1996, p. 7.
- [32] F. Giesselmann, P. Zugenmaier, *Phys. Rev. E*, **55**, (1997), 5613.
- [33] J. D. Brock, R. J. Birgeneau, J. D. Litster, A. Aharony, *Physics Today*, **7**, (1989), 52.

- [34] J. D. Brock, D. Y. Noh, B. R. McClain, J. D. Litster, R. J. Birgeneau, A. Aharony, P. M. Horn, J. C. Liang, *Z. Phys. B: Condens. Matter*, **74**, (1989), 197.
- [35] J. M. Kosterlitz, D. G. Thouless, *J. Phys. (Fr.)*, **6**, (1973), 1181.
- [36] B. I. Halperin, D. R. Nelson, *Phys. Rev. Lett.*, **41**, (1978), 121.
- [37] A. J. Leadbetter, J. C. Frost, M. A. Mazid, *J. Phys. Lett. (Fr.)*, **40**, (1979), L325.
- [38] R. Pindak, D. E. Moncton, S. C. Davey, J. W. Goodby, *Phys. Rev. Lett.*, **36**, (1981), 1135.
- [39] G. Heppke, D. Löttsch, D. Demus, S. Diele, K. Jahn, H. Zschke, *Mol. Cryst. Liq. Cryst.*, **208**, (1991), 9.
- [40] Ch. Bahr, G. Heppke, K. Wuthe, *Liq. Cryst.*, **12**, (1992), 997.
- [41] G. Heppke, D. Löttsch, B. Kampa, K.-D. Scherf, H. Zschke, *J. Prakt. Chem.*, **335**, (1993), 549.
- [42] G. Heppke, D. Löttsch, N. K. Sharma, D. Demus, S. Diele, K. Jahn, M. Neundorff, *Mol. Cryst. Liq. Cryst.*, **241**, (1994), 275.
- [43] J. V. Selinger, D. R. Nelson, *Phys. Rev. A*, **39**, (1989), 3135.
- [44] J. Prost, *Adv. Phys.*, **33**, (1984), 1.
- [45] J. W. Goodby, in *Handbook of Liquid Crystals*, D. Demus, J. Goodby, G. W. Gray, H.-W. Spiess, V. Vill (eds.), Wiley-VCH, Weinheim, 1998, vol. 2A, ch. 1, pp. 1–21.
- [46] P. E. Cladis, *Phys. Rev. Lett.*, **35**, (1975), 48.
- [47] P. E. Cladis, *Liq. Cryst.*, **24**, (1998), 15.
- [48] P. E. Cladis, in *Physical Properties of Liquid Crystals*, D. Demus, J. W. Goodby, G. W. Gray, H.-W. Spiess, V. Vill (eds.), Wiley-VCH, Weinheim, 1999, pp. 289–303.
- [49] S. Diele, P. Göring, in *Handbook of Liquid Crystals*, D. Demus, J. Goodby, G. W. Gray, H.-W. Spiess, V. Vill (eds.), Wiley-VCH, Weinheim, 1998, vol. 2B, ch. XIII, pp. 887–900.
- [50] R. Janoschek (ed.), *Chirality – From Weak Bosons to the α -Helix*, Springer-Verlag, Berlin, 1991.
- [51] Lord Kelvin, *Baltimore Lectures*, C. J. Clay & Sons, London, 1904; cited from I. Hargittai, M. Hargittai, *Symmetry Through the Eyes of a Chemist*, VCH, Weinheim, 1986.
- [52] L. Pasteur, *C. R. Hebd. Séances Acad. Sci. Paris*, **26**, (1848), 535.
- [53] V. Prelog, G. Helmchen, *Angew. Chem.*, **94**, (1982), 614.
- [54] R. S. Cahn, Sir C. Ingold, V. Prelog, *Angew. Chem. Int. Edn.*, **5**, (1966), 385.
- [55] R. B. Meyer, L. Liebert, L. Strzelecki, P. Keller, *J. Phys. Lett. (Fr.)*, **36**, (1975), L69.
- [56] N. A. Clark, S. T. Lagerwall, *Appl. Phys. Lett.*, **36**, (1980), 899.
- [57] S. T. Lagerwall, *Ferroelectric and Antiferroelectric Liquid Crystals*, Wiley-VCH, Weinheim, 1999.
- [58] I. Mušević, R. Blinc, B. Žekš, *The Physics of Ferroelectric and Antiferroelectric Liquid Crystals*, World Scientific, Singapore, 2000.
- [59] H.-S. Kitzerow, C. Bahr (eds.), *Chirality in Liquid Crystals*, Springer-Verlag, Berlin, 2001.

2

Surface Anchoring and Elasticity

For all practical applications of liquid crystals a uniform director orientation is of course essential. Even though “natural” textures obtained by polarizing microscopy usually serve for the characterization of liquid crystals, oriented samples can also elucidate the nature of different phases observed. For this reason we will discuss briefly different alignment conditions and some common preparation techniques. Within the scope of this text only a broad overview can be given; for a detailed treatment of surface anchoring and alignment techniques we refer to the review articles by Cognard [1] and Jérôme [2] and the monograph by Sonin [3].

2.1

Surface Anchoring and Preparation Techniques

The fact that liquid crystals can be oriented by adequate treatment of the confining substrates was already realized by Mauguin [4], who rubbed glass plates with lens paper to obtain partial planar alignment. Others used cotton or similar materials for unidirectional rubbing of glass slides [5, 6] to obtain micro-grooves that promote alignment. But it was not before the commercial use of liquid crystals in display devices looked promising that a whole variety of different techniques was developed to obtain the desired alignment. This should not conceal that, despite the fact that nowadays much is known about macroscopic alignment, the molecular mechanisms behind it still remain not fully understood.

Some general types of molecular orientation are distinguished, which are schematically depicted in Fig. 2.1. For *degenerate planar* alignment the long molecular axis is oriented in the plane of the substrate with the azimuthal angle being arbitrary. We speak of *uniform planar* alignment when the long molecular axis is not only oriented in the plane of the substrate, but also pointing along a preferred azimuthal direction. An orientation of the molecules with their long axis perpendicular to the substrate plane is called *homeotropic*, while oblique orientations are referred to as *tilted* or *uniform tilted*, if the tilt direction is fixed. To avoid confusion when later discussing chiral phases with a helical superstructure, especially the cholesteric phase, we will use the above terms exclusively to indicate the molecular orientation close to the surfaces, i. e. referring to boundary or anchoring condi-

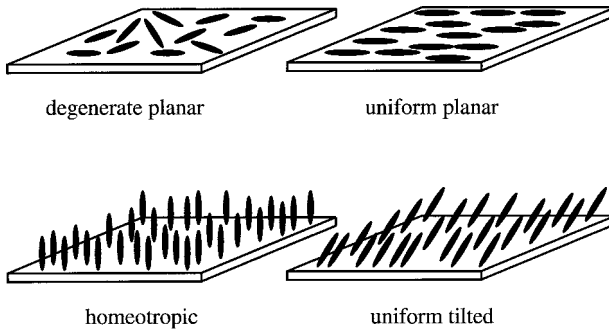


Fig. 2.1. Schematic illustration of different anchoring conditions, which can be obtained by various substrate treatment techniques.

tions, not the orientation of the helix twist axis. In the following, a number of alignment methods are outlined. These are methods based on experience, which often lead to the desired orientation. Nevertheless, it should be mentioned that they do not have to give satisfactory results for all materials.

2.1.1

Planar Alignment of Nematics

To achieve planar alignment of a nematic phase several methods can be employed. One of the most popular is the use of very thin, rubbed polymer layers on a solid glass substrate. Generally, the polymers, which are often polyimides or nylon, are dissolved in a solvent and spin-coated onto the substrate. The solvent quickly evaporates, leaving a thin, optically transparent film on the glass, which is then cured for some time at elevated temperatures. The substrates are subsequently rubbed, often by use of a velvet cloth, which is fixed to a rotating cylinder. A suitably constructed rubbing machine thus allows a variation of the rotation frequency, number of rubbing cycles, and pressure with which the substrate will be unidirectionally rubbed, in order to optimize the surface treatment process for best results. This procedure leads to microscopic grooves in the soft polymer layer, thus inducing anisotropic surface properties and a preferred direction, as has been demonstrated by atomic force microscopy (AFM) [7]. Figure 2.2 gives a schematic view of calamitic mesogens being oriented by a rubbed polymer film on a solid glass substrate. From the AFM investigations [7] two characteristic periodicities of the grooves have been observed, one in the order of 100 nm, which is believed to be related to clustering polymer chains, and another in the order of 2 μm , which corresponds to the width of the rubbing fibers. The microscopic alignment mechanism of rubbed polymer layers is most likely due to a combination of the surface topology (unidirectional grooves) and rubbing induced anisotropic dispersion interactions between the liquid crystal molecules and the oriented polymer chains. Also static electric interactions due to rubbing induced electrical charges can affect the alignment properties of the polymer layer.

Fig. 2.2. Uniform planar alignment of calamitic molecules obtained by unidirectional rubbing of a soft polymer layer deposited on a solid glass substrate.

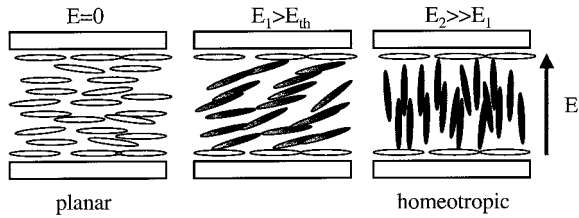
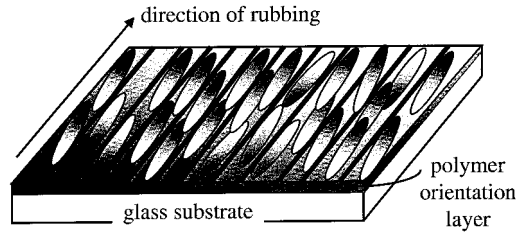


Fig. 2.3. Schematic illustration of the electric Freedericksz effect of a nematic liquid crystal with positive dielectric anisotropy. In the field-free state uniform planar alignment is observed. Application of an electric field above the threshold field results in a bulk reorientation

of the director, until at larger field amplitude a bulk homeotropic alignment is obtained. Depending on initial alignment conditions, sign of the dielectric anisotropy, and electric field direction, a variety of director configurations can be induced.

Oblique evaporation of thin SiO_x films on glass substrates was first reported by Janning [8] to result in planar alignment of nematics. Also other oxides, such as GeO_x or SeO_x , may be used. The preparation technique is relatively simple. The oxide is heated in a vacuum chamber to evaporate and condense on the substrate. Guyon and coworkers [9] showed that the nematic director in cells composed of such substrates is actually tilted. From detailed investigations [10–12] it is now known that either planar or tilted alignment can be achieved, depending on the angle of evaporation α . The narrow angular interval (often in the range $62^\circ < \alpha < 78^\circ$ [13]) at which this continuous anchoring transition occurs is dependent on the thickness of the SiO_x layer [12, 14] and the choice of the liquid crystal material.

Above we discussed how rubbing a polymer film gives rise to grooves, which cause the director to be aligned along this preferred direction. Photolithographic techniques, as introduced by Barbero [15], Kanel et al. [16], and Sugimura and Kawamura [17], allow for the formation of similar surface structures, but with a defined geometry. Rectangular and trapezoid patterns result in uniform planar alignment [16], while a sawtooth surface relief may lead to either homeotropic or planar alignment, depending on the slope of the surface structure [15], i. e. the sawtooth angle.

Electric and magnetic fields can be used to reorient and align the nematic director. This is well known as the Freedericksz effect [18], first reported for application of magnetic fields and schematically illustrated in Fig. 2.3 for application of an

[24–26]. On the molecular level homeotropic alignment results primarily from steric interactions between the LC molecules and the surfactant molecules, and thus alignment quality is crucially dependent on the surface density of the surfactant [27]. If the surface density of the surfactant molecules is too low, in LB film research called the gaseous (G) phase, steric intermolecular interactions are small, which results in random LC orientation. If on the other hand the surfactant surface density is too large, referred to as the condensed (C) phase, interaction between the hydrocarbon tails of the liquid crystal and the surfactant molecules is also reduced, because of strongly limited interpenetration. The resulting alignment is again random. In the intermediate surface density regime, called the expanded (E) phase, homeotropic alignment is achieved (see again Plate 2). In this range the distance r between surfactant molecules is in the order of the molecular length L of the mesogen. The discussion of homeotropic LC alignment by Langmuir–Blodgett films is schematically summarized in Fig. 2.4. Even though the above outlined deposition techniques for obtaining homeotropic alignment generally lead to good results, we should not forget that there are certain problems associated with them. The predominant one is the possible dissolution of surfactant molecules within the liquid crystal as time proceeds. In contrast to the solid SiO_x surfaces or cross-linked polymers, as discussed above, we are here dealing with single molecules, which are much easier to dissolve. This would obviously slowly change the composition of the sample and thus also its physical properties. A likely way to detect possible incorporation of alignment layer molecules within the mesogenic phase is a detection of the phase transition temperatures. Especially the clearing point (Iso–LC transition) generally changes considerably (by a few Kelvins), even for small amounts of non-mesogenic compounds added.

Other methods to produce homeotropic alignment conditions are the above mentioned photolithographic techniques and the respective electric or magnetic field treatment.

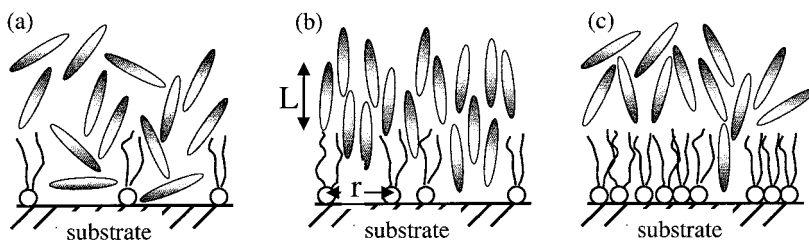


Fig. 2.4. Schematic illustration of homeotropic anchoring induced by a surfactant layer deposited on a solid substrate. (a) If the surfactant surface density is too low (called gaseous phase for Langmuir–Blodgett (LB) films), random alignment is obtained; steric interactions are not sufficient to induce LC alignment. (b) In the expanded phase of the LB layer, where the distance between surfactant molecules is approximately equal to the LC molecular length, homeotropic alignment is obtained. (c) Increasing the surfactant density to the condensed phase again results in random alignment, because of a reduction of steric interactions between the liquid crystal and the aliphatic chains of the surfactant.

2.1.3

Alignment of Smectic Phases

Producing good alignment of smectic phases is sometimes reminiscent of the work of the medieval alchemists. A technique that produces perfect alignment for one compound may not work at all even for similar materials. In that sense we will here only discuss some rules of thumb, which apply to “nicely behaving” compounds. The method that is applied most frequently to obtain planar alignment of smectic LCs is the use of rubbed polymer films deposited on glass substrates, as discussed above for nematics. Also thin Teflon layers have been shown to produce well aligned planar samples [28]. In that case a heated Teflon block is unidirectionally rubbed over the substrate. Homeotropic alignment is often achieved by deposition of surfactants on the substrates, as discussed above, also for dodecylbenzoic acid and silanes. Nevertheless, it is hard to obtain uniform homeotropic alignment over large sample regions. Personally, I have had good experiences with a material abbreviated as JALS 240-R40, a polyimide available from JSR Electronics (Leuven, Belgium) to produce homeotropic alignment. Another method to obtain good homeotropic alignment for smectic phases is the preparation of free-standing films, although these are of course only of limited use when the application of electric fields is required. Generally speaking, one can say that, whatever results in good planar or homeotropic alignment of nematic phases also promotes the same type of orientation for smectic phases.

If the material under investigation has a phase sequence of Iso–N–SmA, usually better alignment is obtained than for a direct Iso–SmA transition. For this reason, most commercially available ferroelectric SmC* liquid crystal mixtures are tuned in such a way that they exhibit a narrow N* phase mediating the Iso* and the smectic A* phase. If the transition to the smectic phase is directly from the isotropic melt, often very slow cooling (0.1 K min^{-1} or less) in combination with a small temperature gradient produces the best alignment.

In the case of ferroelectric liquid crystals (SmC* phase), application of an electric square wave field in the direct vicinity of the transition to the SmA* phase can considerably improve alignment, also in combination with a continuous temperature cycling across the transition. This does not generally apply to ferroelectric liquid crystals (FLCs) with an N*–SmC* transition, where electric field application in the direct vicinity of the transition often results in unoriented samples.

Another procedure to obtain planar alignment of smectic phases is the application of shear forces in the respective smectic phase. In specially constructed cell holders [29], the sample is sheared by a directed mechanical displacement of the upper substrate plate with respect to the lower, fixed one. This treatment can produce very well aligned planar smectic samples, which nevertheless often do not show long term stability and may also sometimes result in homeotropic alignment, flipping the smectic layers by 90° , such that the layer planes are parallel to the substrates.

In conclusion, there is no generally valid recipe on how to orient liquid crystals to obtain a certain desired director configuration. This seems to be a broad field, where only experimental experience and attempts for optimization can produce

good results. Sometimes it looks as if the companies producing large, flat panel displays do indeed have a much deeper understanding of alignment techniques, alignment materials, and the molecular mechanisms driving LC alignment. Nevertheless, be assured that they are (unfortunately) not willing to share their secrets.

2.2

Bulk Elasticity

Compared to solid state materials the elastic constants of liquid crystals, especially those of the nematic and the fluid smectic phases, are several orders of magnitude smaller, in the order of 10^{-11} N. This means that a liquid crystal can easily be deformed by external forces, such as mechanical, electric or magnetic forces, which is in agreement with our everyday experience. Gently press on your laptop display and you will see the deformations causing changes in birefringence, appearing as bright color play. These heal out after some time, due to boundary conditions and the fact that the deformation energies are smaller than the thermal energy. Elasticity of liquid crystals is generally treated in the context of continuum theory, which neglects the structural details on the molecular level. It is assumed that the external forces are small compared to the intermolecular forces, and that the scale of the elastic deformation is much larger than the molecular dimension, meaning that the director field $\mathbf{n}(\mathbf{r})$ varies only slowly and smoothly on the molecular scale. This is usually the case, as elastic deformations occur over length scales of several micrometers and the molecular dimensions are in the order of nanometers.

In solid state materials, deformations are related to a displacement of atoms or molecules from the three dimensional crystal lattice. They are thus described by translational displacement, which involves restoring elastic forces opposing the deformations. In contrast, deformations in (nematic) liquid crystals are related to variations of the director field $\mathbf{n}(\mathbf{r})$. This is described by orientational displacement, which involves restoring elastic torques opposing the deformations. Note that these are absent in common isotropic liquids.

2.2.1

The Nematic and Cholesteric Phase

If a nematic liquid crystal is deformed by external forces, such as boundary forces or other mechanical, electric or magnetic fields, the free energy density F is increased as compared to a completely uniformly aligned nematic director configuration with free energy density F_0 . This increase of F due to deformations, which we may call F_d , is described by the continuum theory, which was first developed by Oseen [30] and Zocher [31] and later outlined in the present form by Frank [32].

All bulk deformations of a nematic phase can be traced back to three fundamental elastic deformations called *splay*, *twist* and *bend*. These are schematically depicted in Fig. 2.5. A pure splay deformation would be observed for a planar nematic in a wedge cell, while a homeotropic nematic in a wedge cell exhibits a pure bend

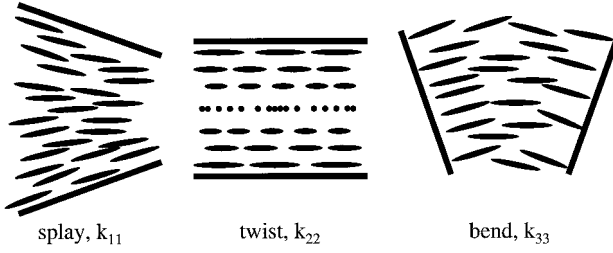


Fig. 2.5. Illustration of the three fundamental bulk distortions of a nematic liquid crystal: splay, twist, and bend. Splay can be realized by a uniform planar nematic in a wedge cell. Bend can correspondingly be achieved for homeotropic anchoring in a wedge cell. Twist distortions are obtained by twisting parallel substrates with uniform planar alignment.

deformation. In the case of a splay deformation one has $\text{div } \mathbf{n} \neq 0$; for a bend deformation one has $\text{curl } \mathbf{n}$ perpendicular to \mathbf{n} and $(\mathbf{n} \text{ curl } \mathbf{n}) \neq 0$. A pure twist deformation can be obtained by twisting two parallel substrates with uniform planar anchoring conditions. One then has $\text{curl } \mathbf{n}$ parallel to \mathbf{n} and $(\mathbf{n} \times \text{curl } \mathbf{n}) \neq 0$. The associated elastic contributions to the free energy density are quadratic terms in the curvature strains with three independent elastic constants: k_{11} for a splay deformation, k_{22} for a twist deformation, and k_{33} for a bend deformation. The unit of the elastic constants k_{ii} is energy per length, thus $\text{J m}^{-1} = \text{N}$. The free energy density associated with these deformations is given by:

$$F_d = \left(\frac{1}{2}\right)k_{11}(\text{div } \mathbf{n})^2 + \left(\frac{1}{2}\right)k_{22}(\mathbf{n} \text{ curl } \mathbf{n})^2 + \left(\frac{1}{2}\right)k_{33}(\mathbf{n} \times \text{curl } \mathbf{n})^2 \quad (2.1)$$

Equation (2.1) is the fundamental equation describing the bulk elasticity of nematics. It is beyond the scope of this text to derive Eq. (2.1) and its implications, which can be followed for example in the book by de Gennes and Prost [33].

For simplicity, often the so-called “one-constant approximation” is used with $k_{11} = k_{22} = k_{33} = K > 0$. The deformational free energy density contribution then reduces to

$$F_d = \left(\frac{1}{2}\right)K[(\text{div } \mathbf{n})^2 + (\text{curl } \mathbf{n})^2] \quad (2.2)$$

In principle, also a term associated with the surfaces should be included in Eq. (2.1), such that

$$F_d = F_{d,\text{bulk}} + F_{d,\text{surface}} \quad (2.3)$$

However, we know from experiment that in most cases the substrates impose definite boundary conditions at the surface, which is called strong anchoring.

Chiral nematic or cholesteric phases exhibit an inherent twist with the twist axis perpendicular to the local director and a pitch P_0 of the undisturbed helix. This is accounted for in the expression for the free energy density of Eq. (2.1) by inclusion of the helical wavevector $q_0 = 2\pi/P_0$ to give [32]:

$$F_d^* = \left(\frac{1}{2}\right)k_{11}(\text{div } \mathbf{n})^2 + \left(\frac{1}{2}\right)k_{22}(\mathbf{n} \text{ curl } \mathbf{n} + q_0)^2 + \left(\frac{1}{2}\right)k_{33}(\mathbf{n} \times \text{curl } \mathbf{n})^2 \quad (2.4)$$

where q_0 is positive for a right-handed and negative for a left-handed twist.

2.2.2

The Fluid Smectic Phases

Introduction of one dimensional positional order makes a description of elasticity increasingly complex, so that we can here only outline the basic observations. A detailed treatment of the elasticity theory of fluid smectic phases can be found in the books by de Gennes and Prost [34] and Lagerwall [35]. Let us first consider the SmA phase, which exhibits solid-like properties in the direction perpendicular to the liquid-like smectic layers. This means that the compression of the smectic layers, i. e. an alteration of the smectic layer thickness d , requires large energies and is therefore unlikely to be observed. Considering in first approximation a constant layer spacing $d = \text{const.}$, this in turn means that the only deformation allowed for SmA is the splay deformation in the director field, corresponding to a smectic layer bend (Fig. 2.6(a)). Bend deformations in the director field, which correspond to a layer splay (Fig. 2.6(b)), as well as twist deformations would both change the layer thickness. These are so-called *hard deformations* and are forbidden for incompressible smectic layers. They require the introduction of defects, namely edge dislocations for bend deformations and screw dislocations for twist deformations. Especially the latter case will be treated in more detail, when discussing the so-called twist grain boundary phases in Chapter 6. Assuming incompressible smectic layers, the free energy density of the SmA phase is thus simply given by:

$$F_d = \frac{1}{2}k_{11}(\text{div } \mathbf{n})^2 \quad (2.5)$$

The elastic constant k_{11} is of the same order of magnitude as observed for nematics. If we now loosen our hard constraint and allow a slight compression of smectic layers, an elastic constant B has to be introduced, analogous to the compressibility of a liquid, which has the dimension of an energy per volume, $\text{J m}^{-3} = \text{N m}^{-2}$. Its order of magnitude is found to be $B \approx 10^{-10} \text{ N cm}^{-2}$. Consider an undisturbed smectic A phase with the layer normal \mathbf{k} along the z direction. If

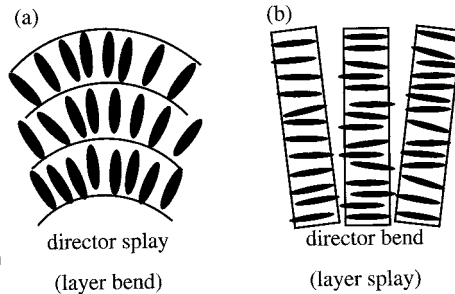


Fig. 2.6. Splay and bend distortions for a SmA phase. Splay in the director field $\mathbf{n}(\mathbf{r})$ corresponds to bend layers, while bend in $\mathbf{n}(\mathbf{r})$ represents a smectic layer splay. Layer splay and twist are hard deformations, which are generally expelled from the SmA phase.

we introduce a new variable $u = u(x, y)$, which describes the distortion of the smectic layer from its initial state, the free energy density of the SmA phase for small distortions is derived as

$$F_d = \frac{1}{2} \left[k_{11} (\text{div } \mathbf{n})^2 + B \left(\frac{\partial u}{\partial z} \right)^2 \right] \quad (2.6)$$

Terms $(\partial u / \partial x)^2$ and $(\partial u / \partial y)^2$ do not appear, as they describe a rotation around the y and x axes, respectively, and do not contribute to the elastic energy. It can be shown that small distortions in fluid smectics are mediated over macroscopic distances [34, 35]. This distinguishes smectic liquid crystals from solid state crystals, where distortions relax over length scales comparable to that of the distortion itself. The elastic properties of the SmA phase are thus described by two elastic constants, which even reduce to one when considering the case of incompressible smectic layers.

For SmC the situation becomes incomparably complex. In addition to the constant B describing the layer compression of SmA, we need a further nine independent constants, leaving us with a total of 10 elastic constants. Four terms are needed to describe distortions of the director field for undistorted smectic layers, which were introduced by Saupe [36]. The remaining five were derived by the Orsay group [37], of which three terms describe the curvature of smectic layers and two terms describe the coupling between director field distortions and layer curvature. If smectic layer splay and twist are disregarded, thus not allowing for a layer compression or hard deformations, like variations in the tilt angle θ , which require large energies, the following expression for the free energy density of the achiral SmC phase is obtained in a first approximation:

$$F_d = \left(\frac{1}{2} \right) B_1 (\text{div } \mathbf{c})^2 + \left(\frac{1}{2} \right) B_2 (\mathbf{c} \text{ curl } \mathbf{c})^2 + \left(\frac{1}{2} \right) B_3 (\mathbf{k} \text{ curl } \mathbf{c})^2 - B_{13} (\mathbf{c} \text{ curl } \mathbf{c}) (\mathbf{k} \text{ curl } \mathbf{c}) \quad (2.7)$$

where the so-called \mathbf{c} director is the local projection of \mathbf{n} on the smectic layer plane and \mathbf{k} is the smectic layer normal (see Fig. 2.7). Note that Eq. (2.7) is only valid for *soft deformations*. The relations between the SmC elastic constants and the Frank–Oseen constants were pointed out by Lagerwall and Dahl [38]. They obtained

$$B_1 = k_{11} \sin^2 \theta \quad (2.8a)$$

describing a splay in the \mathbf{c} director,

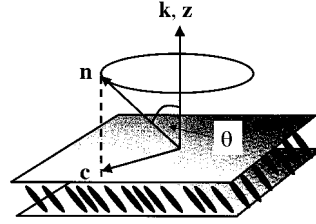
$$B_2 = k_{22} \sin^4 \theta + k_{33} \sin^2 \theta \cos^2 \theta \quad (2.8b)$$

describing a twist in the \mathbf{c} director,

$$B_3 = k_{22} \sin^2 \theta \cos^2 \theta + k_{33} \sin^4 \theta \quad (2.8c)$$

describing a bend in the \mathbf{c} director, and

$$B_{13} = (k_{33} - k_{22}) \sin^3 \theta \cos \theta \quad (2.8d)$$

Fig. 2.7. Definition of the \mathbf{c} director of a SmC phase.

describing the coupling of in-plane bend and layer twist. From experiments it is observed that $k_{33} > k_{22}$, so that $B_{13} > 0$. Equation (2.7) is the SmC analog to Eq. (2.1) derived for the nematic phase.

Comparable to the introduction of a chiral term to account for the spontaneous twist of the N^* phase, also for the chiral SmC * phase additional terms have to be introduced [34, 35], which describe spontaneous deformations:

$$F_d^* = \left(\frac{1}{2}\right) B_1 (\text{div } \mathbf{c})^2 + \left(\frac{1}{2}\right) B_2 (\mathbf{c} \text{ curl } \mathbf{c})^2 + \left(\frac{1}{2}\right) B_3 (\mathbf{k} \text{ curl } \mathbf{c})^2 - B_{13} (\mathbf{c} \text{ curl } \mathbf{c}) (\mathbf{k} \text{ curl } \mathbf{c}) + D_1 (\mathbf{k} \text{ curl } \mathbf{c}) - D_3 (\mathbf{c} \text{ curl } \mathbf{c}) \quad (2.9)$$

with

$$D_1 = k_{22} q_0 \sin \theta \cos \theta + k_{33} \beta \sin^2 \theta \quad (2.10a)$$

describing a bend of the \mathbf{c} director in the plane of the smectic layer and

$$D_3 = k_{22} q_0 \sin^2 \theta - k_{33} \beta \sin^2 \theta \cos \theta \quad (2.10b)$$

where the scalar $\beta \neq 0$ describes the strength of spontaneous bend; $\beta = 0$ for the achiral SmC phase. The D_3 term in Eq. (2.9) is simply a spontaneous twist, accounting for the intrinsic helical superstructure of the SmC * phase (see Chapter 7).

References

- [1] J. Cognard, *Mol. Cryst. Liq. Cryst.*, **5**, (1982), 1.
- [2] B. Jérôme, *Rep. Prog. Phys.*, **54**, (1991), 391.
- [3] A. A. Sonin, *The Surface Physics of Liquid Crystals*, Gordon & Breach, Luxembourg, 1995.
- [4] C. Mauguin, *C. R. Acad. Sci., Paris*, **156**, (1911), 1246.
- [5] H. Zocher, K. Coper, *Z. Phys. Chem.*, **132**, (1928), 295.
- [6] P. Chatelain, *Bull. Soc. Fr. Min.*, **60**, (1937), 300.
- [7] Y. B. Kim, H. S. Kim, J. S. Choi, M. Matuszczyk, H. Olin, M. Buivydas, P. Rudquist, *Mol. Cryst. Liq. Cryst.*, **262**, (1995), 89.
- [8] J. L. Janning, *Appl. Phys. Lett.*, **21**, (1972), 173.
- [9] E. Guyon, P. Piéranski, M. Biox, *Lett. Appl. Eng. Sci.*, **1**, (1973), 19.
- [10] B. Jérôme, P. Piéranski, *J. Phys. (Fr.)*, **49**, (1988), 1601.
- [11] B. Jérôme, P. Piéranski, M. Boix, *Europhys. Lett.*, **5**, (1988), 693.
- [12] M. Monkade, M. Boix, G. Durand, *Europhys. Lett.*, **5**, (1988), 697.
- [13] P. Jägemalm, L. Komitov, *Liq. Cryst.*, **23**, (1997), 1.
- [14] K. Hiroshima, M. Mochizuki, *Jpn. J. Appl. Phys.*, **19**, (1980), 567.
- [15] G. Barbero, *Nuovo Cimento Lett.*, **29**, (1980), 553.
- [16] H. V. Kanel, J. D. Litster, J. Melugalis, H. I. Smith, *Phys. Rev. A*, **24** (1981), 2713.
- [17] A. Sugimura, T. Kawamura, *Jpn. J. Appl. Phys.*, **23**, (1984), 137.
- [18] V. Freedericksz, V. Tsvetkov, *Phys. Z. Sov. Union*, **6**, (1934), 490.
- [19] V. S. U. Fazio, L. Komitov, S. T. Lagerwall, *Liq. Cryst.*, **24**, (1998), 427.
- [20] K. Hiltrop, H. Stegemeyer, *Mol. Cryst. Liq. Cryst.*, **49**, (1978), 61.
- [21] K. Hiltrop, H. Stegemeyer, *Ber. Bunsenges. Phys. Chem.*, **82**, (1978), 884.
- [22] H. Mada, *Mol. Cryst. Liq. Cryst.*, **51**, (1979), 43.
- [23] K. B. Blodgett, I. Langmuir, *Phys. Rev.*, **51**, (1937), 964.
- [24] L. M. Blinov, *Usp. Khim.*, **52**, (1983), 1263.
- [25] L. M. Blinov, *Usp. Fiz. Nauk*, **155**, (1988), 443.
- [26] G. Barbero, A. G. Petrov, *J. Phys.: Condens. Matter*, **6**, (1994), 2291.
- [27] K. Hiltrop, H. Stegemeyer, *Ber. Bunsenges. Phys. Chem.*, **85**, (1981), 582.
- [28] X. Quintana, J. M. Oton, M. Brunet, R. Lotoux, *Ferroelectrics*, **244**, (2000), 275.
- [29] K. Skarp, G. Andersson, *Ferroelectrics Lett.*, **6**, (1986), 67.
- [30] C. W. Oseen, *Trans. Faraday Soc.*, **29**, (1933), 883.
- [31] H. Zocher, *Trans. Faraday Soc.*, **29**, (1933), 945.
- [32] F. C. Frank, *Discuss. Faraday Soc.*, **25**, (1958), 19.
- [33] P. G. de Gennes, J. Prost, *The Physics of Liquid Crystals*, 2nd edn., Clarendon Press, Oxford, 1993, ch. 3, pp. 98–162.
- [34] *Ibid.*, ch. 7, pp. 337–407.
- [35] S. T. Lagerwall, *Ferroelectric and Antiferroelectric Liquid Crystals*, Wiley-VCH, Weinheim, 1999, ch. 11, pp. 275–300.
- [36] A. Saupe, *Mol. Cryst. Liq. Cryst.*, **7**, (1969), 59.
- [37] Orsay Group on Liquid Crystals, *Solid State Commun.*, **9**, (1971), 653.
- [38] S. T. Lagerwall, I. Dahl, *Mol. Cryst. Liq. Cryst.*, **114**, (1984), 151.

3

Polarizing Microscopy

Polarizing microscopy is one of the essential tools for the characterization of newly synthesized mesogenic materials, together with differential scanning calorimetry (DSC) and x-ray investigations. While DSC is easily and quickly carried out, it merely provides information on phase transition temperatures and the order of the transitions. X-ray investigations for actual structural evaluation, i. e. determination of the phase type, have to be performed on macroscopically well oriented samples, which is often time consuming and sometimes hard to realize. Therefore x-ray studies are often carried out on unoriented samples, while the results only allow limited characterization of the structural features. Polarizing microscopy on the other hand can provide a determination of both phase transition temperatures and phase type. This is done by temperature dependent texture investigations between crossed polarizers, the main topic of this book. Characteristic textures and defect structures, which change when passing a phase transition, reveal the phase type observed. These will be discussed phase by phase in the following chapters. At this point it should be stressed that a characterization of liquid crystals by textural appearance requires some experience, especially for the higher ordered and soft crystal phases.

3.1

The Polarizing Microscope

As the polarizing microscope is the essential piece of equipment for texture studies, it will briefly be introduced. A typical setup of a polarizing microscope is shown in Fig. 3.1. It consists of a light source, which is generally a halogen light bulb emitting white light with a wavelength characteristic provided by the producer. The light is reflected upwards by a mirror, passes through a lens, and is linearly polarized by a sheet polarizer, which can often be rotated by 360° . For a white light source we can also insert a wavelength filter at this point, if wavelength dependent experiments have to be carried out. These filters are available for a variety of wavelengths, corresponding to electronic transitions in the visible range of the spectrum, and their bandwidth should be 10 nm or smaller.

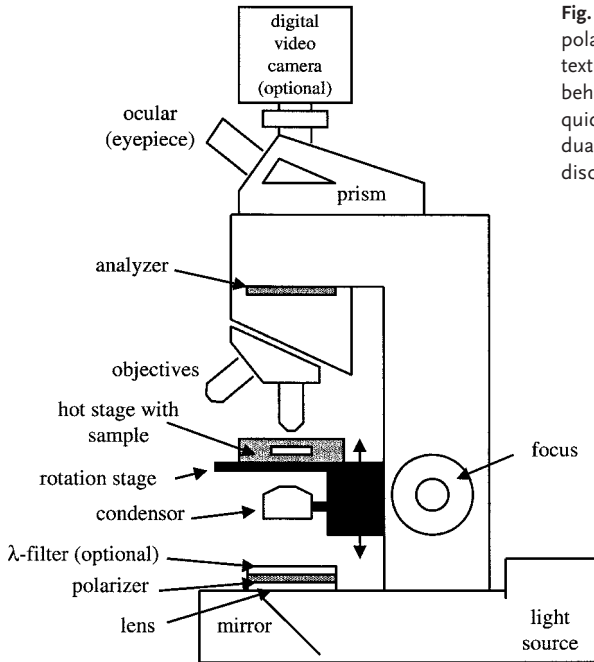


Fig. 3.1. Schematic setup of a polarizing microscope as used for texture studies and the optical behavior of uniformly aligned liquid crystal phases. The individual parts of the microscope are discussed briefly in the text.

The light then enters the condenser, probably the most neglected part of a polarizing microscope, despite its importance for optimal imaging of the sample. The condenser collects the light from the light source and assures a uniform illumination of the sample. For this, the aperture iris must be adjusted correctly. Choosing it open too wide can cause stray light due to refraction to blur the image and reduce contrast. Choosing it too small results in image distortion, reduction of resolution, and too dark an image. Additionally, the distance between the condenser and the sample has to be adjusted to focus the light beam correctly and to assure proper illumination. Sometimes the condenser has to be adjusted for each individual objective.

Microscopes for liquid crystal research are generally equipped with a rotatable stage onto which a hot stage, containing the sample, should be securely mounted, to assure a precise rotation of the sample in a plane perpendicular to the direction of light propagation. The transmitted light then passes into the objective. This is another fundamental part of the microscope, as it crucially determines the quality of the image. Whenever purchasing a new microscope, the objectives are the part where saving money is not well advised. For texture studies, often three different objectives are employed, $\times 5$ (red) for low magnification, and $\times 10$ (yellow) and $\times 20$ (green) for medium magnification. Sometimes also a $\times 40$ (blue) objective can be useful to resolve small structures, or for conoscopic studies. In any case, objectives with a long working distance are advisable, because often a hot stage does not allow focusing of the sample stage too close to the objective.

After passing through the objective, the light passes through the analyzer, a second polarizer that is often rotatable by 360° and is also removable. For texture studies the analyzer is oriented at right angles to the polarizer, i. e. with no birefringent sample present, the field of view is black. The ocular or eyepiece serves to magnify the image further. Often a magnification of $\times 10$ is used. The ocular also determines the field of view.

Alternatively, after opening a shutter or by use of a semi-transmitting mirror, the image can also be projected onto a camera mounted on the microscope by an adjustable tube. High quality images are generally achieved simply with slide films. If a time resolved image acquisition is required to study dynamic effects, analog video cameras in combination with frame grabber hard- and software are used. These provide time resolution of up to 25 frames per second, but only at rather low digital resolution of generally 760×580 pixels. A further alternative are digital CCD (charge coupled device) cameras, but time resolution in combination with high digital resolution can be quite expensive.

Some microscopes are equipped with a second light source, placed between the ocular and the objective. These can illuminate the sample from above, allowing for *reflected light microscopy*, a crucial tool in the study of selective reflection properties of chiral, helical liquid crystal phases, such as N^* or SmC^* . More information about polarizing microscopy can be found in the books by Bradbury and Bracegirdle [1] and Robinson and Bradbury [2]. A good and detailed review with a large amount of technical information on different microscope parts is available from the Molecular Expressions website [3].

3.2

Basic Liquid Crystal Optics

A simple liquid is isotropic and its index of refraction is independent of the direction of the incident light beam. An incident ray is refracted according to Snell's law of refraction. In contrast, the vast amount of crystalline materials are anisotropic, which means that their index of refraction depends on the direction of light propagation. This is a property that is shared by liquid crystals.

3.2.1

Uniaxial Phases

Most liquid crystal phases, such as N and SmA , are optically positive, which means that the index of refraction parallel to the optic axis, $n_{||}$, is larger than that perpendicular to it, n_{\perp} , or in other words $\Delta n = n_{||} - n_{\perp} > 0$. The reverse is true for optically negative materials, such as most cholesteric (N^*) phases, where the optic axis coincides with the helix axis and not with the (local) director. The situation is generally illustrated by the *indicatrix*, an ellipsoid with its long and short axes equal to $n_{||}$ and n_{\perp} for a positive medium or to n_{\perp} and $n_{||}$ for a negative medium, as shown in Fig. 3.2 for a *uniaxial* phase. This is a medium with two principal refractive indices

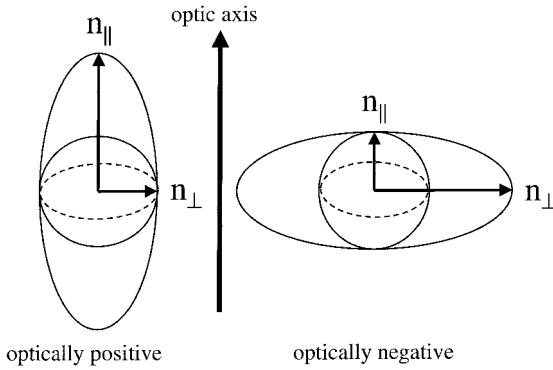


Fig. 3.2. Illustration of the indicatrix of a uniaxial, optically positive (left) and optically negative (right) material. Note that, even if it is tempting to do so, the shape of the indicatrix should not be confused with the elongated shape of a liquid crystal molecule.

and only one optic axis. This is given by the normal to a plane whose cut with the indicatrix is a circle.

An incoming light beam is split into two components, one that follows Snell's law of refraction, called the *ordinary* ray, and one that does not, called the *extraordinary* ray. The two beams propagate in different directions, which leads to the well known double images as is often demonstrated with calcite crystals. Additionally, their polarizations are perpendicular to each other. The ordinary and extraordinary rays propagate through the birefringent medium at different velocities, because they experience different indices of refraction, n_o and n_e , respectively. This leads to a phase difference δ , which is given by

$$\delta = \frac{2\pi}{\lambda} (n_e - n_o) d \quad (3.1)$$

where λ is the vacuum wavelength and d is the distance traveled in the medium (for normal incidence equal to the cell gap). The indices of refraction n_o and n_e are related to the principal indices of refraction $n_{||}$ and n_{\perp} by

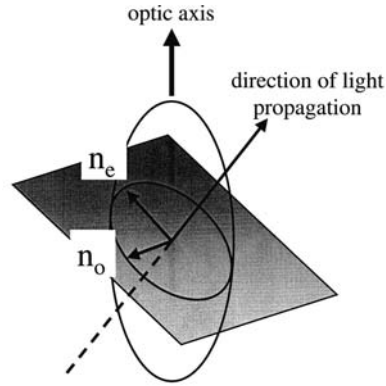
$$n_o = n_{\perp} \quad (3.2a)$$

and

$$n_e = \frac{n_{||} n_{\perp}}{\sqrt{n_{||}^2 \cos^2 \phi + n_{\perp}^2 \sin^2 \phi}} \quad (3.2b)$$

with ϕ being the angle between the optic axis and the direction of light propagation. The construction to determine the refractive indices is schematically shown in Fig. 3.3 for an optically positive medium. The indicatrix is cut by a plane perpendicular to the direction of light propagation and containing the center of the index ellipsoid. This gives an ellipse with the long axis equal to n_e and the short axis equal to n_o . The directions of the long and short axes correspond to the polarization of the extraordinary and ordinary beams, respectively.

Fig. 3.3. Schematic illustration for the determination of the refractive index of the ordinary beam, n_o , and the extraordinary beam, n_e , for an arbitrary direction of light propagation in an optically uniaxial medium.



In the general case, the incident linearly polarized light is converted to elliptically polarized light, with a component that can pass through the crossed analyzer; the sample appears bright. The transmitted intensity is given by

$$I = I_0 \sin^2 2\varphi \sin^2 \frac{\delta}{2} \quad (3.3)$$

where I_0 is the light intensity after the polarizer and φ is the azimuthal angle, i. e. the angle between the analyzer and the projection of the optic axis onto the sample plane (Fig. 3.4). The first term of Eq. (3.3) largely describes the changes in transmitted light intensity when rotating a birefringent sample between crossed polarizers. The second term is responsible for the beautiful colors of the liquid crystal textures.

Let us briefly consider the example of a well aligned uniaxial nematic or SmA phase between crossed polarizers. For homeotropic orientation, the direction of light propagation coincides with the optic axis. In this case $\phi = 0^\circ$ and with Eq. (3.2) we have $n_e - n_o = 0$ and therefore $\delta = 0$. With Eq. (3.3), we see that the transmitted intensity will always be equal to $I = 0$ for all positions φ of the sample between crossed polarizers. For this reason the uniform homeotropic nematic and

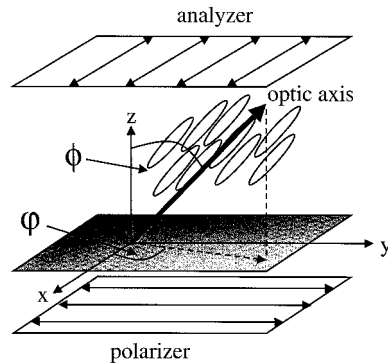


Fig. 3.4. Schematic figure of a uniformly oriented, uniaxial liquid crystal for the definition of different angles as used in the text.

SmA texture is also called *pseudo-isotropic*. For uniform planar alignment $\phi = 90^\circ$, thus $n_o = n_{\perp}$ and $n_e = n_{\parallel}$ or $\Delta n = n_{\parallel} - n_{\perp}$. The transmitted intensity changes with $\sin^2(2\varphi)$. It has a maximum for $\varphi = 45^\circ$ and a minimum for $\varphi = 0^\circ$ and $\varphi = 90^\circ$. The sample appears dark whenever the optic axis is parallel to one of the polarizer directions. The texture appearance has a periodicity of 90° when rotating the sample through crossed polarizers.

3.2.2

Biaxiality

We now leave the constraint of rotational symmetry around the optic axis, as observed for N and SmA phases, and consider phases that do not have C_∞ symmetry, namely the tilted smectics, like SmC. In this case the optics becomes more complicated, as we have a *biaxial* medium. This is characterized by three principal refractive indices, n_1 , n_2 , and n_3 , as schematically depicted in Fig. 3.5 with $n_1 < n_2 < n_3$. The indicatrix is a flattened ellipsoid and the material exhibits two optic axes. These are again given by the normals to the two planes that cut the indicatrix to give a circle. As outlined for the uniaxial case, light propagating along the direction of any of the two optic axes will not experience any birefringence and will leave the sample with its polarization state unchanged. In liquid crystals the biaxiality is generally very small, in the order of 10^{-3} [4, 5]. For this reason it is often neglected.

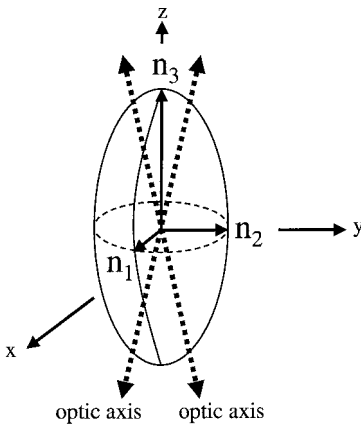


Fig. 3.5. Optical indicatrix of a biaxial, optically positive material.

3.2.3

Optical Activity

A short comment has to be made concerning chiral liquid crystals. As mentioned above, these exhibit optical activity [6, 7]: they turn the polarization plane of propagating light and thus alter the polarization state. This phenomenon is also observed in the isotropic phase. The angle through which the polarization plane is rotated is proportional to the distance that the light beam propagates through the medium.

This *molecular* optical activity of chiral liquid crystals is generally very small, because of the very thin cell gaps in the order of a few micrometers. For this reason it can commonly be disregarded. The situation is completely different when optical activity is observed as a *phase property* of liquid crystal phases with a helical superstructure, namely N^* and SmC^* . This can lead to a rotation of the polarization plane by several thousands of degrees. The optics of helical phases will be discussed in more detail in Chapter 5.

3.3

Conoscopy

Up to now we have discussed polarization optics for parallel light beams, thus *orthoscopic* observation. In principle this gives a magnified image of the sample. Observation of birefringent samples in polarized convergent light on the other hand is called *conoscopy* (Fig. 3.6), which is achieved by insertion of a Bertrand lens between the analyzer and the ocular. We do not see an image of the sample, but rather an interference pattern in the focal plane of the objective behind the sample. Conoscopy is a valuable tool for the general characterization of liquid crystals, as it allows us to discriminate between uniaxial and biaxial samples, and also between optically positive and negative materials. Often the sample is viewed between crossed polarizers with the optic axis oriented approximately along the direction of light propagation, i. e. homeotropic boundary conditions are generally used. Most often, conoscopy is carried out with monochromatic light and an objective of rather large numerical aperture, $\times 40$ (blue) or even higher if possible. A good general treatment of conoscopic observation of uniaxial and biaxial materials can be found in the classic monograph by Born and Wolf [8].

For a uniaxial sample like the nematic or smectic A phase, a characteristic cross-like interference feature, called a Maltese cross, is observed, as shown in Fig. 3.7(a). The arms of the cross, also called isogyres, are parallel to the direction of the polarizers. The center of the pattern is dark. The interference pattern does not change when rotating the sample between the two crossed polarizers (in the plane perpen-

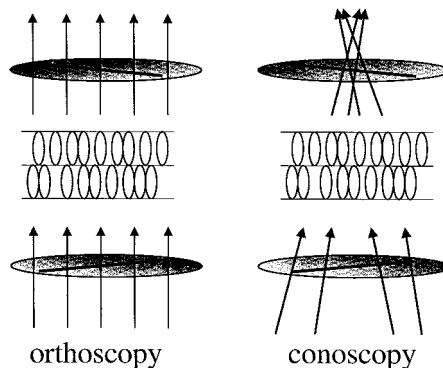


Fig. 3.6. Schematic illustration of orthoscopic (left) and conoscopic (right) imaging of a liquid crystal. In the former case a magnified image of the sample is observed, while in the latter case a characteristic interference pattern is obtained.

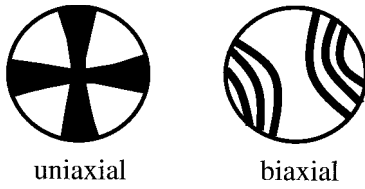


Fig. 3.7. Schematic conosopic interference pattern observed for a uniaxial phase with optic axis along the direction of light propagation (left) and a typical pattern obtained for a biaxial phase (right).

dicular to the direction of light propagation), as long as the direction of light propagation is parallel to the optic axis, because this is the axis of C_{∞} symmetry (this does not hold for samples with a pretilt at the substrates). For slightly oblique incidence (direction of light propagation not exactly parallel to the optic axis), the center of the Maltese cross is translated out of the center of the field of view. Rotating the sample results in a circular translation of the interference pattern, but without changing it.

For biaxial samples like the SmC phase, the respective interference pattern is far more complicated. Here, the two arms of the Maltese cross are of different widths and the interference pattern does change as the sample is rotated. Basically, a rotation of the sample results in two sets of hyperbolic lines, with their apexes being the points where the optic axis pierces the plane perpendicular to the direction of light propagation (Fig. 3.7(b)). In summary, we can thus easily distinguish between uniaxial and biaxial liquid crystal phases.

To find out whether a sample is optically positive or negative, a λ -plate is additionally inserted into the optical path. If, for a uniaxial phase, illuminated by white light, the top left and bottom right areas besides the Maltese cross (second and fourth quadrants) appear yellow and the top right and bottom left areas (first and third quadrants) are blue, the sample is optically positive with $\Delta n > 0$. If the situation is just reversed, the material is optically negative (Fig. 3.8). This corresponds to a determination whether the extraordinary beam is faster or slower than the ordinary beam and we can distinguish between optically positive and negative materials.

Also here we have to add a short word about phases composed of chiral molecules, which show optical activity. We can imagine a chiral, uniaxial phase with its optic axis along the direction of light propagation. This could be a SmA* phase subjected to homeotropic boundary conditions, but also a cholesteric twist

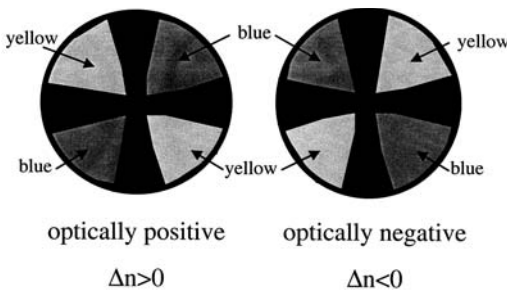


Fig. 3.8. Conoscopic observation with an inserted λ -plate leads to a distinction between optically positive (left) and optically negative (right) materials.

inversion compound (a cholesteric phase with infinite pitch, thus a nematic director configuration, in a certain temperature interval, N_{∞}^*). In this case the center of the conoscopic interference pattern would not be dark like discussed above, but rather bright. Also a rotation of the sample would not change this appearance. This is due to the rotation of the plane of polarization of light, caused by the molecular optical activity. Only a rotation of the analyzer with respect to the direction of the polarizer will bring the center of the Maltese cross to extinction.

The polarization optics of uniformly aligned liquid crystals, in parallel as well as convergent light, is completely analogous to that of respective solid state crystals [9–11]. For a more detailed and elaborate treatment of the subject of polarization optics, the reader may also refer to the respective textbooks of optics [8, 12–14]. A good introductory treatment can also be found in Refs. [15, 16].

At this point it seems necessary also to mention some more recent microscopic methods that are employed in the study of liquid crystal textures, namely *scanning near field microscopy* [17] and especially *fluorescence confocal polarizing microscopy* (FCPM) [18]. The latter experimental method represents an elegant technique to actually image liquid crystal director fields in three dimensions, while conventional polarizing microscopy allows only information from two dimensions, on account of the optical integration along the path of light propagation.

References

- [1] S. Bradbury, B. Bracegirdle, *Introduction to Light Microscopy*, BIOS Scientific Publishers, Oxford, 1998.
- [2] P. C. Robinson, S. Bradbury, *Qualitative Polarized-Light Microscopy*, Oxford Science Publications, New York, 1992.
- [3] M. W. Davidson, M. Abramowitz, *Optical Microscopy*, available as PDF document (<http://microscopy.fsu.edu>).
- [4] T. E. Lockhart, D. W. Allender, E. Gelerinter, D. L. Johnson, *Phys. Rev. A*, **20**, (1979), 1655.
- [5] H. Schmiedel, A. Frieser, *Cryst. Res. Technol.*, **22**, (1987), 581.
- [6] S. F. Mason, *Molecular Optical Activity and the Chiral Discrimination*, Cambridge University Press, Cambridge, 1982.
- [7] J. F. Nye, *Physical Properties of Crystals*, Clarendon Press, Oxford, 1985.
- [8] M. Born, E. Wolf, *Principles of Optics*, 7th edn., Cambridge University Press, Cambridge, 1999.
- [9] N. H. Hartshorne, A. Stuart, *Crystals and the Polarizing Microscope*, 2nd edn., Arnold, London, 1950.
- [10] W. Kleber, H.-J. Bautsch, J. Bohm, *Einführung in die Kristallographie*, 17th edn., Verlag Technik, Berlin, 1990.
- [11] N. H. Hartshorne, *The Microscopy of Liquid Crystals*, Microscope Publications, London, 1974.
- [12] R. D. Guenther, *Modern Optics*, John Wiley & Sons, New York, 1990.
- [13] E. Hecht, *Optics*, Addison-Wesley Longman, Amsterdam, 2000.
- [14] K. Weber, in Bergmann-Schäfer, *Lehrbuch der Experimentalphysik*, vol. 3, *Optik*, Walter de Gruyter, Berlin, 1993, ch. 4.
- [15] E. A. Wood, *Crystals and Light: An Introduction to Optical Crystallography*, 2nd edn., Dover Publications, New York, 1977.
- [16] D. R. Lovett, *Tensor Properties of Crystals*, Adam Hilger, Bristol, 1989.
- [17] T. Huser, T. Lacoste, H. Heinzelmann, H.-S. Kitzerow, *J. Chem. Phys.*, **108**, (1998), 7876.
- [18] I. I. Smalyukh, S. V. Shiyankovskii, O. D. Lavrentovich, *Chem. Phys. Lett.*, **336**, (2001), 88.

4

The Blue Phases

After introducing the basic structures and properties of the different liquid crystal phases, together with some outlines of orientation techniques and elasticity, we are now ready to take our virtual tour through the variety of phases and their texture appearance in polarizing microscopy, which is a fundamental tool in the characterization of novel mesogenic materials. We will start at elevated temperatures in the isotropic phase, which of course appears black between crossed polarizers for all orientations of the cell, due to the lack of birefringence. The first class of phases we encounter on slow cooling can in fact only be observed for chiral materials, the so-called *Blue Phases* (BP*). It is very likely that Friedrich Reinitzer observed the Blue Phase, as some passages in his paper [1] point towards a description of what we would nowadays call an anomaly at the isotropic to cholesteric transition: “... *Die Farberscheinung, welche beim Auskühlen der geschmolzenen Substanz eintritt, verläuft etwas anders als beim Acetat. Beim Abkühlen der klar geschmolzenen Verbindung tritt an einer Stelle eine tief violettblaue Farbe auf, die sich rasch über die ganze Masse ausbreitet und fast ebenso rasch wieder verschwindet, indem an ihrer Stelle eine gleichmässige Trübung tritt. Die Masse bleibt dann eine Zeit lang trübe, aber flüssig ...*” [... The color play, which is encountered on cooling the molten substance, is somewhat different from that observed for the acetate. On cooling the clearly molten compound, a deeply violet-blue color is observed, which quickly spreads over the whole sample and vanishes again just as quickly, leaving it uniformly cloudy. The sample then stays cloudy, but fluid ...]. Apparently, Reinitzer reports a state that is observed just below the isotropic phase and only exists over a narrow temperature interval, with liquid crystalline behavior still being observed at lower temperatures. This is a characteristic of Blue Phases and, in fact, many mesogenic cholesteryl derivatives do exhibit BP* phases.

In any case, the discovery of the Blue Phases as individual thermodynamic phases dates back to the 1970s and the work of Coates and Gray [2], although there is also unpublished work by Stegemeyer's group [3]. BP* are frustrated defect phases, generally observed in a temperature interval smaller than 1 K, between the isotropic phase and the cholesteric or smectic phases of highly chiral mesogens, where the low temperature N* phase often exhibits a twist with a pitch P well below $P < 1 \mu\text{m}$ with the wavelength of selective reflection in the visible range of the spectrum.

4.1

Structure and Textures of Blue Phases

Three different (cholesteric) Blue Phases are distinguished, which have been demonstrated by high resolution calorimetric measurements to exist even in one single compound, for example in a well studied material abbreviated as CE8. The three phases are denoted as BPI*, BPII*, and BPIII*. The BPIII* phase is the one observed at highest temperatures, and in the literature is also referred to as the “fog phase” or the “blue fog”. In contrast to BPI* and BPII*, which are cubic phases, BPIII* is an amorphous phase which nevertheless reflects circularly polarized light, thus indicating some kind of helical superstructure. In high resolution calorimetric investigations a rather large transition enthalpy is observed for the Iso*–BPIII* transition, but much smaller enthalpies for subsequent transitions between different Blue Phases and into the cholesteric phase [4, 5].

The appearance of the BPIII* phase is often quite hard to detect by polarizing microscopy, as generally only a dark bluish to black, foggy image without any structure is observed. An example is given in Plate 3, which was taken with a rather long exposure time. The BPIII* phase exhibits a selective reflection of circularly polarized light [6, 7] of a specific handedness, depending on the chiral configuration of the constituent molecules. In contrast to the other Blue Phases or the cholesteric phase, the reflection band is rather broad, in the order of 100 nm, with no higher order reflections observed [8, 9]. The BPIII* phase is amorphous and its symmetry is the same as that of the isotropic phase. A number of different theoretical models have been proposed to account for the appearance of the BPIII* phase, which include the already disregarded pretransitional fluctuation model by Brazovskii et al. [10, 11], the emulsion model of Finn and Cladis [12], and cubic domain models by Belyakov et al. [13] and Collings [14], which suggest a local cubic structure with short correlation lengths. Alternatively, other models, like that of entangled double twist cylinders by Hornreich et al. [15] or the icosahedral model [16–19], may in fact account for the appearance of BPIII*. Thus the microscopic structure of this phase does not seem to have been conclusively established yet.

The structures of BPII* and BPI* are less enigmatic. The building structural elements are so-called *double twist cylinders*, as schematically shown in Fig. 4.1, which represent a local structure of minimum free energy. Within a double twist cylinder the local director rotates around any given radius of the cylinder. The double twist cylinders spatially arrange perpendicular to each other, which for elastic reasons is only possible by introducing a lattice of topological defects [20] (see Fig. 4.2). This makes the Blue Phases belong to the group of frustrated phases. BPII* is generally only observed over a certain region in the temperature–chirality diagram, disappearing in the high chirality regime, while the stability of the BPI* phase increases with increasing chirality [21–24] (and also that of BPIII* until it terminates in a critical point). A schematic temperature–chirality diagram of the Blue Phases is shown in Fig. 4.3. Combined interpretation of experimental investigations on Bragg scattering [6, 7, 25–29], Kossel diagrams [30–34], careful texture observation, and crystallite growth [35–46] have revealed that the BPII* phase has a simple cubic unit cell of

Fig. 4.1. Schematic illustration of a double twist cylinder. At the core the director is oriented parallel to the cylinder axis. Moving outwards the local director twists along any radius until the twist is approximately 45° at the edge of the double twist cylinder.

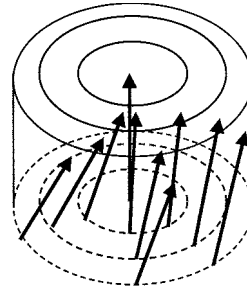


Fig. 4.2. Local arrangement of three double twist cylinders forming a defect region, which eventually leads to the three dimensional, cubic lattice of defects observed in Blue Phases.

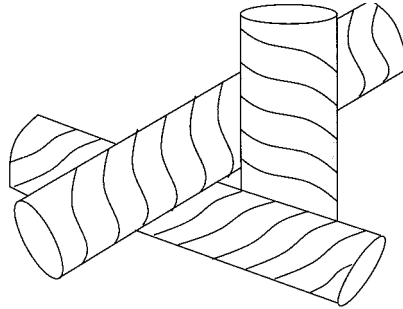
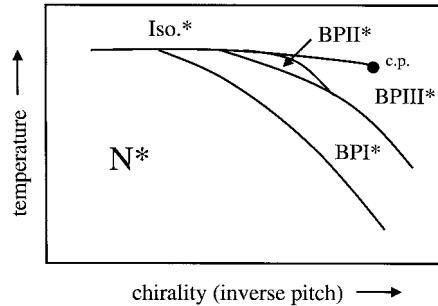


Fig. 4.3. Temperature–chirality diagram in the vicinity of the isotropic to liquid crystal transition point. At low chirality no Blue Phases are observed, but rather a direct isotropic–cholesteric transition. With increasing chirality the BPIII* and BPI* phases are stabilized. BPII* is only observed in the range of intermediate chirality.



lattice defects (space group $P4_232$), while the BPI* phase is body centered cubic (space group $I4_132$), both with lattice parameters in the order of several hundred nanometers (the wavelength of visible light). The Blue Phases are thus optically isotropic, i. e. linear birefringence is absent. The corresponding arrangements of the double twist cylinders and the unit cells of defect lines are depicted for BPII* and BPI* in Figs. 4.4(a) and (b), respectively (after Ref. [47]).

The visual appearance of the cubic Blue Phases in polarizing microscopy is quite characteristic, generally with a texture called *platelet texture*, an example of which is shown in Plate 4. This demonstrates that the Blue Phases do not have to appear blue, but can also exhibit different colors, while of course still being referred to as BP*. The different colors are due to the different orientations of the system of double twist cylinders, i. e. different “crystal planes” are observed, which show

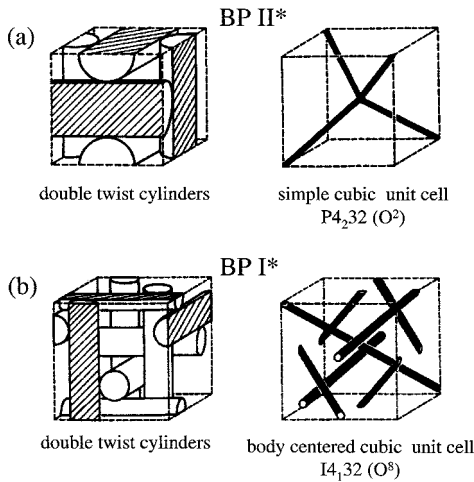


Fig. 4.4. Model structures of the BP II* and BP I* phases. (a) Spatial arrangement of double twist cylinders that lead to the simple cubic structure of BP II* (left) and corresponding unit cell of disclination lattices (right). (b) Arrangement of double twist cylinders to form the body centered cubic structure of the BP I* phase (left) and corresponding unit cell of disclination lattices (right). (After Dubois-Violette and Pansu [47].)

Bragg scattering at different wavelengths, because the condition for constructive interference depends on the distance between lattice planes and their orientation with respect to the direction of incident light. On very slow cooling with a well stabilized temperature controller, single crystals of Blue Phases can be obtained, sometimes even with facets being visible [41, 42]. An example of a growing single crystal BP I* is shown in Plate 5.

Further cooling the BP I* phase results in a transition to a single twist phase, the cholesteric or chiral nematic N* phase. This is demonstrated in Plate 6(a), with a BP I* platelet texture, and Plate 6(b), showing the same sample area at a slightly lower temperature, with a cholesteric fan-shaped texture (left) growing into the platelet BP I* texture (right).

For more detailed information on the structure and physical properties of cholesteric blue phases we refer to the review article [47] and those of Stegemeyer et al. [48], Crooker [49], and Pansu [50]. More theoretical aspects have been reviewed by Wright and Mermin [51] and Seideman [52]. A very recent comprehensive overview of the physical properties of Blue Phases was given by Crooker [53].

Recently, Pansu et al. [54, 55] reported on a chiral tolane liquid crystal, which exhibits Blue Phases, very similar in texture appearance to the Blue Phases discussed above (see Plate 7), but with persisting smectic order. On cooling, these Blue Phases transform via a first order transition into the twist grain boundary (TGB) phase [56] or directly into SmC* [57]. The existence of a lamellar spacing, confirmed by x-ray investigations within the BP* temperature interval, had also been reported by Li et al. [58, 59]. X-ray studies on presumably large monodomains clearly revealed a fourfold symmetry [55], as would be expected from a cubic phase with smectic order, but also one phase with hexagonal symmetry was reported [60, 61]. The lamellar correlation length was found to be smaller than that of the underlying TGB phase. These investigations are of preliminary nature and at this point it is too early to decide whether these reported phases are indeed novel phases, or

conventional Blue Phases with smectic fluctuations. In any case there seem to exist defect phases with three dimensional orientational order as in the common BP* phases, but with additional positional order. It has been pointed out by geometric constructions that in principle a double twist can be combined with lamella ordering to produce cubic “smectic” blue phases [62, 63]. Also the relation and possible similarities between these phases and the smectic Q* phase [64–67], which appears between the isotropic melt and the antiferroelectric SmC_A* phase of chiral mesogens, remains a question to be answered by future experimental and theoretical investigations.

4.2

Kossel Diagrams

The Blue Phases exhibit lattice constants in the order of the wavelength of visible light. A technique introduced by Kossel et al. [68] for the investigation of crystal structures by x-rays has been shown first by Pieranski [30] to be valuable also in the study of Blue Phases by monochromatic light. A single crystal Blue Phase is illuminated with convergent monochromatic light and viewed in reflection in a polarizing microscope with an objective of large aperture, as schematically shown in Fig. 4.5. When the Bragg condition is satisfied the corresponding cone of backscattered light passes the objective and is focused on the back focal plane where the Kossel diagram is obtained. Depending on the structure of the Blue Phase, its lattice constant, and lattice orientation, i. e. the Miller indices $[h k l]$, different sets of lattice planes give rise to an arc on the observed diagram. The Kossel diagram of Fig. 4.6 for example shows the $(1 0 0)$, $(0 1 0)$, and $(0 0 1)$ reflections along the $[1 1 1]$ lattice direction of a BP11* phase, with the threefold symmetry of the Kossel diagram indicating a cubic structure.

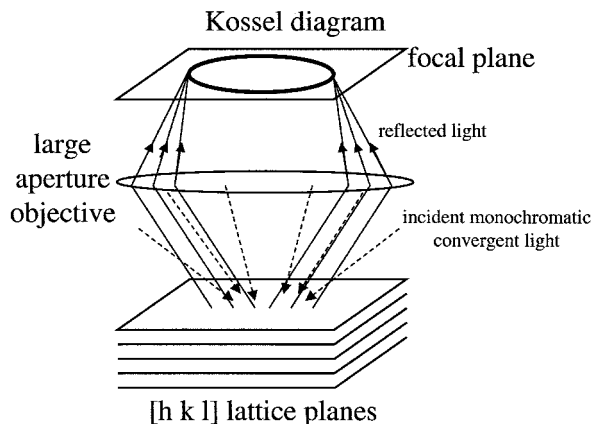


Fig. 4.5. Schematic principle of the Kossel technique used in structure studies of Blue Phases. Monochromatic convergent light illuminates the lattice plane of the phase, and is reflected and focused through the objective onto the back focal plane, where the Kossel diagram is observed.

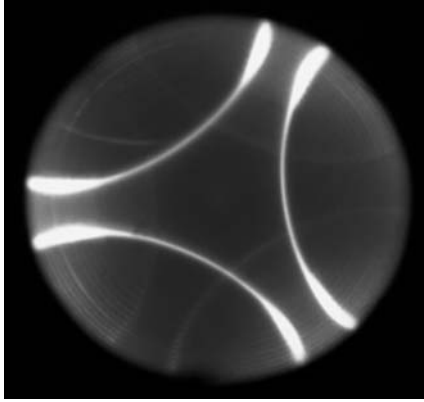


Fig. 4.6. Experimental example of a Kossel diagram showing the $(1\ 0\ 0)$, $(0\ 1\ 0)$, and $(0\ 0\ 1)$ reflections along the $[1\ 1\ 1]$ lattice direction of a BPII* phase. (Courtesy of R. J. Miller and H. F. Gleeson.)

References

- [1] F. Reinitzer, *Monatsh. Chem.*, **9**, (1888), 421.
- [2] D. Coates, G. W. Gray, *Phys. Lett.*, **45A**, (1973), 115.
- [3] H. Stegemeyer, U. Müller, unpublished; U. Müller, Thesis, Berlin, 1974, pp. 111–112.
- [4] R. N. Kleiman, D. J. Bishop, R. Pindak, P. Taborek, *Phys. Rev. Lett.*, **53**, (1984), 2137.
- [5] J. Thoen, *Phys. Rev. A*, **37**, (1987), 1754.
- [6] S. Meiboom, M. Sammon, *Phys. Rev. Lett.*, **44**, (1980), 882.
- [7] S. Meiboom, M. Sammon, *Phys. Rev. A*, **24**, (1981), 468.
- [8] E. I. Demikhov, V. K. Dolganov, S. P. Krylova, *JETP Lett.*, **42**, (1985), 15.
- [9] D.-K. Yang, P. P. Crooker, K. Tanimoto, *Phys. Rev. Lett.*, **61**, (1988), 2685.
- [10] S. A. Brazovskii, S. G. Dmitriev, *Sov. Phys. JETP*, **42**, (1975), 497.
- [11] S. A. Brazovskii, V. M. Filev, *Sov. Phys. JETP*, **48**, (1978), 573.
- [12] P. L. Finn, P. E. Cladis, *Mol. Cryst. Liq. Cryst.*, **84**, (1982), 159.
- [13] V. A. Belyakov, E. I. Demikhov, V. E. Dmitrienko, V. K. Dolganov, *Sov. Phys. JETP*, **62**, (1986), 1173.
- [14] P. J. Collings, *Phys. Rev. A*, **30**, (1984), 1990.
- [15] R. M. Hornreich, M. Kugler, S. Shtrikman, *Phys. Rev. Lett.*, **48**, (1982), 1404.
- [16] R. M. Hornreich, S. Shtrikman, *Phys. Rev. Lett.*, **56**, (1986), 1723.
- [17] R. M. Hornreich, S. Shtrikman, *Phys. Lett. A*, **115**, (1986), 451.
- [18] D. S. Rokhsar, J. P. Sethna, *Phys. Rev. Lett.*, **56**, (1986), 1727.
- [19] V. M. Filev, *JETP Lett.*, **43**, (1986), 677.
- [20] W. F. Brinkman, P. E. Cladis, *Phys. Today*, **35**, (1982), 48.
- [21] K. Tanimoto, P. P. Crooker, G. C. Koch, *Phys. Rev. A*, **32**, (1985), 1893.
- [22] J. D. Miller, P. R. Battle, P. J. Collings, D. K. Yang, P. P. Crooker, *Phys. Rev. A*, **35**, (1987), 3959.
- [23] M. B. Atkinson, P. J. Collings, *Mol. Cryst. Liq. Cryst.*, **136**, (1986), 141.
- [24] D. K. Yang, P. P. Crooker, *Phys. Rev. A*, **35**, (1987), 4419.
- [25] K. Bergmann, H. Stegemeyer, *Ber. Bunsenges. Phys. Chem.*, **82**, (1978), 1309.
- [26] K. Bergmann, P. Pollmann, G. Scherer, H. Stegemeyer, *Z. Naturforsch.*, **38a**, (1979), 253.
- [27] K. Bergmann, H. Stegemeyer, *Z. Naturforsch.*, **38a**, (1979), 1031.
- [28] D. L. Johnson, J. H. Flack, P. P. Crooker, *Phys. Rev. Lett.*, **45**, (1980), 641.
- [29] S. Meiboom, M. Sammon, D. Berreman, *Phys. Rev. A*, **28**, (1983), 3553.
- [30] P. Pieranski, E. Dubois-Violette, F. Rohten, L. Strelecki, *J. Phys. (Fr.)*, **42**, (1981), 53.
- [31] P. E. Cladis, T. Garel, P. Pieranski, *Phys. Rev. Lett.*, **57**, (1986), 2841.
- [32] P. Pieranski, P. E. Cladis, *Phys. Rev. A*, **35**, (1987), 355.
- [33] R. J. Miller, H. F. Gleeson, *Phys. Rev. E*, **52**, (1995), 5011.
- [34] R. J. Miller, H. F. Gleeson, *J. Phys. II*, **6**, (1996), 909.
- [35] M. Marcus, *J. Phys. (Fr.)*, **42**, (1981), 61.
- [36] H. Onusseit, H. Stegemeyer, *Z. Naturforsch.*, **36a**, (1981), 1083.

- [37] M. Marcus, *Phys. Rev. A*, **25**, (1982), 2272.
- [38] H. Onusseit, H. Stegemeyer, *J. Cryst. Growth*, **61**, (1983), 409.
- [39] H. Onusseit, H. Stegemeyer, *Z. Naturforsch.*, **38a**, (1983), 1114.
- [40] T. Blümel, H. Stegemeyer, *J. Cryst. Growth*, **66**, (1984), 163.
- [41] P. E. Cladis, P. Pieranski, M. Joanicot, *Phys. Rev. Lett.*, **52**, (1984), 542.
- [42] R. Barbet-Massin, P. E. Cladis, P. Pieranski, *Phys. Rev. A*, **30**, (1984), 1161.
- [43] T. Blümel, H. Stegemeyer, *Z. Naturforsch.*, **40a**, (1985), 260.
- [44] P. Pieranski, R. Barbet-Massin, P. E. Cladis, *Phys. Rev. A*, **31**, (1985), 3912.
- [45] P. Pieranski, P. E. Cladis, R. Barbet-Massin, *J. Phys. (Fr.)*, **47**, (1986), 129.
- [46] P. Pieranski, P. E. Cladis, T. Garel, R. Barbet-Massin, *J. Phys. (Fr.)*, **47**, (1986), 139.
- [47] E. Dubois-Violette, B. Pansu, *Mol. Cryst. Liq. Cryst.*, **165**, (1988), 151.
- [48] H. Stegemeyer, T. Blümel, K. Hiltrop, H. Onusseit, F. Porsch, *Liq. Cryst.*, **1**, (1986), 1.
- [49] P. P. Crooker, *Liq. Cryst.*, **5**, (1989), 751.
- [50] B. Pansu, *J. Phys. II*, **5**, (1995), 573.
- [51] D. C. Wright, N. D. Mermin, *Rev. Mod. Phys.*, **61**, (1989), 385.
- [52] T. Seideman, *Rep. Prog. Phys.*, **53**, (1990), 659.
- [53] P. P. Crooker, in *Chirality in Liquid Crystals*, H.-S. Kitzerow, C. Bahr (eds.), Springer-Verlag, Berlin, 2001, ch. 7.
- [54] B. Pansu, M. H. Li, H. T. Nguyen, *J. Phys. II*, **7**, (1997), 751.
- [55] B. Pansu, M. H. Li, H. T. Nguyen, *Eur. Phys. J. B*, **2**, (1998), 143.
- [56] E. Grelet, B. Pansu, H. T. Nguyen, *Liq. Cryst.*, **28**, (2001), 1121.
- [57] C. da Cruz, E. Grelet, J. C. Rouillon, J. P. Marcerou, G. Sigaud, B. Pansu, H. T. Nguyen, *Liq. Cryst.*, **28**, (2001), 1415.
- [58] M. H. Li, H. T. Nguyen, G. Sigaud, *Liq. Cryst.*, **20**, (1996), 361.
- [59] M. H. Li, V. Laux, H. T. Nguyen, G. Sigaud, P. Barois, N. Isaert, *Liq. Cryst.*, **23**, (1997), 389.
- [60] B. Pansu, E. Grelet, M. H. Li, H. T. Nguyen, *Phys. Rev. E*, **62**, (2000), 658.
- [61] E. Grelet, B. Pansu, M. H. Li, H. T. Nguyen, *Phys. Rev. Lett.*, **86**, (2001), 3791.
- [62] J. M. Gilli, Kamaye, *Liq. Cryst.*, **12**, (1992), 545.
- [63] R. D. Kamien, *J. Phys. II*, **7**, (1997), 743.
- [64] A. M. Levelut, C. Germain, P. Keller, L. Liebert, J. Billard, *J. Phys. (Fr.)*, **44**, (1983), 623.
- [65] D. Bennemann, G. Heppke, A. M. Levelut, D. Löttsch, *Mol. Cryst. Liq. Cryst.*, **260**, (1995), 351.
- [66] A. M. Levelut, E. Hallouin, D. Bennemann, G. Heppke, D. Löttsch, *J. Phys. II*, **7**, (1997), 981.
- [67] A. M. Levelut, D. Bennemann, G. Heppke, D. Löttsch, *Mol. Cryst. Liq. Cryst.*, **299**, (1997), 433.
- [68] W. Kossel, V. Loeck, H. Voges, *Z. Phys.*, **94**, (1935), 139.

5

The Nematic and Cholesteric Phases

The nematic N and the cholesteric N* phases, being constituents of achiral and chiral molecules respectively, are thermodynamically almost equivalent. Disregarding the frustrated BP* phases as discussed in the previous chapter, they are often the first liquid crystal phases to be observed on cooling from the isotropic melt. They exhibit the least order and thus the highest symmetry. Owing to the helical superstructure of the cholesteric phase, its textural appearance and optical properties are quite different from those of nematic phases. For this reason we will discuss the achiral nematic and chiral cholesteric phases separately.

5.1

The Nematic Phase

The general structure of the nematic phase has already been introduced in Chapter 1. We recall that the long molecular axes of the molecules orient more or less parallel to each other, while their centers of mass are isotropically distributed. The nematic phase exhibits solely long range orientational order.

5.1.1

Nematic Textures Under Planar Boundary Conditions

5.1.1.1 The Nematic Schlieren Texture

Nematics between untreated glass plates often orient with their director parallel to the substrates. If this orientation is not homogeneous, but varies slowly in the plane of the substrate, so-called *Schlieren* textures [1–3] are observed between crossed polarizers. An example is given in Plate 8 at a rather low magnification. Schlieren textures exhibit characteristic sets of often curved dark brushes, as can easily be seen in Plate 9. These correspond to the extinction position of the nematic director field, with $\mathbf{n}(\mathbf{r})$ coinciding with the direction of either the polarizer or the analyzer. A closer look reveals that the brushes come together in a singular point and can be twofold (Plate 10) or fourfold (Plate 11). The singularities are topological defects, which are assigned a certain strength s (see for example Ref. [4]). The absolute value of the strength of the disclination is obtained by dividing by four the

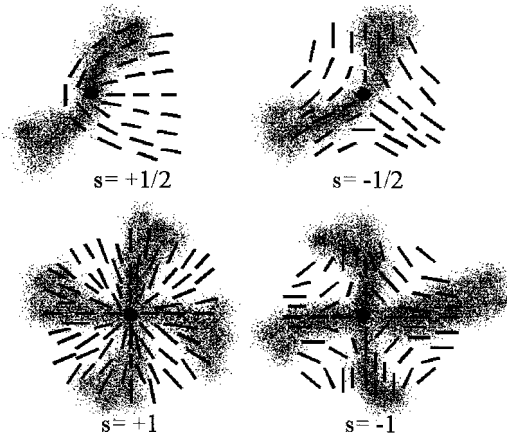


Fig. 5.1. Director configurations in the vicinity of defect lines observed in nematic Schlieren textures.

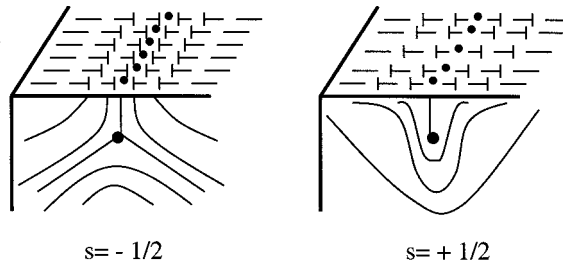
number of brushes cutting a 2π circle around the center, i.e. $||s|| = \text{number of brushes}/4$. In the example textures we thus observe an $s = \pm 1/2$ defect in Plate 10 and an $s = \pm 1$ defect in Plate 11. The sign of the defect strength can be obtained by rotation of the polarizers: the defect is assigned a plus (+) sign if the dark brushes rotate in the same direction as the polarizers, and a minus (-) sign if they rotate in the opposite direction. Note that in any case the point singularities do not move and the rotation of the brushes is continuous, due to a continuous variation of the director field $\mathbf{n}(\mathbf{r})$. Experimentally, $s = \pm 1/2$ and $s = \pm 1$ defects are all observed for nematic liquid crystals. Twofold and fourfold singularities, also of different sign, generally occur simultaneously in the same sample, as shown in Plate 12. The corresponding director configurations are schematically shown in Fig. 5.1 as a top view on the substrate plane.

As mentioned above, there are no singular defects within a sample – rather the brushes connect different defects. The sum over all defect strengths (including their sign) of a large sample generally tends to vanish. Characteristically, each of two connected defects have opposite signs. We should note that the overall defect distribution of a sample is not a static feature. Defects of the same strength but opposite sign can attract each other and eventually annihilate to yield a uniform, defect-free sample area. On the other hand, two defects with different strengths cannot annihilate, but may form a different singularity with the strength being the sum of those of the two original defects.

5.1.1.2 The Thread-like Texture

The thread-like texture is the one that gave the nematic phase its name, from *νημα* (*nema*), the Greek word for “thread”. An example of this texture is shown in Plate 13. The dark lines, so-called threads, are line singularities, which either connect two $s = \pm 1/2$ point defects or form closed loops. The lines are π disclinations and end at the substrates [2, 5]. A texture that appears very similar to the thread-

Fig. 5.2. Possible director configurations in the vicinity of surface disclination lines.



like texture is that of surface inversion walls [6–8], which correspond to a 180° turn of the director in the plane of the substrate (Fig. 5.2). Two closely spaced dark lines are visible, as in Plate 14.

5.1.1.3 The Marble Texture

The nematic marble texture [1] is usually observed in thin preparations of samples, especially for substrates that have not been rubbed or treated in any way. This is probably the most frequently observed natural nematic texture. Different areas of the sample appear quite uniform but may slightly change in color, due to a change in birefringence from in-plane but also out-of-plane variation of the director. An example of the marble texture is shown in Plate 15. Areas of different director orientations are often separated by inversion walls, but also by other defect lines. For mesogens exhibiting a Cryst–N transition, the marble texture may appear on heating crystallites into the nematic phase [1]. In this case the crystallites melt while maintaining the direction of the long molecular axis. Thus areas with a uniform director orientation are formed, while one preferred direction may vary from area to area.

5.1.1.4 Uniform Planar Nematic Samples

Although of crucial importance for applications, uniform textures of liquid crystals obviously lack the aesthetic appeal of the natural textures. Subjecting a nematic to uniform planar boundary conditions, for example by using commercial, parallel rubbed LC sandwich cells, a sample is obtained that behaves optically just like a uniaxial, birefringent plate of a crystal with the optic axis in the plane of the substrate. The transmitted light intensity between crossed polarizers varies according to a $I \sim \sin^2(2\varphi)$ dependence, with φ being the azimuthal angle (rotation angle of the sample in a plane perpendicular to the direction of light propagation). Whenever the optic axis (the director) is oriented along one of the polarizer directions, the sample appears black. Maximum intensity is observed when the optic axis is oriented at 45° between polarizer and analyzer (Fig. 5.3). A uniform planar nematic sample shows a 90° periodicity in its texture appearance. To distinguish a well oriented N phase from the corresponding SmA phase, which exhibits identical optical properties, one may observe the characteristic shimmer or flickering that is

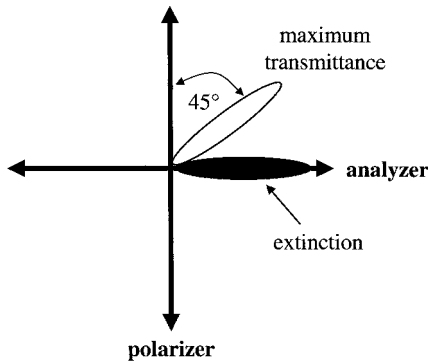


Fig. 5.3. Director orientation of a uniform planar uniaxial nematic phase between crossed polarizers in extinction position (black) and at maximum transmittance at 45° .

exhibited by nematics, caused by Brownian motion of the molecules, but not by smectic phases. This is best observed when rotating the sample to just a few degrees out of its extinction position.

5.1.2

The Pseudo-Isotropic Texture Under Homeotropic Boundary Conditions

When the nematic phase is subjected to homeotropic boundary conditions the director orients perpendicular to the substrates. In this case the direction of light propagation coincides with the optic axis of the phase. As discussed in Chapter 3, there is no birefringence and the sample appears black between crossed polarizers for all positions of the azimuthal angle, i. e. rotation of the sample does not produce any change in color or intensity. This is called the *pseudo-isotropic* texture, because the sample appears like the isotropic phase. To distinguish between the real isotropic and the pseudo-isotropic texture of the nematic phase, one can gently press on the top glass substrate. In doing so, a bright flash will appear in the case of the nematic phase, due to mechanical reorientation of the director and therefore also the optic axis. Because the elastic constants are very small, even slight pressure is sufficient to produce this effect. Also conoscopy will reveal the difference between a pseudo-isotropic nematic and the real isotropic phase.

5.2

The Cholesteric Phase

The cholesteric N^* phase, being the chiral version of the nematic phase, also possesses solely orientational order of the long molecular axis. In contrast to the N phase, we now observe a spontaneous macroscopic helical superstructure with a twist axis perpendicular to the local director. Thus the phase consists of local nematic “layers”, which are continuously twisted with respect to each other. Assuming the helix axis to be along the z direction, the cholesteric phase exhibits a director field $\mathbf{n}(\mathbf{r})$, which is described by

$$\mathbf{n}(\mathbf{r}) = \begin{pmatrix} \cos\left(\frac{2\pi}{P}z + \varphi_0\right) \\ \sin\left(\frac{2\pi}{P}z + \varphi_0\right) \\ 0 \end{pmatrix} \quad (5.1)$$

where P is the temperature dependent pitch of the helical superstructure and φ_0 is a constant that depends on the boundary conditions. The magnitude of the pitch of a cholesteric phase can vary considerably, from values as small as $P \approx 100$ nm to large values of P equal to many micrometers. A schematic structural view of the corresponding director configuration is shown in Fig. 5.4. Note that, owing to the head–tail symmetry of the molecules ($\mathbf{n} = -\mathbf{n}$), the periodicity L of the N^* phase along the helix axis is given by half the pitch, $L = P/2$.

Being a chirality dependent quantity, the cholesteric twist can be right- or left-handed, depending on the configuration of the chiral element(s) within the molecule, similar to the spiral staircases shown in Fig. 5.5, two photographs of a depart-

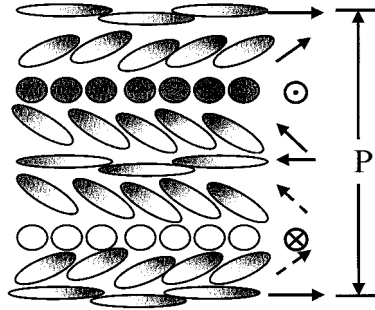


Fig. 5.4. Schematic illustration of the helical superstructure of the cholesteric (chiral nematic) phase. Note that the pitch length is typically many hundreds or thousands of times larger than the molecular width.



Fig. 5.5. Enantiomeric mesogens are molecular mirror images of each other and exhibit macroscopic cholesteric helices of opposite handedness, just like the spiral staircases of

this department building at Chalmers University, Gothenburg, Sweden, where the left and right parts of the building are separated by a mirror plane.

ment building at Chalmers University, Gothenburg, Sweden, which has a mirror plane perpendicular to the ground level. The cholesteric helix handedness is accounted for by a generally accepted convention: a *positive* pitch P corresponds to a *right*-handed helical superstructure and a *negative* pitch to a *left*-handed helix. At this point, it is important to realize that up to now we have no means to predict which chiral molecular configuration will produce a certain macroscopic helix handedness. Although there have been empirical rules proposed [9], the relationship between molecular chirality and macroscopic phase chirality still remains a question that has not conclusively been answered.

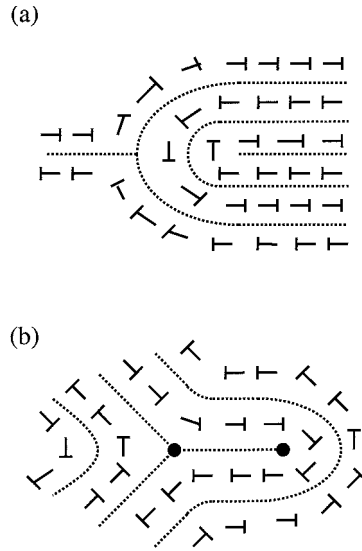
5.2.1

Natural Textures of the N^* Phase

One of the most commonly observed textures of the cholesteric phase prepared between two untreated glass substrates is the so-called *oily streaks* texture, which was already described by Lehmann as “*ölige Streifen*” [10] and referred to by Friedel as “*stries huileuses*” [1]. A typical example of this texture is shown in Plate 16 for a sample with a pitch in the order of $P \approx 2 \mu\text{m}$, and in Plate 17 for a cholesteric with selective reflection in the visible range of the spectrum ($P \approx 450 \text{ nm}$). The oily streaks can also appear in large bundles, as can be seen in Plate 18. The director is basically anchored under planar conditions at the substrates, i. e. with the long molecular axis parallel to the bounding plates, which implies that the cholesteric helix axis is oriented perpendicular to the glass plates. The actual oily streaks can be seen as a network of defect lines dispersed in uniformly helical regions. The structure of an oily streak is complicated and depends mainly on elasticity and surface anchoring [8, 11, 12]. Friedel [1] suggested that they consisted of pairs of edge dislocations. The oily streaks network is generally not a static feature, but may coarsen with time, leaving a uniformly oriented sample with twist axis perpendicular to the substrate plane. The orientation of the helix axis along the direction of light propagation can be verified in transmittance polarizing microscopy by rotation of the sample between crossed polarizers. For a helical structure with at least several 2π twist turns (about 10), neither the observed color nor the transmitted intensity will change. Once the pitch is of comparable magnitude to the cell gap, elastic interactions with the substrates deform the helical superstructure and a slight intensity variation will be observed when rotating the sample between crossed polarizers. This elastic deformation can lead all the way to the extreme case, where a uniform planar nematic texture is observed, even though the phase is constituted by chiral molecules. In this case the cholesteric pitch will be larger than twice the cell gap, $P > 2d$.

Another natural texture that is often observed in cholesterics is the so-called *fan-shaped* or *fan-like* texture, which can be very similar to those observed in SmA phases. The cholesteric fan textures have been reported by Friedel [1] and were later treated in detail by Bouligand [13, 14]. Fan-like textures (see Plate 19) are observed for strongly twisted materials, while fan-shaped textures that exhibit focal conics (see Plate 20) are found for materials with a slightly smaller twist. Especially

Fig. 5.6. Some common defects that can be observed in cholesterics with polygonal texture: (a) edge dislocations and (b) pinches.



the latter textures are very similar to that of the SmA phase (Chapter 7), but with a somewhat smoother appearance of the fans. They are interpreted by assigning the cholesteric phase a virtual layering, often with $P/2$ taken as the “layer thickness”, and then discussing the structure in terms of the SmA models [1, 15–17] (see also Chapter 7). The twist axis of the cholesteric fan textures naturally deviates from the substrate normal, in contrast to the oily streaks or Grandjean textures.

Further increasing the pitch, such that the helical superstructure can be resolved by microscopy, can give rise to the so-called cholesteric *polygonal* texture, an example of which is given in Plate 21. Also here the twist axis is generally inclined with respect to the substrate plane. A variety of defects, such as edge dislocations and pinches (Fig. 5.6), may exist in these textures [18].

5.2.2

Short Pitch Cholesterics

As mentioned before, the cholesteric phase, due to its helical arrangement of molecules, exhibits some unique optical properties. The most striking is the so-called *selective reflection*, where circularly polarized light of a specific handedness and wavelength is reflected. This phenomenon can readily be observed by the naked eye as an iridescent color play when the pitch of the cholesteric structure is in the range of the visible spectrum. Also in nature the selective reflection of cholesteric-like structures is well known from the bright colors exhibited by some beetles [19, 20]. An analysis shows that the reflected light is in fact circularly polarized under specific geometrical orientations, while different families of beetles may reflect light of a different handedness.

Let us consider the propagation of light in a helical medium in a bit more detail by following the description of de Vries [21]. He solved the Maxwell equations for light propagating along the helix axis of a continuously twisted birefringent medium and obtained an expression for the optical rotation φ (in radians per unit length) as a function of wavelength λ :

$$\varphi = \frac{\pi \Delta n^2 P}{4\lambda^2} \frac{1}{1 - (\lambda/\lambda_0)^2} \quad (5.2)$$

where Δn is the birefringence of a quasi-nematic layer, P is the cholesteric pitch and $\lambda_0 = \bar{n}P$ is the wavelength of selective reflection (\bar{n} is the average index of refraction of a quasi-nematic layer). Equation (5.2) is valid in the regime $\lambda \approx P$ and was derived by applying the following simplifying assumptions: (1) molecular optical activity is neglected; (2) the material is non-absorbing; (3) only non-ferromagnetic materials are considered, i. e. the magnetic permeability tensor is assumed to be unity; and (4) the sample dimension is infinite, which in reality is accomplished by samples with more than approximately 10 full 2π twists. Note that for $\lambda = \lambda_0$ the optical rotation diverges and changes sign. The functionality of Eq. (5.2) is schematized in Fig. 5.7.

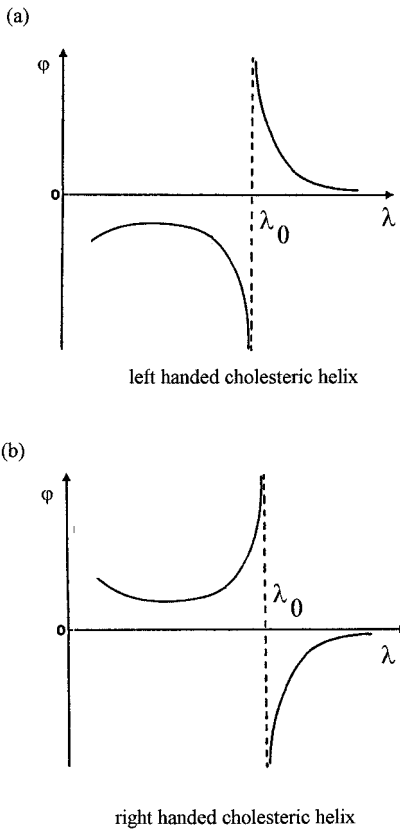
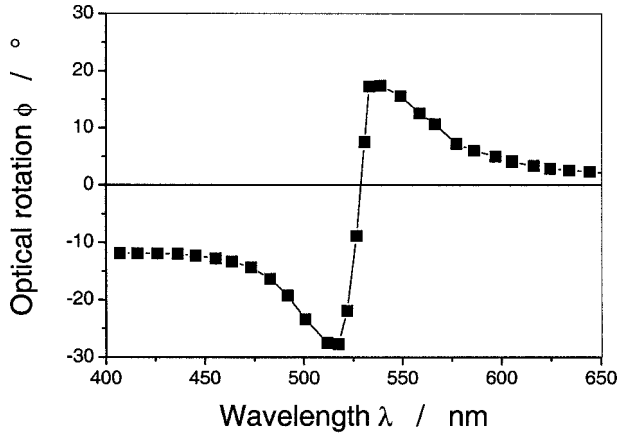


Fig. 5.7. Schematic illustration of the optical rotation φ as a function of wavelength λ of a cholesteric liquid crystal in the vicinity of the wavelength of selective reflection λ_0 according to the de Vries equation (Eq. (5.2)): (a) for a left-handed helix and (b) for a right-handed helix. For wavelengths $\lambda < \lambda_0$ (but above the Mauguin limit) the sign of the optical rotation gives the handedness of the cholesteric helix.

Fig. 5.8. An experimental example of the wavelength dependence of the optical rotation for light propagation along the helix axis for a left-handed cholesteric structure. (Data after Ref. [22].)



tically depicted in Fig. 5.7 for a left-handed as well as a right-handed cholesteric helix. For $\lambda < \lambda_0$ the sign of the optical rotation gives the handedness of the cholesteric helix. An experimental example of the wavelength dependence of the optical rotation is given in Fig. 5.8 (after Ref. [22]).

Consider incident linearly polarized light, which can be thought of consisting of a left and a right circularly polarized component. At λ_0 one of these components is completely reflected without phase change, unlike reflection on conventional mirrors. The reflected component is the one which does not match the spatial handedness of the cholesteric helix. A right-handed cholesteric thus selectively reflects right-handed circularly polarized light, as this describes a left-handed helix in space. This is following the convention of Born: the electric field vector of right circularly polarized light moves clockwise when viewed on to the light source, i. e. against the direction of light propagation.

A description of the optical properties of cholesterics for light incidence parallel to the helix axis by means of the Jones matrix method [23–26] can be found in Ref. [27]. A general description of light propagation through a helical medium in an arbitrary direction was given by Berremann and Scheffer [28, 29] and Oldano et al. [30], which is obviously much more complicated than the treatment by de Vries. A rigorous treatment of the optics of helical liquid crystal phases in general can be found in the monograph by Belyakov [31].

5.2.2.1 Planar Boundary Conditions and Selective Reflection

Cholesteric phases with a pitch smaller than approximately $P < 1 \mu\text{m}$ are generally referred to as short pitch materials. If the pitch adopts values such that $\lambda_0 = \bar{n}P$ lies within the range of the visible spectrum, the wavelength of selective reflection can easily be obtained by reflection microscopy. To observe a narrow reflection band, the compound is introduced into cells with planar boundary conditions and thus with the N^* helix axis being oriented parallel to the direction of light propagation. This is the so-called *Grandjean orientation*. An adequate cell gap d should be chosen

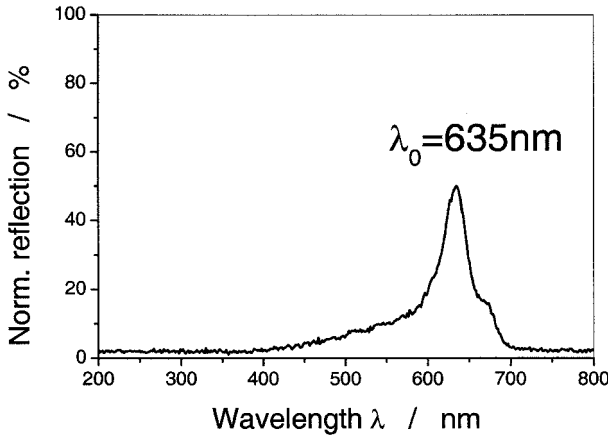


Fig. 5.9. Selective reflection band of a short pitch cholesteric in Grandjean orientation illuminated from above with linearly polarized white light. The center wavelength is located at $\lambda_0 = \bar{n}P$ in the red end of the visible spectrum, corresponding to the texture (a) of Plate 22 [32].

such that the formation of at least 10 full 2π turns of the director is assured, i. e. $d > 4 \mu\text{m}$. The wavelength of selective reflection λ_0 can then be determined with a spectrometer mounted on the phototube of the microscope while the sample is illuminated from above with linearly polarized white light. An experimental example is given in Fig. 5.9, showing a reflection band with λ_0 located in the red, corresponding to the texture of part (a) of Plate 22, which shows a sample in Grandjean orientation at increasing temperature from (a) to (d), with the photographs taken in reflection [32].

Accordingly, λ_0 can also be determined from transmission microscopy of samples in Grandjean orientation. Owing to selective reflection the spectra should exhibit a clear minimum at λ_0 , which is in fact observed, as demonstrated in Fig. 5.10 with temperature dependent spectra taken on the same compound as shown in Plate 22. The closely spaced smaller transmission minima in Fig. 5.10 are due to cell gap interference. Spectral measurements of the reflected or transmitted light intensity thus allow a determination of the temperature dependence of the magnitude of the

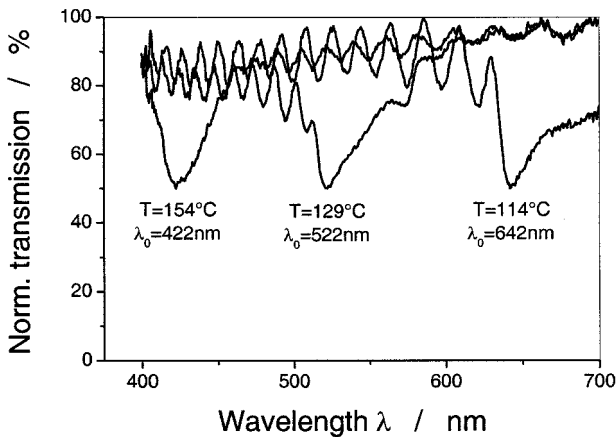


Fig. 5.10. Temperature dependent transmission spectra of a short pitch cholesteric in Grandjean orientation illuminated by linearly polarized white light. The deep minima in the transmission spectra correspond to the wavelength of selective reflection λ_0 . The other small minima are due to cell gap interference. Clearly, a decreasing pitch with increasing temperature can be deduced.

pitch $P(T)$ of the cholesteric phase, provided that the refractive indices are known. In almost all cases a decreasing pitch is observed with increasing temperature.

We are now left with the question of the handedness of the respective sample under investigation, i. e. the sign of the cholesteric pitch. This can also be determined in a polarizing microscope on a sample in Grandjean orientation, provided that the wavelength of selective reflection λ_0 is known. In principle, this method is the qualitative version of optical rotation dispersion, as discussed above (Fig. 5.7): Using different filters we illuminate the sample in transmission with linearly polarized, monochromatic light of wavelengths $\lambda < \lambda_0$ and $\lambda > \lambda_0$. If, looking in the direction towards the light source, the analyzer has to be rotated clockwise for $\lambda < \lambda_0$ and counterclockwise for $\lambda > \lambda_0$ to obtain a darker texture appearance (extinction), the cholesteric helix is right-handed. If the situation is reversed, we are looking at a left-handed cholesteric superstructure.

5.2.2.2 Homeotropic Boundary Conditions and the Flexoelectric Effect

When a short pitch cholesteric phase is subjected to homeotropic boundary conditions the helix axis, which represents the optic axis of the system, will orient parallel to the substrate plane. In the general case, every in-plane orientation of the helix axis is possible, and thus it will vary slowly over macroscopic distances, similar to the director of the nematic phase under planar boundary conditions. Considering a region of uniform helix axis orientation between crossed polarizers, this will behave optically like a uniaxial plate with the optic axis in the substrate plane. This is due to the fact that we cannot microscopically resolve structures smaller than the wavelength of light, and thus the modulation due to local director variations are optically averaged to yield a uniform appearance. For the observation of such a sample in a polarizing microscope, this implies that we observe an extinction position whenever the short pitch helix axis is parallel to one of the polarizers and maximum transmittance is obtained for an orientation of the helix axis at 45° between the polarizers at zero azimuth angle of the helix axis. The system behaves optically just like a uniform planar nematic or SmA phase. Note that this discussion only holds for short pitch cholesterics; the case of long pitch materials under homeotropic anchoring will be discussed below. In short pitch cholesteric materials subjected to homeotropic boundary conditions, an interesting linear electrooptic effect may be observed, the so-called flexoelectrooptic effect, which was first reported by Patel and Meyer [33] and which we will discuss in a bit more detail below.

Flexoelectricity is a very general effect in liquid crystals and can be observed for shape polar molecules with a permanent dipole moment. It has to be stressed that, even though we will discuss the flexoelectrooptic effect in relation to short pitch cholesteric materials, flexoelectricity is by no means related to the presence of chirality. Consider drop-shaped molecules with a permanent dipole moment along the drop's symmetry axis, forming a nematic phase as depicted in Fig. 5.11(a). In the field-free case, head–tail symmetry causes a vanishing macroscopic polarization. If an electric field is applied to the sample, this will cause the molecular dipoles to

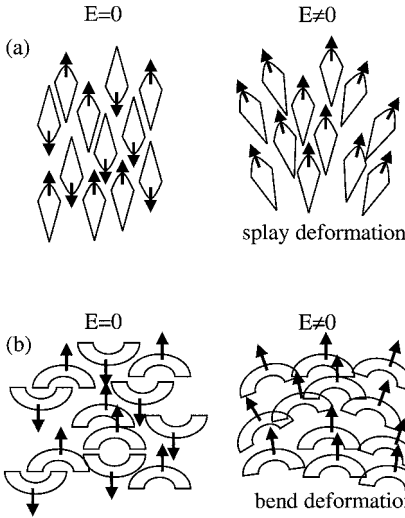


Fig. 5.11. A very schematic illustration of flexoelectricity for shape polar molecules with a dipole moment. (a) For drop-shaped mesogens no polarization is observed at zero field. Application of an electric field results in partial alignment of the molecular dipoles, which induces a splay deformation in the nematic director field. (b) Similarly, a bend deformation is induced for bow-shaped mesogens.

align, leading to a nonzero macroscopic polarization and at the same time inducing a splay deformation of the director, due to shape polarity of the molecules (Fig. 5.11(a)). In reverse, subjecting a nematic phase constituent of drop-shaped molecules to a splay deformation induces a flexoelectric polarization. In a similar way, application of an electric field to bow-shaped molecules will induce a bend deformation as depicted in Fig. 5.11(b). Real molecules generally combine drop- and bow-shaped contributions, and thus a splay–bend deformation is observed on application of an electric field. The flexoelectric polarization in this case is given by [34]

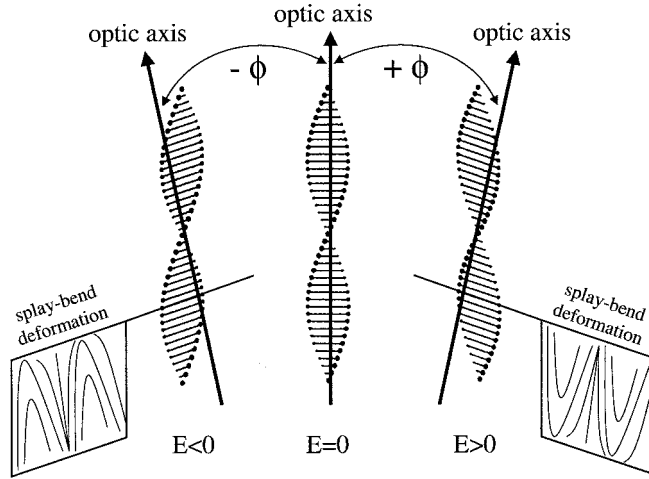
$$\mathbf{P} = e_s \mathbf{n}(\nabla \cdot \mathbf{n}) + e_b (\mathbf{n} \times \nabla \times \mathbf{n}) \quad (5.3)$$

with e_s and e_b being the flexoelectric coefficients for splay and bend deformations, respectively. Let us now consider a short pitch cholesteric phase with its helix axis uniformly aligned along the x direction in the plane of the substrate and the electric field applied perpendicular to it, along the z direction. This will induce a splay–bend deformation, resulting in an in-plane tilting of the helix axis and therefore a deviation of the optic axis of the system. The tilt direction depends on the polarity of the electric field, while the tilt magnitude depends on its amplitude. The effect is schematically depicted in Fig. 5.12. The free energy of the system is given by [33]

$$F = F_0 + \frac{1}{2} K \left(\frac{\partial \varphi}{\partial y} \right)^2 + \frac{1}{2} K_{22} \left(q_0 - \frac{\partial \varphi}{\partial z} \right)^2 - e_{av} E \frac{\partial \varphi}{\partial y} + \frac{1}{8\pi} \Delta \varepsilon E^2 \sin^2 \varphi \quad (5.4)$$

where K is an average splay–bend elastic constant and e_{av} is the average splay–bend flexoelectric coefficient. Neglecting surface anchoring effects and

Fig. 5.12. Schematic illustration of the linear flexoelectro-optic effect of a short pitch cholesteric phase with uniformly aligned helix axis in the plane of the substrate. Depending on the polarity of the applied electric field an in-plane deflection of the optic axis is observed, due to a rotation of the N^* helix axis caused by induced splay-bend deformations.



(for small electric field amplitudes) also the dielectric anisotropy term, minimization of the free energy yields the field induced deviation angle of the optic axis [35]:

$$\phi(E) = \arctan\left(\frac{\epsilon_{av} E}{q_0 K}\right) \quad (5.5)$$

which for small induced deviation angles results in

$$\phi(E) \approx \frac{\epsilon_{av} E P_0}{2\pi K} \quad (5.6)$$

In first approximation (for small electric fields and far from the vicinity of phase transitions) the induced deviation angle of the optic axis is linear in the electric field amplitude $\phi(E) \sim E$ and follows the temperature dependence of the cholesteric pitch $\phi(P(T)) \sim P(T)$. These relationships have been confirmed experimentally by

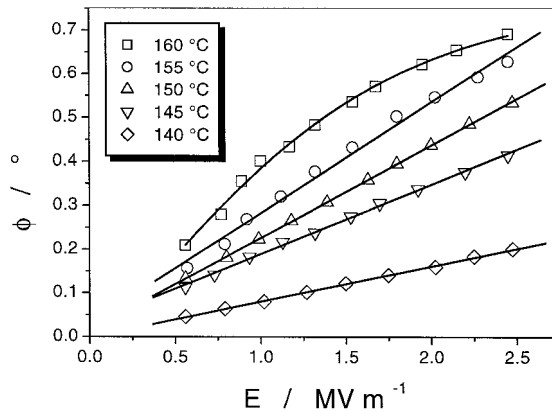


Fig. 5.13. Experimental example of the electric field dependent deviation angle ϕ of the optic axis of a uniform lying cholesteric helix texture for different temperatures. This demonstrates the linear flexoelectro-optic effect.

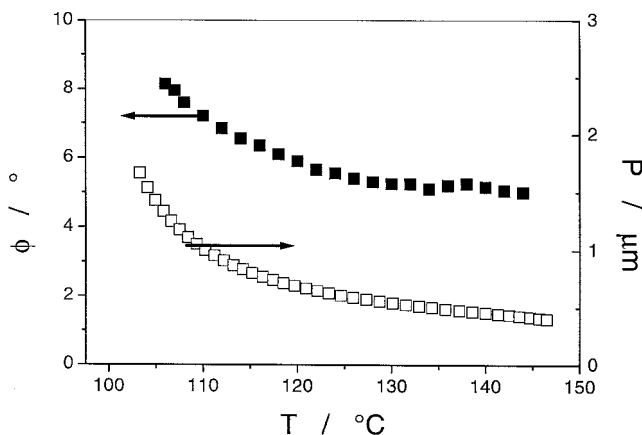


Fig. 5.14. Experimental example of the temperature dependence of the field induced deviation angle ϕ of the optic axis due to the linear flexoelectrooptic effect in short pitch cholesterics (closed symbols), which follows the temperature dependence of the pitch (open symbols).

several groups [33–41] and are demonstrated in Figs. 5.13 and 5.14, respectively (data after Ref. [41]). Field induced deviation angles are generally quite small, in the range of $\phi < 10$, but there have also been reports of larger angles [39] in a range that is certainly of interest for device application, especially because the linearity of the effect allows for easy gray-scale generation. The response times are found to be in the lower microsecond range and are essentially independent of electric field amplitude, but vary with a change of the cholesteric pitch.

5.2.3

Long Pitch Cholesterics

Cholesteric phases with a long pitch, clearly larger than $P > 1 \mu\text{m}$, do not exhibit Blue Phases at elevated temperatures but rather a direct $\text{Iso}^* - \text{N}^*$ transition. On cooling, this transition is accomplished via nucleation and growth of spherical cholesteric domains within the isotropic melt, as depicted in Plate 23. At a later point these domains coalesce (Plate 24) and eventually the cholesteric texture completely fills the microscope field of view.

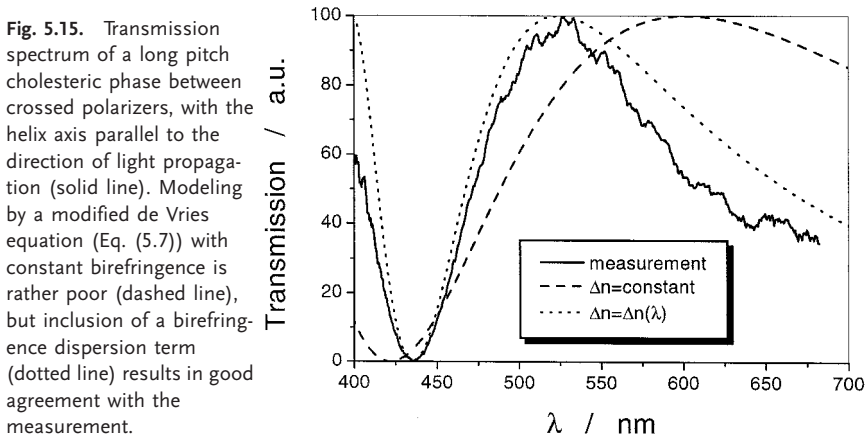
5.2.3.1 Planar Boundary Conditions

We should note in the beginning of this chapter that long pitch cholesterics in principle are no different from those with a short pitch. Their only difference is that some characteristic features of the cholesteric phase can be observed better or easier in respective materials. For example, the phenomenon of selective reflection can readily be seen in short pitch N^* materials subjected to planar boundary conditions, while the wavelength of selective reflection of a long pitch material lies in the far-infrared (far-IR). Similarly, a direct visualization of the helical superstructure can optically best be resolved for long pitch cholesterics under homeotropic boundary conditions, while the short pitch helical superstructure cannot be resolved by conventional microscopy.

Parallel rubbed cells and discontinuous pitch jumps For cholesteric phases with a relatively large pitch, the boundary conditions of the confining substrates become increasingly important. Realistic experimental conditions often involve a cholesteric with a pitch changing in the range of a few micrometers with temperature, being confined to a cell of gap 5–15 μm with planar anchoring conditions due to parallel rubbing. The system still exhibits a selective reflection, but not in the visible range of the spectrum as discussed above, but rather in the IR or far-IR. Nevertheless, long pitch cholesterics with helix axis parallel to the direction of propagation of linearly polarized white light show a uniform color between crossed polarizers (see Plate 16). This color is not related to selective reflection. Owing to the boundary conditions the director at the surfaces is forced to point along the rubbing direction on both the top and bottom substrates. This implies that the director configuration adopts a structure with an integer number of π twists within the cell gap. The color of such a structure can be calculated from the transmitted intensity by a modified de Vries equation for crossed polarizers [42] and accounting for birefringence dispersion in the single band model [43] and the cell gap d :

$$I(T, \lambda) = 100 \sin^2 \left[\frac{\pi P(T)}{4\lambda^2} \left(G(T) \frac{\lambda^2 (\lambda^*)^2}{\lambda^2 - (\lambda^*)^2} \right)^2 \frac{1}{1 - [\lambda/\bar{n}P(T)]^2} d \right] \quad (5.7)$$

The term in the large round brackets describes the birefringence dispersion, with $G(T)$ a temperature dependent factor, which in first approximation can be taken as a constant; λ^* is the mean resonance vacuum wavelength of the first ultraviolet (UV) absorption band, which is often dominated by the absorption of the phenyl and carbonyl groups to give $\lambda^* \approx 270$ nm. A typical measured spectrum in the visible range (solid line) is shown in Fig. 5.15 together with the modelled spectrum according to Eq. (5.7) with (dotted line) and without (dashed line) inclusion of a wavelength dependent birefringence. This clearly indicates that birefringence dispersion cannot be neglected in this case. Note that the modelling of transmission



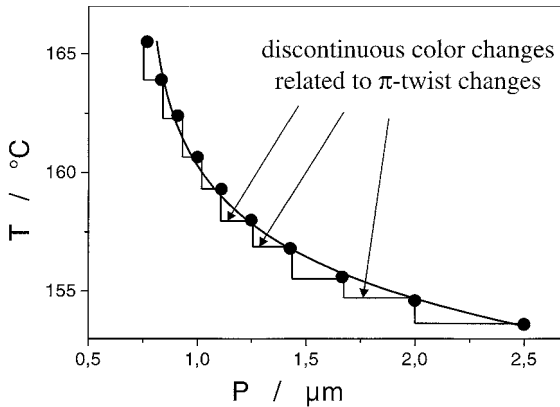


Fig. 5.16. Measurement (symbols) and schematic illustration (step function) of the temperature dependence of the cholesteric pitch determined by discontinuous color changes due to pitch jumps.

spectra according to Eq. (5.7) fails for helical structures with less than approximately five π twists, due to strong elastic deformations.

As mentioned before, the cholesteric pitch generally decreases with increasing temperature (although there exist some mixtures and even pure compounds that do exhibit the opposite behavior or even twist inversion phenomena – see below). If the temperature is varied for the planar cell geometry, the pitch remains constant until the helical structure is allowed to add (on heating) or subtract (on cooling) another π twist. This can be seen by polarizing microscopy as a discontinuous change of color, a new twist state nucleating and quickly spreading across the field of view, as shown in Plate 25. Depending on pitch and chosen cell gap, a number of color changes can be observed, covering colors from red (large pitch) to blue (smaller pitch) [44]. This effect can be used for a determination of the temperature dependence of the cholesteric pitch, provided that P is known for one single temperature T . If this is not the case, modelling of the recorded transmission spectra can give a good starting value [42]. The principle of the outlined pitch determination method is depicted in Fig. 5.16, which is in fact an indirect method, recording the temperature at a known pitch value (predetermined by the number of π twists and given cell gap), thus measuring $T(P)$. The handedness of the cholesteric superstructure can again be determined by rotation of the analyzer, as outlined above, taking into account that $\lambda < \lambda_0$ (see also Refs. [45, 46]).

The Grandjean–Cano geometries A similar, but more conventional, technique for pitch determination is the so-called Grandjean–Cano method. This goes back to the work of Grandjean [47], who realized that a cholesteric prepared under planar anchoring conditions in a wedge cell exhibits dark lines (now called Grandjean steps) whenever the helical structure changes its number of integer multiples of the spatial identity period $L = P/2$, i. e. whenever the twist changes by π . The schematic geometry is depicted in Fig. 5.17, and a corresponding texture can be found in Plate 26. From the distance s between the Grandjean lines, one can determine the cholesteric pitch for a known wedge angle α :

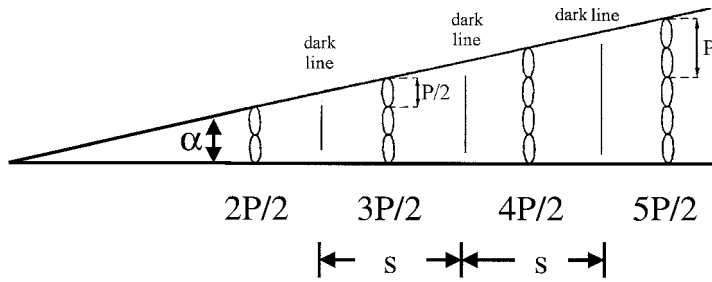


Fig. 5.17. Schematic illustration of the Grandjean wedge-shaped sample preparation for a determination of the pitch value of cholesterics.

$$P = 2s \tan \alpha \tag{5.8}$$

For an accurate determination of P , several lines should be evaluated for each temperature and the first few lines at very small cell gaps neglected. Variation of temperature changes the equilibrium structure in the wedge cell and leads to a different distance between the disclination lines, thus giving $P(T)$. A detailed interpretation of the Grandjean steps has been proposed by Cano [48], with the corresponding director configuration illustrated in Fig. 5.18. He had also designed a similar geometry, which up to this day is often used for pitch determination: the N^* phase is prepared between a planar glass plate and a lens of known radius r (Fig. 5.19). In complete accordance to the Grandjean preparation, we now observe a set of concentric rings at distances x_i from the center, as depicted in Plate 27. In fact, this observation had been reported long before by Stumpf [49], but without any interpretation given. From geometrical considerations the pitch is obtained from

$$P = \Delta x^2 / r \tag{5.9}$$

with $\Delta x^2 = x_{i+1}^2 - x_i^2$. Also here several rings should be evaluated to obtain an accurate measure of the pitch and the innermost rings of disclination lines neglected. As pointed out by Heppke and Oestreicher [50, 51] the Cano geometry can also be used to determine the handedness of the helical superstructure by turning the lens

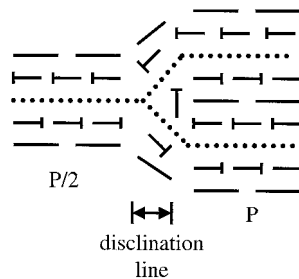


Fig. 5.18. Director configuration in the vicinity of a Grandjean step.

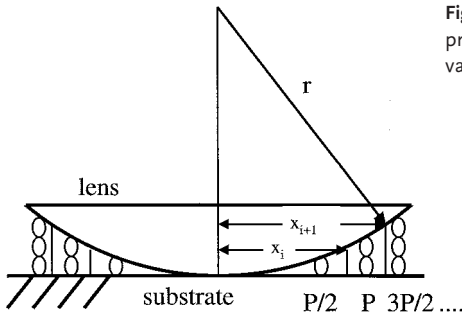


Fig. 5.19. Schematic illustration of the Cano preparation for the determination of the pitch value of a cholesteric phase.

with respect to the glass plate, which produces characteristic double spirals of disclination lines.

Cholesteric pitch in the vicinity of the smectic transition The presence of low temperature smectic phases has a pronounced effect on the cholesteric pitch in the vicinity of the respective transition [52]. For a N^* – SmA^* transition a strongly diverging pitch is generally observed [53–55], which is due to the incompatibility of twist deformations and smectic layer ordering, as discussed in Chapter 2. This divergence is much less pronounced for N^* – SmC^* transitions [56], as demonstrated in Fig. 5.20. The cholesteric pitch divergence is attributed to a pretransitional formation of local clusters of smectic ordering, which couples to the cholesteric director, causing a drastic increase of the twist elastic constant K_{22} close to the transition and thus resulting in a strong increase of the pitch [57–60]. This pretransitional formation of cybotactic clusters has been demonstrated by the x-ray experiments of de Vries [61–63]. A simulation of this behavior can be obtained by a contact preparation, i. e. the continuous variation of the concentration of two compounds, one with a N^* and another with a SmA^* phase, which is in principle analogous to a temperature gradient across the cell. An illustrative example is

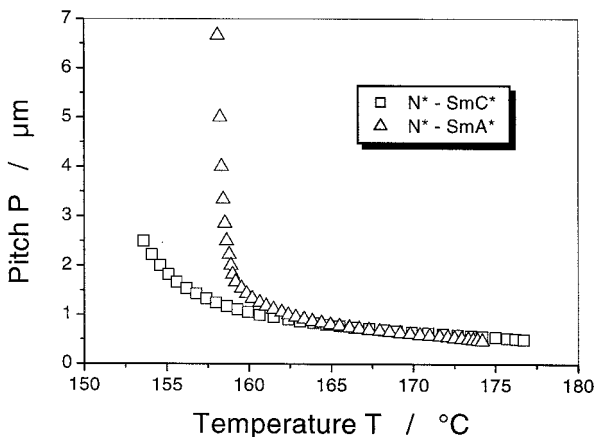


Fig. 5.20. Temperature dependence of the cholesteric pitch in the vicinity of the transition to a smectic phase. For two consecutive members of a homologous series it can clearly be observed that the divergence of the pitch is much stronger for a N^* – SmA^* (triangles) than for a N^* – SmC^* transition (squares).

shown in Plate 28, with the cholesteric phase at the bottom and the SmA* at the top. Across the contact region a strongly increasing cholesteric pitch is observed, with Grandjean lines separating regions of different twist states. For small cell gaps even a quasi-nematic director configuration can be obtained.

Twist inversion compounds An easy way [64, 65] to determine the helix handedness of a cholesteric structure goes back to the contact preparation discussed in Chapter 1. It relies on bringing the cholesteric phase of the compound whose twist sense is to be determined into contact with that of a reference compound of known handedness. If a cholesteric texture is observed throughout the contact region the twist sense is the same. For compounds of opposite handedness there will be a concentration region where pitch compensation and thus a nematic texture is observed. It is nevertheless worth noting that there are some uncertainties associated with the use of this method. These refer to so-called twist inversion materials, which are most often mixtures of two different components, exhibiting a reversal of the twist handedness with variation of concentration, even though the pure components may have the same twist sense [66]. In other cases the twist inversion occurs on variation of temperature [67]. This phenomenon has also been reported for mixtures of cholesterics and nematics [68, 69] and was theoretically treated by Stegemeyer and Finkelmann [70, 71] and later by Hansen et al. [72]. However, for few materials a twist inversion by temperature variation has been reported [44, 73–79] even for single component systems. This is a rather unusual phenomenon, but can easily be detected by polarizing microscopy (see Plate 29). On slowly lowering the temperature of the cholesteric under planar boundary conditions, discontinuous color changes are observed as discussed above. The sample cannot be brought into an extinction position by rotation between crossed polarizers. At a certain temperature T_{inv} a domain nucleates with a nematic director configuration, thus zero twist and $P = \infty$, which appears black whenever the director is oriented along one of the polarizer directions. This N_{∞}^* state eventually covers the whole microscope field of view. The width of the N_{∞}^* temperature region depends on the cell gap. Further lowering the temperature results in the reappearance of the cholesteric texture. Ferrarini et al. [80] have treated this phenomenon by a geometrical model, and recently Osipov and Kuball [81] have proposed a molecular model for the twist inversion of single component materials.

Li et al. [82] have demonstrated that in the unwound cholesteric state N_{∞}^* , i. e. a uniform planar nematic director configuration of *chiral* molecules, a linear electro-optic effect, similar to the electroclinic effect in SmA*, can be observed. For this effect the deviations of the optic axis from the field-free state are extremely small and increase linearly with applied electric field amplitude (Fig. 5.21), while the response is only slightly dependent on temperature with switching times being very fast, down to the nanosecond range [41, 83–87] (Fig. 5.22).

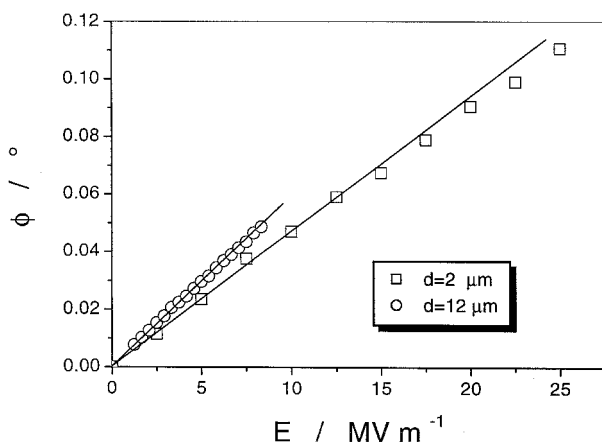


Fig. 5.21. An experimental example of the chiral nematic electroclinic effect in the N_{c^*} state of a twist inversion compound, i. e. for a uniform planar director configuration of chiral mesogens. Dependence of the induced angular deviation of the optic axis as a function of electric field amplitude.

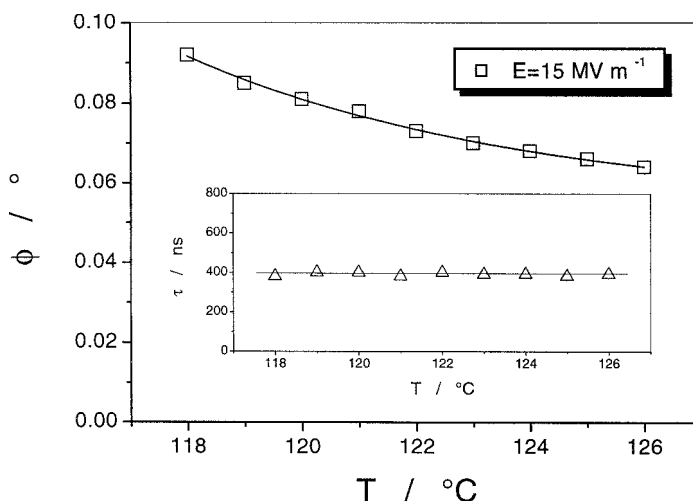
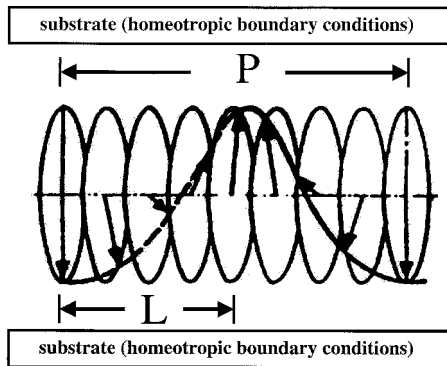


Fig. 5.22. Temperature dependence of the chiral nematic electroclinic effect in the N_{c^*} state of a twist inversion compound. The inset depicts the very fast response time of this linear electrooptic effect.

5.2.3.2 Homeotropic Boundary Conditions

Subjecting a long pitch cholesteric phase to homeotropic boundary conditions results in a helical structure with the twist axis lying in the plane of the substrate, as schematically shown in Fig. 5.23. Within the substrate plane there is no preferred direction, and thus the direction of the twist axis is allowed to vary smoothly over macroscopic distances. The varying director field leads to an equidistant pattern of dark lines, which in contrast to short pitch cholesterics can now be resolved by polarizing microscopy, as depicted in Plates 21, 30 and 31, showing what is called a *fingerprint* texture. Dark stripes appear, whenever the local director is oriented along the direction of light propagation, i. e. at vanishing birefringence. For choles-

Fig. 5.23. Schematic illustration of the cholesteric director configuration in the fingerprint texture observed for homeotropic boundary conditions.



teric liquid crystals the periodicity of the equidistant stripe pattern is given by $P/2$ and can thus be used to determine the pitch P . For rather small cell gaps, with d approaching the pitch length (Plate 31), this method becomes quite inaccurate, due to deformations of the helical superstructure by elastic interactions with the bounding substrate plates. Increasing the pitch still further leads to more and more distorted director configurations, as demonstrated in Plate 32, which shows a fingerprint-like cholesteric texture coexisting with so-called *cholesteric fingers* (bright lines) and even a pseudo-isotropic area (black). For very long pitch N^* samples, for example in the vicinity of a twist inversion temperature, the whole texture may exhibit cholesteric fingers, as depicted in Plate 33. Plate 34 shows a close-up of a cholesteric fingers region.

At this point it should also be mentioned that in natural preparations of a cholesteric phase both planar and homeotropic texture features may be observed at the same time. An example of this is shown in Plate 35 with uniformly colored areas corresponding to the Grandjean orientation and areas with an equidistant line pattern corresponding to a fingerprint orientation. Often the fingerprint regions vanish with time to later yield a uniform Grandjean texture.

References

- [1] G. Friedel, *Ann. Phys. (Fr.)*, **18**, (1922), 273.
- [2] J. Nehring, A. Saupe, *J. Chem. Soc., Faraday Trans. II*, **68**, (1972), 1.
- [3] A. Saupe, *Mol. Cryst. Liq. Cryst.*, **21**, (1973), 211.
- [4] H.-R. Trebin, *Adv. Phys.*, **31**, (1982), 195.
- [5] J. Nehring, *Phys. Rev. A*, **7**, (1973), 1737.
- [6] R. B. Meyer, *Solid State Commun.*, **12**, (1973), 585.
- [7] M. Kléman, "Points lines and walls", in *Liquid Crystals, Magnetic Systems and Various Ordered Media*, John Wiley & Sons, New York, 1983.
- [8] M. Kléman, C. E. Williams, *Philos. Mag.*, **28**, (1973), 725.
- [9] G. W. Gray, D. G. McDonnell, *Mol. Cryst. Liq. Cryst.*, **34**, (1977), 211.
- [10] O. Lehmann, *Z. Phys. Chem.*, **4**, (1889), 462.
- [11] M. Kléman, C. E. Williams, *J. Phys. Lett.*, **35**, (1974), L49.
- [12] P. Boltenhagen, O. D. Lavrentovich, M. Kléman, *J. Phys. II*, **1**, (1991), 1233.
- [13] Y. Bouligand, *J. Phys. (Fr.)*, **34**, (1973), 603.
- [14] Y. Bouligand, *J. Microsc. (Fr.)*, **17**, (1973), 145.
- [15] G. Friedel, F. Grandjean, *Bull. Soc. Fr. Minér.*, **33**, (1910), 192.
- [16] *Ibid.*, p. 409.
- [17] G. Friedel, F. Grandjean, *C. R. Hebd. Séances Acad. Sci.*, **151**, (1910), 762.
- [18] Y. Bouligand, *J. Phys. (Fr.)*, **33**, (1972), 715.
- [19] A. C. Neville, S. Caveney, *Biol. Rev. Camb. Phil. Soc.*, **44**, (1969), 531.
- [20] G. H. Brown, J. J. Wolken, *Liquid Crystals and Biological Structures*, Academic Press, New York, 1979.
- [21] H. de Vries, *Acta Crystallogr.*, **4**, (1951), 219.
- [22] S. Chandrasekhar, J. S. Prasad, *Mol. Cryst. Liq. Cryst.*, **14**, (1971), 115.
- [23] R. C. Jones, *J. Opt. Soc. Am.*, **31**, (1941), 488.
- [24] R. C. Jones, *J. Opt. Soc. Am.*, **31**, (1941), 493.
- [25] R. C. Jones, *J. Opt. Soc. Am.*, **32**, (1942), 486.
- [26] A. Gerrard, J. M. Burch, *Introduction to Matrix Methods in Optics*, Dover Publications, New York, 1994.
- [27] S. Chandrasekhar, *Liquid Crystals*, 2nd edn., Cambridge University Press, Cambridge, 1992, ch. 4.
- [28] D. W. Berreman, T. J. Scheffer, *Phys. Rev. Lett.*, **25**, (1970), 577.
- [29] D. W. Berreman, T. J. Scheffer, *Mol. Cryst. Liq. Cryst.*, **11**, (1970), 315.
- [30] C. Oldano, P. Allia, L. Trossi, *J. Phys. (Fr.)*, **46**, (1975), 573.
- [31] V. A. Belyakov, *Diffraction Optics of Complex-Structured Periodic Media*, Springer-Verlag, Berlin, 1992.
- [32] I. Dierking, F. Giesselmann, P. Zugenmaier, K. Mohr, H. Zschke, W. Kuczynski, *Liq. Cryst.*, **18**, (1995), 443.
- [33] J. S. Patel, R. B. Meyer, *Phys. Rev. Lett.*, **58**, (1987), 1538.
- [34] P. Rudquist, S. T. Lagerwall, *Liq. Cryst.*, **23** (1997), 503
- [35] J. S. Patel, S.-D. Lee, *J. Appl. Phys.*, **66**, (1989), 1879.
- [36] S.-D. Lee, J. S. Patel, R. B. Meyer, *J. Appl. Phys.*, **67**, (1990), 1293.

- [37] S.-D. Lee, J. Patel, R. B. Meyer, *Mol. Cryst. Liq. Cryst.*, **209**, (1991), 85.
- [38] L. Komitov, S. T. Lagerwall, B. Stebler, A. Strigazzi, *J. Appl. Phys.*, **76**, (1994), 3762.
- [39] P. Rudquist, M. Buivydas, L. Komitov, S. T. Lagerwall, *J. Appl. Phys.*, **76**, (1994), 7778.
- [40] P. Rudquist, L. Komitov, S. T. Lagerwall, *Phys. Rev. E*, **50**, (1994), 4735.
- [41] I. Dierking, P. Rudquist, L. Komitov, S. T. Lagerwall, B. Stebler, *Mol. Cryst. Liq. Cryst.*, **304**, (1997), 389.
- [42] I. Dierking, F. Giesselmann, P. Zugenmaier, *Z. Naturforsch.*, **50a**, (1995), 589.
- [43] S.-T. Wu, *Phys. Rev. A*, **33**, (1986), 1270.
- [44] I. Dierking, F. Giesselmann, P. Zugenmaier, W. Kuczynski, S. T. Lagerwall, B. Stebler, *Liq. Cryst.*, **13**, (1993), 45.
- [45] J.-P. Berthault, J. Billard, J. Jaques, *C. R. Acad. Sci., Paris*, **284c**, (1977), 155.
- [46] P. R. Gerber, *Z. Naturforsch.*, **35a**, (1980), 619.
- [47] M. F. Grandjean, *C. R. Acad. Sci., Paris*, **172**, (1921), 71.
- [48] R. Cano, *Bull. Soc. Fr. Minér. Cristallogr.*, **91**, (1968), 20.
- [49] F. Stumpf, *Ann. Phys. (Ger.)*, **37**, (1912), 351.
- [50] G. Heppke, F. Oestreicher, *Z. Naturforsch.*, **32a**, (1977), 899.
- [51] G. Heppke, F. Oestreicher, *Mol. Cryst. Liq. Cryst. Lett.*, **41**, (1978), 245.
- [52] J. Voss, E. Sackmann, *Z. Naturforsch.*, **28a**, (1973), 1496.
- [53] R. S. Pindak, C. C. Huang, J. T. Ho, *Phys. Rev. Lett.*, **32**, (1974), 43.
- [54] R. S. Pindak, J. T. Ho, *Phys. Lett.*, **59A**, (1976), 277.
- [55] S.-H. Chen, J. J. Wu, *Mol. Cryst. Liq. Cryst.*, **87**, (1982), 197.
- [56] K.-C. Lim, J. T. Ho, *Mol. Cryst. Liq. Cryst.*, **67**, (1981), 199.
- [57] R. Alben, *Mol. Cryst. Liq. Cryst.*, **20**, (1973), 231.
- [58] P. G. de Gennes, *Mol. Cryst. Liq. Cryst.*, **21**, (1973), 49.
- [59] J. H. Chen, T. C. Lubensky, *Phys. Rev. A*, **14**, (1976), 1202.
- [60] K. C. Chu, W. L. McMillan, *Phys. Rev. A*, **15**, (1977), 1181.
- [61] A. de Vries, *Mol. Cryst. Liq. Cryst.*, **10**, (1970), 31.
- [62] A. de Vries, *Mol. Cryst. Liq. Cryst.*, **10**, (1970), 219.
- [63] A. de Vries, *Mol. Cryst. Liq. Cryst.*, **11**, (1970), 361.
- [64] M. J. Billard, *C. R. Acad. Sci., Paris*, **274b**, (1972), 333.
- [65] N. Isaert, B. Soulestine, J. Malthete, *Mol. Cryst. Liq. Cryst.*, **37**, (1976), 321.
- [66] H. Finkelmann, H. Stegemeyer, *Z. Naturforsch.*, **28a**, (1973), 1046.
- [67] E. Sackmann, S. Meiboom, L. C. Snyder, A. E. Meixner, R. E. Dietz, *J. Am. Chem. Soc.*, **90**, (1968), 3567.
- [68] F. D. Saeva, J. Wysocki, *J. Am. Chem. Soc.*, **93**, (1971), 5928.
- [69] H. Finkelmann, H. Stegemeyer, *Z. Naturforsch.*, **28a**, (1973), 799.
- [70] H. Stegemeyer, H. Finkelmann, *Chem. Phys. Lett.*, **23**, (1973), 227.
- [71] H. Stegemeyer, H. Finkelmann, *Ber. Bunsenges. Phys. Chem.*, **78**, (1974), 869.
- [72] H. Hanson, A. J. Dekker, F. van der Woude, *J. Chem. Phys.*, **62**, (1975), 1941.
- [73] H. Stegemeyer, K. Siemensmeyer, W. Sucrow, L. Appel, *Z. Naturforsch.*, **44a**, (1989), 1127.
- [74] A. J. Slaney, I. Nishiyama, P. Styring, J. W. Goodby, *J. Mater. Chem.*, **2**, (1992), 805.
- [75] P. Styring, J. D. Vuijk, I. Nishiyama, A. J. Slaney, J. W. Goodby, *J. Mater. Chem.*, **3**, (1993), 399.
- [76] A. I. Galatina, A. A. Gerasimov, R. V. Kondratyeva, N. L. Kramarenko, V. E. Kuzmin, I. B. Stelmakh, N. M. Shkabar, *Mol. Mater.*, **2**, (1993), 213.
- [77] C. Loubser, P. L. Wessels, P. Styring, J. W. Goodby, *J. Mater. Chem.*, **4**, (1994), 71.
- [78] I. Dierking, F. Giesselmann, P. Zugenmaier, K. Mohr, H. Zschke, W. Kuczynski, *Z. Naturforsch.*, **49a**, (1994), 1081.
- [79] V. Vill, H.-W. Tunger, H. Stegemeyer, K. Diekmann, *Tetrahedron: Asymmetry*, **5**, (1994), 2443.
- [80] A. Ferrarini, G. J. Moro, P. L. Nordio, *Phys. Rev. E*, **53**, (1996), 681.
- [81] M. A. Osipov, H.-G. Kuball, *Phys. Rev. E*, **82**
- [82] Z. Li, R. G. Petschek, C. Rosenblatt, *Phys. Rev. Lett.*, **62**, (1989), 796.

- [83] Z. Li, A. Di Lisi, R. G. Petschek, C. Rosenblatt, *Phys. Rev. A*, **41**, (1990), 1997.
- [84] Z. Li, R. Ambigapathy, R. G. Petschek, C. Rosenblatt, *Phys. Rev. A*, **43**, (1991), 7109.
- [85] L. Komitov, S. T. Lagerwall, B. Stebler, G. Andersson, K. Flatischler, *Ferroelectrics*, **114**, (1991), 167.
- [86] J. Etxebarria, J. Zubia, *Phys. Rev. A*, **44**, (1991), 6626.
- [87] J. Zubia, J. Etxebarria, M. A. P. Jubindo, *Liq. Cryst.*, **16**, (1994), 941.

6

Twist Grain Boundary Phases

Twist grain boundary (TGB) phases are frustrated phases, generally located between the cholesteric and the respective smectic phase. Like the Blue Phases, they can only be observed in chiral materials with large twisting power. In single component compounds their temperature region of phase existence is generally rather small, in the order of 1 K, while in mixtures the range of existence can sometimes be greatly enhanced. The TGBA* phase was theoretically predicted by Renn and Lubensky [1] in 1988, based on a formal analogy between the SmA phase and superconductors, as introduced by de Gennes [2]. In this analogy the twist grain boundary phase is the liquid crystal equivalent of the Abrikosov flux lattice phase of a type II superconductor in an external magnetic field [1, 3].

Although not being related to the textures of these phases, let us briefly outline this analogy. Consider a type I superconductor in its normal conducting (metal) phase at elevated temperatures. In this phase the magnetic induction lines of a relatively weak applied magnetic field will completely penetrate the material. Cooling into the superconducting state will result in an expulsion of the magnetic flux lines from the material, which is called the Meissner effect [4]. In a type II superconductor at a temperature below the conductor–superconductor transition, the material behaves like type I up to a certain critical field. Further increase of the magnetic field strength will result in a state where an incomplete Meissner effect is observed, with magnetic flux lines partially penetrating the material [5]. In this state, called the Abrikosov phase, flux lattice phase or vortex state, the superconducting properties are decreased. The distance to which the magnetic field can penetrate the superconducting material is called the London penetration depth [6]. The de Gennes analogy [2] treats the case of a second order nematic to SmA transition. In the analogy, a twist penetrates the SmA structure via a lattice of screw dislocations, just as the magnetic flux lines penetrate a type II superconductor via a lattice of vortices. In this case the nematic phase corresponds to a normal metal and the SmA phase to the Meissner phase of the superconductor. Thus twist expulsion in the liquid crystal is the analog to the Meissner effect. The de Gennes analogy was extended to chiral systems by Renn and Lubensky [1], i. e. to the N*–SmA* transition. Here the cholesteric phase corresponds to the conducting phase (normal metal) in a magnetic field, and thus the twist is the equivalent to the magnetic

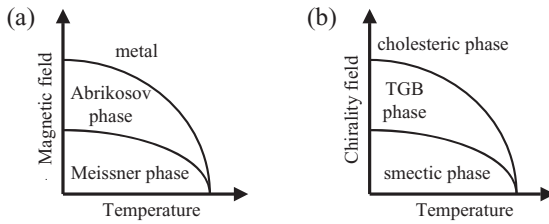


Fig. 6.1. Schematic phase diagram of (a) a type II superconductor in an applied magnetic field and (b) a chiral liquid crystal, illustrating the analogy of the Abrikosov flux lattice phase and the twist grain boundary TGBA* phase.

Tab. 6.1. Summary of some key quantities in the analogy between liquid crystals and superconductors.

<i>Liquid crystal</i>	<i>Superconductor</i>
nematic phase	normal metal
SmA phase	Meissner phase
cholesteric phase	normal metal in a magnetic field
nematic director, \mathbf{n}	magnetic vector potential, \mathbf{A}
“chirality field”, $h = k_{22}q_0$	magnetic field, \mathbf{H}
twist, $q_0 = \mathbf{n} (\nabla \times \mathbf{n})$	magnetic induction, $\mathbf{B} = \nabla \times \mathbf{A}$
elastic energy	magnetic energy
screw dislocation	magnetic vortex (magnetic flux tube)
TGB phase	Abrikosov phase

induction in the case of superconductors. The twist penetration depth takes the role of the London penetration depth of the type II superconducting material. Associating the formed screw dislocations of the liquid crystal material with a vortex or magnetic flux tube of the superconductor, we arrive at the analogy of the TGBA* phase with the Abrikosov phase. This formal analogy is illustrated by the respective phase diagrams of both the type II superconducting material and the liquid crystal (Fig. 6.1) and is summarized in Tab. 6.1 [7].

After this brief excursion, let us now return to the structure and textures of twist grain boundary phases. TGB phases exhibit three basic key structural features:

- layered structure,
- helical superstructure,
- helix axis parallel to the smectic layer plane.

The TGB helix axis is thus perpendicular to the local director, which illustrates the close relationship between twist grain boundary phases and the high temperature cholesteric phase. The first experimental observation of a twist grain boundary phase was reported by Goodby et al. [8, 9], one year after its theoretical prediction.

6.1

The TGBA* Phase

As we have pointed out on several occasions above (Chapter 3), a twist such as observed in the cholesteric phase is for elastic reasons in general not compatible with the layered structure of the smectic A* phase. If on the other hand the tendency to helical superstructure formation is very strong, the competition between twist formation and smectic layer formation can result in a defect stabilized, frustrated structure, as shown in Fig. 6.2. Grains with a local SmA* layer structure are separated by regular arrays of screw dislocations, which can be realized by splay deformations in the director field and whose direction is parallel to the Burgers vector. These form the grain boundaries between adjacent grains (Fig. 6.3). The parallel screw dislocations of a single grain boundary are rotated by an angle $\Delta\alpha$ with respect to those of the adjacent grain, thus forming a helical superstruc-

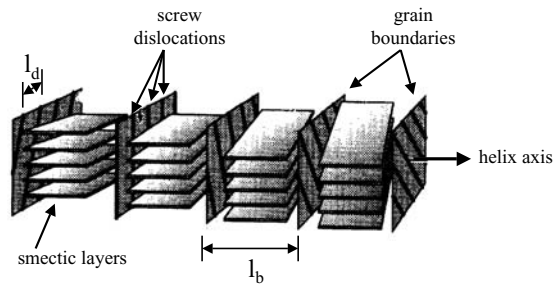


Fig. 6.2. Model structure of the twist grain boundary TGBA* phase.

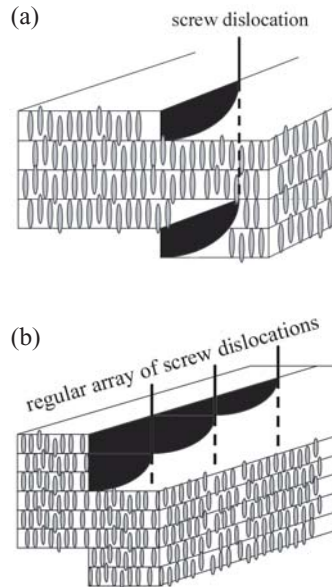


Fig. 6.3. Model structure of (a) a single screw dislocation and (b) a regular array of screw dislocations separating consecutive SmA* slabs of the TGBA* phase.

ture with twist axis perpendicular to the directors of each individual grain. This arrangement is quite similar to the structure of the N* phase and has directly been demonstrated by freeze–fracture transmission electron microscopy (TEM) studies [10].

The basic structural parameters of the TGBA* phase are the smectic layer thickness l , the helical pitch P , the thickness of smectic layer blocks l_b , i. e. the distance between adjacent grain boundaries, the distance between dislocation lines within a grain boundary l_d , and the twist between consecutive blocks $\Delta\alpha$ (see Figs. 6.2 and 6.3). From geometric considerations these parameters are related by the following relationships:

$$\Delta\alpha \approx l/l_d \quad (6.1)$$

and

$$\Delta\alpha = 2\pi l_b/P \quad (6.2)$$

(see Fig. 6.2). Combination of Eqs. (6.1) and (6.2) gives

$$P = 2\pi l_b l_d/l \quad (6.3)$$

From the x-ray investigations of Navailles et al. [11] (on a TGBC* phase), we can estimate the order of magnitude of the distance between screw dislocations by taking the grain block thickness to be in the order of $l_b \approx 1000 \text{ \AA}$ and the pitch to be $P \approx 2 \text{ \mu m}$. This yields a ratio of $l_d/l \approx 3$ or $l_d \approx 100 \text{ \AA}$. So far, x-ray investigations indicate that the structure of the TGBA* phase is often incommensurate [12–14], i. e. $360^\circ/\Delta\alpha$ is an irrational number. This means that we do not have an integer number of grain blocks along a 2π twist (Fig. 6.4(b)). Recently however, also an example of a commensurate TGBA* phase has been reported [15] (Fig. 6.4(a)).

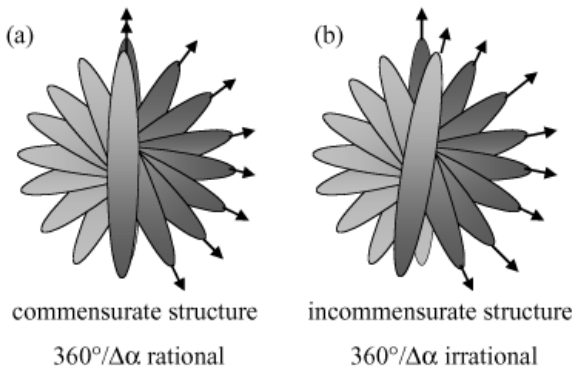


Fig. 6.4. Schematic illustration of (a) a commensurate and (b) an incommensurate structure of the TGBA* phase. An incommensurate structure is observed when it is formed by an irrational number of smectic slabs, while a commensurate structure consists of a rational number of smectic A* blocks within one pitch turn of the TGB helix.

6.1.1

Natural Textures

Owing to the often narrow temperature range of existence it is sometimes hard to detect the TGBA* phase not only by differential scanning calorimetry, but also by polarizing microscopy and texture observation. One method that can help to verify a twist grain boundary phase is the application of a temperature gradient across the sample, which results in a texture showing all three phases involved simultaneously, as shown in Plate 36 [16]. The temperature gradient is along the short edge of the texture photograph, exhibiting the SmA* fan-shaped texture at lower temperature at the top and the N* oily streaks texture at higher temperatures at the bottom of the image. In the middle part one can clearly detect the two phase boundaries separating the TGBA* phase.

Even for a larger temperature range of TGBA* phase existence it can sometimes not very easily be detected from natural textures with quasi-planar surface anchoring. Often the transition is only characterized by a smearing out of the high temperature phase texture, which in the case of a cholesteric oily streaks texture can be observed by the transformation of the sharp oily streaks defects into a slightly blurred structure (Plate 37). This texture cannot be clearly focused in the polarizing microscope. A similar appearance can also be observed when the TGBA* phase adopts a fan-like texture. An example is shown in Plates 38 and 39 on cooling. In Plate 38 the TGBA* phase is seen, appearing as a blurred fan-shaped texture, which cannot be clearly focused. Cooling across the TGBA* to SmA* transition one can observe a sudden sharpening of the fans, as seen in Plate 39. The discussed behavior can also be seen in Plate 36 on both sides of the phase boundaries, i.e. the N*–TGBA* transitions with a blurred Grandjean texture region and the TGBA*–SmA* transition with a blurred fan-shaped region.

For relatively thick samples, prepared between untreated glass plates, the TGBA* phase exhibits a quite unoriented appearance and can thus often be distinguished from the cholesteric and the SmA* phase. The series of texture photographs of Plates 40–42 [17] across the N*–TGBA*–SmA* temperature region illustrates this behavior.

6.1.2

Textures for Planar Anchoring Conditions

Subjecting the TGBA* phase to planar boundary conditions orients the molecular long axis parallel to the substrate and thus the smectic layer planes perpendicular to the glass plates. This implies that the TGBA* helix axis is oriented perpendicular to the substrate planes, similar to the Grandjean orientation of the cholesteric phase. The resulting structure is schematically depicted in Fig. 6.5, with an integer number of π twists fitting into the fixed cell gap. A typical texture of this arrangement is shown in Plate 43 [16] for a TGBA* phase with a pitch of several micrometers, confined to a cell gap of $d = 8 \mu\text{m}$ and in Plate 44 for

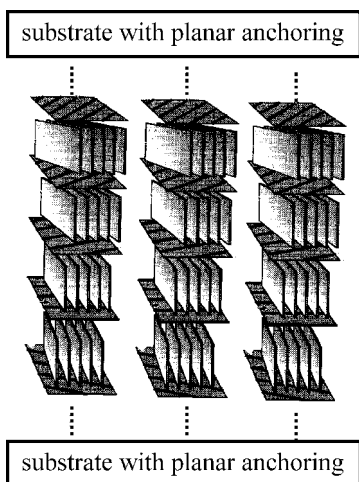


Fig. 6.5. Schematic illustration of a TGBA* phase confined to a cell with planar boundary conditions. TGB Grandjean steps may be observed whenever the pitch of the helical superstructure is changed by a π twist.

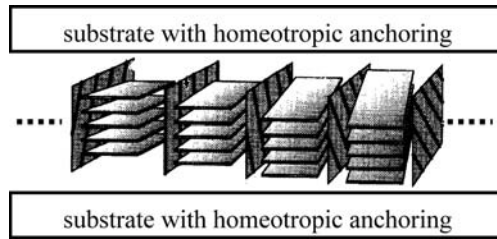
a short pitch material. The texture photographs were taken on cooling, with different colors corresponding to different twist states, due to the temperature dependence of the TGBA* pitch in the vicinity of the transition to SmA*. Rotation of the TGBA* phase maintaining the helix axis parallel to the direction of light propagation does not result in an extinction position between crossed polarizers, which is indicative of a helical superstructure. If the bounding substrates are not parallel to each other, the formation of TGBA* Grandjean steps is observed, resulting from half-pitch variations, i. e. changes of consecutive π twists. A corresponding texture is shown in Plate 45, which once again illustrates the close relationship between the TGBA* appearance and that of the cholesteric phase (compare to Plate 26).

6.1.3

Textures for Homeotropic Anchoring Conditions

If the TGBA* phase is subjected to homeotropic boundary conditions, the molecules orient with their long molecular axes perpendicular to the substrates, which results in an arrangement where the helix axis is lying in the plane of the bounding glass plates. Within the substrate plane the helix axis does not exhibit any preferred direction, just as discussed above for the N* phase. The resulting image observed between crossed polarizers is the so-called filament texture, an example of which is shown in Plate 46 at the transition from N* (left) to TGBA* (right) and in Plate 47 for the transition from SmA* (black) to TGBA* (filaments). For a sample with a long pitch TGBA* phase an equidistant pattern of dark lines is observed, which results from the helical orientation of the director, with a dark line appearing whenever the local director is oriented along the direction of light propagation (Plates 48 and 49). The periodicity L of the TGBA* phase is equal to half the pitch, so that the pitch can be estimated from $P = 2L$. The corresponding cell

Fig. 6.6. Schematic illustration of a TGBA* phase confined to a cell with homeotropic anchoring conditions. For a sample where the pitch can be resolved by optical microscopy, P is given by twice the identity period, i. e. the distance between two adjacent dark lines of the equidistant line pattern corresponds to half the value of the TGB pitch.



configuration is schematically depicted in Fig. 6.6. At the transition to the SmA* phase the texture changes to the pseudo-isotropic texture, which is illustrated by the dark sample region at the top left of Plate 50.

6.1.4

Wedge Cell Preparations

Preparation of a sample in a wedge cell geometry under a temperature gradient is quite illustrative with respect to structural similarities and differences of N*, TGBA*, and SmA* textures [16]. Let us first consider the case of planar anchoring conditions, for which the respective texture photograph is shown in Plate 51, with the temperature gradient applied from right to left. At the low temperature side (right) the SmA* phase is observed with the director in the plane of the substrate. This part of the texture can be brought into an extinction position, when the optic axis is oriented along one of the polarizer directions. In the middle part of the texture the TGBA* is formed, which shows Grandjean steps. The TGBA* region cannot be brought to extinction. This indicates that the helical superstructure is oriented with the twist axis along the direction of light propagation, and different twist states are observed due to the wedge cell geometry. In the left part of the texture, the high temperature cholesteric phase can be seen with its typical oily streaks. Also here, the optic axis points along the direction of light propagation and no intensity change is observed by rotation between crossed polarizers. Fig. 6.7 schematically depicts the sample configuration discussed [16].

In a second preparation we subject the same sample to homeotropic boundary conditions. The respective texture photograph is shown in Plate 52 [16]. The low temperature SmA* phase on the right side is dark for all orientations of the sample between crossed polarizers, i. e. the optic axis is oriented parallel to the direction of light propagation. At the transition region into the TGBA* phase in the middle part of the texture, the typical filaments are observed, while at somewhat higher temperatures the TGBA* phase adopts a fan-like texture. The helix axis in this part is basically oriented in the substrate plane. The high temperature N* phase also exhibits a fan-like texture, but can easily be distinguished from the TGBA* phase by the change in birefringence. The respective sample configuration is schematically summarized in Fig. 6.8 [16].

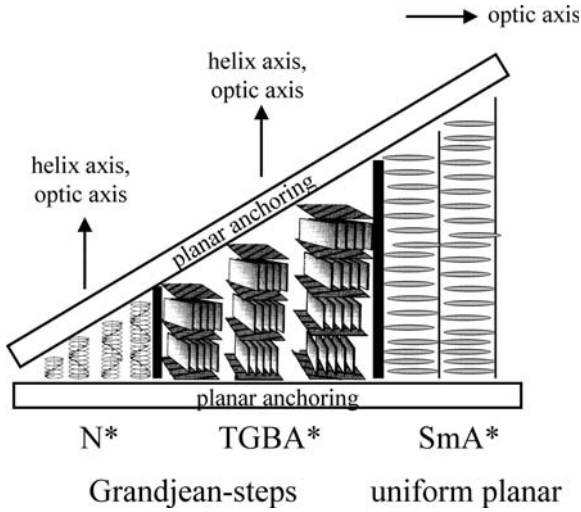


Fig. 6.7. Schematic illustration of a wedge cell preparation with planar boundary conditions of a sample with a N^* – $TGBA^*$ – SmA^* phase sequence under a temperature gradient. Corresponding to the texture photograph of Plate 51, the SmA^* phase at the right part of the figure exhibits a director oriented in the plane of the substrate; the sample can be brought to extinction when the optic axis is oriented along one of the polarizer directions. The $TGBA^*$ phase in the middle of the figure exhibits a twist axis along the direction of light propagation; it thus shows a director configuration that cannot be rotated into an extinction position. Discontinuous Grandjean steps are observed due to the temperature dependence of the $TGBA^*$ pitch. In the left part of the figure the cholesteric phase is shown with its helix axis parallel to the incident light beam.

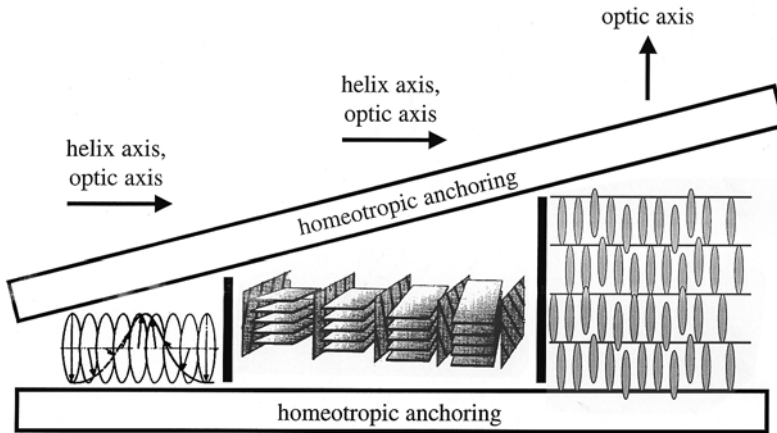


Fig. 6.8. Schematic illustration of a homeotropic boundary condition wedge cell preparation of a sample with a N^* – $TGBA^*$ – SmA^* phase sequence under a temperature gradient. Corresponding to the texture photograph of Plate 52, the pseudo-isotropic director configuration of the SmA^* phase is illustrated at the right of the figure. In the center part the director orientation of the fan-like and filament $TGBA^*$ texture is illustrated, while the left part of the figure depicts the N^* director orientation.

6.1.5

Droplet Preparation

The helix axis orientation of the TGBA* phase in comparison to that of the cholesteric and the SmC* phase can be nicely demonstrated by the observation of a droplet [17]. The sample with a phase sequence N*–TGBA*–SmC* is prepared as a droplet with an approximate diameter of 500 μm with a coverslip very gently placed on top. The sequence of Plates 53–55 shows the textures of the N*, TGBA*, and SmC* phases, respectively. In Plate 53 it can be seen that the cholesteric helix axis is basically oriented in the plane of the substrate, but without any preferred in-plane direction. Cooling the sample into the TGBA* phase the formation of a radially symmetric stripe pattern can be observed (Plate 54). This results from smectic layers being formed in a concentric fashion, with the TGBA* helix axis along the smectic layer planes and perpendicular to the long molecular axis. A schematic illustration of this arrangement is depicted in Fig. 6.9 [16]. Further cooling leads to the formation of the SmC* phase, which is shown in Plate 55. This is accompanied by a turn of the helical superstructure by 90° , because in SmC* the helix axis is oriented perpendicular to the smectic layer plane. In a droplet preparation with a concentric arrangement of smectic layers, the helix axis adopts a radial configuration and we thus observe a concentric pattern of equidistant lines due to the SmC* helical superstructure (see also Chapter 7). The corresponding schematic illustration is depicted in Fig. 6.10 [16].

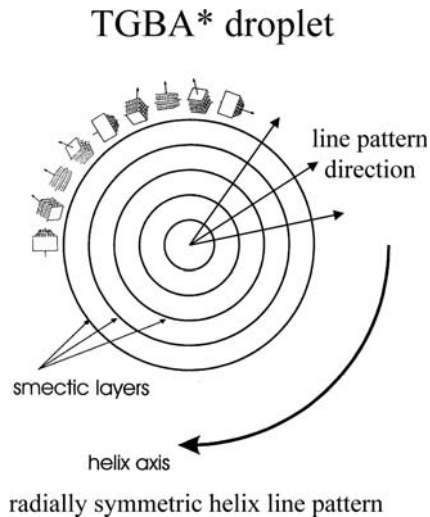


Fig. 6.9. Schematic illustration of the smectic layer orientation and TGBA* helix axis configuration in a droplet preparation with planar anchoring conditions. The TGBA* phase exhibits a helix axis that is oriented parallel to the smectic layer planes, resulting in a line pattern of radial symmetry. (Reproduced by permission of Taylor & Francis, I. Dierking, S. T. Lagerwall, *Liq. Cryst.*, **26**, (1999), 83 (<http://www.tandf.co.uk/journals>).)

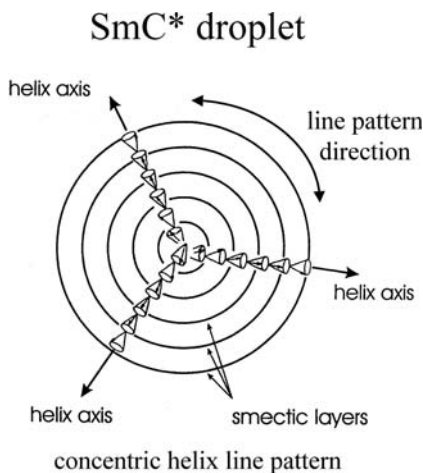


Fig. 6.10. Schematic illustration of the smectic layer orientation and SmC* helix axis configuration in a droplet preparation with planar anchoring conditions. The smectic C* helix axis is oriented perpendicular to the smectic layer plane, observable as a line pattern of equidistant concentric rings parallel to the smectic layer planes. (Reproduced by permission of Taylor & Francis, I. Dierking, S. T. Lagerwall, *Liq. Cryst.*, **26**, (1999), 83 (<http://www.tandf.co.uk/journals>).)

6.1.6

Suppression of the TGBA* Structure

Confining a TGB material to rather thin cell gaps, as compared to the pitch of its helical superstructure, can result in the suppression of the twist structure, due to a competition between elasticity and helix formation [17–19]. Let us again consider the sample discussed in the previous subsection, which exhibits a $N^* - TGBA^* - SmC^*$ phase sequence. Observation of the compound in a $4 \mu\text{m}$ cell with monostable planar boundary conditions clearly shows that the helical superstructure of the TGBA* phase is unwound and only the structure of the constituent smectic slabs remains. This is demonstrated in Plate 56 [16], which shows a typical uniform planar SmA^* texture (right part of the photograph), which is here rotated out of the direction of the polarizers, but can be brought to extinction. This SmA^* phase is transforming into SmC^* (left part), which can be seen by the partial formation of helix lines. The phase sequence in thin cells is now $N^* - SmA^* - SmC^*$, but it is emphasized again that the *bulk sample* does not exhibit a SmA^* but rather a TGBA* phase (see droplet preparation in Plates 53–55).

6.2

The TGBC* Phases

While the structure and textures of the TGBA* phase seem to be quite well understood, these are to some extent still the subject of controversial discussion for the TGBC* phases. The possible occurrence of a TGBC* phase was theoretically predicted by Renn and Lubensky [3, 20], and again experimental evidence was provided soon after its prediction, this time by Nguyen and coworkers [21]. Owing to the local SmC^* tilt of the molecules with respect to the smectic layer normal

and to the existence of a spontaneous polarization, several different structures may in principle occur in the TGBC* phase [20]. Generally, the SmC* phase exhibits a helical superstructure in bulk samples (see Chapter 7). For several possible TGBC* structures this twist is expelled into the twist grain boundaries, which means that the local smectic C* slabs exhibit a uniform tilted director configuration. Concerning the nomenclature, there seems to be no agreement on how to name the different possible TGBC* structures. For this reason we will here refer to some of the proposed designations and schematic figures of the respective phases.

One possible configuration is schematically depicted in Fig. 6.11, which we will here call TGBC₁* and which is referred to as TGB_C in the notation of Luk'yanchuk [22]. Like in the TGBA* phase the smectic layer normal is perpendicular to the macroscopic twist axis, but the local director \mathbf{n} is oriented under the molecular tilt angle θ with respect to the layer normal \mathbf{k} . The vector of the spontaneous polarization \mathbf{P}_S lies in the smectic layer plane and is perpendicular to the helix axis. Variation of the direction of the spontaneous polarization from slab to slab results in a macroscopic compensation of \mathbf{P}_S , and the phase would thus be helielectric, similar to SmC*.

A second possible structure is shown in Fig. 6.12 and is here referred to as TGBC₂*, corresponding to TGB_{Cp} in Ref. [22]. In this structure the director \mathbf{n} is oriented along the direction of the screw dislocations and perpendicular to the helix axis. This implies that the smectic layer planes are tilted with respect to

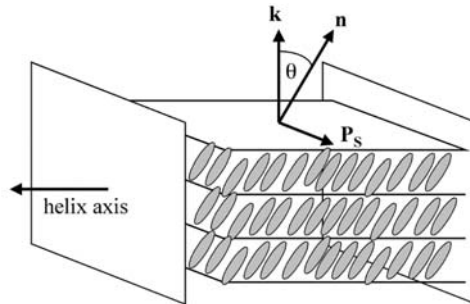


Fig. 6.11. Schematic model of the discussed TGBC₁* structure. The smectic layer normal \mathbf{k} is perpendicular to the twist axis and the director \mathbf{n} tilted with respect to the direction of screw dislocations. \mathbf{P}_S spirals around the twist axis and macroscopically vanishes. The structure is helielectric.

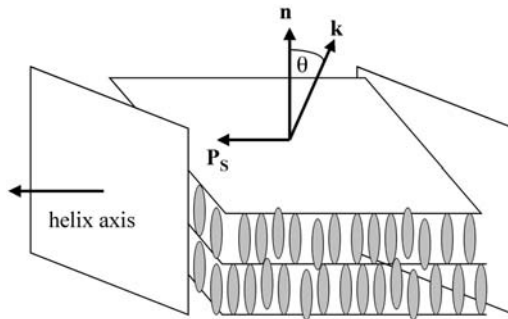


Fig. 6.12. Schematic model of the discussed TGBC₂* structure. The smectic layer normal \mathbf{k} is tilted with respect to the direction of screw dislocations, while the director is parallel to them. The spontaneous polarization in all smectic slabs points along the helix axis. The structure is ferroelectric.

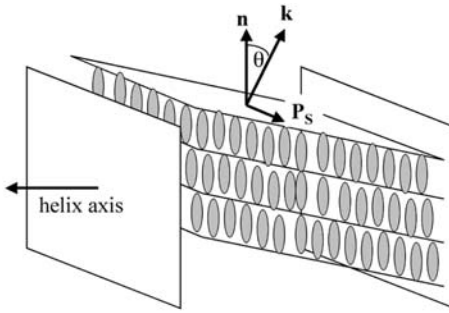


Fig. 6.13. Schematic model of the discussed TGBC₃* structure, which is in accordance with the x-ray investigations of Navailles et al. [11, 25]. The smectic layer planes are tilted with respect to the grain boundaries and the director \mathbf{n} is parallel to the direction of the screw dislocations. The polarization vector spirals around the twist direction and the structure is helielectric.

the local director and the layer normal \mathbf{k} makes an angle θ with the direction of the screw dislocations. The vectors of the spontaneous polarization of all smectic slabs point along the helix axis, and the phase would thus be truly ferroelectric.

Yet another possible TGBC* structure was proposed by Dozov et al. [23, 24] and is schematically depicted in Fig. 6.13. This will here be referred to as TGBC₃* and was named TGB_{Ct} in Ref. [22] and melted grain boundary (MGB) phase in Refs. [23, 24], indicating a vanishing smectic order parameter at the grain boundaries. The structure shows a director \mathbf{n} parallel to the screw dislocations and a layer normal \mathbf{k} that is inclined by the tilt angle θ with respect to the grain boundary plane. The vector of the spontaneous polarization is perpendicular to the helix axis and spirals around it as we proceed in direction of the twist axis, leading to a macroscopic compensation of \mathbf{P}_s and thus to a helielectric phase. The synchrotron x-ray investigations performed by Navailles et al. [11, 25] on oriented samples indicate that the TGBC₃* is in fact the one generally observed. In contrast to the TGBA* phase the TGBC₃* phase generally seems to exhibit a commensurate structure [11, 25].

The textures of the TGBC₃* phase are analogous to those observed for TGBA*: Grandjean textures for planar boundary conditions and fingerprint/filament textures for homeotropic anchoring. One way to distinguish between the two phases may be the application of an electric field along the twist axis, while slowly increasing its amplitude. In TGBA* an electroclinic-like response should be observed [26, 27] and result in an unwound SmA* state at large field amplitudes [28]. The coupling between \mathbf{E} and \mathbf{P}_s in TGBC₃* should on the other hand distort the helical superstructure until unwinding [29] and lead to the observation of a ferroelectric response [30].

There is however another variant of a TGBC* phase, which can easily be recognized and has become known as the *square grid* texture [31, 32], depicted in Plate 57 for planar anchoring conditions [33]. There seems to be good evidence that the square grid pattern is in fact due to a TGBC* structure predicted by Renn [20]. In this case not only the occurrence of a helical superstructure due to the TGB helix is observed, but also the SmC* slabs exhibit the director helix of the bulk SmC* phase, with the helix axis perpendicular to that of the TGB twist. Following the suggestion of Kuczynski and Stegemeyer [31, 32] we will refer to this phase as

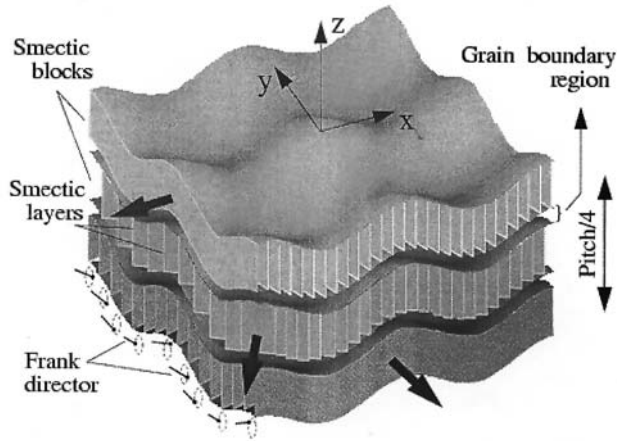


Fig. 6.14. Model structure of the UTGBC* phase to explain the square grid texture. (Reproduced by permission of Taylor & Francis, P.A. Pramod et al., *Liq. Cryst.*, **28**, (2001), 525 (<http://www.tandf.co.uk/journals>).)

TGBC_#^{*}, where “#” is used to indicate the square grid pattern. When cooling the square grid texture of Plate 57, the planar domain texture of the SmC* phase is observed to appear (Plate 58). In the texture of Plate 57 the TGB helix axis is oriented parallel to the direction of light propagation. This implies that the SmC* helix axis lies in the plane of the substrate. To obtain a square grid pattern due to the intrinsic SmC* twist, the helix axes of consecutive smectic grains also have to be perpendicular. Plate 59 [34] depicts the TGBC_#^{*} phase prepared in a wedge cell. Here one can clearly see the TGB helical superstructure (twist axis perpendicular to the substrate) by the appearance of Grandjean steps superimposed by a two dimensional director modulation (square grid) in the plane of the substrate, presumably due to the SmC* pitch. Pramod et al. [35] have proposed a two dimensionally undulated structure shown in Fig. 6.14 to explain the square grid texture and called this the undulated twist grain boundary C* (UTGBC*) phase. At this point it is not clear what the structural differences and similarities between TGBC_#^{*} and UTGBC* really are, and we cannot conclusively decide which model actually accounts for the occurrence of the square grid pattern. In any case, the TGBC* phase exhibiting the square grid texture must be a three dimensionally modulated phase.

6.3

The TGBC_A^{*} Phase

Very recently, the first experimental example of a presumably *antiferroelectric* twist grain boundary phase, named TGBC_A^{*}, was reported [36, 37]. The difference in smectic grain structure as compared to TGBC₃^{*} was illustrated by switching experiments and a structure with a locally anticlinic order was proposed,

as depicted in Fig. 6.15. A more detailed microscopic structural model of the director configuration in the vicinity of a grain boundary was discussed in Ref. [38], based on texture studies for applied electric fields (Fig. 6.16). To confirm this model, further experimental work will be needed in the future.

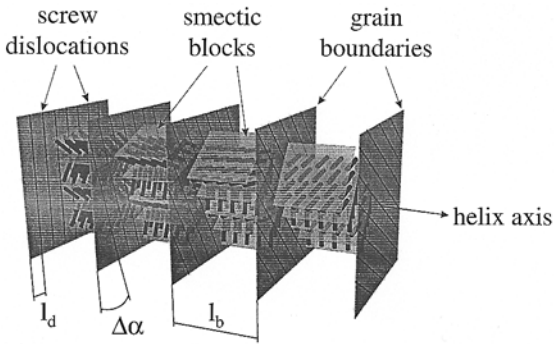


Fig. 6.15. Proposed model structure of the $TGBC_A^*$ phase. (Reproduced by permission of Taylor & Francis, J. G. Meier et al. *Liq. Cryst.* **29**, (2002), 179 (<http://www.tandf.co.uk/journals>).)

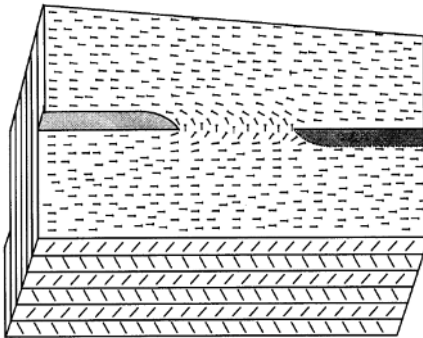


Fig. 6.16. Proposed director configuration around screw dislocations in the vicinity of a grain boundary of a $TGBC_A^*$ phase. (Reproduced by permission of Taylor & Francis, J. G. Meier et al. *Liq. Cryst.* **29**, (2002), 179 (<http://www.tandf.co.uk/journals>).)

References

- [1] S. R. Renn, T. C. Lubensky, *Phys. Rev. A*, **38**, (1988), 132.
- [2] P. G. de Gennes, *Solid State Commun.*, **10**, (1972), 753.
- [3] S. R. Renn, T. C. Lubensky, *Mol. Cryst. Liq. Cryst.*, **209**, (1991), 349.
- [4] W. Meissner, R. Ochsenfeld, *Naturwissenschaften*, **21**, (1933), 787.
- [5] A. A. Abrikosov, *Sov. Phys. JETP*, **5**, (1957), 1174.
- [6] F. London, H. London, *Proc. R. Soc. A*, **149**, (1935), 72.
- [7] T. C. Lubensky, *Physica A*, **220**, (1995), 99.
- [8] J. W. Goodby, M. A. Waugh, S. M. Stein, E. Chin, R. Pindak, J. S. Patel, *Nature*, **337**, (1989), 449.
- [9] J. W. Goodby, M. A. Waugh, S. M. Stein, E. Chin, R. Pindak, J. S. Patel, *J. Am. Chem. Soc.*, **111**, (1989), 8119.
- [10] K. Ihn, J. A. N. Zasadzinski, R. Pindak, A. J. Slaney, J. W. Goodby, *Science*, **258**, (1992), 275.
- [11] L. Navailles, P. Barois, H. T. Nguyen, *Phys. Rev. Lett.*, **71**, (1993), 545.
- [12] G. Srajer, R. Pindak, M. A. Waugh, J. W. Goodby, *Phys. Rev. Lett.*, **64**, (1990), 1545.
- [13] F. Hardouin, M. F. Achard, J.-I. Jin, J.-W. Shin, Y.-K. Yun, *J. Phys. II*, **4**, (1994), 627.
- [14] Y. Galerne, *J. Phys. II*, **4**, (1994), 1699.
- [15] L. Navailles, B. Pansu, L. Gorre-Talini, H. T. Nguyen, *Phys. Rev. Lett.*, **81**, (1998), 4168.
- [16] I. Dierking, S. T. Lagerwall, *Liq. Cryst.*, **26**, (1999), 83.
- [17] I. Dierking, F. Giesselmann, P. Zugenmaier, *Liq. Cryst.*, **17**, (1994), 17.
- [18] W. Kuczynski, H. Stegemeyer, *Ber. Bunsenges. Phys. Chem.*, **98**, (1994), 1322.
- [19] W. Kuczynski, H. Stegemeyer, *Mol. Cryst. Liq. Cryst.*, **260**, (1995), 377.
- [20] S. R. Renn, *Phys. Rev. A*, **45**, (1992), 953.
- [21] H. T. Nguyen, A. Bouchta, L. Navailles, P. Barois, N. Isaert, R. J. Twieg, A. Maaroufi, C. Destrade, *J. Phys. II*, **2**, (1992), 1889.
- [22] I. Luk'yanchuk, *Phys. Rev. E*, **57**, (1998), 574.
- [23] I. Dozov, G. Durand, *Europhys. Lett.*, **28**, (1994), 25.
- [24] I. Dozov, *Phys. Rev. Lett.*, **74**, (1995), 4245.
- [25] L. Navailles, R. Pindak, P. Barois, H. T. Nguyen, *Phys. Rev. Lett.*, **74**, (1995), 5224.
- [26] C. Destrade, S. Payan, P. Cluzeau, H. T. Nguyen, *Liq. Cryst.*, **17**, (1994), 291.
- [27] M. Petit, M. Nobili, P. Barois, *Eur. Phys. J. B*, **6**, (1998), 341.
- [28] R. Shao, J. Pang, N. A. Clark, J. A. Rego, D. M. Walba, *Ferroelectrics*, **147**, (1993), 255.
- [29] M. Petit, P. Barois, H. T. Nguyen, *Europhys. Lett.*, **36**, (1996), 185.
- [30] P. Barois, M. Nobili, M. Petit, *Mol. Cryst. Liq. Cryst.*, **302**, (1997), 215.
- [31] W. Kuczynski, H. Stegemeyer, *SPIE*, **3318**, (1997), 90.
- [32] W. Kuczynski, in *Selforganization in Chiral Liquid Crystals*, W. Kuczynski (ed.), Scientific Publishers OWN, Poznan, 1997.
- [33] I. Dierking, *Liq. Cryst.*, **28**, (2001), 165.

- [34] G. G. Nair, S. K. Prasad, D. S. Shankar Rao, C. V. Yelamaggad, *8th Int. Conf. on Ferroelectric Liquid Crystals*, Washington, DC, 2001, poster P1-43.
- [35] P. A. Pramod, R. Pratibha, N. V. Madhusudana, *Curr. Sci.*, **73**, (1997), 761.
- [36] J. W. Goodby, A. Petrenko, M. Hird, R. A. Lewis, J. Meier, J. C. Jones, *Chem. Commun.*, **13**, (2000), 1149.
- [37] A. S. Petrenko, M. Hird, R. A. Lewis, J. G. Meier, J. C. Jones, J. W. Goodby, *J. Phys.: Condens. Matter*, **12**, (2000), 8577.
- [38] J. G. Meier, P. Rudquist, A. S. Petrenko, J. W. Goodby, S. T. Lagerwall, *Liq. Cryst.*, **29** (2002), 179.

7

The Fluid Smectic Phases

The fluid smectic phases are characterized by a one dimensional positional order of the molecules' centers of mass in addition to the orientational order of the long molecular axis, and thus the formation of a more or less pronounced layer structure. Within a particular smectic layer the molecules' centers of mass are isotropically distributed, making the fluid smectic phase locally a two dimensional liquid. (This of course also holds for the somewhat unconventional TGB phases that have been introduced in detail in Chapter 6.)

7.1

The SmA/SmA* Phase

Let us briefly recall the basic structural features of the SmA phase, as depicted in Figs. 1.7 and 1.8. Instead of static, sharp smectic layers, the structure is quite often more realistically described by a sinusoidal density distribution. The director \mathbf{n} , which also represents the optic axis of this uniaxial phase, is oriented along the smectic layer normal \mathbf{k} and the scalar orientational order parameter is generally found to be in the range of $S_2 = 0.7-0.8$.

7.1.1

Natural Textures

The phase transition from the isotropic to the SmA/SmA* phase can easily be distinguished from that of Iso-N/N*. While for the latter basically spherical nuclei are observed to grow from the black background of the isotropic melt (see Plate 23), the direct transition to a fluid smectic phase is often accomplished by the growth of elongated germs, so-called smectic *bâtonnets* [1–3], as shown in Plate 60. Single *bâtonnets* show a pronounced anisotropy of their growth kinetics [4, 5], which is believed to be caused by the existence of screw dislocations [6].

The most commonly observed natural SmA appearance is that of the *fan-shaped* texture, which is shown in Plate 61. Its topology consists of focal domains [2, 3], which are schematically depicted in Fig. 7.1. The smectic layers are arranged in so-called Dupin cyclides [7, 8], which contain a pair of *focal conics*. These can be

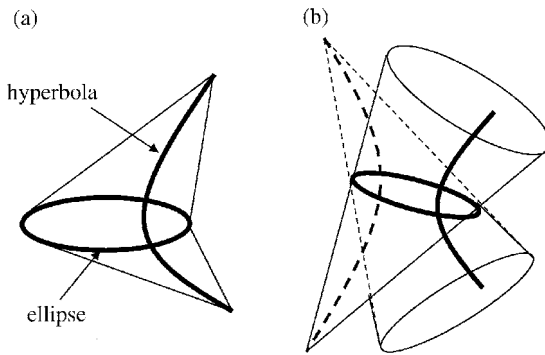


Fig. 7.1. Topology of the fan-shaped or focal conic texture, consisting of focal domains.

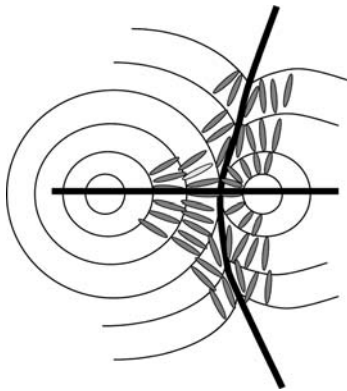


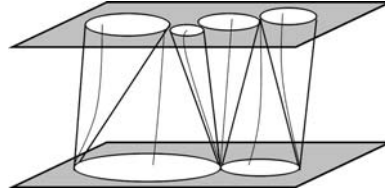
Fig. 7.2. Schematic illustration of the focal conic texture as a top view of the cell. The smectic layers are basically perpendicular to the substrate plane and arranged in Dupin cyclides, which contain a pair of focal conics.

seen in more detail in Plate 62, which is also called a focal conic texture. In this case the smectic layers are basically perpendicular to the substrate plane and so is the ellipse of Fig. 7.1. We thus observe the projection of the confocal curves into the plane of the hyperbola with the ellipse degenerating to a line. The corresponding smectic layer and director configuration is schematically shown in Fig. 7.2 as a view onto the substrate plane. The fan-shaped or focal conic textures are preferably observed in rather thin sample preparations. Note that the backs of the fans are not as smooth in appearance as those of the cholesteric fan-shaped texture (compare to Plate 20).

If on the other hand the focal ellipses lie in the plane of the substrates on both the top and the bottom glass plates, with the tip of the focal domains attached to the respectively opposite plate, we observe a microscopic appearance that is shown in Plate 63 and is called the *polygonal* texture [1–3, 7]. The schematic arrangement of the focal domains is shown in Fig. 7.3. Note that this topology is space filling and is preferably observed in thick sample preparations.

At this point it should also be made clear that from a texture point of view the achiral SmA and the chiral SmA* phases are equivalent in appearance.

Fig. 7.3. Schematic illustration of the arrangement of focal domains of the polygonal texture, with the focal ellipses lying in the plane of the substrate. The topology of the smectic domain arrangement is space filling.



7.1.2

Planar Anchoring Conditions and the Electroclinic Effect

Subjecting a SmA phase to planar boundary conditions results in a structure where the director \mathbf{n} and thus the optic axis lie in the plane of the substrate, along the direction of rubbing. The uniform planar SmA phase optically simply behaves like a uniaxial crystal plate (see Plate 64), just as was discussed in more detail above for the nematic phase. In fact, under planar anchoring, the textures of SmA and N phases are rather similar, except that for the smectic phase the typical nematic flickering cannot be observed. Also the optical behavior for rotation of a SmA sample between crossed polarizers is equivalent to that of the nematic phase (see Section 5.1.1.4). The same is true for the SmA* phase, as long as there are no electric fields applied and molecular optical activity is disregarded.

If a chiral SmA* is subjected to an electric field perpendicular to the director, we may observe what is called the *electroclinic effect*, originally introduced as the piezoelectric effect in liquid crystals by Garoff and Meyer [9]. It describes a field induced deviation of the optic axis in the plane of the substrate by an angle θ_{ind} from its zero field equilibrium position. The deviation of the optic axis is linear for moderate field amplitudes in the not too close vicinity of the SmA*–SmC* transition, as schematically depicted in Fig. 7.4. This leads to a shrinkage of the smectic layer thickness in an electrostrictive nature. The electroclinic effect is inherently con-

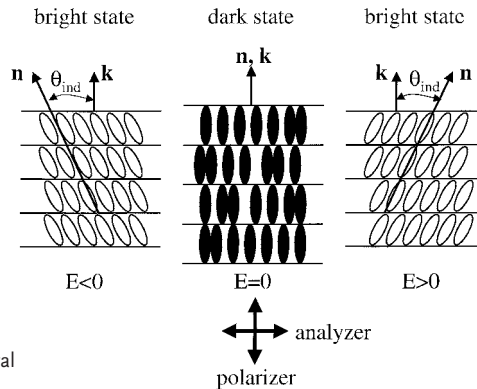


Fig. 7.4. Schematic illustration of the electroclinic effect in the orthogonal chiral SmA* phase.

nected to the chirality of the system, and is present not only in orthogonal smectic phases such as SmA^* [10], SmB^* or SmE^* [11], but also in tilted chiral smectic phases, although in the latter case it is often obscured by the ferroelectric properties. The effect cannot be observed in achiral phases, as has been demonstrated by investigations of the induced tilt angle as a function of enantiomeric excess [12, 13], θ_{ind} vanishing as the racemic mixture is approached. The linearity of the electroclinic effect, $\theta_{ind} \sim E$, is easily demonstrated by recording the light transmission of a planar oriented SmA^* sample between crossed polarizers under the application of an AC electric field with different waveforms. From Fig. 7.5 we readily see that the transmitted light intensity follows the waveform of the applied electric field, and the switching angle is thus directly proportional to the field amplitude. This can

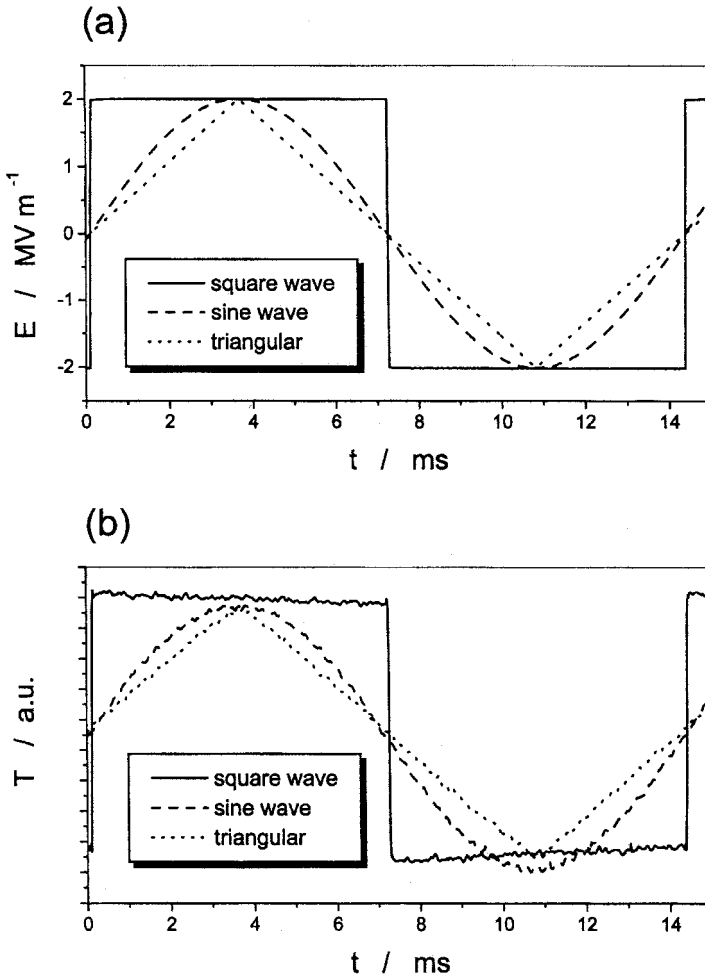


Fig. 7.5. Demonstration of the linearity of the electroclinic electrooptic response: (a) applied electric field waveforms and (b) corresponding transmission response.

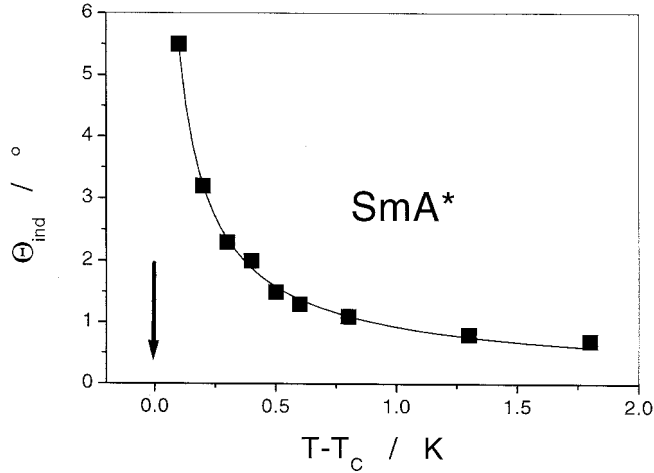


Fig. 7.6. Temperature dependence of the electroclinically induced tilt angle θ_{ind} in the SmA* phase in the vicinity of the SmA*–SmC* transition at T_C .

be used to differentiate between SmA* and SmC*, as the latter exhibits a strongly nonlinear electrooptic response (compare to Fig. 7.17) and may serve to detect the transition between both phases.

The electrooptic behavior of the electroclinic effect is obviously of potential importance for display applications, because it allows for a simple generation of gray-scales and excellent viewing angle characteristics. Unfortunately, often the values of the induced tilt angles are rather small ($\theta_{ind} < 10^\circ$), which strongly reduces the modulation depth. In the ideal case θ_{ind} should reach values close to 45° to either side of the polarizer direction (Fig. 7.4), in order to achieve maximum contrast, while at the same time allowing for DC balanced addressing. In another configuration (polarizer direction along one of the switched states), values of $\theta_{ind} = 22.5^\circ$ are sufficient to achieve maximum contrast. These have been obtained for some SmA* materials [14–17]. Another applicational drawback of the electroclinic effect is its strong dependence of the induced tilt angle on temperature (Fig. 7.6), which is described by

$$\theta_{ind} = \frac{eE}{\alpha(T - T_C)} \quad (7.1)$$

where e is the electroclinic coefficient, $\alpha(T - T_C) = a$ is the coefficient of the first term in the Landau expansion of the free energy density, and T_C is the SmA*–SmC* phase transition temperature. According to Eq. (7.1) the induced tilt angle strongly decreases on either side of the phase transition and diverges as T_C is approached. The response times of the electroclinic effect are intrinsically fast, in the low microsecond range or even below [18–20], and are generally more than an order of magnitude smaller than those of the ferroelectric response of the

low temperature SmC* phase. Also the switching time is strongly temperature dependent on approaching the SmA*–SmC* transition (critical slowing down):

$$\tau = \frac{\gamma_\theta}{\alpha(T - T_C)} \quad (7.2)$$

where γ_θ is the so-called electroclinic or soft-mode viscosity. Note that, in contrast to ferroelectric and dielectric director reorientations, the response time of the electroclinic effect is essentially independent of the amplitude of the applied electric field. The reason for this lies in the fact that an increase of the field amplitude by a certain factor results in an increase of the angular velocity of the director by that same factor, but in turn also in a respective increase of the induced switching angle. Only for large electric fields in the close vicinity of the SmA*–SmC* transition does the electroclinic effect become nonlinear, because here the electroclinic coefficient becomes field dependent. This leads to a saturation behavior of the induced tilt angle θ_{ind} . For a detailed account of theory and experimental work on the electroclinic effect one may refer to the review by Lagerwall et al. [21].

7.1.3

Homeotropic Anchoring Conditions

Subjecting a SmA or SmA* phase to homeotropic boundary conditions results in a structure with the smectic layers parallel to the substrate plane, and thus a director orientation perpendicular to the bounding glass plates. In this case the optic axis is parallel to the direction of light propagation and, as discussed for the case of the homeotropically aligned nematic, there is no birefringence for any in-plane rotational position of the sample between crossed polarizers. The texture thus simply appears black, also called *pseudo-isotropic*. As mentioned above, the pseudo-isotropic nematic texture shows a light flash under slight mechanical deformation by pressing on the sample, which is caused by a fast, *reversible* reorientation of the director (self-healing). In contrast, application of the same mechanical procedure to a pseudo-isotropic SmA texture, generally results in an *irreversible* change of the smectic layer and director configuration, often leading to a (local) fan-shaped texture.

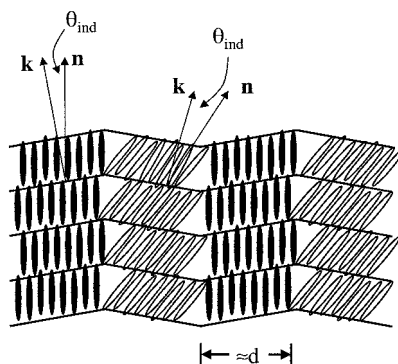
In some more rarely observed cases also a SmA oily streaks texture can be formed, as depicted in Plate 65. This is characterized by bands of bright lines embedded in the pseudo-isotropic background of the homeotropic SmA director configuration [1, 8, 22].

7.1.4

Electric Field Induced Striped Domain Textures

For SmA* materials with a rather large electroclinic coefficient (often those compounds that also show a large spontaneous polarization in the SmC* phase), one may observe the formation of a periodic stripe pattern by application of an

Fig. 7.7. Schematic illustration of the smectic layer and director configuration of a striped domain texture (cf. Plate 66).



AC electric field [23–26]. This occurs preferentially in thin cells and the pattern is maintained even after field removal. An example of such a *striped domain texture* is shown in Plate 66. The smectic layer structure is broken, with the layer normal being alternately inclined to either side of the rubbing direction, as schematically depicted in Fig. 7.7 and confirmed by x-ray studies [27, 28]. The angle of the layer inclination is often found to increase with increasing electric field amplitude, indicating that the electroclinic effect is the driving force for the stripe formation. The stripe width is generally equal to the cell gap, which may indicate that also electrohydrodynamic effects caused by ionic flow might play a significant role in the stripe formation process, similar to the formation of regular patterns known as Williams domains in nematics. Spatially resolved phase retardation measurements [29] and dynamic light scattering experiments [30] indicate a periodic fine structure within individual stripes of the texture.

7.2

The SmC/SmC* Phase

The basic structure of the SmC phase was already introduced in Fig. 1.10. The molecules form a lamellar structure, while in an individual smectic layer the centers of mass are isotropically distributed. The director \mathbf{n} makes an angle θ , the so-called *tilt angle*, with the smectic layer normal \mathbf{k} and is temperature dependent, vanishing at the transition to the high temperature phase. Without appropriate boundary conditions the orientation of the director on the tilt cone is arbitrary and not predetermined. Also here, the direction of the director \mathbf{n} represents the optic axis of the SmC phase in the uniaxial approximation, which is often used for reasons of simplicity, although the SmC phase is in fact biaxial, even though biaxiality is generally small. At this point it may be interesting to point out that the definition of the tilt angle is not as unambiguous in all cases as it might seem. It has been shown by optical as well as x-ray experiments [31] that different methods of tilt angle determination may lead to significantly

different results. An explanation of this behavior was proposed by Giesselmann and Zugenmaier [32], based on different tilt averages within the framework of a statistical molecular model of the SmC phase, similar to the Weiss model of the para- to ferromagnetic transition in solids [33] and Born's theory of the nematic state [34]. Furthermore, due to optic axis dispersion [35], the value of the (optical) tilt angle slightly depends on the wavelength of light used for the respective measurements [36]. But let us now proceed with the different texture appearances of the SmC and especially the chiral SmC* phase.

7.2.1

The Achiral SmC Phase

The tilted SmC phase is often preceded by the orthogonal SmA phase. This transition is most often (but not always) of second order, characterized by a *continuous* change of the appropriate order parameter, which is the tilt angle θ . This in turn sometimes makes it hard to detect the SmA–SmC transition by microscopy on planar samples, but also by other experimental methods, for example calorimetry, where only a small step in the heat capacity c_p is observed, in contrast to the easily detectable transition enthalpy ΔH of a first order transition. In fact we will see below that this transition is much easier to observe by microscopy and to characterize by electrooptic methods for chiral materials (SmA*–SmC*) than for achiral ones.

7.2.1.1 Natural Textures of SmC

The direct isotropic to SmC transition is very similar to that discussed above for SmA. Often SmC *bâtonnets* nucleate [37], which grow anisotropically until they merge, forming a texture similar to the fan-shaped appearance of SmA. If the SmC phase is formed directly from a nematic phase, an appearance that is called *striated texture* can often be observed directly below the N–SmC transition [38–40], as shown in Plate 67(a). This is also sometimes referred to as myelinic or chevron texture, with a line pattern of transition bars. It should not be confused with the textures of ferroelectric liquid crystals discussed below; Plate 67(a) shows a sample of an *achiral* compound and transition bars vanish on cooling further below the N–SmC transition. Also the transition from a nematic (right) to an SmC (left) Schlieren texture, as shown in Plate 67(b), can readily be observed (same sample area as Plate 8).

An often observed SmC appearance is that of the so-called *broken fan-shaped texture* [37]. It results from cooling the SmA fan-shaped texture across the transition into SmC. Both textures look rather similar, because the smectic layer configuration does not change during the transition. Only the director tilts with respect to the layer normal. As the tilt direction is not predetermined, small domains of different tilt direction are formed on the back of the fans, which gives rise to the broken fan-shaped appearance. An example of the fan-shaped SmA and broken fan-shaped SmC texture is given in Plates 68 and 69, respectively, depicting the

same sample area. But as in SmA, also focal conic textures can be obtained for SmC (Plate 70), when the smectic layer plane is more or less perpendicular to the substrate.

If on the other hand the smectic layer planes are parallel to the substrates, the molecules long molecular axes adopt an orientation that can be considered as tilted homeotropic. The director points along a direction that is tilted with respect to the normal of the substrate plane by a value close to that of the tilt angle θ . In contrast to the SmA phase, this smectic layer and director arrangement gives rise to the SmC *Schlieren texture* [41–45], as depicted in Plate 71. The smectic C Schlieren texture is very similar to that of the nematic phase, but with one distinct difference: in SmC Schlieren textures, only defects of strength $s = \pm 1$ are observed. This means that the SmC phase only exhibits fourfold brushes. The topology of the defects is essentially equivalent to the treatment for the nematic phase, as outlined in Section 5.1.1.1. A less pronounced difference of the SmC Schlieren texture as compared to that of the nematic phase is that the brushes appear smoother in the latter case and somewhat washed out for SmC.

7.2.1.2 SmC Under Planar Anchoring Conditions

Under planar boundary conditions the director \mathbf{n} is oriented in the plane of the substrate. We have seen above that in the SmA phase the director points along the smectic layer normal, which is parallel to the rubbing direction. On cooling across the SmA to SmC transition, the director can no longer take an arbitrary position on the tilt cone $\theta(T)$, but is now confined to the cut between the tilt cone and the substrate plane, as schematically depicted in Fig. 7.8. This leaves two positions, $+\theta$ and $-\theta$, corresponding to the domain texture of Plate 72. Rotation of the sample between crossed polarizers allows each domain type to be brought to extinction, the angular difference between those states corresponding to twice the tilt angle.

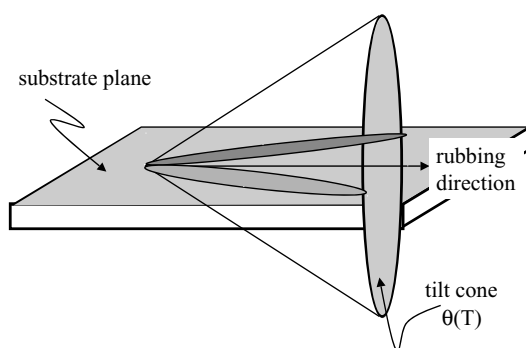


Fig. 7.8. The two possible director orientations in a SmC phase under planar anchoring conditions are determined by the cut of the tilt cone with the substrate plane. This results in the SmC domain texture, as illustrated in Plate 72.

7.2.1.3 SmC Under Homeotropic Anchoring Conditions

As outlined in Section 7.1.3, a SmA sample under homeotropic boundary conditions is in pseudo-isotropic orientation, i. e. the director points along the direction of light propagation and is therefore oriented perpendicular to the substrate plane. This configuration appears black, due to the lack of birefringence. This in turn means that the smectic layer plane is parallel to the substrate plane. On cooling across the transition into SmC, the smectic layer orientation is retrained, but the molecules have to tilt away from the substrate normal. In this case all tilt directions are allowed and the director is free to adopt any position on the tilt cone. In SmC the direction of light propagation is no longer parallel to the optic axis and we now observe a slight birefringence, which can be detected by a texture that looks grayish instead of black, as observed in the case of SmA. All tilt directions are optically equivalent, and, the larger the tilt angle becomes on lowering the temperature, the more pronounced this birefringence can be observed. In fact we often observe not only a uniform grayish texture, but also Schlieren textures as discussed above.

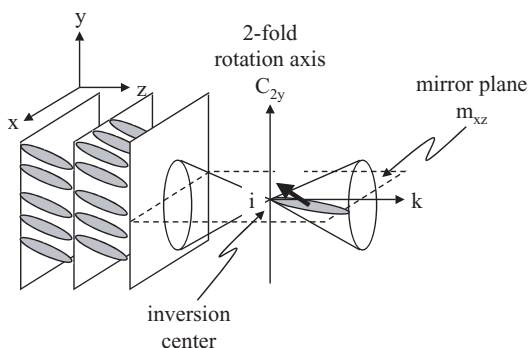
7.2.2

The Chiral SmC* Phase

The chiral SmC* phase has taken on a special role in liquid crystal research over the past two decades. This was induced by a ground-breaking publication from R. B. Meyer and coworkers [46] in 1975, where it was deduced from symmetry considerations that all chiral tilted smectic phases exhibit a (local) spontaneous polarization \mathbf{P}_s , and thus show *pyroelectricity*. In the case where this spontaneous polarization can be reoriented between two stable states by application of an electric field, we speak of *ferroelectricity*. In fact, the bulk SmC* phase does not show this behavior, because in the field-free state it exhibits a helical superstructure, such that the spontaneous polarization vanishes over the distance of the pitch. The SmC* phase is thus more correctly called *helielectric* [47]. Nevertheless, this phase has attracted researchers not only due to its interesting fundamental physics, but also due to its promising properties for applications in fast switching, high contrast, and large viewing angle displays, and other, non-display applications. This was triggered by a second ground-breaking paper in the field of ferroelectric liquid crystals, the discovery of the *surface stabilized ferroelectric liquid crystal* (SSFLC) state by Clark and Lagerwall [48]. This has led to extensive investigations of SmC* materials, which have been summarized in several monographs [49–51]. Ferroelectric properties have also been demonstrated for chiral tilted hexatic phases, namely SmI* and SmF* [52–57], although they have been investigated in much less detail.

Let us come back to the symmetry considerations of Meyer et al. [46]. Fig. 7.9 schematically shows the achiral SmC phase, whose local symmetry is described by point group C_{2h} . The structure contains the following symmetry elements: (i) a twofold rotation axis C_{2y} , due to head–tail symmetry, i. e. the equivalence of \mathbf{n} and $-\mathbf{n}$; (ii) a mirror plane m_{xz} , which is spun up by the layer normal \mathbf{z} and the

Fig. 7.9. Schematic illustration of the symmetry elements of the achiral SmC phase, whose local symmetry is described by point group C_{2h} , containing a twofold rotation axis C_{2y} , a mirror plane m_{xz} and an inversion center i .



director \mathbf{n} ; and therefore (iii) a resultant inversion center i . Application of inversion symmetry to an arbitrary, permanent molecular dipole moment $\mu = (\mu_x, \mu_y, \mu_z)$ yields $\mu_i = (-\mu_x, -\mu_y, -\mu_z)$, which results in a net dipole moment of the achiral SmC phase of $\mu_{\text{SmC}} = (0, 0, 0)$, and thus a vanishing spontaneous polarization. Making the respective molecules chiral, thus considering the SmC* phase, still preserves the twofold rotation axis along the y direction, but the mirror plane and therefore also the inversion center are lacking. Consider again an arbitrary, permanent molecular dipole moment $\mu = (\mu_x, \mu_y, \mu_z)$, which is now subjected to the only remaining symmetry element, the twofold rotation axis C_{2y} . This yields $\mu_{\text{rot}} = (-\mu_x, \mu_y, -\mu_z)$ and thus a resultant dipole moment $\mu_{\text{SmC}^*} = (0, \mu_y, 0)$. The lateral dipole moment components of the SmC* phase do not compensate and we are left with a spontaneous polarization \mathbf{P}_S along the polar C_{2y} axis, which is given by

$$\mathbf{P}_S = P_0(\mathbf{z} \times \mathbf{n}) \quad (7.3)$$

with P_0 the linear tilt–polarization coupling constant. The spontaneous polarization of the SmC* phase is thus always directed perpendicular to the smectic layer normal, as well as to the director.

7.2.2.1 Natural Textures

As mentioned above, the spontaneous polarization in bulk SmC* samples is diminished by the formation of a helical superstructure. On proceeding along the smectic layer normal, the \mathbf{P}_S vector spirals around this direction, as schematically illustrated in Fig. 7.10, and because the spontaneous polarization is always perpendicular to the director, the long molecular axes describe a helical superstructure with \mathbf{n} being confined to the tilt cone. If the pitch of the helix is in the order of several micrometers, this can be observed by polarizing microscopy as an equidistant line pattern superimposed on the SmC* fans, as shown in Plate 73. In fact the

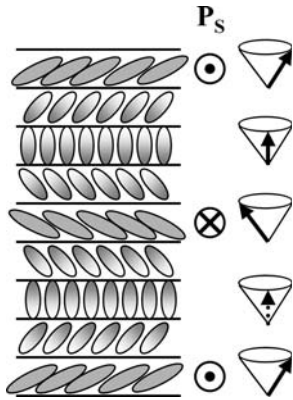


Fig. 7.10. Schematic illustration of the helical superstructure of the chiral bulk SmC^* phase and the corresponding direction of the vector of the spontaneous polarization P_s together with the respective direction of the director on the tilt cone.

helical superstructure of the chiral SmC^* phase was reported a few years before it was actually realized that the phase also exhibits ferroelectric properties [58–60]. From the distance between two dark lines the SmC^* pitch can be estimated [61]. Note that in contrast to the cholesteric phase, where homeotropic boundary conditions result in a helix axis in the plane of the substrate, the SmC^* helix lines are observed when the local director is basically oriented in the plane of the substrate. Unlike the N^* phase, where the identity period is $P/2$, the distance between two dark lines in SmC^* gives the full pitch P when the polarizer direction is along one of the in-plane director positions. Owing to the coupling of the spontaneous polarization and an external electric field, the helical superstructure can easily be unwound by application of a DC voltage perpendicular to the helix axis [62, 63].

The formation of the SmC^* phase from the cholesteric phase is often observed as nucleating SmC^* *bâtonnets* from the uniform N^* Grandjean texture. As the *bâtonnets* grow larger, they are superimposed by the equidistant line pattern due to the SmC^* helix. An example of such a texture at the N^* – SmC^* transition is shown in Plate 74. From the micrograph it becomes immediately clear that the helix axes of the cholesteric and the SmC^* phases are perpendicular to each other. That of the former is oriented perpendicular to the substrate plane while that of the latter lies in the plane of the substrate.

This formation of a helical superstructure in chiral bulk SmC^* samples also makes it easy to detect the SmA^* to SmC^* transition. While in SmA^* the backs of the fans of focal conic or fan-shaped textures appear smooth, the occurrence of an arced equidistant line pattern indicates the transition to SmC^* . Two typical textures illustrating this behavior are shown in Plates 75 and 76, exhibiting the same section of a sample. In Plate 75 we observe a typical fan-shaped SmA^* texture. By cooling across the transition, this is transformed into a broken fan-shaped texture with a partially developed SmC^* helix (Plate 76). Note that in SmC^* the helix line pattern follows the smectic layer planes, while the helix axis gives the local direction of the smectic layer normal.

7.2.2.2 SmC* Under Planar Anchoring Conditions

Short pitch SmC* and DHF effect Just like in the case of the short pitch cholesteric phase, with the helix axis unidirectionally oriented in the plane of the substrate, the short pitch SmC* phase also behaves optically to good approximation as a uniaxial crystal plate between crossed polarizers, as long as the pitch is clearly shorter than the resolution of the microscope. Application of an electric field perpendicular to the helix axis and below the threshold for unwinding results in a deformation of the helical superstructure, which appears as an effective linear deviation of the optic axis in the plane of the substrate, with its direction depending on the polarity of the field. The effect is monostable, proportional to the electric field amplitude, and has no memory. It has become known as the *deformed helix ferroelectric* (DHF) effect [64–67]. Its electrooptic behavior is quite similar to that of the flexoelectric effect in N* or the SmA* electroclinic effect, although being of a different nature. The principle of the DHF effect is schematically depicted in Fig. 7.11. The applicational advantages of this electrooptic effect include its linearity with the electric field (thus an easy generation of gray-scales), a rather small dependence on temperature, and fast switching in the lower microsecond range. But it can be quite difficult to obtain the necessary unidirectional alignment of the SmC* helix axis by use of conventional cells. Nevertheless, ferroelectric liquid crystal (FLC) materials and mixtures have been presented that show a linear electrooptic response with deflection angles of the optic axis in excess of 22.5° , response times of approximately $10\ \mu\text{s}$, and contrast ratios of $100 : 1$ over a wide temperature range [68–70].

Long pitch SmC* and pitch determination Subjecting a SmC* sample with a pitch $P > 2\ \mu\text{m}$ to planar boundary conditions often results in a uniformly oriented structure with helix axis in the plane of the substrate. This is observed in polarizing microscopy as a unidirectional line pattern, as demonstrated in Plate 77. The spatial periodicity observed in the texture allows an estimation of the SmC* pitch. At this point it should be stressed that the pitch of the helical superstructure deter-

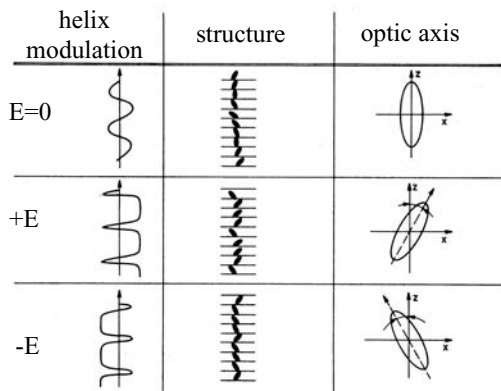


Fig. 7.11. Schematic illustration of the deformed helix ferroelectric (DHF) effect. The deformation of the helix of a short pitch SmC* phase with helix axis in the plane of the substrate by an applied electric field results in an effective linear deviation of the optic axis.

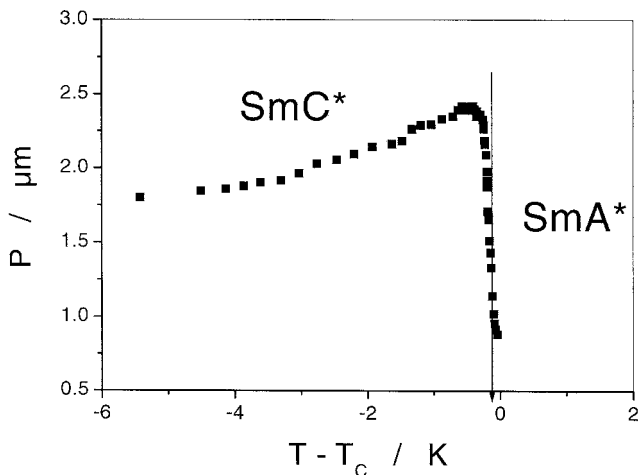


Fig. 7.12. Typical data for the reduced temperature dependence of the SmC^* helical pitch in the vicinity of the SmA^* transition. (Data after Ref. [69].)

mined in this way is indeed often only an estimate. Especially when the cell gap is rather narrow, deformations of the helix due to elastic interactions with the substrate can lead to pitch values that are larger than those of the undisturbed bulk material. Generally, P is only weakly dependent on temperature within the phase range of the SmC^* phase. Only in the vicinity of the transition to SmA^* is the pitch observed first to increase before it sharply decreases [71–73]. An illustration of the temperature dependence of the SmC^* pitch is depicted in Fig. 7.12, with data after Ref. [72].

7.2.2.3 SmC^* Under Homeotropic Anchoring Conditions

Short pitch SmC^* and selective reflection When a SmC^* sample is subjected to homeotropic boundary conditions, the smectic layer plane is often oriented parallel to the substrate planes. This implies that the helix axis is perpendicular to the substrate. In principle this situation is very similar to the cholesteric phase, only that for N^* the Grandjean orientation is obtained for planar boundary conditions. Also the optics of both phases with helix axis parallel to the direction of light propagation are essentially equivalent [74, 75]. Similar to the short pitch cholesteric phase, also the short pitch SmC^* phase exhibits the phenomenon of selective reflection, as discussed above in Section 5.2.2.1, and, as for N^* phases, this may be used for an estimation of the SmC^* pitch, provided that one has knowledge of the refractive indices and the tilt angle. A distinct difference in the reflection/transmission spectra between N^* and SmC^* can only be observed for distorted helical structures and especially for oblique incidence. In this case the N^* phase only exhibits the so-called “half pitch band” (with selective reflection wavelength proportional to the full pitch), while for the SmC^* phase the “full pitch band” (with selective reflection

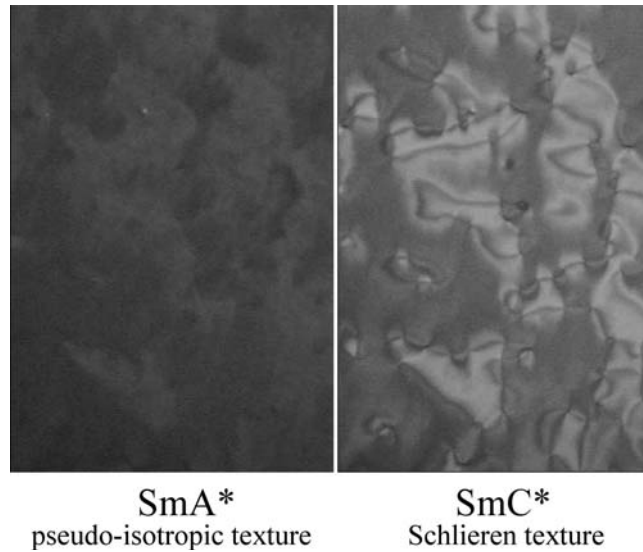


Fig. 7.13. The pseudo-isotropic texture of the high temperature SmA^* phase (left) changes to a grayish Schlieren texture of the SmC^* phase on cooling (right).

wavelength proportional to twice the pitch) can additionally be observed. This is due to the different periodicity of the spiraling dielectric ellipsoid experienced by the propagating light beam, which is $P/2$ for the cholesteric and P for the SmC^* phase. In an analogous way as discussed for the N^* phase, also the Cano or a wedge cell preparation can be used to determine the SmC^* pitch or even that of hexatic smectic phases [76], although the respective sample preparation is not trivial.

Long pitch SmC^* For long pitch SmC^* samples with the helix axis oriented along the direction of light propagation, selective reflection cannot be observed in polarizing microscopy. The observed textures are essentially the same as for non-chiral compounds. The birefringence is small, because light propagates through the material closely along the direction of the optic axis and only a more or less uniform grayish appearance of the sample is found, which changes to a SmC^* Schlieren texture for large tilt angles. Approaching the transition to SmA^* the transmission decreases and the pseudo-isotropic texture is formed at T_C . Fig. 7.13 demonstrates this behavior, with the left part of the figure showing the SmA^* phase at elevated temperatures and the right part depicting the homeotropically oriented SmC^* phase.

7.2.2.4 Surface Stabilized Ferroelectric Liquid Crystals

Bookshelf geometry and ferroelectric properties In 1980 Clark and Lagerwall [48] demonstrated that confinement of a SmC^* liquid crystal to cells with a gap

smaller than the pitch of the helical superstructure ($d < P$) leads to an unwinding of the helix and the formation of a bistable, ferroelectric device. The ideal case of this structure has the smectic layer planes oriented perpendicular to the substrate plane and is called *bookshelf geometry*. The director can adopt two stable positions in the plane of the substrate, one with the polarization pointing up, the other with P_S pointing down, as illustrated in Fig. 7.14. In the field-free case, this leads to the formation of two domain types shown in Plate 78, with the optic axis of one domain type oriented along one of the polarizer directions (black). Depending on the direction of the crossed polarizers with respect to the optic axes, either domain type can be brought into an extinction position. If the polarizers are oriented between the optic axes of the two domains, these appear optically equivalent (Fig. 7.15), while the domain boundaries are still visible.

Figure 7.16 illustrates the smectic layer and director configuration of a surface stabilized ferroelectric liquid crystal (SSFLC) sample between crossed polarizers. Application of an electric field above the threshold amplitude causes a reorientation of the spontaneous polarization between $+P_S$ and $-P_S$, depending on the polarity of the field. This is accompanied by a reorientation of the director on the tilt cone between the states $+\theta$ and $-\theta$, which in turn gives rise to an optical response. Note that removal of the field in any one of the stable ferroelectric states leaves the director in this position. This gives the bookshelf SSFLC structure its *bistable* nature, which is of applicational interest, because in contrast to traditional nematic devices, only pixels that have to be changed need to be addressed, which reduces the overall power consumption. The electrooptic response of an SSFLC cell is shown in Fig. 7.17 for different electric waveforms applied. In all cases the transmission changes in a strongly nonlinear fashion with the electric field and a square wave electrooptic response is obtained. The change in transmission characteristic between ferroelectric SmC^* (Fig. 7.17) and electroclinic SmA^* (Fig. 7.5) switching makes it easy to locate the respective phase transition for chiral materials.

In addition to the electrooptic response, the reversal of the direction of the spontaneous polarization also causes a characteristic current response, as shown in Fig. 7.18 for an applied triangular electric field, which can be used to determine the value of P_S [77]. The current through the cell consists of three contributions:

- The ohmic contribution $I_R = Ed/R$, with E the amplitude of the applied field, d the cell gap, and R the resistivity of the cell, which is largely due to ionic impurities within the liquid crystal – this response follows the field form of the applied voltage.
- A capacitive contribution $I_C = dC dE/dt$, with C the capacitance of the (filled) cell, which acts like a plate capacitor – this response is proportional to the time derivative of the applied field, i. e. has a square wave shape for applied triangular fields.
- The contribution from the reversal of the spontaneous polarization $I_p \sim dP_S/dt$, which can be observed as a peak.

Fig. 7.14. Schematic illustration of the SmC^* bookshelf structure. Reversal of the electric field polarity results in a reversal of the direction of the spontaneous polarization \mathbf{P}_s , which is accompanied by a reorientation of the director (optic axis) on the tilt cone between the two stable switching states. For appropriately arranged crossed polarizers this geometry switches between a dark and a bright state.

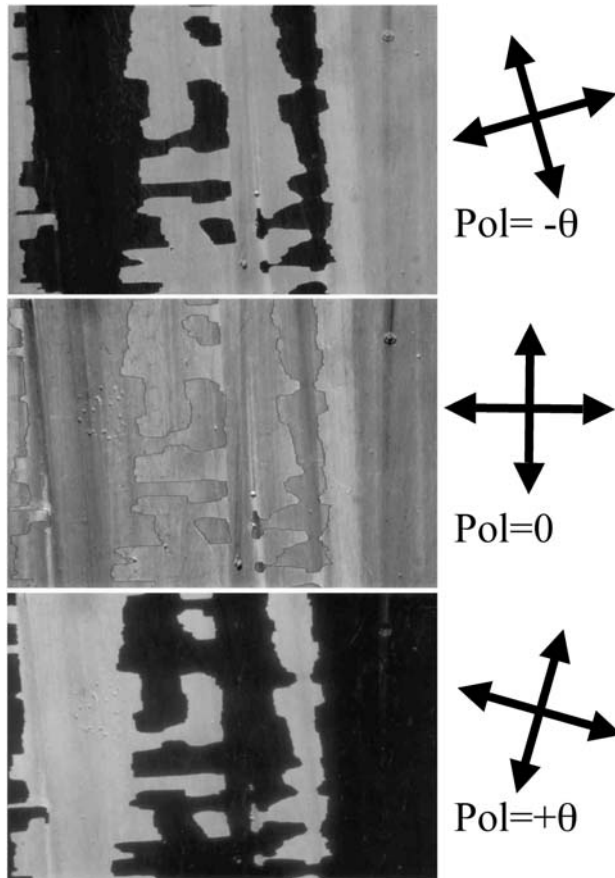
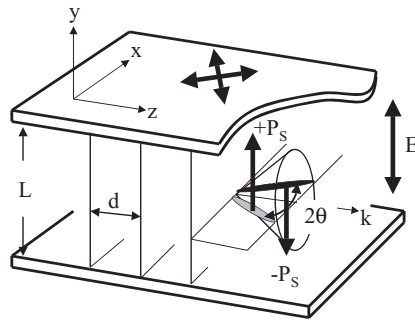


Fig. 7.15. Bookshelf sample between crossed polarizers, with the rubbing direction parallel to the short side of the image. With one polarizer directed along the $-\theta$ state, these domains appear dark, while the second domain type is bright (top); for one polarizer along the rubbing

direction, both domains appear optically equivalent (middle); while one polarizer directed along the $+\theta$ state causes extinction of the second domain type (bottom). The angular difference in polarizer direction between the top and the bottom images gives an estimate of 2θ .

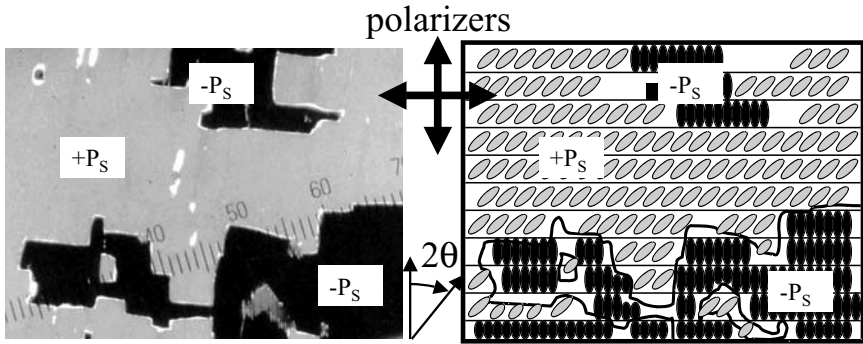


Fig. 7.16. Schematic illustration of the smectic layer and director arrangement of a bookshelf sample. The angular difference between the optic axes of the $-P_S$ and $+P_S$ domains is equal to twice the tilt angle.

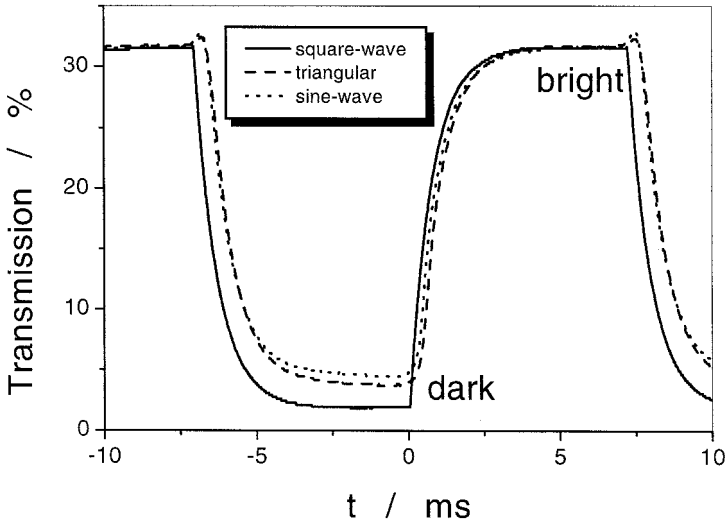


Fig. 7.17. Bistable optical response of the SmC* phase to an applied electric field off different waveform. The optical transmission is always a square wave electrooptic response, illustrating the bistability.

The first two contributions can easily be separated from the curve, and integration of the current reversal peak yields twice the value of P_S (because the reversal takes place from $+P_S$ to $-P_S$):

$$P_S = \frac{\int U dt}{2R_m A} \tag{7.4}$$

where U is the voltage across a measuring resistor R_m , detected with an oscilloscope, and A is the electrode area. The measuring resistor R_m should be chosen

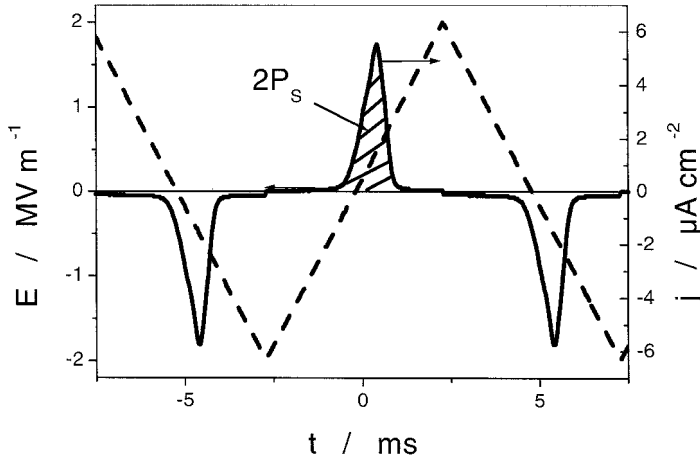


Fig. 7.18. Typical polarization reversal current response (solid line) to an applied electric triangular field (dashed line). Integration of the peak area allows a determination of the spontaneous polarization P_s .

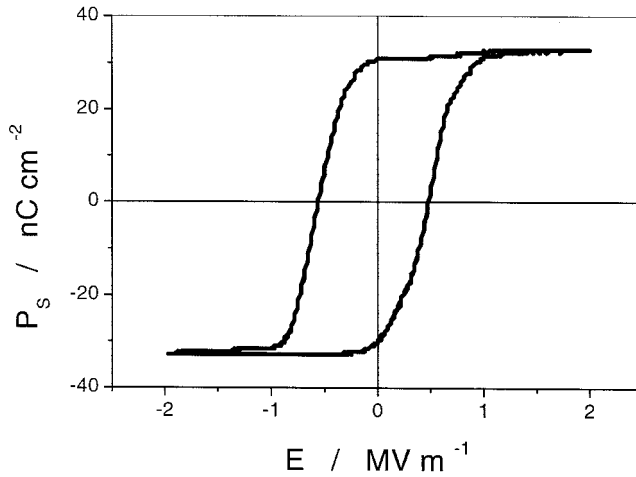


Fig. 7.19. Typical hysteresis loop of the spontaneous polarization for a ferroelectric liquid crystal.

such that the main voltage drop is across the cell, i.e. it should be much smaller than the resistance R of the cell, which is generally in the order of $R = 1\text{--}10\text{ M}\Omega$. Plotting the spontaneous polarization as a function of the applied electric field yields a typical ferroelectric hysteresis loop, shown in Fig. 7.19. The spontaneous polarization is a secondary order parameter of the SmC^* phase and depends on temperature. It can exhibit the characteristics of a first order phase transition, as depicted by the open symbols for the $\text{SmC}^*\text{--N}^*$ transition of Fig. 7.20, where P_s changes discontinuously at T_C . It can also exhibit the characteristics of a typical second order transition $\text{SmC}^*\text{--SmA}^*$, with a continuous change of P_s at the tran-

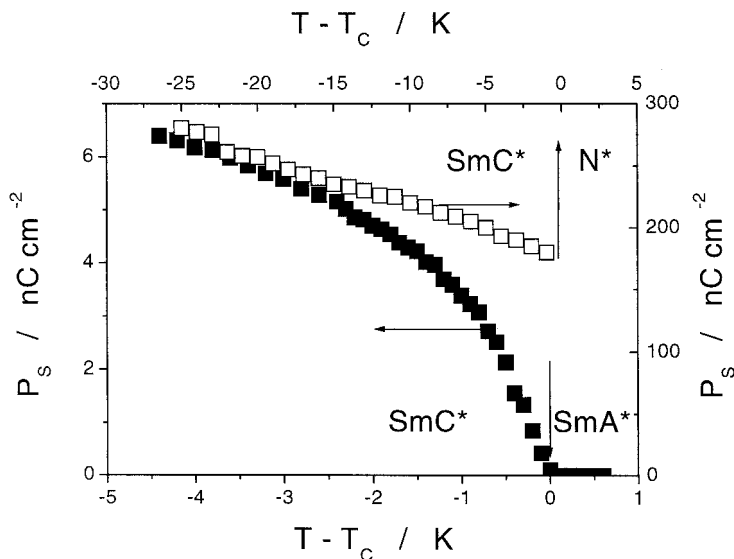


Fig. 7.20. Typical data for the reduced temperature dependence of the spontaneous polarization for an FLC material with a first order SmC*–N* transition (open symbols) and a compound with a second order SmC*–SmA* transition (closed symbols).

sition to the high temperature paraelectric phase (closed symbols in Fig. 7.20), which resembles a typical Curie–Weiss behavior.

Vertical chevrons and zigzag defects For many real cells, the above discussion of the bookshelf ferroelectric liquid crystal geometry is too idealized, as it implies that at the SmA* to SmC* transition the layers remain perpendicular throughout the cell and that the director uniformly tilts away from the rubbing direction. In reality, often tilted layer structures are observed [78, 79], which are due to the anchoring of the molecules at the substrates. In the SmA* phase the anchoring length is equal to the smectic layer thickness. Cooling across the transition to SmC*, the smectic layer thickness decreases, due to the occurrence of the tilt angle θ . Maintaining a bookshelf geometry of the layers would involve a change of the anchoring length as well as the director orientation. This case is generally not observed, but instead the anchoring length is maintained, while the smectic layers tilt with respect to the substrate normal. For antiparallel rubbed substrates, the so-called *layer tilted geometry* is formed [80], where the smectic layers are uniformly tilted by an angle δ throughout the cell. For parallel rubbed substrates, the resultant layer structure is called (*vertical*) *chevron geometry*, which is schematically depicted in Fig. 7.21 and has been confirmed by the x-ray experiments of Rieker et al. [78, 79, 81] and Ouchi et al. [82]. The layer tilt angle δ is generally found to be in the order of the molecular tilt angle θ , $\delta \approx \theta$. At the chevron interface the layer tilt angle abruptly changes its sign, which makes the area where the layer tilt direction changes a planar defect, which locally acts like a mirror plane [79].

Fig. 7.21. Schematic illustration of the (vertical) chevron structure observed for parallel rubbed substrates. The smectic layers are inclined to the substrate normal by an angle δ , which is generally close to the director tilt angle θ .

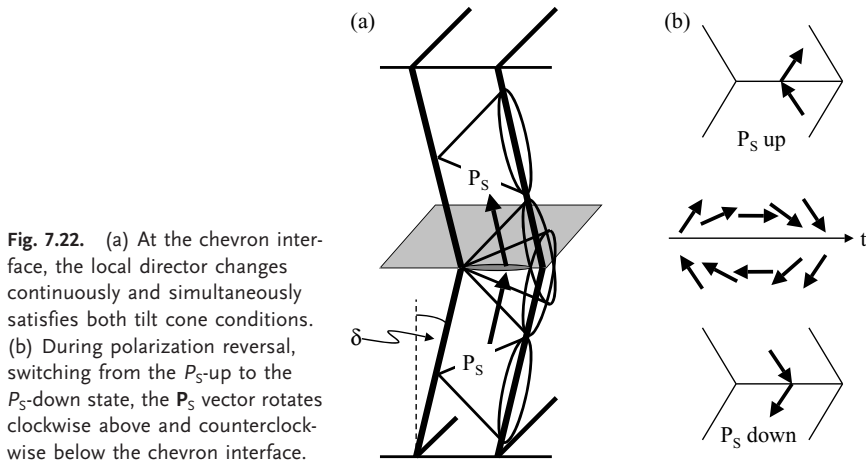
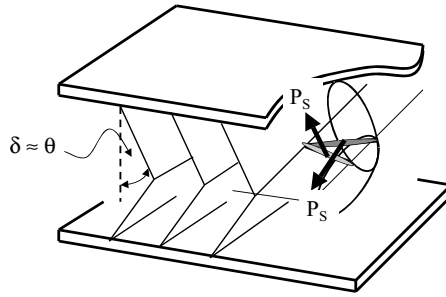


Fig. 7.22. (a) At the chevron interface, the local director changes continuously and simultaneously satisfies both tilt cone conditions. (b) During polarization reversal, switching from the P_S -up to the P_S -down state, the P_S vector rotates clockwise above and counterclockwise below the chevron interface.

Note that the chevron interface does not necessarily need to be located in the middle of the cell, although it often is. The local director at the chevron interface is continuous, i.e. the director field $\mathbf{n}(\mathbf{r})$ at the interface satisfies the two tilt cone conditions above and below the chevron plane simultaneously (Fig. 7.22(a)). The local polarization on the other hand is discontinuous at the chevron interface, abruptly changing its direction. Switching from the P_S -up to the P_S -down state, the P_S vector rotates clockwise above the chevron interface and counterclockwise below it (Fig. 7.22(b)). In any case, the effective director switching angle is reduced as compared to the bookshelf geometry and is always smaller than 2θ , which results in a reduction of the achievable contrast ratio. For this reason, the chevron structure is not the ideal configuration for applicational devices.

The formation of chevron layer structures leads to defects, wherever regions of opposite chevron direction meet. This is schematically illustrated in Fig. 7.23, where defect regions of the $\langle\langle\langle\rangle\rangle\rangle$ type are called thin walls, while those of the $\rangle\rangle\rangle\langle\langle\langle$ type are called thick walls. The defects characteristically appear as long, so-called *zigzag streets* or *lightning* [82, 83], shown in Plate 79, but may also form closed loops, as schematically depicted in Fig. 7.24. In the latter case, the region

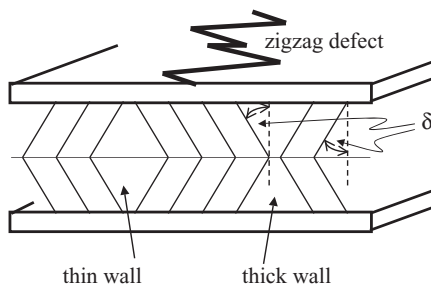


Fig. 7.23. Schematic illustration of zigzag defects in regions where chevrons of opposite inclination meet. Individual zigzag lines run nearly parallel to the smectic layer normal, while the whole zigzag street runs parallel to the smectic layer plane.

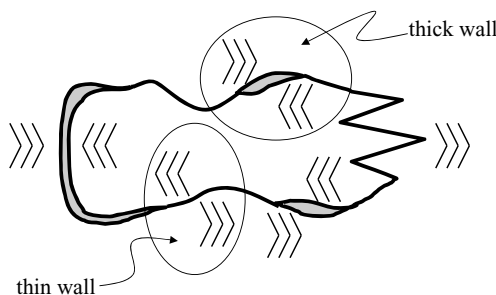


Fig. 7.24. Schematic illustration of zigzag lines forming a closed loop, separating regions of opposite chevron inclination inside and outside the loop.

within the closed loop has a uniform chevron direction, while outside the loop the chevron inclination is in the opposite direction. Note that the individual defect lines are nearly parallel to the smectic layer normal, while the zigzag streets are basically running along the smectic layer plane.

It was long believed that once formed, a smectic layer structure is in principle static and cannot easily be changed. But, as the vector of the spontaneous polarization always lies in the plane of the smectic layer, we note for the chevron geometry that \mathbf{P}_S is *not* collinear to the vector of an applied electric field \mathbf{E} , which is perpendicular to the substrate planes. This gives rise to a torque on the smectic layer, which may cause a *reversible* layer straightening. X-ray investigations [84–87] as well as electrooptical studies [88] have unambiguously demonstrated this smectic layer straightening. But application of an electric field with sufficiently large amplitude can also lead to an *irreversible* reorientation of the smectic layer structure, which will be discussed in greater detail in the following subsection.

Horizontal chevrons and rotational smectic layer instabilities The direction of chevron folding obviously does not change abruptly, but is mediated by a defect, which is essentially of the bookshelf type (Fig. 7.25). This can easily be demonstrated by building a cardboard model with chevron tilt in different directions, as shown in Fig. 7.26. At the same time the vector of the spontaneous polarization is not parallel to an applied electric field, and thus a torque acts upon the smectic layers. This can lead to a field induced smectic layer structure, which is quite often observed, but not that often talked about, due to its negative effect on the electro-

Fig. 7.25. Defects mediating regions of opposite (vertical) chevron inclination are essentially of the bookshelf type.

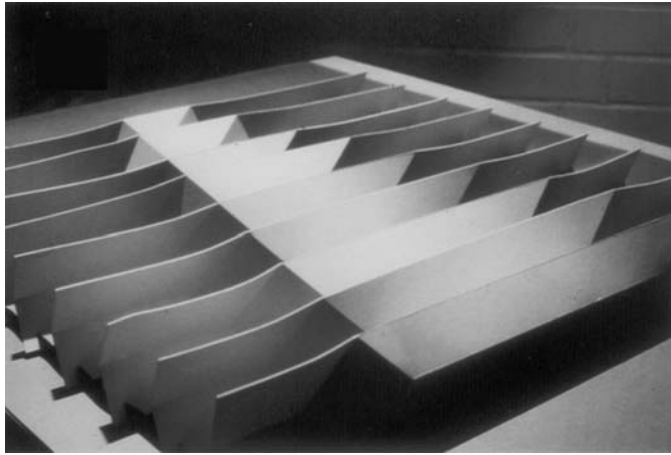
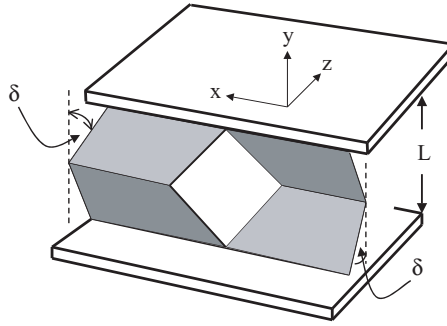


Fig. 7.26. Model of a pair of zigzag lines mediating two regions of opposite uniform (vertical) chevron inclination. Building a cardboard model of the respective structure gives an intuitive idea of why the mediating regions are oriented in bookshelf geometry, with the

normal to the layer plane being tilted with respect to the rubbing direction. (Reproduced by permission of Taylor & Francis, I. Dierking et al., *Liq. Cryst.*, **19**, (1995), 179 (<http://www.tandf.co.uk/journals>).)

optic performance of cells. Application of a sufficiently large *symmetric* electric field in the SmC^* phase (close to the transition to SmA^* or N^*) causes the smectic layer normal \mathbf{k} to tilt in the substrate plane by the amount of the molecular tilt angle θ with respect to the rubbing direction \mathbf{z} , preserving the director along \mathbf{z} and maintaining the anchoring length. Such a structure was first reported by Patel and Goodby [89] for a material with SmC^*-N^* phase sequence and is schematically depicted in Fig. 7.27 as a top view of the cell. It somewhat resembles a conventional (vertical) chevron turned by 90° and is therefore called a *horizontal chevron* structure [90]. Since the SmC^* helix line pattern indicates the direction of smectic layer planes, the in-plane tilted domain structure proposed in Fig. 7.27 can be evidenced directly from texture observations, as shown in Plate 80 and in Fig. 7.28. Boundaries between domains of different in-plane layer tilt direction can be thin

walls for continuous layers and thick walls with layer discontinuities. The general structure of horizontal chevrons is in principle similar to the striped bookshelf texture, which in addition to SmA^* materials (Plate 66) may also be observed for SmC^* [91]. Nevertheless, there are some fundamental differences: the stripe width of the striped texture is observed to be essentially equal to the cell gap [24, 90, 92], while horizontal chevron domains are one to two orders of magnitude larger and not necessarily uniformly elongated along the rubbing direction. Also,

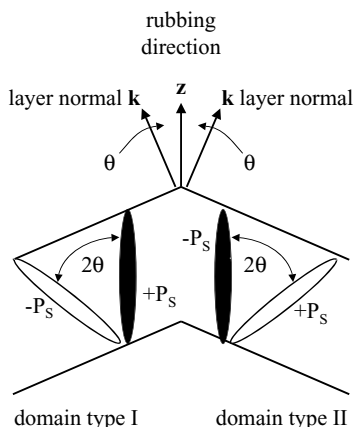


Fig. 7.27. Schematic illustration of a *horizontal* chevron structure as a top view of the cell. The smectic layer normal is inclined to either side of the rubbing direction by the amount of the director tilt angle, which results in the formation of two domain types (see also Plate 80).

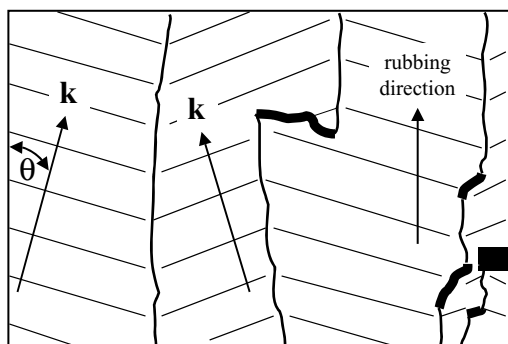
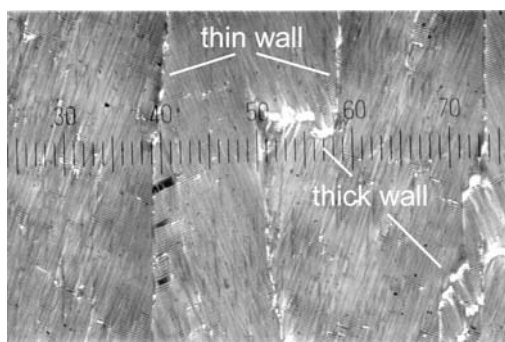


Fig. 7.28. Micrograph and respective schematic structural model of a horizontal chevron domain texture. The helix lines of the photograph directly indicate the direction of the smectic layer planes. Thin walls are formed for continuous layers, while thick walls indicate smectic layer discontinuities.

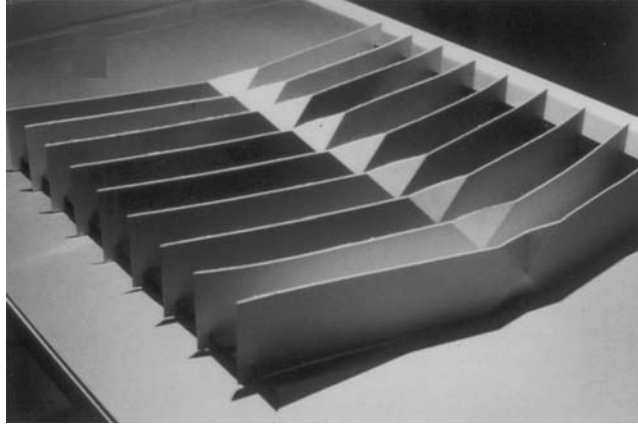


Fig. 7.29. Model of a horizontal chevron structure. Building a cardboard model of the respective structure directly shows why the defect mediating two bookshelf regions of opposite layer inclination has to be of the vertical chevron type. (Reproduced by permission of Taylor & Francis, I. Dierking et al., *Liq. Cryst.*, **19**, (1995), 179 (<http://www.tandf.co.uk/journals>).)

for the striped texture the layer inclination angle is generally smaller than the molecular tilt angle [93].

From texture studies and electrooptic investigations a qualitative model for the formation of horizontal chevrons can be derived [94]. Starting from a vertical chevron structure with bookshelf defects mediating regions of opposite chevron tilt direction, a symmetric electric field is applied. This enforces a smectic layer straightening via the growth of the bookshelf regions at the expense of the vertical chevron structure. Eventually these bookshelf regions eliminate the chevron structure and we are left with bookshelf layers being inclined to the rubbing direction; the horizontal chevron structure is formed. Regions where bookshelf layers with different inclination meet consist of a defect of the vertical chevron type. Also this structure can easily be made plausible by use of a cardboard model, as shown in Fig. 7.29. For application of *symmetric* electric fields during the horizontal chevron formation, domains of opposite layer normal tilt are equally distributed [95].

Let us now discuss the director configuration of a horizontal chevron SSFLC structure [94]. After symmetric field application and formation of the horizontal chevron structure, the texture observed between crossed polarizers with one of the polarizer directions along the rubbing direction is essentially dark with only domain walls appearing bright (Fig. 7.30(a)). This means that in both domain types the director \mathbf{n} is parallel to the rubbing direction \mathbf{z} , but domains of opposite layer tilt $\pm\mathbf{k}$ have a different sign of the spontaneous polarization $\pm\mathbf{P}_S$, as shown in the respective schematic diagram. Application of a positive electric bias field causes a reorientation of the director by 2θ in one domain type, which now appears bright, as shown in Fig. 7.30(b). In both domain types \mathbf{P}_S is now pointing along the direction of light propagation and the width of the domain walls is reduced. Reversal of the bias field direction causes both domain types to switch by 2θ , the formally dark domains are

now bright and vice versa (Fig. 7.30(c)). In both domain types P_S is now pointing opposite to the direction of light propagation. This also illustrates the devastating effect of horizontal chevrons on device performance: with an equal distribution of both domain types, the overall transmission change on field reversal diminishes and the overall contrast vanishes. An interesting feature of these horizontal chevron

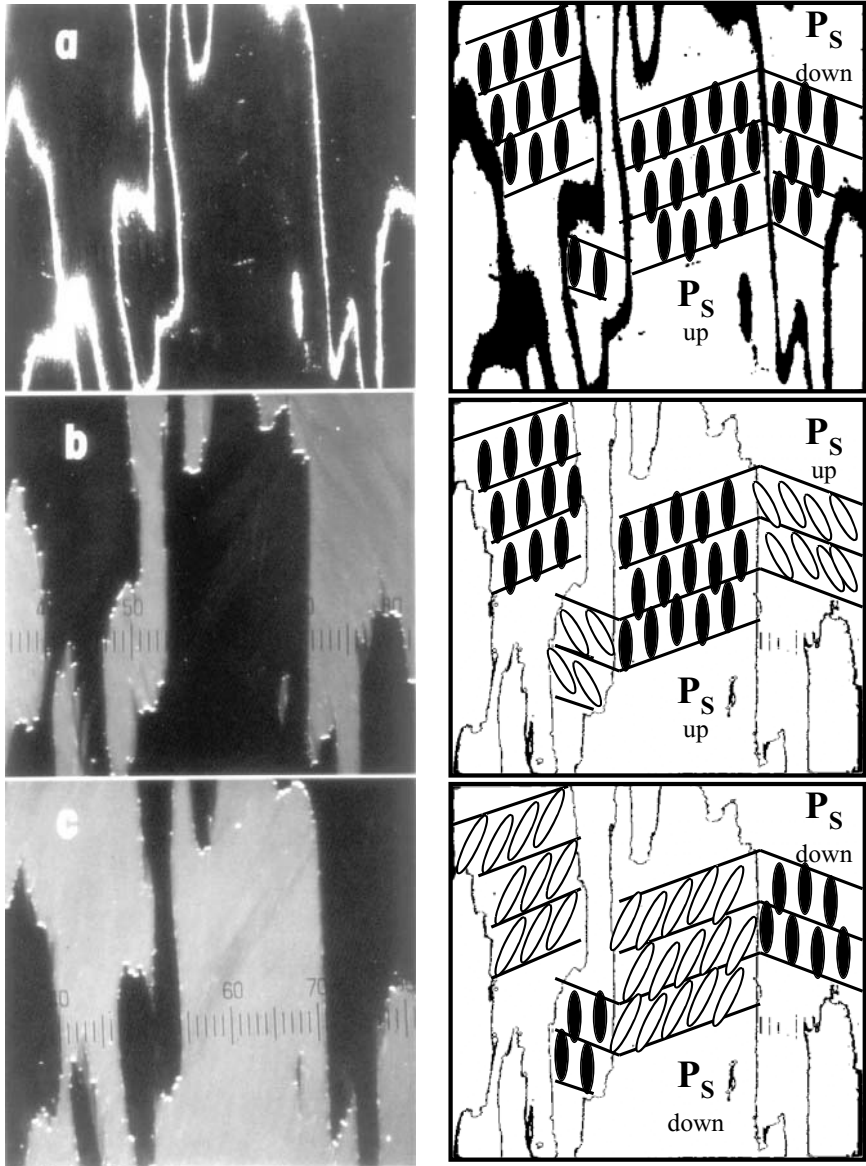


Fig. 7.30. Texture example and respective structural model of an SSFLC horizontal chevron structure (a) in the field-free case, and with the electric field vector pointing (b) out of the plane and (c) into the plane.

structures is their electric response (current reversal curves under applied triangular voltages), which resembles that of an antiferroelectric liquid crystal [96].

Another interesting phenomenon can be observed when a horizontal chevron texture is subjected to an *asymmetric* electric field: the smectic layers begin to rotate in the plane of the substrate, and a reorientation of the layer structure from one inclination direction (with respect to the rubbing direction) to the other is observed, depending on the asymmetry of the field. This effect was first reported by Andersson et al. [97–99] for the SmA* phase subjected to a sawtooth field, but never published. They reported a continuous rotation of smectic layers for cells with degenerate planar boundary conditions, which exhibited a threshold behavior and changed the rotation direction as the asymmetry was reversed. Nakayama et al. [100] confirmed the observations for SmA*, and the same group also reported a continuous rotation of smectic layers above a threshold for an antiferroelectric liquid crystal [101, 102], as well as a thresholdless layer rotation for a SmC* material [103]. It has since been shown [104] that the reorientation of smectic layers can either be continuous in the case of degenerate planar boundary conditions, or limited to values twice the tilt angle for monostable anchoring (unidirectional rubbing). For SmC* materials, the reorientation of smectic layers can be induced by all kinds of asymmetric waveforms, including amplitude asymmetry (bias), time asymmetry (square wave fields with different times of pulse duration), shape asymmetry (sawtooth), and combinations thereof [105].

Figure 7.31 demonstrates the discussed behavior for the tilt angle limited layer reorientation. First a horizontal chevron texture with two domain types inclined to either side of the rubbing direction is induced by application of a symmetric electric field (Fig. 7.31(a)). Helix lines directly indicate the direction of smectic layer planes. Changing the field to an asymmetric waveform results in the growth of the energetically favored domain type, until the whole electrode area exhibits a uniform layer tilt direction (Fig. 7.31(b)). Reversal of the field asymmetry causes nucleation and growth of the domain type with opposite layer inclination, until the whole sample again exhibits a uniform layer tilted configuration (Fig. 7.31(c)). The discussed smectic layer rotational instabilities have unambiguously been demonstrated not only by texture investigations, but also by time resolved synchrotron x-ray experiments [106]. Note that for SSFLC cells, this non-mechanical procedure can be used to obtain bookshelf samples with high quality alignment [107]. The dynamics of the domain growth process depends not only on a variety of applied parameters [107–109], such as field asymmetry ratio, amplitude, frequency, temperature, and cell gap, but also on material parameters and processing conditions, such as smectic polymorphism [110], enantiomeric excess [111], ionic contamination [112, 113], and substrate treatment [114, 115]. From the view of applications it might be noteworthy that the layer reorientation under asymmetric fields (like they are also used in addressing schemes for ferroelectric liquid crystal displays) can be avoided by a small amount of a dispersed polymer network, without significant alteration of the FLC electrooptic performance [116].

For weak, degenerate planar anchoring the smectic layers may actually rotate thousands of degrees, sometimes leading to spiral rotational smectic layer instabil-

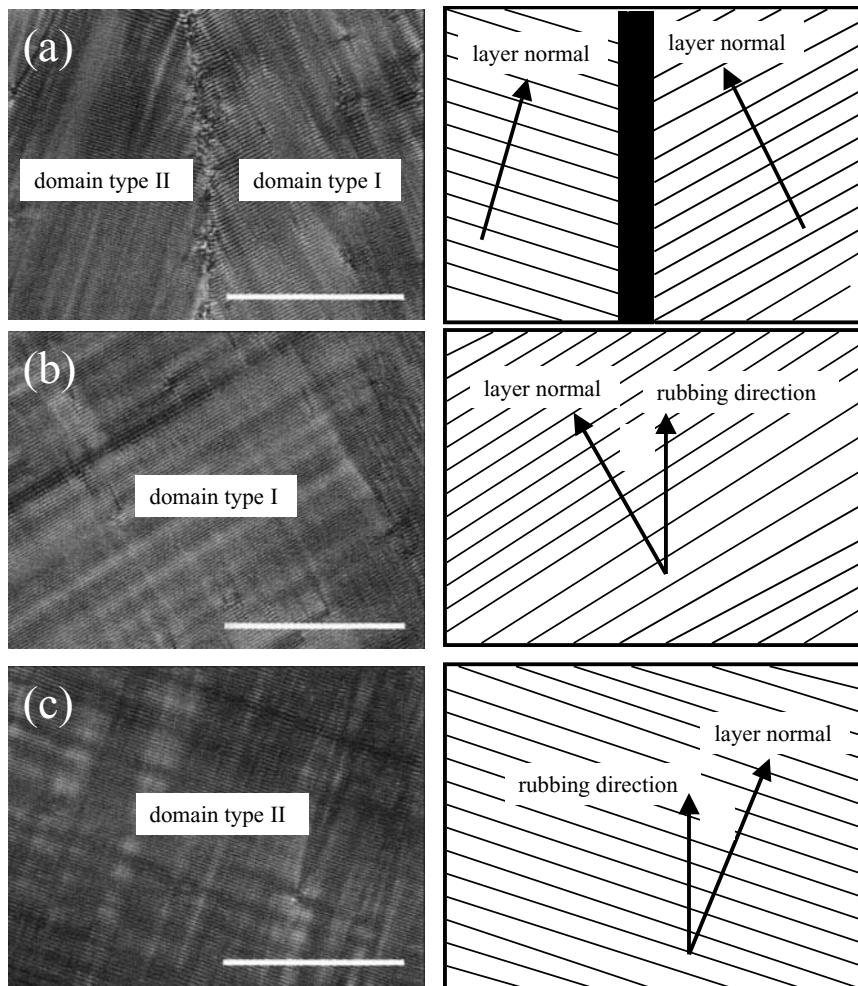


Fig. 7.31. Texture example and respective structural model of (a) a horizontal chevron structure induced by a symmetric electric field, (b) uniformly inclined smectic layers after “layer rotation” by an asymmetric field, and (c) after

layer rotation into the opposite inclination direction by reversal of the field asymmetry. The SmC^* helix lines directly indicate the direction of the smectic layer planes.

ities, a texture example of which is shown in Plate 81. A first theoretical explanation of the observed phenomenon was recently proposed by Carlsson and Osipov [117] for the SmA^* phase, the model being based on the dynamics of the electroclinic effect. This general model can obviously only point out the underlying physics of the smectic layer rotation, but can account for neither the effects of material properties, nor the smectic layer breaking and permeation flow associated with the layer reorientation [118].

References

- [1] G. Friedel, *Ann. Phys. (Fr.)*, **18**, (1922), 273.
- [2] G. Friedel, F. Grandjean, *Bull. Soc. Fr. Miner.*, **33**, (1910), 192.
- [3] G. Friedel, F. Grandjean, *Bull. Soc. Fr. Miner.*, **33**, (1910), 409.
- [4] I. G. Chistyakov, *Kristallografiya*, **8**, (1963), 123 (in Russian).
- [5] I. Dierking, C. Russell, *Physica B*, **325**, (2003) 281.
- [6] K. Morawietz, D. Demus, *Cryst. Res. Technol.*, **22**, (1987), 1391.
- [7] M. Kléman, *Points, Lines and Walls*, John Wiley & Sons, Chichester, 1983.
- [8] Y. Bouligand, *J. Phys. (Fr.)*, **33**, (1972), 525.
- [9] S. Garoff, R. B. Meyer, *Phys. Rev. Lett.*, **38**, (1977), 848.
- [10] S. Garoff, R. B. Meyer, *Phys. Rev. A*, **19**, (1979), 338.
- [11] Ch. Bahr, G. Heppke, *Phys. Rev. A*, **37**, (1988), 3179.
- [12] Ch. Bahr, G. Heppke, B. Sabaschus, *Ferroelectrics*, **84**, (1988), 103.
- [13] M. Glogarová, Ch. Destrade, J. P. Marcerou, J. J. Bonvent, H. T. Nguyen, *Ferroelectrics*, **121**, (1991), 285.
- [14] G. Andersson, I. Dahl, L. Komitov, M. Matuszczyk, S. T. Lagerwall, K. Skarp, B. Stebler, D. Coates, M. Chambers, D. M. Walba, *Ferroelectrics*, **114**, (1991), 137.
- [15] P. A. Williams, N. A. Clark, M. B. Ros, D. M. Walba, M. D. Wand, *Ferroelectrics*, **121**, (1991), 143.
- [16] B. R. Ratna, G. P. Crawford, S. K. Prasad, J. Naciri, P. Keller, R. Shashidhar, *Ferroelectrics*, **148**, (1993), 425.
- [17] J. Naciri, J. Ruth, G. P. Crawford, R. Shashidhar, B. R. Ratna, *Chem. Mater.*, **7**, (1995), 1397.
- [18] Ch. Bahr, G. Heppke, *Liq. Cryst.*, **2**, (1987), 825.
- [19] G. Andersson, I. Dahl, P. Keller, W. Kuczynski, S. T. Lagerwall, K. Skarp, B. Stebler, *Appl. Phys. Lett.*, **51**, (1987), 640.
- [20] G. Andersson, I. Dahl, L. Komitov, S. T. Lagerwall, K. Skarp, B. Stebler, *J. Appl. Phys.*, **66**, (1989), 4983.
- [21] S. T. Lagerwall, M. Matuszczyk, P. Rodhe, L. Ödman, in *The Optics of Thermotropic Liquid Crystals*, S. J. Elston, J. R. Sambles (eds.), Taylor & Francis, London, 1997.
- [22] O. Lehmann, *Flüssige Kristalle*, Verlag von Wilhelm Engelmann, Leipzig, 1904.
- [23] J. Pavel, M. Glogarova, *Liq. Cryst.*, **9**, (1991), 87.
- [24] R. Shao, P. C. Willis, N. A. Clark, *Ferroelectrics*, **121**, (1991), 127.
- [25] K. Skarp, G. Andersson, T. Hirai, A. Yoshizawa, K. Hiraoka, H. Takezoe, A. Fukuda, *Jpn. J. Appl. Phys.*, **31**, (1992), 1409.
- [26] S.-D. Lee, J.-H. Kim, J. S. Patel, J. W. Goodby, *Mol. Cryst. Liq. Cryst.*, **227**, (1993), 39.
- [27] G. P. Crawford, R. E. Geer, J. Naciri, R. Shashidhar, B. R. Ratna, *Appl. Phys. Lett.*, **65**, (1994), 2937.
- [28] A. G. Rappaport, P. A. Willis, B. N. Thomas, N. A. Clark, M. B. Ros, D. M. Walba, *Appl. Phys. Lett.*, **67**, (1995), 362.

- [29] J. R. Lindle, F. J. Bartoli, S. R. Flom, A. T. Harter, B. R. Ratna, R. Shashidhar, *Appl. Phys. Lett.*, **70**, (1997), 1536.
- [30] A. Tang, S. Sprunt, *Phys. Rev. E*, **57**, (1998), 3050.
- [31] B. I. Ostrovskii, *Sov. Sci. Rev., Sect. A*, **12**, (1989), 85; reproduced in L. M. Blinov, V. G. Chigrinov, *Electrooptic Effects in Liquid Crystal Materials*, Springer, New York, 1994, p. 7.
- [32] F. Giesselmann, P. Zugenmaier, *Phys. Rev. E*, **55**, (1997), 5613.
- [33] P. Weiss, *J. Phys. (Fr.)*, **6**, (1907), 667.
- [34] M. Born, *Ann. Phys. (Ger.)*, **55**, (1918), 221.
- [35] N. H. Hartshorne, A. Stuart, *Crystals and the Polarizing Microscope*, Arnold, London, 1970.
- [36] F. Giesselmann, A. Langhoff, P. Zugenmaier, *Liq. Cryst.*, **23**, (1997), 927.
- [37] H. Arnold, H. Sackmann, *Z. Elektrochem.*, **63**, (1959), 1171.
- [38] S. L. Arora, J. L. Ferguson, A. Saupe, *Mol. Cryst. Liq. Cryst.*, **10**, (1970), 243.
- [39] T. J. Scheffer, H. Gruler, G. Meier, *Solid State Commun.*, **11**, (1972), 253.
- [40] R. B. Meyer, P. S. Pershan, *Solid State Commun.*, **13**, (1973), 989.
- [41] H. Arnold, D. Demus, H. Sackmann, *Z. Phys. Chem.*, **222**, (1963), 15.
- [42] J. Nehring, A. Saupe, *J. Chem. Soc., Faraday Trans. II*, **68**, (1972), 1.
- [43] D. Demus, *Krist. Tech.*, **10**, (1975), 933.
- [44] A. Saupe, *Mol. Cryst. Liq. Cryst.*, **7**, (1969), 59.
- [45] A. Saupe, *Mol. Cryst. Liq. Cryst.*, **21**, (1973), 211.
- [46] R. B. Meyer, L. Liébert, L. Strzelecki, P. Keller, *J. Phys. Lett.*, **36**, (1975), L69.
- [47] G. Durand, Ph. Martinot-Lagarde, *Ferroelectrics*, **24**, (1980), 89.
- [48] N. A. Clark, S. T. Lagerwall, *Appl. Phys. Lett.*, **36**, (1980), 899.
- [49] J. W. Goodby, R. Blinc, N. A. Clark, S. T. Lagerwall, M. A. Osipov, S. A. Pikin, T. Sakurai, K. Yoshino, B. Žekš, *Ferroelectric Liquid Crystals, Principles, Properties and Applications*, Gordon & Breach, Philadelphia, 1991.
- [50] S. T. Lagerwall, *Ferroelectric and Antiferroelectric Liquid Crystals*, Wiley-VCH, Weinheim, 1999.
- [51] I. Mušević, R. Blinc, B. Žekš, *The Physics of Ferroelectric and Antiferroelectric Liquid Crystals*, World Scientific, Singapore, 2000.
- [52] J. W. Goodby, J. S. Patel, T. M. Leslie, *Ferroelectrics*, **59**, (1984), 121.
- [53] J. Wahl, S. C. Jain, *Ferroelectrics*, **59**, (1984), 161.
- [54] A. M. Biradar, W. Haase, *Liq. Cryst.*, **7**, (1990), 143.
- [55] R. Shao, Z. Zhuang, N. A. Clark, *Ferroelectrics*, **122**, (1991), 213.
- [56] I. Dierking, F. Giesselmann, J. Kuserow, P. Zugenmaier, *Liq. Cryst.*, **17**, (1994), 243.
- [57] J. Schacht, I. Dierking, F. Giesselmann, K. Mohr, H. Zschke, W. Kuczynski, P. Zugenmaier, *Liq. Cryst.*, **19**, (1995), 151.
- [58] S. L. Arora, J. L. Ferguson, A. Saupe, *Mol. Cryst. Liq. Cryst.*, **10**, (1970), 243.
- [59] W. Helfrich, C. S. Oh, *Mol. Cryst. Liq. Cryst.*, **14**, (1971), 289.
- [60] W. Z. Urbach, J. Billard, *C. R. Acad. Sci., Paris, Ser. B*, **274**, (1972), 1287.
- [61] Ph. Martinot-Lagarde, *J. Phys., Colloq.*, **37**, (1976), C3-129.
- [62] Ph. Martinot-Lagarde, *Mol. Cryst. Liq. Cryst.*, **66**, (1981), 61.
- [63] Ph. Martinot-Lagarde, R. Duke, G. Durand, *Mol. Cryst. Liq. Cryst.*, **75**, (1981), 249.
- [64] B. I. Ostrovskij, A. Z. Rabinovich, A. S. Sonin, B. A. Strukov, *Zh. Eksp. Teor. Fiz.*, **74**, (1978), 1748.
- [65] B. I. Ostrovskij, V. G. Chigrinov, *Kristallografiya*, **25**, (1980), 560.
- [66] B. I. Ostrovskij, A. Z. Rabinovich, V. G. Chigrinov, *Advances in Liquid Crystal Research and Applications*, L. Bata (ed.), Pergamon Press, Oxford, 1980.
- [67] L. A. Beresnev, V. G. Chigrinov, D. I. Dergachev, E. I. Poshidaev, J. Fünfschilling, M. Schadt, *Liq. Cryst.*, **5**, (1989), 1171.
- [68] J. Fünfschilling, M. Schadt, *J. Appl. Phys.*, **66**, (1989), 3877.
- [69] J. Fünfschilling, M. Schadt, *Ferroelectrics*, **213**, (1998), 195.

- [70] L. Beresnev, W. Haase, *Opt. Mater.*, **9**, (1998), 201.
- [71] B. I. Ostrovskij, A. Z. Rabinovich, A. S. Sonin, B. A. Strukov, S. A. Taraskin, *Ferroelectrics*, **20**, (1978), 189.
- [72] I. Mušević, B. Žekš, R. Blinc, L. Jansen, A. Seppen, P. Wyder, *Ferroelectrics*, **58**, (1984), 71.
- [73] F. Gouda, A. Dahlgren, S. T. Lagerwall, B. Stebler, J. Bömelburg, G. Heppke, *Ferroelectrics*, **178**, (1996), 187.
- [74] O. Parodi, *J. Phys., Colloq.*, **36**, (1975), C1-22.
- [75] I. Abdulhalim, L. Benguigui, R. Weil, *J. Phys. (Fr.)*, **46**, (1985), 815.
- [76] W. Kuczynski, H. Stegemeyer, *Liq. Cryst.*, **5**, (1989), 553.
- [77] K. Miyasato, S. Abe, H. Takezoe, A. Fukuda, E. Kuze, *Jpn. J. Appl. Phys. Lett.*, **22**, (1983), L661.
- [78] T. P. Rieker, N. A. Clark, G. S. Smith, D. S. Parma, E. B. Sirota, C. R. Safinya, *Phys. Rev. Lett.*, **59**, (1987), 2658.
- [79] N. A. Clark, T. P. Rieker, *Phys. Rev. A*, **37**, (1988), 1053.
- [80] I. Dahl, S. T. Lagerwall, *Ferroelectrics*, **58**, (1984), 215.
- [81] T. P. Rieker, N. A. Clark, G. S. Smith, C. R. Safinya, *Liq. Cryst.*, **6**, (1989), 565.
- [82] Y. Ouchi, H. Takano, H. Takezoe, A. Fukuda, *Jpn. J. Appl. Phys.*, **27**, (1988), 1.
- [83] Y. Ouchi, J. Lee, H. Takezoe, A. Fukuda, K. Kondo, T. Kitamura, A. Mukoh, *Jpn. J. Appl. Phys. Lett.*, **27**, (1989), L725.
- [84] M. John, A. D. L. Chandani, Y. Ouchi, H. Takezoe, A. Fukuda, M. Ichihashi, K. Furukawa, *Jpn. J. Appl. Phys. Lett.*, **28**, (1989), L119.
- [85] K. Itoh, M. John, Y. Takanishi, Y. Ouchi, H. Takezoe, A. Fukuda, *Jpn. J. Appl. Phys.*, **30**, (1991), 735.
- [86] M. Oh-E, M. Isogai, T. Kitamura, *Liq. Cryst.*, **11**, (1992), 101.
- [87] H. F. Gleeson, A. S. Morse, *Liq. Cryst.*, **21**, (1996), 755.
- [88] F. Giesselmann, P. Zugenmaier, *Mol. Cryst. Liq. Cryst.*, **237**, (1993), 121.
- [89] J. S. Patel, J. W. Goodby, *J. Appl. Phys.*, **59**, (1986), 2355.
- [90] A. Jakli, A. Saupe, *Phys. Rev. A*, **45**, (1992), 5674.
- [91] L. Lejcek, S. Pirk, *Liq. Cryst.*, **8**, (1990), 871.
- [92] Y. Asao, T. Uchida, *Jpn. J. Appl. Phys. Lett.*, **32**, (1993), L604.
- [93] G. Andersson, K. Flatischler, L. Komitov, S. T. Lagerwall, K. Skarp, B. Stebler, *Ferroelectrics*, **113**, (1991), 361.
- [94] I. Dierking, F. Giesselmann, J. Schacht, P. Zugenmaier, *Liq. Cryst.*, **19**, (1995), 179.
- [95] I. Dierking, L. Komitov, S. T. Lagerwall, *Liq. Cryst.*, **24**, (1998), 769.
- [96] I. Dierking, F. Giesselmann, P. Zugenmaier, *Ferroelectrics*, **198**, (1997), 41.
- [97] G. Andersson, I. Dahl, L. Komitov, S. T. Lagerwall, M. Matuszczyk, K. Skarp, presented at *13th Int. Liquid Crystal Conf.*, Vancouver, 1990.
- [98] K. Skarp, G. Andersson, T. Hirai, A. Yoshizawa, K. Hiraoka, H. Takezoe, A. Fukuda, presented at *14th Int. Liquid Crystal Conf.*, Pisa, 1992.
- [99] G. Andersson, T. Carlsson, S. T. Lagerwall, M. Matuszczyk, T. Matuszczyk, presented at *4th Int. Conf. on Ferroelectric Liquid Crystals*, Tokyo, 1993.
- [100] K. Nakayama, M. Ozaki, K. Yoshino, *Jpn. J. Appl. Phys.*, **35**, (1996), 6200.
- [101] M. Ozaki, H. Moritake, K. Nakayama, K. Yoshino, *Jpn. J. Appl. Phys. Lett.*, **33**, (1994), L1620.
- [102] H. Moritake, K. Nakayama, M. Ozaki, K. Yoshino, *Ferroelectrics*, **178**, (1996), 277.
- [103] K. Nakayama, H. Moritake, M. Ozaki, K. Yoshino, *Jpn. J. Appl. Phys. Lett.*, **34**, (1995), L1599.
- [104] I. Dierking, L. Komitov, S. T. Lagerwall, *Jpn. J. Appl. Phys. Lett.*, **37**, (1998), L525.
- [105] I. Dierking, L. Komitov, S. T. Lagerwall, *Jpn. J. Appl. Phys. Lett.*, **37**, (1998), L57.
- [106] I. Dierking, B. Glösen, S. T. Lagerwall, C. K. Ober, *Phys. Rev. E*, **61**, (2000), 1593.
- [107] I. Dierking, L. Komitov, S. T. Lagerwall, *Liq. Cryst.*, **24**, (1998), 775.
- [108] I. Dierking, *J. Phys.: Condens. Matter*, **12**, (2000), 2657.
- [109] I. Dierking, *Ferroelectrics*, **256**, (2001), 103.
- [110] I. Dierking, L. Komitov, S. T. Lagerwall, *Ferroelectrics*, **211**, (1998), 259.
- [111] I. Dierking, S. T. Lagerwall, *Ferroelectrics*, **227**, (1999), 97.

- [112] K. Nakayama, M. Ozaki, K. Yoshino, *Appl. Phys. Lett.*, **70**, (1997), 2117.
- [113] I. Dierking, L. Komitov, S. T. Lagerwall, *Ferroelectrics*, **211**, (1998), 165.
- [114] I. Dierking, L. Komitov, S. T. Lagerwall, *Ferroelectrics*, **215**, (1998), 11.
- [115] I. Dierking, G. Scalia, *Liq. Cryst.*, **27**, (2000), 1059.
- [116] I. Dierking, L. Komitov, S. T. Lagerwall, T. Wittig, R. Zentel, *Liq. Cryst.*, **26**, (1999), 1511.
- [117] T. Carlsson, M. A. Osipov, *Phys. Rev. E*, **60**, (1999), 5619.
- [118] I. Dierking, *Ferroelectrics*, **234**, (1999), 171

8

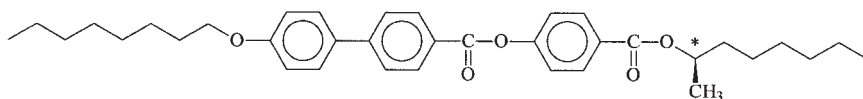
The SmC* Subphases

8.1

General Introduction and Structural Models

The story of the smectic C* subphases goes back to the discovery of antiferroelectric liquid crystals (AFLCs), whose possible existence was theoretically predicted by Michelson et al. [1–3], based on a Landau model of the SmA–SmC transition. The first experimental evidence for antiferroelectric ordering in chiral smectic liquid crystals was probably obtained by the electric field dependent pyroelectric measurements reported by Beresnev et al. [4, 5], but were seemingly ignored. (The herringbone antiferroelectric structure of a mixture of 80 wt% 4-nonyloxybenzylidene-4'-aminopentyl-cinnamate (NOBAPC, achiral) and 20 wt% hexyloxybenzylidene-amino-2-chloro- α -propyl-cinnamate (HOBACPC, chiral) was also reproduced in one of the first extensive reviews on ferroelectric liquid crystals, published as a special issue of *Molecular Crystals and Liquid Crystals*, chapter 3.7 [5].) Only one year later Levelut et al. [6] reported on a fluid smectic phase observed for methyl-heptyl-terephthalidene-bis-4-amino-cinnamate (MHTAC) [7], different from SmA* and SmC*, which they called SmO^(*). Galerne and Liebert [8, 9] proposed an antiferroelectric herringbone structure for the SmO* phase, which in fact has since been demonstrated to be equivalent to the antiferroelectric SmC_A* phase [10–12].

In the mid-1980s the now classic compound 4-1-methyl-heptyloxy-carbonyl-4'-phenyl-octyloxy-biphenyl-4-carboxylate (MHPOBC)



was first synthesized by Inukai et al. [13], for which Hiji et al. [14] reported the observation of a stable, nonpolar state at zero field with extinction position, when the smectic layer plane is oriented parallel to one of the crossed polarizers. Furukawa et al. [15] pointed out that in the low temperature range of the SmC* phase the switching process exhibits a considerable threshold, while at the same time the dielectric constant shows very small values. Both observations are in striking contrast to the general behavior observed for SmC* phases, and the existence of a novel phase was suggested. Chandani et al. [16, 17] reported on “tristable switching”

in MHPOBC, which is in fact not a “tristable” but rather a tristate monostable electrooptic response, as the only stable state is that at zero field. As a double hysteresis loop (Fig. 8.1) and two current peaks per half cycle of the applied electric field (Fig. 8.2) are observed, which is characteristic for antiferroelectric behavior (and distinctly different from the single hysteresis loop of ferroelectrics), it was suggested that MHPOBC does in fact exhibit an antiferroelectric phase [18], named SmC_A^* , below the ferroelectric SmC^* phase. Since the time of the discovery of antiferroelectric liquid crystals, numerous other materials exhibiting the SmC_A^* phase

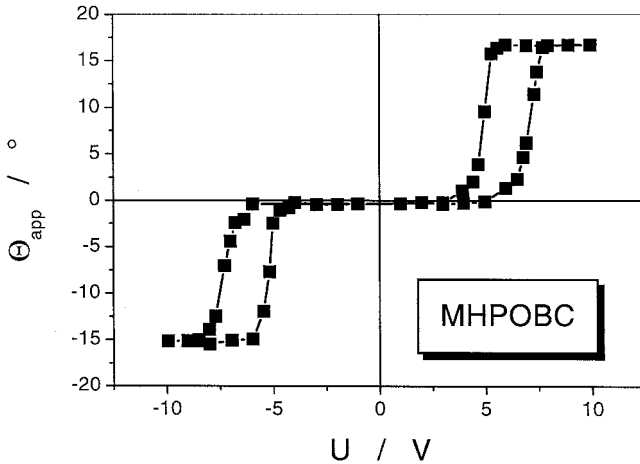


Fig. 8.1. Optical hysteresis curve of the SmC_A^* phase of MHPOBC, demonstrating its antiferroelectric behavior by the double hysteresis loop. (Data after Ref. [16].)

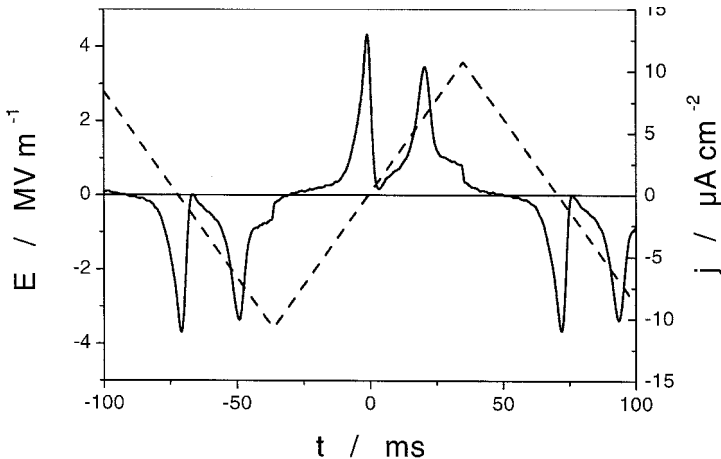
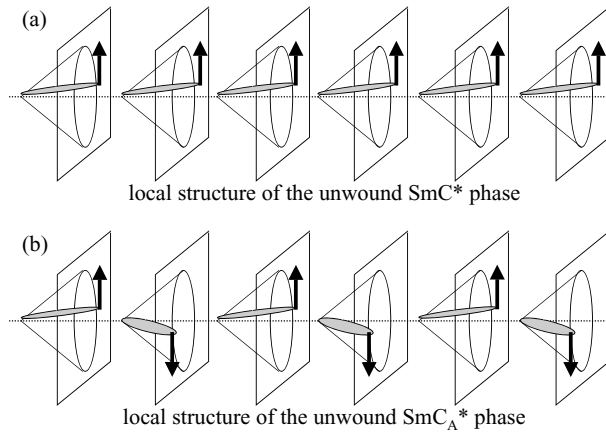


Fig. 8.2. Polarization reversal current response (solid curve) of an antiferroelectric SmC_A^* phase on triangular electric field application (dashed curve). Note that for increasing frequencies the two current peaks per half cycle will merge, such that the antiferroelectric behavior will no longer be resolvable.

Fig. 8.3. Simplified non-helical model of the local structure of (a) the ferroelectric SmC^* and (b) the antiferroelectric SmC_A^* phase.



have been synthesized, also due to its great applicational potential for display devices [19]. Over the past years, several additional SmC^* subphases with various electrooptic behaviors have been discovered, which will be discussed in more detail below.

Considering the fact that many polar solid state materials exhibit antiferroelectric order and to a much lesser extent ferroelectric properties [20], it seems surprising that the discovery of AFLCs took quite some time. It is interesting to note that in liquid crystals the antiferroelectric SmC_A^* phase is observed as the low temperature phase to ferroelectric SmC^* , while in solid state materials, for example in $NaNbO_3$, $(NH_4)_2BeF_4$ or solid solutions $(Pb,Ba)ZrO_3$, antiferroelectric order is observed at higher temperatures than ferroelectric order [20]. This indicates that the polar ordering mechanism in liquid crystals is different from that of solid state materials.

The proposed local model structure of the (unwound) SmC_A^* phase [18] is essentially equivalent to that shown in Refs. [4, 5] and is schematically depicted in Fig. 8.3(b), compared to that of the SmC^* phase (Fig. 8.3(a)). In the antiferroelectric state the orientation of the long molecular axis alternates between the $+\theta$ and $-\theta$ positions, thus P_S -up and P_S -down, in adjacent smectic layers. But like the SmC^* phase, also the bulk SmC_A^* phase exhibits a helical superstructure, which is schematically illustrated in Fig. 8.4, again in comparison to that of the SmC^* phase. As the vector of the spontaneous polarization is oriented antiparallel in adjacent smectic layers, the helical SmC_A^* phase can be considered to consist of a structure with a double helix and a helix phase shift of one half pitch.

Besides the originally reported antiferroelectric SmC_A^* phase, several subphases have been reported [21] since the early work on MHPOBC. Their terminology to date is quite confusing and inconsistent, and no standard nomenclature seems to have been agreed on. The subphases that are nowadays established with a good amount of certainty are the so-called SmC_α^* phase [18], probably exhibiting

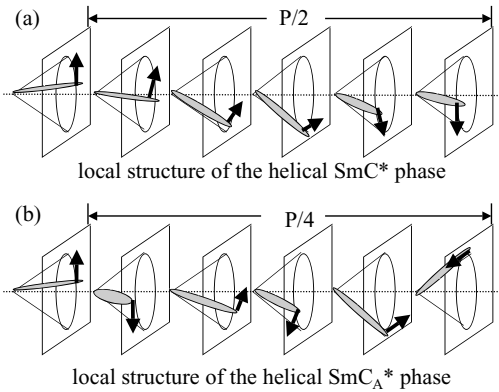


Fig. 8.4. Simple helical model of the local structure of (a) the ferroelectric SmC^* and (b) the antiferroelectric SmC_A^* phase.

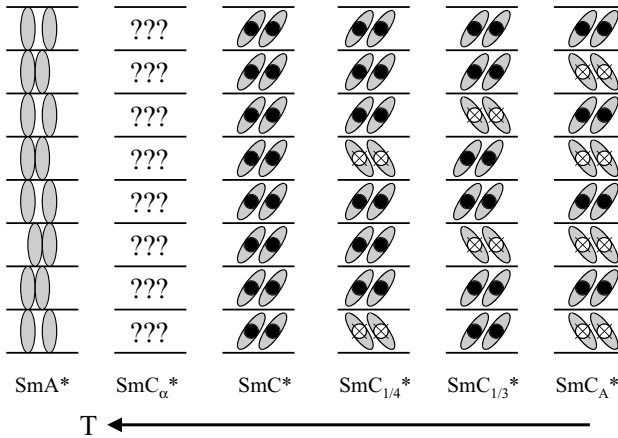


Fig. 8.5. Schematic overview of the non-helical local model structures of the chiral fluid smectic phases. Note that this view is indeed oversimplified.

an incommensurate structure, and the misleadingly termed “ferrielectric phases” [22] $\text{SmC}_{\text{FI1}}^*$, also referred to as SmC_β^* , and $\text{SmC}_{\text{FI2}}^*$, also referred to as SmC_γ^* , which are commensurate. The “ferrielectric” phases do in fact not exhibit any polarization at zero applied field and therefore rather represent helielectric phases. We will here call these latter phases $\text{SmC}_{1/4}^*$ and $\text{SmC}_{1/3}^*$ [23], respectively, with the subscript indicating the wavevector of the unit cell. The only reason for doing so lies in the hypothetical option of possible discovery of additional subphases, for example $\text{SmC}_{1/5}^*$, $\text{SmC}_{1/6}^*$ etc., without need to revise the nomenclature. All the above mentioned subphases (besides SmC^* and SmC_A^* , the latter of which we could also call $\text{SmC}_{1/2}^*$) are generally only observed over a rather small temperature interval of 1–2 K. Figure 8.5 summarizes in an oversimplified view the general phase sequence including the subphases, but disregarding any helical superstructures, which in reality are certainly present. These structures in turn would lead to the following behavior under applied electric fields. The ferroelectric SmC^* phase exhibits two stable states and the familiar hysteresis loop, as

schematically depicted in Fig. 8.6(a). The antiferroelectric SmC_A^* ($SmC_{1/2}^*$) phase is monostable and exhibits three states, the antiferroelectric ground state at $E = 0$ and the ferroelectric states at $\pm E$, thus leading to a double hysteresis curve (Fig. 8.6(b)). Intermediate phases in the non-helical model would indeed be ferroelectric with a nonzero polarization at zero electric field and, as schematically illustrated for the $SmC_{1/3}^*$ phase, a triple hysteresis curve would be observed (Fig. 8.6(c)). This is in fact not in accordance with experimental findings, as demonstrated in Fig. 8.7 with the spontaneous polarization recorded as a function

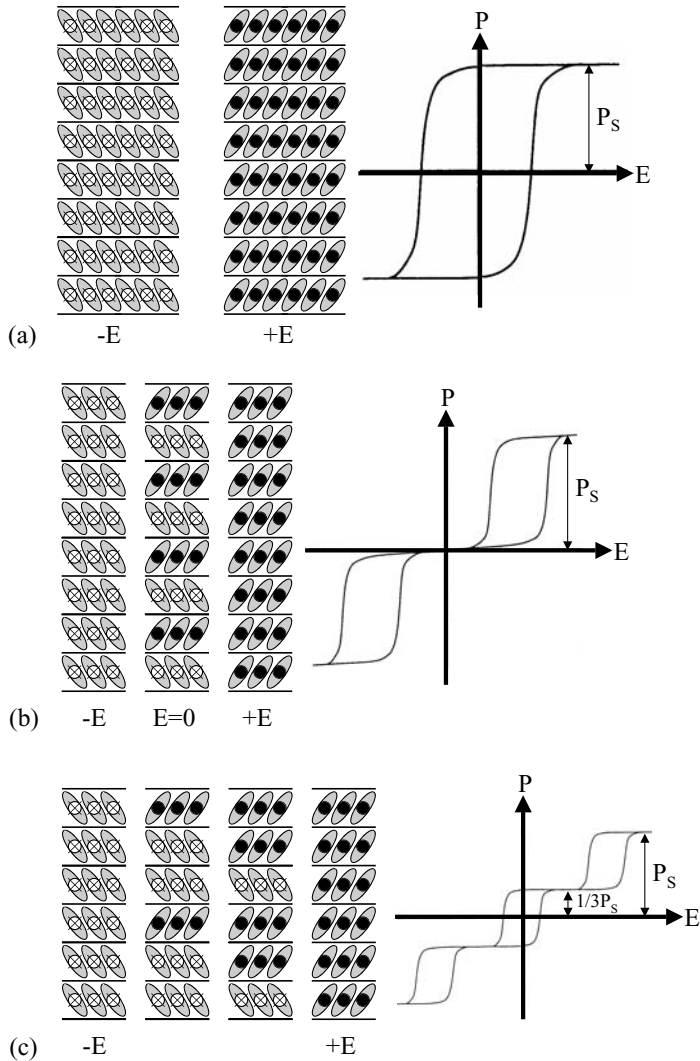


Fig. 8.6. Non-helical model structures and expected hysteresis curves for (a) a ferroelectric, (b) an antiferroelectric, and (c) a ferrielectric phase.

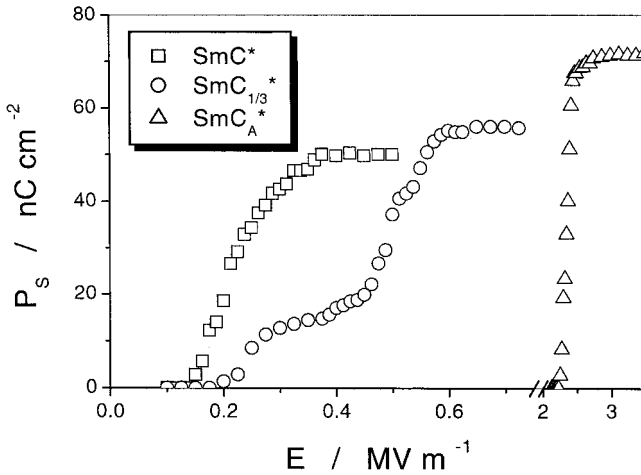


Fig. 8.7. Electric field dependence of the spontaneous polarization of the ferroelectric SmC^* phase (squares), the so-called ferrielectric $\text{SmC}_{1/3}^*$ phase (circles), and the antiferroelectric SmC_A^* phase (triangles). Note that for neither the SmC^* nor the $\text{SmC}_{1/3}^*$ phase a spontaneous polarization is observed at zero field; these phases are helielectric (cf. Fig. 8.6). The threshold voltage for switching of the antiferroelectric SmC_A^* phase is generally about one order of magnitude larger than that of the SmC^* phase.

of applied electric field amplitude. For the ferroelectric SmC^* phase a single hysteresis loop with small threshold field is observed (squares), while the antiferroelectric SmC_A^* phase exhibits a double hysteresis loop with much larger threshold field (triangles), as expected. But the so-called “ferrielectric” phase (circles) intermediate between ferro- and antiferroelectric behavior, clearly exhibits a vanishing polarization at zero field, in spite of the plateau at $1/3 P_{S\text{max}}$. This indicates a helielectric rather than a ferrielectric behavior. The temperature dependence of the maximum spontaneous polarization (Fig. 8.8) exhibits the well known behavior throughout all three phases.

The experimental discoveries concerning the antiferroelectric and SmC^* sub-phases obviously triggered a large effort for the development of theoretical models to explain their existence. The first continuous models by Orihara and Ishibashi [24] and Zeks et al. [25, 26], based on an extended Landau description, were able to predict a $\text{SmA}^*-\text{SmC}^*-\text{SmC}_{1/3}^*-\text{SmC}_A^*$ phase sequence, but failed to explain the existence of the SmC_α^* phase. Ising models [27–31] qualitatively accounted for a variety of different ferrielectric phases, including devil’s staircase behavior, for which some experimental evidence might have been given by ellipsometric investigations on free-standing films [32], but they do not allow for helical superstructures, thus reflecting the simplified view of Fig. 8.5, and were later disregarded because of these discrepancies in relation to experimental findings. A more realistic description is obtained from discrete XY models [33–36], the so-called “clock model”, which does allow for the experimentally observed helical superstructures. In fact, the model of Roy and Madhusudana [36] predicts a double twisted SmC_A^*

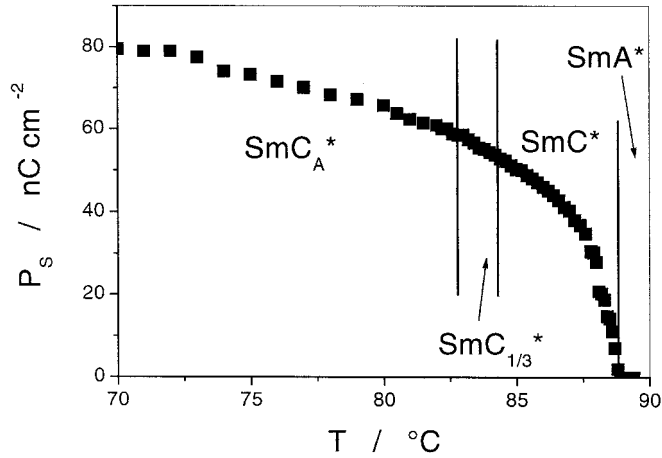


Fig. 8.8. Dependence of the spontaneous polarization over the temperature interval of the fluid smectic phases. Often, no significant discontinuities are observed across the ferro- to ferri- and antiferroelectric transitions.

phase and a tightly twisted phase between SmA^* and SmC^* , which can readily be associated with the experimentally observed SmC_α^* phase. It is interesting to note that the model also predicts an inversion of the helical twist sense between SmC^* and SmC_A^* , which is in fact quite generally observed in experiments [37, 38]. Finally, the currently accepted structures seem to be those predicted by the “distorted clock model” [39–41]. Resonant x-ray scattering investigations [42–44], i.e. x-ray scattering at energies close to the absorption edge of an atom (often sulfur), indeed provided convincing experimental evidence for the “clock model”, which is summarized in Fig. 8.9. Besides Fig. 8.9(a) trivially showing the SmA^* phase, Fig. 8.9(b) schematically illustrates the SmC_α^* phase, presumably an incommensurate structure with a periodicity of approximately 5–8 smectic layers, a relatively small tilt angle [45, 46], and tight pitch [47–49], which may exhibit ferrielectric but also antiferroelectric electrooptic behavior [21, 45, 50]. Fig. 8.9(c) depicts the familiar structure of the well known SmC^* phase. The structures of the so-called “ferrielectric” phases, $SmC_{1/4}^*$ and $SmC_{1/3}^*$, are schematically shown in Figs. 8.9(d) and (e), respectively, while Fig. 8.9(f) illustrates the antiferroelectric SmC_A^* phase.

Before we proceed to the discussion of the SmC^* subphase textures, the effects of confinement of respective materials to thin sandwich cells should be mentioned. For cell gaps smaller than approximately 6–8 μm , liquid crystals can show pronounced deviations from their bulk properties. Frustrated phases and the SmC^* subphases are especially sensitive to boundary conditions and confinement, which can lead to reduced phase transition temperatures and even to the complete disappearance of those phases in thin cells [51–55]. An experimental example of the suppression of a $SmC_{1/3}^*$ phase by confinement is depicted in Fig. 8.10, where the electric field dependence of the spontaneous polarization is shown for

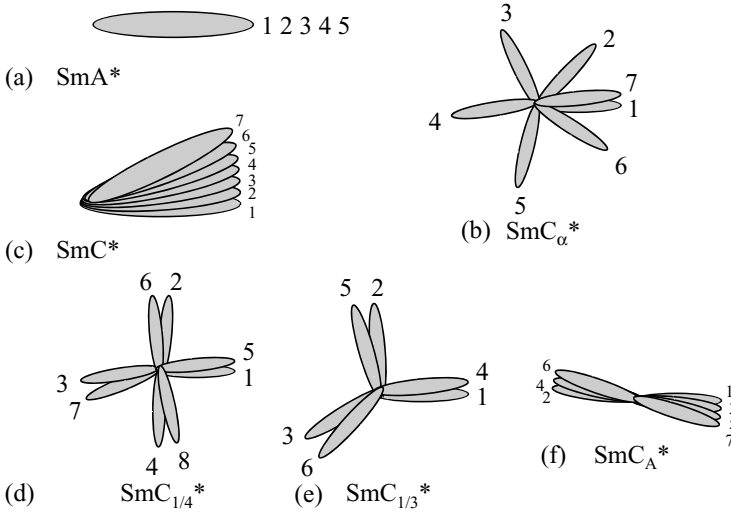


Fig. 8.9. Schematic summary of the proposed structural features of the chiral fluid smectic phases, including the SmC* subphases, of the “distorted clock model” by looking at the smectic layer plane. The phase sequence observed on cooling is: SmA*–SmC_α*–SmC*–SmC_{1/4}*–SmC_{1/3}*–SmC_A*.

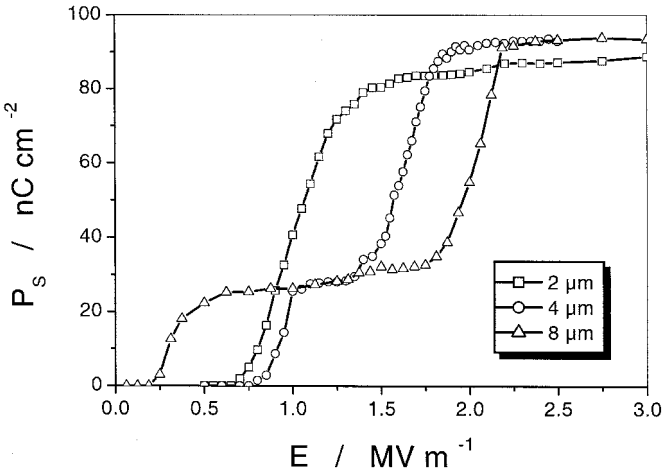


Fig. 8.10. Electric field dependence of the spontaneous polarization in the temperature interval of the “ferrielectric” SmC_{1/3}* phase for different sandwich cell gaps. While for thin cells the ferrielectric behavior is completely suppressed ($d = 2 \mu\text{m}$, squares), it becomes increasingly apparent as the sample cell gap is increased ($d = 4 \mu\text{m}$, circles), and finally behaves nearly bulk-like ($d = 8 \mu\text{m}$, triangles).

varying cell gaps. In cells of gap $d = 8 \mu\text{m}$ (triangles) a clear plateau is observed at $P_S = 1/3 P_{S_{\text{max}}}$, which becomes less pronounced on decreasing the cell gap to $d = 4 \mu\text{m}$ (circles) and eventually vanishes for thin cells of gap $d = 2 \mu\text{m}$ (squares).

8.2

Textures of the SmC* Subphases

To say it frankly, to distinguish between the different SmC* subphases by polarizing microscopy can be quite demanding. At first sight, many of these phases appear very much alike, and only very subtle texture changes can be detected. Often additional methods, such as differential scanning calorimetry, electrooptic techniques, polarization reversal current curves, and the temperature and electric field dependence of the spontaneous polarization have to be employed to characterize such materials. For this reason we will here present different series of texture photographs, taken of the same sample preparation and area displayed, hopefully to demonstrate some of these subtle texture changes.

Mesogenic materials which exhibit SmC* subphases and the antiferroelectric SmC_A^* phase generally show a direct transition from the isotropic to a smectic phase, omitting the cholesteric N^* phase. Thus, most often fan-shaped textures are observed for these materials. The texture series of Plate 82 depicts the transformation of such a commonly observed fan-shaped texture on successive cooling from the SmA^* phase all the way to the antiferroelectric SmI_A^* phase. The transition from SmA^* (Plate 82(a)) to SmC_α^* (Plate 82(b)) can in general hardly be detected by texture observation only. It is sometimes accompanied by small changes in birefringence, slightly changing the color appearance of the fans, or merely by a slightly more pronounced rippling of the fans in the direction perpendicular to the smectic layer plane, as shown in the additional Plates 83(a) and (b), depicting the SmA^* and SmC_α^* phase, respectively. Also the texture changes on cooling into the SmC* phase (Plate 82(c)) are generally very subtle. Proceeding into the so-called ferrielectric phases, $\text{SmC}_{1/4}^*$ and/or $\text{SmC}_{1/3}^*$ (Plate 82(d)), changes in birefringence may be observed, which are sometimes accompanied by the development of a line pattern across the fans, a behavior that is shown more pronouncedly in the additional Plates 84(a) and (b), presumably caused by a noticeable change of the pitch of the helical superstructure. At this point it might be necessary to point out that we cannot distinguish between $\text{SmC}_{1/3}^*$ and $\text{SmC}_{1/4}^*$ by polarizing microscopy alone, if only one of these intermediate phases is present in the investigated material. For such a distinction, further experimental methods need to be employed. It was recently pointed out by Jan Lagerwall et al. [55] that the focal conic defects discussed above show a peculiar behavior at the transition into the $\text{SmC}_{1/3}^*$ and/or $\text{SmC}_{1/4}^*$ phase. The defects formed by the associated ellipses and the hyperbolas clearly break up and separate within the temperature range of the so-called “ferrielectric” phases. The reason for this optical appearance is not clear at the present time, but seems to be observed for most of the respective compounds. A texture example of the

breaking and separation of focal conic defect lines is given in Plate 85 at the transition from SmC^* (Plate 85(a)) to $\text{SmC}_{1/3}^*$ (Plate 85(b)). Finally, the transition into the antiferroelectric SmC_A^* phase is then quite clearly detectable by the development of large arced transition bars along the direction of the smectic layer plane and a pronounced change in birefringence (Plate 82(e)). Also the transition to possible antiferroelectric phases with hexatic order, here the SmI_A^* phase (Plate 82(f)), is in general easier to observe.

Considering a sample with homeotropic boundary conditions, the transition of the pseudo-isotropic SmA^* texture to that of the SmC_α^* phase cannot in general be detected by polarizing microscopy, but may be better resolved for free-standing films. The subsequent transition into SmC^* is accompanied by a slight birefringence, i. e. a grayish appearance of the homeotropic regions due to the tilt of the molecules with respect to the smectic layer plane, as discussed above. The eventual transition into a $\text{SmC}_{1/3}^*$ and/or $\text{SmC}_{1/4}^*$ subphase can then clearly be recognized by the development of a grayish, strongly fluctuating texture, which is for obvious reasons not reproducible here. Nevertheless, once you encounter this transition under homeotropic boundary conditions, which is in fact best realized by preparations of free-standing films, you will indeed recognize it easily. The strongly fluctuating texture of the “ferrielectric” phases is most likely related to the diverging pitch of the helical superstructure, as it changes its handedness between SmC^* and SmC_A^* . Plate 86 shows the transition between $\text{SmC}_{1/3}^*$ and SmC_A^* for the homeotropic region of a sample preparation. Although the observed texture fluctuations cannot be imaged here, Plate 86(a) shows the grayish appearance of $\text{SmC}_{1/3}^*$, which noticeably transforms into a black, pseudo-isotropic texture on cooling into the antiferroelectric SmC_A^* phase (Plate 86(b)). Trying to characterize smectic C^* subphases only by observation of natural textures in polarizing microscopy is a very demanding, if not impossible task. Nevertheless, the study of free-standing films, which has admittedly been quite neglected in this text, represents an experimental technique that can certainly make such a characterization much easier.

References

- [1] A. Michelson, D. Cabib, L. Benguigui, *J. Phys. (Fr.)*, **38**, (1977), 961.
- [2] A. Michelson, L. Benguigui, D. Cabib, *Phys. Rev. A*, **16**, (1977), 394.
- [3] A. Michelson, L. Benguigui, *Phys. Rev. A*, **18**, (1978), 2736.
- [4] L. A. Beresnev, L. M. Blinov, V. A. Baikalov, E. P. Pozhidayev, G. V. Purvanetskias, A. I. Pavluchenko, *Mol. Cryst. Liq. Cryst.*, **89**, (1982), 327.
- [5] L. A. Beresnev, L. M. Blinov, M. A. Osipov, S. A. Pikin, *Mol. Cryst. Liq. Cryst.*, **158A**, (1988), 3–150.
- [6] A. M. Levelut, C. Germain, P. Keller, L. Liebert, J. Billard, *J. Phys. (Fr.)*, **44**, (1983), 623.
- [7] P. Keller, L. Liebert, L. Strzelecki, *J. Phys., Colloq.*, **37**, (1976), C3-27.
- [8] Y. Galerne, L. Liebert, presented at *2nd Int. Conf. on Ferroelectric Liquid Crystals*, Göteborg, 1989, oral presentation O-27.
- [9] Y. Galerne, L. Liebert, *Phys. Rev. Lett.*, **66**, (1991), 2891.
- [10] G. Heppke, P. Kleineberg, D. Löttsch, *Liq. Cryst.*, **14**, (1993), 67.
- [11] Y. Takanishi, H. Takezoe, M. Johno, T. Yui, A. Fukuda, *Jpn. J. Appl. Phys.*, **32**, (1993), 4605.
- [12] P. E. Cladis, H. R. Brand, *Liq. Cryst.*, **14**, (1993), 1327.
- [13] T. Inukai, K. Furukawa, K. Terashima, S. Saitoh, M. Isogai, T. Kitamura, A. Mukoh, *Japanese National Liquid Crystal Meeting*, Kanazawa, 1985, Book of Abstracts, p. 172 (in Japanese); referenced after H. Takezoe, Y. Takanishi, in *Chirality in Liquid Crystals*, H.-S. Kitzerow, Ch. Bahr (eds.), Springer-Verlag, Berlin, 2001, ch. 9.
- [14] N. Hiji, A. D. L. Chandani, S. Nishiyama, Y. Ouchi, H. Takezoe, A. Fukuda, *Ferroelectrics*, **85**, (1988), 99.
- [15] K. Furukawa, K. Terashima, M. Ichihashi, S. Saitoh, K. Miyazawa, T. Inukai, *Ferroelectrics*, **85**, (1988), 63.
- [16] A. D. L. Chandani, T. Hagiwara, Y. Suzuki, Y. Ouchi, H. Takezoe, A. Fukuda, *Jpn. J. Appl. Phys. Lett.*, **27**, (1988), L729.
- [17] M. Johno, A. D. L. Chandani, Y. Ouchi, H. Takezoe, A. Fukuda, M. Ichihashi, K. Furukawa, *Jpn. J. Appl. Phys. Lett.*, **28**, (1989), L119.
- [18] A. D. L. Chandani, E. Gorecka, Y. Ouchi, H. Takezoe, A. Fukuda, *Jpn. J. Appl. Phys. Lett.*, **28**, (1989), L1265.
- [19] N. Yamamoto, Y. Yamada, N. Koshobu, K. Mori, K. Nakamura, H. Orihara, Y. Ishibashi, Y. Suzuki, I. Kawamura, *Jpn. J. Appl. Phys.*, **31**, (1992), 3182.
- [20] F. Jona, G. Shirane, *Ferroelectric Crystals*, Dover Publications, New York, 1993.
- [21] A. Fukuda, Y. Takanishi, T. Isozaki, K. Ishikawa, H. Takezoe, *J. Mater. Chem.*, **4**, (1994), 997.
- [22] H. T. Nguyen, J. C. Rouillon, P. Cluzeau, G. Sigaud, C. Destrade, N. Isaert, *Liq. Cryst.*, **17**, (1994), 571.
- [23] S. T. Lagerwall, *Ferroelectric and Antiferroelectric Liquid Crystals*, Wiley-VCH, Weinheim, 1999.
- [24] H. Orihara, Y. Ishibashi, *Jpn. J. Appl. Phys. Lett.*, **29**, (1990), L115.
- [25] B. Zeks, R. Blinc, M. Cepic, *Ferroelectrics*, **122**, (1991), 221.
- [26] B. Zeks, M. Cepic, *Liq. Cryst.*, **14**, (1993), 445.

- [27] M. Nakagawa, *J. Phys. Soc. Jpn.*, **62**, (1993), 2260.
- [28] M. Nakagawa, *Liq. Cryst.*, **14**, (1993), 1763.
- [29] T. Koda, H. Kimura, *J. Phys. Soc. Jpn.*, **65**, (1996), 2880.
- [30] M. Yamashita, *J. Phys. Soc. Jpn.*, **65**, (1996), 2904.
- [31] M. Yamashita, *J. Phys. Soc. Jpn.*, **66**, (1997), 130.
- [32] Ch. Bahr, D. Fliegner, C. J. Booth, J. W. Goodby, *Phys. Rev. E*, **51**, (1995), R3823.
- [33] H. Sun, H. Orihara, Y. Ishibashi, *J. Phys. Soc. Jpn.*, **62**, (1993), 2066.
- [34] M. Cepic, B. Zeks, *Mol. Cryst. Liq. Cryst.*, **263**, (1995), 61.
- [35] S. A. Pikin, *Mol. Cryst. Liq. Cryst.*, **262**, (1995), 425.
- [36] A. Roy, N. V. Madhusudana, *Europhys. Lett.*, **36**, (1996), 221.
- [37] P. Gisse, V. L. Lorman, J. Pavel, H. T. Nguyen, *Ferroelectrics*, **178**, (1996), 297.
- [38] P. Gisse, M. Sidir, V. L. Lorman, R. Farhi, J. Pavel, H. T. Nguyen, *J. Phys. II*, **7**, (1997), 1817.
- [39] V. L. Lorman, *Liq. Cryst.*, **20**, (1996), 267.
- [40] T. Akizuki, K. Miyachi, Y. Takanishi, K. Ishikawa, H. Takezoe, A. Fukuda, *Jpn. J. Appl. Phys.*, **38**, (1999), 4832.
- [41] P. M. Johnson, D. A. Olson, S. Pankratz, H. T. Nguyen, J. W. Goodby, M. Hird, C. C. Huang, *Phys. Rev. Lett.*, **84**, (2000), 4870.
- [42] P. Mach, R. Pindak, A. M. Levelut, P. Barois, H. T. Nguyen, C. C. Huang, L. Furenlid, *Phys. Rev. Lett.*, **81**, (1998), 1015.
- [43] P. Mach, R. Pindak, A. M. Levelut, P. Barois, H. T. Nguyen, H. Baltes, M. Hird, K. Toyne, A. Seed, J. W. Goodby, C. C. Huang, L. Furenlid, *Phys. Rev. E*, **60**, (1999), 6793.
- [44] L. S. Hirst, S. J. Watson, H. F. Gleeson, P. Cluzeau, P. Barois, R. Pindak, J. Pitney, A. Cady, P. M. Johnson, C. C. Huang, A. M. Levelut, G. Srajer, J. Pollmann, W. Caliebe, A. Seed, M. R. Herbert, J. W. Goodby, M. Hird, *Phys. Rev. E*, **65**, (2002), 041705.
- [45] Y. Takanishi, K. Hiraoka, V. K. Agrawal, H. Takezoe, A. Fukuda, M. Matsushita, *Jpn. J. Appl. Phys.*, **30**, (1991), 2023.
- [46] P. Cluzeau, P. Barois, H. T. Nguyen, C. Destrade, *Eur. Phys. J. B*, **3**, (1998), 73.
- [47] V. Laux, N. Isaert, H. T. Nguyen, P. Cluzeau, C. Destrade, *Ferroelectrics*, **179**, (1996), 25.
- [48] V. Laux, N. Isaert, V. Faye, H. T. Nguyen, *Liq. Cryst.*, **27**, (2000), 81.
- [49] C. Da Cruz, J. C. Rouillon, J. P. Marcerou, N. Isaert, *Liq. Cryst.*, **28**, (2001), 125.
- [50] T. Isozaki, K. Hiraoka, Y. Takanishi, H. Takezoe, A. Fukuda, Y. Suzuki, I. Kawamura, *Liq. Cryst.*, **12**, (1992), 59.
- [51] M. Cepic, G. Heppke, J. M. Hollidt, D. Löttsch, B. Zeks, *Ferroelectrics*, **147**, (1993), 159.
- [52] H. Moritake, N. Shigeno, M. Ozaki, K. Yoshino, *Liq. Cryst.*, **14**, (1993), 1283.
- [53] Y. P. Panarin, O. Kalinovskaya, J. K. Vij, J. W. Goodby, *Phys. Rev. E*, **55**, (1997), 4345.
- [54] P. Jägemalm, J. P. F. Lagerwall, A. Dahlgren, L. Komitov, A. Matharu, C. Grover, F. Gouda, A. Kutub, *Ferroelectrics*, **244**, (2000), 147.
- [55] J. P. F. Lagerwall, D. D. Parghi, D. Krüerke, P. Jägemalm, F. Gouda, *Liq. Cryst.*, **29**, (2002), 163

9

The Hexatic Phases

With increasing order on decreasing temperature, the changes in textures of the various liquid crystal phases involved often become more and more subtle, even though respective phase transitions may clearly be detected by calorimetry. The hexatic phases are the first to exhibit order within the smectic layers, so-called *bond-orientational order*, which represents a long range hexagonal orientational order, while the hexatic positional order only extends over short distances and there is no interlayer positional correlation. The general structural features of hexatic smectic phases were already introduced in Chapter 1.

9.1

The SmB^(*) Phase

Like in SmA^(*), the long molecular axis of the SmB^(*) phase [1–4] is on average oriented along the direction of the smectic layer normal. This often makes the transition between the two phases hard to detect in polarizing microscopy. Generally, the textural features of the high temperature SmA phase are retained when crossing the transition into SmB, i.e. a SmA fan-shaped texture will transform into a SmB fan-shaped texture, as depicted in Plates 87 and 88, respectively, showing the same part of a sample area. Only very subtle changes in the texture are noticed, with the SmB phase being slightly more homogeneous in its optical appearance. It has been reported [5, 6] that the SmB fan-shaped texture gradually transforms into a mosaic texture (see below), when annealed for a long time at elevated temperatures, which led to the conclusion that the mosaic texture represents the most stable configuration of SmB. In some cases transition bars are observed during the transition from SmA to SmB [6–8], which were attributed to chemical impurities of the sample and which was latter doubted [9]. A case where transition bars are in fact observed is that of the SmA to soft crystal B transition [9]. Similarly, as discussed above, if the original SmA phase is oriented homeotropically (pseudo-isotropic texture), i.e. appears dark between crossed polarizers, also the SmB phase will adopt a homeotropic orientation, and thus equally appears dark with no major changes being observed in the respective textures.

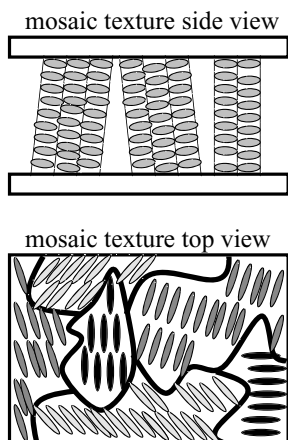


Fig. 9.1. Schematic illustration of the smectic layer and director configuration in the *mosaic texture*, often observed for higher ordered and soft crystal phases.

The *mosaic texture* [6, 7, 10] is a very common appearance of the SmB phase, especially for materials with a direct SmB transition from the isotropic melt. An example is depicted in Plate 89. Mosaic textures exhibit large areas of uniform optical appearance, mediated by grain boundaries. The smectic layers are basically perpendicular to the substrate plane, which makes the director lie close to the plane of the bounding glass plates. Within areas of uniform optical appearance the director is oriented along a constant direction, which varies from grain to grain. Rotating the mosaic texture between crossed polarizers successively brings individual grains into extinction position. The layer and director configuration of the mosaic texture is schematically depicted in Fig. 9.1.

Another texture variant called *oval texture*, which is discussed in more detail in Ref. [11], may be observed for the SmB phase. Also in this case the textural features are commonly retained when cooling the sample into an even higher ordered orthogonal phase like soft crystal E.

Cooling a sample with a direct Iso–SmB transition below the clearing temperature often results in dendritic-like growth patterns [6, 12], as shown in Plate 90. This may also be observed by growth of the SmB phase from the nematic phase. The growth structures often reflect the sixfold symmetry of the phase by growing aggregates with six arms, exhibiting tip splitting during growth.

In the same way that the chiral SmA* phase exhibits equivalent natural textures as compared to the achiral SmA phase, the analogous behavior is also observed for SmB* and SmB.

9.2 The $SmI^{(*)}$ and $SmF^{(*)}$ Phases

In contrast to the orthogonal SmB phase, the director of the SmI [13, 14] and SmF [15–17] phases is tilted with respect to the smectic layer normal. Depending on the

tilt direction with respect to the hexagonal bond-orientational order lattice, two phases are distinguished, SmI being tilted towards the apex, while SmF is tilted towards the side of the hexagon (see Chapter 1). For the chiral versions of both phases, helical superstructures have been observed, in complete analogy to the above discussion of the SmC* phase. This has been demonstrated by the work of Kuczynski and Stegemeyer [18] on Cano preparations of the respective phases. As the distinction between different phases on the basis of polarizing microscopy now becomes increasingly difficult, we will progress our discussion by primarily showing texture series of the same sample areas on successive cooling. Furthermore, as we have put a certain emphasis on the textures of chiral materials throughout this text, the following discussion of these texture series will be focused on such mesogens, especially in relation to the textures of the respective fluid smectic phases.

9.2.1

Natural Textures and Planar Anchoring Conditions

Our first texture series is shown in Plate 91, successively depicting how an original SmA* phase with a common fan-shaped texture (Plate 91(a)) will evolve on cooling. At the transition to the SmC* phase the familiar development of the equidistant line pattern is observed across the fans, due to the formation of the intrinsic helical superstructure of SmC*, which can clearly be observed (Plate 91(b)), while the actual smectic layer structure is retained. Also first indications of a broken fan-shaped texture are observed in regions where the helical superstructure is not fully developed. The texture changes are equivalent to the situation discussed above in Chapter 7 (Plates 68, 69, 75, and 76). On further cooling we observe the transition into the SmI* phase, which is accompanied by a partial loss of the helical superstructure and a more pronounced development of the broken fan-shaped texture, although remnants of the original SmC* equidistant line pattern can still be observed (Plate 91(c)). The transition into the SmF* phase eventually shows the break-up of the fan-shaped texture into pronounced domains, while some remnants of the original fans are still visible (Plate 91(d)). At this point also the indications of a helical superstructure are mostly lost.

Confining the material to rather thin samples of cell gap $2\ \mu\text{m}$ with uniform planar boundary conditions, one may observe the development of four distinct domains in SmI^(*), as shown in Plate 92, in contrast to the high temperature two domain SSFLC structure of SmC^(*) (Plate 78). The two additional domain types are oriented in the direction of the two metastable states on the hexagon of the tilt cone, as schematically depicted in Fig. 9.2. Note that we cannot trivially distinguish between domains in positions 2 and 6 or in positions 3 and 5 by polarizing microscopy. In this situation there will be two pairs of domains with mutually quite similar birefringence. All four domains can be brought into extinction by successive rotation of the sample between crossed polarizers. The azimuthal rotation angles for the pairs of mutual domains are only a few degrees apart.

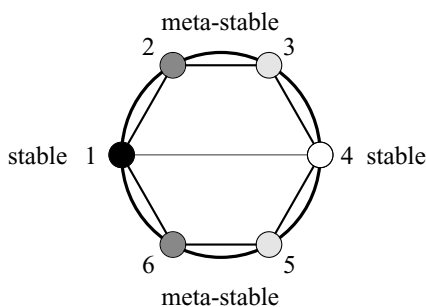


Fig. 9.2. Schematic illustration of possible director orientations of a homogeneously planar oriented $SmI^{(*)}$ phase in the surface stabilized bookshelf geometry (no helical superstructure, no chevron formation). The view is onto the smectic layer plane, with the molecules being tilted towards the apex of the hexagon (position 1 or 4). This leads to four domain types, which can successively be brought to extinction by rotation of the sample between crossed polarizers. Two domain types (i. e. states 1/2 and 3/4) mutually exhibit a similar birefringence. (It is not possible to distinguish states 2/6 and 3/5 by polarizing microscopy.)

9.2.2

Homeotropic Boundary Conditions

Sometimes, samples that are prepared simply between two glass plates exhibit regions of both planar and homeotropic anchoring at the same time. Such preparations can be quite useful in the determination of phase transitions and the characterization of liquid crystal phases by polarized microscopy. An example series of textures of the same sample area is shown in Plate 93, illustrating the $SmA^* - SmC^* - SmI^* - SmF^*$ phase sequence for both planar and homeotropic aligned sample regions. For the SmA^* phase (Plate 93(a)) we encounter the familiar appearance of the fan-shaped texture (top right) at planar anchoring and the pseudo-isotropic texture (bottom left) for homeotropic anchoring. Cooling into the SmC^* phase (Plate 93(b)), planar regions exhibit the broken fan-shaped texture, while homeotropic areas begin to show a grayish appearance, due to the tilt of the molecules and the small birefringence. These homeotropic regions will eventually show a SmC^* Schlieren texture at large tilt angles, before being transformed into a SmI^* Schlieren texture on further cooling (Plate 93(c)), with a clearly increased birefringence and fewer defects. In the respective planar area of the sample we observe a pronounced broken fan-shaped texture. Cooling into the SmF^* phase, the formerly broken fan-shaped texture in the region of planar anchoring conditions eventually exhibits pronounced domains, while the homeotropic area transforms into a SmF^* Schlieren mosaic texture (Plate 93(d)).

Plates 94 and 95 show a purely homeotropic preparation of a chiral SmI^* and SmF^* phase, respectively (same sample area). The SmI^* phase already exhibits a pronounced birefringence, due to a relatively large tilt angle of approximately 30° inclined to the direction of light propagation (Plate 94). Moving fronts of differing birefringence may be attributed to changing twist states with the twist axis perpendicular to the substrate plane. The helical pitch of the structure ($P > 1 \mu m$) is well outside the range of selective reflection. Lowering the temperature into the SmF^* phase, the diverging pitch behavior becomes more pronounced and regions of large birefringence are formed (Plate 95). Eventually, the SmF^* appearance evolves into a mosaic-like texture, similar to that of the bottom left part of Plate 93(d).

References

- [1] H. Sackmann, D. Demus, *Mol. Cryst. Liq. Cryst.*, **2**, (1966), 81.
- [2] A.-M. Levelut, M. Lambert, *C. R. Acad. Sci., Paris*, **272**, (1971), 1018.
- [3] A. J. Leadbetter, J. C. Frost, M. A. Mazid, *J. Phys. Lett.*, **40**, (1979), 325.
- [4] R. Pindak, D. E. Moncton, S. C. Davey, J. W. Goodby, *Phys. Rev. Lett.*, **46**, (1981), 1135.
- [5] D. Demus, L. Richter, *Textures of Liquid Crystals*, Verlag Chemie, Weinheim, 1978.
- [6] D. Demus, *Wiss. Z. Univ. Halle*, **XXI**(3), (1972), 41.
- [7] H. Arnold, D. Demus, H. Sackmann, *Z. Phys. Chem.*, **222**, (1963), 15.
- [8] G. W. Smith, Z. G. Gardlund, R. J. Curtis, *Mol. Cryst. Liq. Cryst.*, **19**, (1973), 327.
- [9] G. W. Gray, J. W. Goodby, *Smectic Liquid Crystals, Textures and Structures*, Leonard Hill, Glasgow, 1984.
- [10] J. Nehring, M. A. Osman, *Z. Naturforsch.*, **31a**, (1976), 786.
- [11] D. Demus, P. Schiller, N. K. Sharma, *Cryst. Res. Technol.*, **19**, (1984), 577.
- [12] D. Demus, M. Klapperstück, R. Rurainski, D. Marzotko, *Z. Phys. Chem.*, **246**, (1971), 385.
- [13] L. Richter, D. Demus, H. Sackmann, *Mol. Cryst. Liq. Cryst.*, **71**, (1981), 269.
- [14] P. A. C. Gane, A. J. Leadbetter, P. G. Wrighton, *Mol. Cryst. Liq. Cryst.*, **66**, (1981), 247.
- [15] D. Demus, S. Diele, M. Klapperstück, V. Link, H. Zschke, *Mol. Cryst. Liq. Cryst.*, **15**, (1971), 161.
- [16] A. J. Leadbetter, J. P. Gaughan, B. A. Kelly, G. W. Gray, J. W. Goodby, *J. Phys. (Fr.)*, **40**, (1979), 178.
- [17] J. J. Benattar, J. Doucet, M. Lambert, A.-M. Levelut, *Phys. Rev. A*, **20**, (1979), 2505.
- [18] W. Kuczynski, H. Stegemeyer, *Liq. Cryst.*, **5**, (1989), 553.

10

Soft Crystal Phases and Crystallization

Frankly speaking, the soft crystal phases cannot unambiguously be distinguished by polarizing microscopy alone. Sometimes the changes in texture appearance are so small, if present at all, that a phase transition is hardly detected. To determine the transitions between different soft crystal phases, it is often useful to employ the technique of *differential scanning calorimetry* (DSC), which at least often verifies that there actually is a phase transition present. To distinguish clearly between different soft crystal phases and to identify their structures, generally extensive x-ray studies on oriented samples are necessary [1, 2]. (The latter book [2] includes an extensive section of reprinted original articles on structural investigations of all smectic phases.) If the high temperature hexatic phase is orthogonal, it is likely that also the succeeding soft crystal phase will belong to the orthogonal type. Likewise, if the high temperature phase is already tilted, also the low temperature soft crystal phase is mostly of the tilted type. But this is a rule of thumb, which by no means has to apply for all compounds. Soft crystal phases mainly exhibit mosaic textures [3–7], which all look very much alike. If the high temperature phase shows a fan-shaped texture, this feature is often retained by cooling into the soft crystal phase, although annealing will in most cases eventually lead to a slow transformation into a mosaic texture.

10.1

The Orthogonal Soft Crystal Phases

During the transition from a hexatic SmB to a soft crystal B phase, the hexagonal distribution of the molecules centers of mass is retained, and only the positional order becomes long range [8, 9]. This is a transition that is in general not readily observable by polarizing microscopy, neither for initial mosaic textures, nor for homeotropic boundary conditions (pseudo-isotropic texture). Only when cooling from a high temperature SmA phase with fan-shaped texture may the transition to either SmB or soft crystal B be recognized [4]. In the former case the texture remains unchanged (Plates 87 and 88), maybe accompanied by a very slight change in birefringence, while in the latter case transition bars may be observed. To distinguish a SmB to B transition by polarizing microscopy, very careful investigations

and miscibility studies have to be carried out [10, 11]. On the other hand, a transition that is in fact quite readily detected is that between the hexatic SmB and the soft crystal E phase. This is demonstrated by cooling from a fan-shaped SmB texture across the transition into soft crystal E, where a very pronounced striation [7], the formation of a non-equidistant arc pattern, which can also be colored, becomes visible across the fans, i. e. along the smectic layers (Plate 96, showing the same sample area as Plates 87 and 88). This arc pattern is stable and does not vanish on further cooling through the E phase, i. e. it is not related to transition bars. Also the subsequent crystallization is readily observed (Plate 97), while remains of the original fan-shaped structure and the striation bands are still visible. Plate 98 finally depicts an example of a soft crystal E sample preparation with both planar (bright) and homeotropic (dark) regions.

10.2

The Tilted Soft Crystal Phases

As pointed out above, the most commonly observed texture of soft crystal phases is that of a mosaic pattern. Within the individual grains the optic axis is oriented uniformly and homogeneously, while discontinuous direction changes of the long molecular axes are encountered advancing from grain to grain, leading to differently colored mosaic patches. An example of such a texture is shown in Plate 99 for a soft crystal G phase. The subsequent crystallization on further cooling is observed by the grain boundaries becoming more irregular and less smooth in appearance, as depicted for the same sample area in Plate 100.

We had mentioned that the transitions between different soft crystal phases are rather hard to detect by polarizing microscopy. The texture series of Plate 101 to some extent illustrates this behavior. Plate 101(a) exhibits a mosaic texture of the soft crystal G phase [6, 8, 12–16]. (Note that the letter H was initially used [12] to designate an apparently novel phase SmH, but this was later shown [13] to be equivalent to the soft crystal G phase. Sackmann [17] assigned the letter H to the low temperature phase of G.) Some slight optical irregularities are observed within the uniform and optically homogeneous areas of individual mosaic grains. These diminish as the transition into the soft crystal H phase [17, 18] is passed. The mosaic grains adopt a very smooth and regular optical appearance, as shown in Plate 101(b). Further cooling eventually leads to the crystallization of the sample, again accompanied by the formation of more irregular grain boundaries and optical impurities (Plate 101(c)), possibly caused by fracture of the layered structure due to thermal contraction.

10.3

Crystallization of Calamitic Mesogenic Compounds

At this point, we have nearly completed our virtual tour through the different liquid crystalline phases observed on cooling calamitic molecules. There are only a few points that should be mentioned with respect to the final crystallization at low temperatures. This can be accomplished in several ways, one of which we have already encountered above, when the sample crystallizes from a soft crystal phase. In this case the texture changes are generally quite subtle and the original macroscopic features, such as fans or mosaic patterns, are to a great extent retained. The material crystallizes into a three dimensionally ordered lattice of (often) different structure, while the overall morphology is retained (pseudo-morphology). This behavior can also be observed nicely for many materials on heating a mesogenic compound from its crystal phase. On the other hand, crystallization from a nematic or fluid smectic phase often proceeds via the process of nucleation and growth of so-called *spherulites*, as shown in Plate 102, with the crystal phase forming as a spherical germ, growing from the fan-shaped texture of a SmA phase. After complete crystallization a spherulite texture shows a pattern of radially arranged, elongated domains with sharp grain boundaries, as depicted in Plate 103 (not related to Plate 102). Sometimes also structures of growing crystalline needles are exhibited, as commonly observed for the direct crystallization of organic molecules from the isotropic phase, without mesogenic behavior being observed (Plate 104).

References

- [1] A. J. Leadbetter, in *Thermotropic Liquid Crystals*, G. W. Gray (ed.), John Wiley & Sons, Chichester, 1987, and references therein.
- [2] P. S. Pershan, *Structure of Liquid Crystal Phases (World Scientific Lecture Notes in Physics, vol. 23)*, World Scientific, Singapore, 1988, and references therein.
- [3] D. Demus, L. Richter, *Textures of Liquid Crystals*, Verlag Chemie, Weinheim, 1978.
- [4] G. W. Gray, J. W. Goodby, *Smectic Liquid Crystals – Textures and Structures*, Leonard Hill, Glasgow, 1984.
- [5] H. Sackmann, D. Demus, *Mol. Cryst. Liq. Cryst.*, **21**, (1973), 239.
- [6] D. Demus, S. Diele, M. Klapperstück, V. Link, H. Zschke, *Mol. Cryst. Liq. Cryst.*, **15**, (1971), 161.
- [7] D. Demus, K.-H. Kölz, H. Sackmann, *Z. Phys. Chem.*, **252**, (1973), 93.
- [8] A. J. Leadbetter, M. A. Mazid, B. A. Kelly, J. W. Goodby, G. W. Gray, *Phys. Rev. Lett.*, **43**, (1979), 630.
- [9] D. E. Moncton, R. Pindak, *Phys. Rev. Lett.*, **43**, (1979), 701.
- [10] J. W. Goodby, *Mol. Cryst. Liq. Cryst.*, **72**, (1981), 95.
- [11] G. Poeti, E. Fanelli, D. Guillon, *Mol. Cryst. Liq. Cryst. Lett.*, **82**, (1982), 107.
- [12] A. de Vries, D. L. Fishel, *Mol. Cryst. Liq. Cryst.*, **16**, (1972), 311.
- [13] L. Richter, D. Demus, H. Sackmann, *J. Phys. (Fr.)*, **37**, (1976), 41.
- [14] A.-M. Levelut, J. Doucet, M. Lambert, *J. Phys. (Fr.)*, **35**, (1974), 773.
- [15] A.-M. Levelut, *J. Phys. (Fr.)*, **37**, (1976), 51.
- [16] J. Doucet, A.-M. Levelut, *J. Phys. (Fr.)*, **38**, (1977), 1163.
- [17] H. Sackmann, *J. Phys. (Fr.)*, **40**, (1979), 5.
- [18] P. A. C. Gane, A. J. Leadbetter, P. G. Wrighton, *Mol. Cryst. Liq. Cryst.*, **66**, (1981), 247.

11

Other Liquid Crystal Phases

Owing to limitations of space, some soft crystal phases (B, J, K), whose texture appearance is basically equivalent to that discussed above, were omitted also because of our emphasis on textures of *chiral* materials. We have so far also left out some more rarely observed, but nevertheless distinct, phases, namely the cubic D phase, but also the SmQ* phase, both of which we will briefly mention below. In this last chapter of our virtual polarizing microscopy tour through the liquid crystalline state of matter, we will further encounter a number of mesogenic phases formed by molecules that are not calamitic, but rather disk-shaped, the *discotic phases*, or bow-shaped, the so-called “*banana*” phases. But let us first remain with the rod-like, calamitic mesogens.

11.1

The Cubic D (CubD) Phase

The cubic D phases [1–5] should briefly be mentioned, because of their unique optical appearance among the various liquid crystalline phases discussed throughout this text. A detailed and comprehensive overview of various mesogens exhibiting the cubic D phase has been given in Ref. [6]. On numerous occasions we have stressed the anisotropic properties of liquid crystals and their resultant birefringence, leading to all the different texture images shown so far. The CubD phases are distinctly different from all of these phases. They are phases with a macroscopic cubic structure, whose unit cell consists of several hundred molecules. It often manifests itself between the fluid SmA and SmC phases of some mesogens or mesogenic mixtures. Its structure is most likely of a nature of micellar aggregates [5], similar to the cubic phase of lyotropic liquid crystals. But cubic D phases have also been observed between the isotropic and the SmC phase or occurring below the SmC phase. The fact that CubD is a cubic phase makes it optically isotropic, just like cubic crystal phases are optically isotropic, and thus it shows no birefringence and appears black between crossed polarizers. A variety of somewhat unconventional mesogens, including amphiphilic molecules, swallow-tailed or double swallow-tailed compounds, have been shown to exhibit cubic D phases [6]. Phases of different structures have been reported, while those of space groups

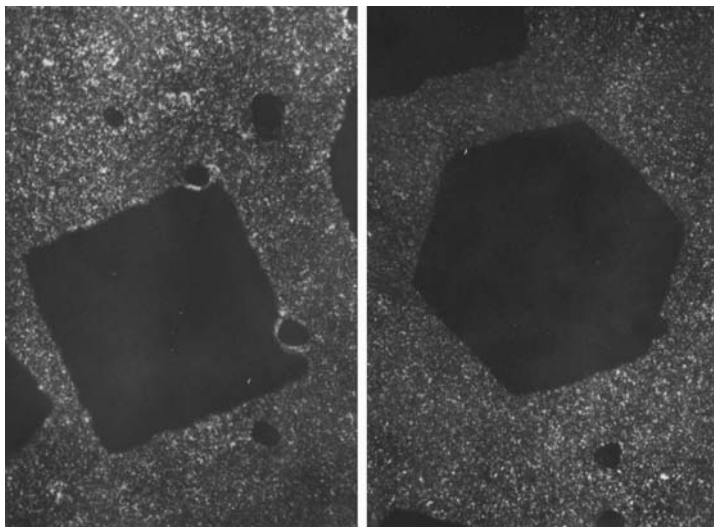


Fig. 11.1. Textures of the cubic D phase (black) growing from the background of the SmC phase (disordered, bright). Depending on the orientation of the cube with respect to the substrate plane, a square (side of the cube parallel to the substrate, left) or a hexagon (tip of the cube at the substrate, right) of the growing phase is observed. (Texture images are taken from: G. Kunicke, Diploma Thesis, Halle, 1964. Courtesy of G. Pelzl.)

$\text{Ia}3\text{d}$ and $\text{Im}3\text{m}$ seem to be most frequently encountered. Two typical textures of a cubic D “single crystal” growing from a disordered SmC phase on heating are depicted in Fig. 11.1, unambiguously indicating the cubic symmetry of this liquid crystalline phase.

11.2 The SmQ^* Phase

The appearance of the SmQ^* phase [7–11] is observed quite rarely and is still rather enigmatic. It was first reported by Levelut et al. in 1983 [7] and is only observed for chiral materials, apparently appearing between the isotropic melt and the antiferroelectric SmC_A^* phase. The SmQ^* phase shows a grayish, mosaic-like texture, which is in some respects quite similar to the platelet texture of Blue Phases (see also the texture photograph in Ref. [11]), although missing the phenomenon of selective reflection. The phase has been shown to exhibit smectic-like order, and a typical texture of the SmQ^* phase, taken on the originally reported compound, is presented in Plate 105.

11.3

Discotic Liquid Crystals

By only scratching the surface of this undoubtedly very well established field of liquid crystal research, and furthermore by placing discotic phases under the heading of “other liquid crystal phases”, I surely run the risk of criticism from those colleagues working in this field. Nevertheless, I presume that many of us who are active in the field of liquid crystal research have actually merely made casual contact with discotic materials in their own laboratory. Also, since a strong emphasis of this text lies on chiral phases of calamitic mesogens, I have decided to place these materials into this section, admittedly not paying adequate tribute to the academic as well as applicational potential of these materials.

Discotic liquid crystals are composed of disk-like mesogens, an example having been shown in Fig. 1.2. It was first demonstrated by Chandrasekhar et al. [12] that not only rod-like, but also disk-like molecules are capable of exhibiting liquid crystalline properties, and we may refer to the earlier review articles [13, 14]. For a detailed treatment concerning the structure, properties, and applications of discotic phases, the respective chapters in the *Handbook of Liquid Crystals* are recommended for further reading. For a general introduction to the topic, the contribution by Chandrasekhar [15] to that volume is surely most adequate.

Discotic mesogens may show nematic and/or columnar phases, of which the latter can exhibit order or disorder within the columns (referring to the stacking of disks), and which can in addition be tilted (Fig. 11.2). A schematic overview of the possible structures of columnar discotic liquid crystal phases is shown in Fig. 11.3 as a top view onto the columns, with ellipses indicating disks being tilted with respect to the column axis (after Ref. [16]). Discotic nematic phases are named

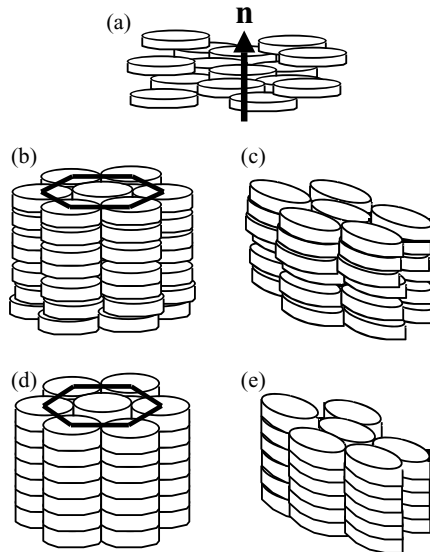


Fig. 11.2. Schematic overview of the structure of different discotic mesophases: (a) nematic discotic phase, (b) disordered columnar, (c) tilted disordered columnar, (d) ordered columnar, and (e) tilted columnar ordered phase.

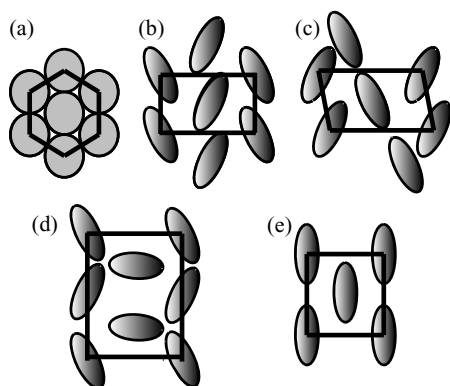


Fig. 11.3. Schematic illustration of discotic phases as a top view onto the columns: (a) hexagonal, (b) rectangular, (c) oblique, and (d,e) rectangular.

N_D or N_D^* , denoting achiral or chiral molecular constituent molecules, respectively. Subscripts following the symbol “D” (not to be confused with the cubic D phase), indicating discotic columnar phases of different structure, seem to have been generally accepted in denoting different (discotic) phases: “h” for a hexagonal lattice of columns, “r” for a rectangular lattice of columns, “d” for a disordered stacking of molecules within a column, “o” for the respective ordered stacking of molecules, and “t” for tilted columns. This makes D_{hd} a columnar hexagonal disordered, D_{rd} a columnar rectangular disordered, D_{ho} a columnar hexagonal ordered, and D_t a columnar tilted phase (see also Figs. 11.2 and 11.3).

The nematic phase of discotic mesogens N_D shows textures that are equivalent to those of calamitic molecules, namely the above encountered *Schlieren texture*, an example of which can be found in Ref. [17]. Columnar phases forming from the isotropic melt often exhibit dendritic-like growth aggregates as shown in Plate 106, sometimes directly reflecting the generally sixfold symmetry of the constituent molecules [18, 19]. Textures generally appear to be very much alike for different columnar discotic phases, and a typical image of a texture of a columnar phase is shown in Plate 107.

Despite this admittedly very short excursion into the field of discotic liquid crystals, one should not forget that these materials may also exhibit the respective chiral phases, an overview of whose properties can be found in Ref. [20] and in an interesting paper by Krüerke et al. [21], exploring the borderlines between thermotropic and lyotropic liquid crystals.

11.4

Bent-core Mesogens, “Banana” Liquid Crystal Phases

The so-called “banana” phases, formed by bent-core mesogens, i. e. bow-shaped molecules, are so far the last class of liquid crystal materials to have been added to the zoo of mesogenic phases. Banana phases were first reported by Niori and coworkers [22, 23] to exhibit unusual properties, distinctly different from those

of calamitic materials. The most striking phenomenon of banana phases is the occurrence of *polar* order and *chiral* properties from *achiral* molecules. We may thus observe macroscopic chirality, for example ferro- and antiferroelectric behavior, second harmonic generation, and optical activity, although the constituent molecules of the phase are in fact *achiral* [22]. This behavior is attributed to steric packing effects of the bow-shaped molecules [24]. The banana phases show at least one dimensional positional order, i. e. smectic-like layering, but are not continuously miscible with any of the known calamitic smectic phases. Accordingly, they represent a novel class of liquid crystalline materials. It is at this point too early to designate a reasonable scheme of nomenclature for the banana phases, and here we will thus follow the preliminary suggestions agreed to during the first “Banana Workshop”, held in Berlin in 1997, successively naming the phases B_1 through B_7 . It is likely that this scheme of nomenclature may be revised in the future. In any case, the banana phases should not be confused with the soft crystal B phase, and their index number, as used here, by no means indicates increasing order for larger integers. In lack of any other agreement accepted so far, we follow the same nomenclature, which was also adopted throughout the first comprehensive survey on these phases [25] with respect to molecular constitution, structure, and properties, to which we also refer for further references.

According to preliminary x-ray investigations [25, 26] the B_1 phase seems to exhibit a fluid smectic structure. The general appearance observed is that of a mosaic texture as shown in Plate 108. When cooling from the isotropic melt, often dendritic growth of the B_1 phase is observed (Plate 109(a)), with dendrites coalescing to form a mosaic texture (Plate 109(b)) at somewhat lower temperatures. The B_1 phase has been observed as the high temperature phase to B_2 [27], but also as the low temperature phase to B_6 , and it was noted in Ref. [25] that in the latter case a B_6 Schlieren texture transforms into a fan-shaped B_1 texture, while no distinct texture changes can be observed if the high temperature B_6 phase exhibits a fan-shaped texture itself.

The B_2 phase is probably the most extensively studied of the banana phases to date. It is a fluid smectic-like phase [28–30] and generally exhibits antiferroelectric switching behavior [24, 28, 31], i. e. double peaks in the polarization reversal current per half period of applied electric field (analogous to Fig. 8.2), although possible ferroelectric behavior cannot be excluded. The B_2 phase can occur in various appearances, including focal-conic-like textures, as shown in Plate 110, but also fan-like textures with a striation across the fans (Plate 111(a), bottom left). For textures under electric field application, we refer to Refs. [22, 24, 28]. Of particular interest are sample regions with domains of smectic layers perpendicular to the substrate plane and arranged in a circular fashion. In these areas a rotation of the extinction cross can be observed on changing the polarity of an applied electric field [24, 30], as also depicted in Plate 112. This switching process is not accompanied by a net electrooptic effect, as is commonly observed for respective calamitic systems. It is interesting to note that the growth process of the B_2 phase from the isotropic melt, as depicted in Fig. 11.4, is distinctly different from that of calamitic phases. The latter grow in regular geometric forms, such as spherical and elongated germs (see for example Plate 23 for N^* and Plate 60 for SmA), while the banana phases exhibit intrinsic fractal

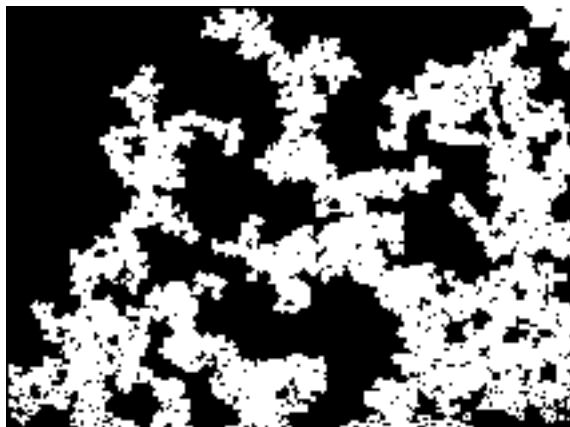


Fig. 11.4. Image of a B_2 phase (white) growing from the isotropic melt (black). The complex, irregular aggregates exhibit a fractal dimension in the order of $D = 1.9$, possibly related to a percolation growth process.

growth structures [32, 33], a behavior that is generally quite common to soft matter materials. This is probably also the reason why these materials cannot be uniformly aligned by any of the commonly employed substrate treatment techniques.

Following the x-ray investigations of Ref. [28], the B_3 phase [34, 35] seems to be a higher ordered smectic or soft crystal phase. It may be observed below the B_2 phase, as shown in Plates 111(a) for B_2 and (b) for B_3 . The striated, only poorly developed, fans of B_2 become more pronounced at the transition and indications of the formation of focal conics can be observed. The structure and nature of this phase still seem to be quite unclear.

The B_4 phase can easily be identified by a transition to a texture with only weak birefringence, but an intensive blue color [36], as shown in Plate 113. In earlier literature this phase was also referred to as SmBlue, a designation that now seems to be quite unfortunate, as there is no connection to the recently reported “smectic Blue Phases” (see Chapter 4, Plate 7). The B_4 phase has so far been observed to form below the B_2 or B_3 phase and seems to belong to the class of soft crystal phases. It exhibits second harmonic generation [37–39], thus indicating a polar structure, and different domains show optical activity of opposite sign [31].

The B_5 phase is only rarely observed, forming from B_2 on cooling [29]. Texture changes are apparently very subtle, if observable at all. Also the electrooptic behavior of B_5 seems to be analogous to that of B_2 , only exhibiting a much increased viscosity [25].

In contrast to the somewhat enigmatic textures of the other banana phases, the B_6 phase exhibits the familiar fan-shaped texture (Plate 114), which we have already encountered above, especially for the SmA phase. According to x-ray investigations, B_6 is an intercalated tilted smectic phase lacking in-plane order [25].

Finally, the B_7 phase of bent-core molecules is unmatched in complexity of its textural appearance. This, in turn, makes it *seemingly* easy to identify. On cooling from the isotropic melt, spiral and double spiral lancets quickly grow [40,41], as shown in Plate 115. These spirals can be left- or right-handed and are generally observed in equal numbers throughout the sample. They clearly indicate a helical

superstructure, just like the circular or sometimes elongated domains, which grow in a spiral fashion and exhibit an equidistant line pattern (see also Plate 116). The reason for this helicity most likely lies in the steric packing of the molecules, which gives the individual smectic layers a polar order. This is also indicated by the ability to switch the B_7 phase, similarly to B_2 only at larger applied electric field amplitudes. Besides sample areas with a pronounced line pattern, sometimes also exhibiting a two dimensional structure, we can also observe highly birefringent domains that are very smooth in appearance, without any internal structure (Plates 116 (top left) and 117 (middle)). These are attributed to racemic regions of the sample [25]. The appearance of spiral and double spiral germs is generally attributed to be a typical feature of the B_7 phase. Recently, however, materials have been studied that clearly show spiral growth [42, 43], but may nevertheless differ from the B_7 phase, exhibiting either a novel phase or a different variant of B_2 [44]. To clarify this behavior, further x-ray studies on (admittedly hard to obtain) monodomain samples have to be carried out and are awaited.

Although the investigations of banana phases have been one of the central topics of liquid crystal research in the past few years, it seems to be very likely that this section will have to be rewritten and revised in the future, possibly due to yet more and different phases to be discovered, but maybe also due to possible simplifications in their characterization scheme and possible equivalence to previously reported phases. The study of banana phases is at this time a still evolving field of research, and their texture appearance as presented here should be seen as just a present day snapshot.

We have now finally concluded our tour through the vast variety of appearances of liquid crystals, this fascinating state of matter on the borderline between order and disorder. I sincerely hope that the above excursion into polarizing microscopic textures of mesogenic phases has to some extent been educational enough to enable students and visitors to the field to identify the phases they observe. But at the same time, I also hope to have been able to remind more senior colleagues about the beauty and aesthetic appeal of liquid crystals, waiting in their laboratories to be looked at, and sometimes even looking back at us (Fig. 11.5). Maybe this last figure exemplifies why some physicists refer to liquid crystals as being “funny fluids”.

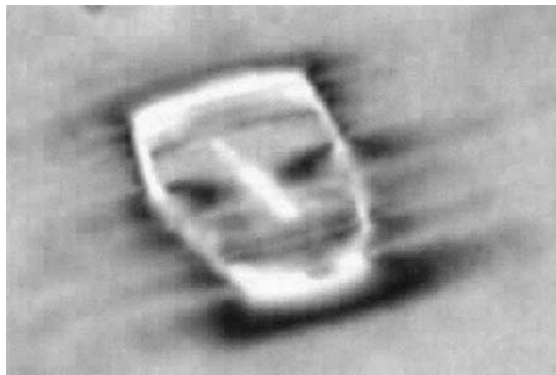


Fig. 11.5. Texture of a nematic liquid crystal, whose defect lines resemble a face, smiling at you. Application of an electric field of moderate amplitude pronounces the smile. (Image was taken by D. Green. Courtesy of H. F. Gleeson.)

References

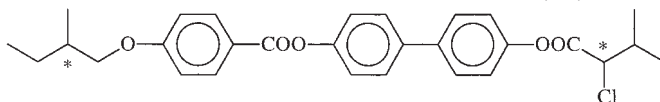
- [1] G. W. Gray, B. Jones, F. Marson, *J. Chem. Soc.*, **1**, (1957), 393.
- [2] D. Demus, G. Kunicke, J. Neelsen, H. Sackmann, *Z. Naturforsch.*, **23a**, (1968), 84.
- [3] S. Diele, P. Brand, H. Sackmann, *Mol. Cryst. Liq. Cryst.*, **17**, (1972), 163.
- [4] A. Tardieu, J. Billard, *J. Phys., Colloq.*, **37**, (1976), C3-79.
- [5] G. Etherington, A. J. Leadbetter, X. J. Wang, G. W. Gray, A. Tajbakhsh, *Liq. Cryst.*, **1**, (1986), 209.
- [6] S. Diele, P. Göring, *Handbook of Liquid Crystals*, D. Demus, J. Goodby, G. W. Gray, H.-W. Spiess, V. Vill (eds.), Wiley-VCH, Weinheim, 1998, vol. 2B, ch. XIII, pp. 887–900.
- [7] A. M. Levelut, C. Germain, P. Keller, L. Liebert, J. Billard, *J. Phys. (Fr.)*, **44**, (1983), 623.
- [8] D. Bennemann, G. Heppke, A. M. Levelut, D. Löttsch, *Mol. Cryst. Liq. Cryst.*, **260**, (1995), 351.
- [9] A. M. Levelut, E. Hallouin, D. Bennemann, G. Heppke, D. Löttsch, *J. Phys. II*, **7**, (1997), 981.
- [10] A. M. Levelut, D. Bennemann, G. Heppke, D. Löttsch, *Mol. Cryst. Liq. Cryst.*, **299**, (1997), 433.
- [11] J. G. Meier, P. Rudquist, A. S. Petrenko, J. W. Goodby, S. T. Lagerwall, *Liq. Cryst.*, **29**, (2002), 179.
- [12] S. Chandrasekhar, B. K. Sadashiva, K. A. Suresh, *Pramana*, **9**, (1977), 471.
- [13] H. P. Hinov, *Mol. Cryst. Liq. Cryst.*, **136**, (1986), 221, and references therein.
- [14] S. Chandrasekhar, G. S. Ranganath, *Rep. Prog. Phys.*, **53**, (1990), 57, and references therein.
- [15] S. Chandrasekhar, *Handbook of Liquid Crystals*, D. Demus, J. Goodby, G. W. Gray, H.-W. Spiess, V. Vill (eds.), Wiley-VCH, Weinheim, 1998, vol. 2B, ch. VIII, pp. 749–780.
- [16] A. M. Levelut, *J. Chim. Phys.*, **80**, (1983), 149.
- [17] C. Destrade, M. C. Bernaud, H. Gasparoux, A. M. Levelut, N. H. Tinh, in S. Chandrasekhar reproduced, *Liquid Crystals*, 2nd edn., Cambridge University Press, Cambridge, 1992, p. 412.
- [18] Y. Bouligand, *J. Phys. (Fr.)*, **41**, (1980), 1297.
- [19] Y. Bouligand, *J. Phys. (Fr.)*, **41**, (1980), 1307.
- [20] H. Bock, in *Chirality in Liquid Crystals*, H.-S. Kitzerow, Ch. Bahr (eds.), Springer-Verlag, Berlin, 2001, ch. 11.
- [21] D. Krüerke, P. Rudquist, S. T. Lagerwall, H. Sawade, G. Heppke, *Ferroelectrics*, **243**, (2000), 207.
- [22] T. Niori, T. Sekine, J. Watanabe, T. Furukawa, H. Takezoe, *J. Mater. Chem.*, **6**, (1996), 1231.
- [23] T. Sekine, T. Niori, M. Sone, J. Watanabe, S. W. Choi, Y. Takanishi, H. Takezoe, *Jpn. J. Appl. Phys.*, **36**, (1997), 6455.
- [24] D. R. Link, G. Natale, R. Shao, J. E. MacLennan, N. A. Clark, E. Körblova, D. M. Walba, *Science*, **278**, (1997), 1924.
- [25] G. Pelzl, S. Diele, W. Weissflog, *Adv. Mater.*, **11**, (1999), 707.
- [26] J. Watanabe, T. Niori, T. Sekine, H. Takezoe, *Jpn. J. Appl. Phys. Lett.*, **37**, (1998), L139.

- [27] D. Shen, C. Tschierske, S. Diele, I. Wirth, *Chem. Commun.*, issue 23, (1998), 2573.
- [28] W. Weissflog, C. Lischka, I. Benné, T. Scharf, G. Pelzl, S. Diele, H. Kruth, *Proc. SPIE: Int. Soc. Opt. Eng.*, **3319**, (1998), 14.
- [29] S. Diele, S. Grande, H. Kruth, C. Lischka, G. Pelzl, W. Weissflog, I. Wirth, *Ferroelectrics*, **212**, (1998), 169.
- [30] G. Pelzl, S. Diele, S. Grande, A. Jákli, C. Lischka, H. Kresse, H. Schmalzfuss, I. Wirth, W. Weissflog, *Liq. Cryst.*, **26**, (1999), 401.
- [31] G. Heppke, D. Krüerke, C. Löhning, D. Löttsch, S. Rauch, N. K. Sharma, presented at the *Freiburger Arbeitstagung Flüssigkristalle*, Freiburg, 1997, poster P70.
- [32] I. Dierking, *CHEMPHYCHEM*, **2**, (2001), 59.
- [33] I. Dierking, *J. Phys.: Condens. Matter*, **13**, (2001), 1353.
- [34] T. Sekine, Y. Takanishi, T. Niori, J. Watanabe, H. Takezoe, *Jpn. J. Appl. Phys. Lett.*, **36**, (1997), L1201.
- [35] T. Niori, T. Sekine, J. Watanabe, T. Furukawa, H. Takezoe, *Mol. Cryst. Liq. Cryst.*, **301**, (1997), 337.
- [36] G. Heppke, D. Moro, *Science*, **279**, (1998), 1872.
- [37] S.-W. Choi, Y. Kinoshita, B. Park, H. Takezoe, T. Niori, J. Watanabe, *Jpn. J. Appl. Phys.*, **37**, (1998), 3408.
- [38] F. Kentischer, R. Macdonald, P. Warnick, G. Heppke, *Liq. Cryst.*, **25**, (1998), 341.
- [39] R. Macdonald, F. Kentischer, P. Warnick, G. Heppke, *Phys. Rev. Lett.*, **81**, (1998), 4408.
- [40] G. Pelzl, S. Diele, A. Jákli, C. Lischka, I. Wirth, W. Weissflog, *Liq. Cryst.*, **26**, (1999), 135.
- [41] C. K. Lee, L.-C. Chien, *Liq. Cryst.*, **26**, (1998), 609.
- [42] G. Heppke, D. D. Parghi, H. Sawade, *Ferroelectrics*, **243**, (2000), 269.
- [43] I. Dierking, H. Sawade, G. Heppke, *Liq. Cryst.*, **28**, (2001), 1767.
- [44] G. Pelzl, S. Diele, W. Weissflog, private communication

Appendix A: Structural formulas of some of the compounds used in the texture studies

A.1 M96

The contact preparation of Plate 1 was prepared with (s/r)-M96



at the bottom left in contact with TBAA4



at the top right at temperatures (a) $t = 180\text{ }^{\circ}\text{C}$, (b) $t = 130\text{ }^{\circ}\text{C}$, (c) $t = 120\text{ }^{\circ}\text{C}$, (d) $t = 110\text{ }^{\circ}\text{C}$, (e) $t = 100\text{ }^{\circ}\text{C}$, and (f) $t = 80\text{ }^{\circ}\text{C}$.

Plates 6, 19, 22, and 70 were taken for the (s/r)-configured compound M96.

A.2 MBBA

Plates 2 and 9–12 were obtained with MBBA (4-butyl-n-(4-methoxy-benzylidene)-aniline)

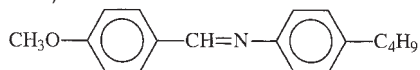
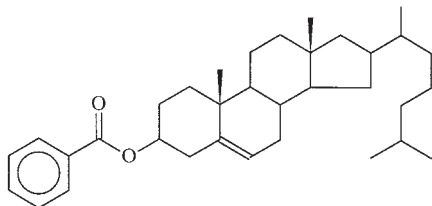


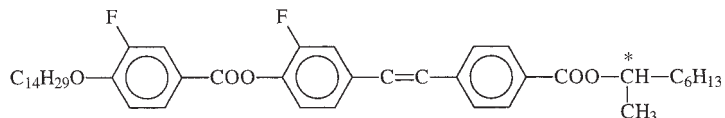
Plate 4 was taken on compound M96 in the (racemic/s) configuration (see Section A.1).

The single crystal BP texture of Plate 5 was taken with a mixture of 70 % 8OBE (4-n-octyloxyphenyl-4'-n-octyloxybenzoate) with 30 % cholesteryl benzoate



A.3 14BTMHC

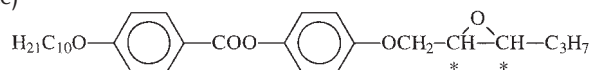
The texture of Plate 7 was obtained from the compound 14BTMHC



Plates 14 and 15 resulted from a commercial room temperature nematic liquid crystal mixture (Merck).

A.4 EPHDBPE (W46)

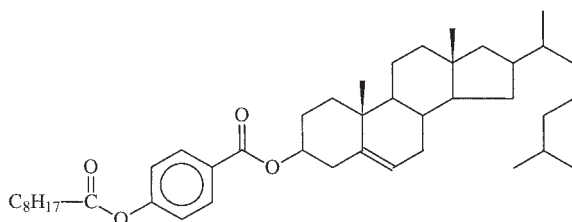
The compound EPHDBPE (4-[(s/s)-2,3-epoxyhexyloxy]-phenyl-4-(decyloxy)-benzoate)



is shown in Plates 16, 18, 20, 25, 29, 30, 77, and 80.

A.5 Cholesteryl pelargonate

Textures of cholesteryl pelargonate

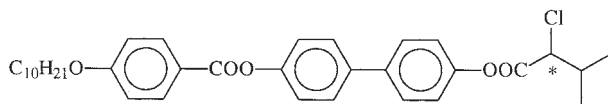


are shown in Plates 17, 38, 39, 47, and 102.

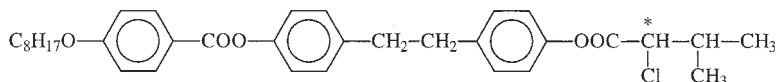
Plates 23, 24, and 64 were taken with the commercial ferroelectric liquid crystal mixture ZLI-5014-100, formerly available from Merck.

A.6 M10

The texture with simultaneous exhibition of planar and fingerprint regions of the N^* phase was taken on M10

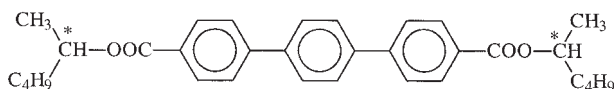
**A.7 D8**

The compound abbreviated as D8

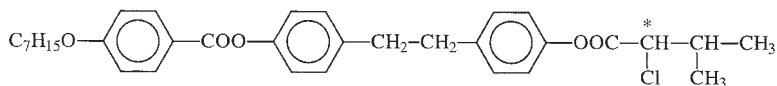


exhibits a great wealth of mesogenic phases. Its textures are shown in Plates 36, 40–43, 49–52, 61, 75, 76, and 91–95.

Plates 37, 57, and 58 show textures of 95 % D8 doped with 5 % of a highly chiral dopant C4

**A.8 D7**

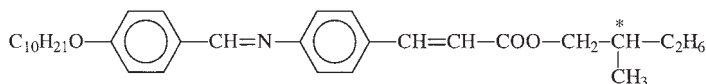
D7



is a homolog of the above mentioned compound D8 (Section A.7). Plates 53–56 depict some of its textures.

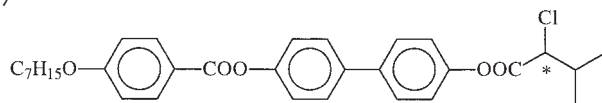
A.9 DOBAMBC

The growth of smectic bâtonnets from the isotropic melt is shown in Plate 60 for the classic ferroelectric liquid crystal DOBAMBC (D-2-methylbutyl-4-(4-n-decyloxy-benzylideneamino)-cinnamate)



A.10 M7

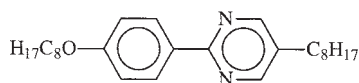
M7



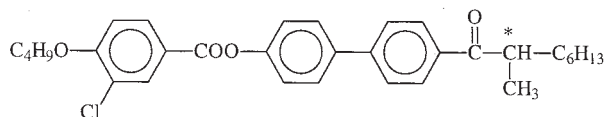
is a shorter chain homolog of the above mentioned compound M10 (Section A.6). Some of its textures are depicted in Plates 71 and 74.

A.11 C1

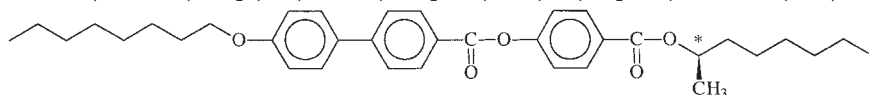
Plate 72 shows the SmC domain texture of the achiral compound C1

**A.12**

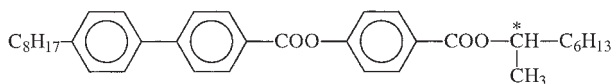
The spiral layer rotational instabilities of Plate 81 were observed on

**A.13 MHPOBC**

Plates 82, 85, and 86 were obtained for the classic antiferroelectric liquid crystal MHPOBC (4-(1-methyl-heptyloxy-carbonyl)-4'-phenyl-octyloxy-biphenyl-4-carboxylate)

**A.14 MHPBC**

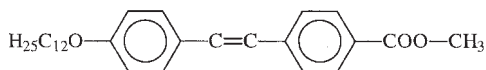
MHPBC ((r)4-(1-methylheptyloxy-carbonyl)phenyl-4'-octyl-biphenyl-4-carboxylate) is a compound very similar to MHPOBC (see Section A.13)



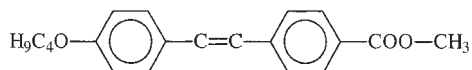
some of the textures of its smectic C* subphases are depicted in Plates 83 and 84.

A.15 12OStCOOMe

The texture series of Plates 87, 88, 96, 97, and 98, involving orthogonal phases with varying degree of order, was taken on the achiral compound 12 OStCOOMe

**A.16 4OStCOOMe**

Plates 89 and 90 were obtained for the direct Iso-SmB transition of 4OStCOOMe

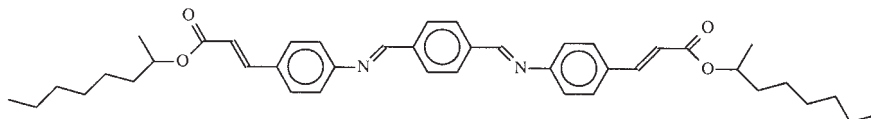


a short chain homologue of 12OStCOOMe (see Section A.15).

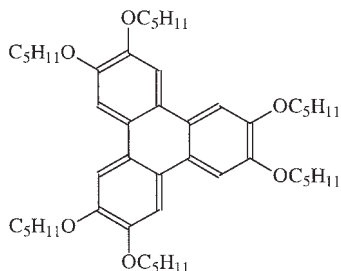
Plates 99 and 100 were taken for the compound M96 (see Section A.1) in (racemic/s)-configuration.

A.17 MHTAC

The texture of the SmQ* phase shown in Plate 105 was taken on the originally reported material MHTAC (1-methylheptyl-terephthalidene-bis-aminocinnamate)

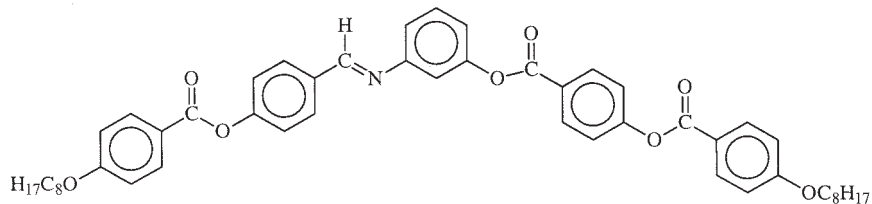
**A.18 HAT**

The discotic textures of Plates 106 and 107 were taken for a common discotic mesogen, HAT (hexapentyloxytriphenylene)

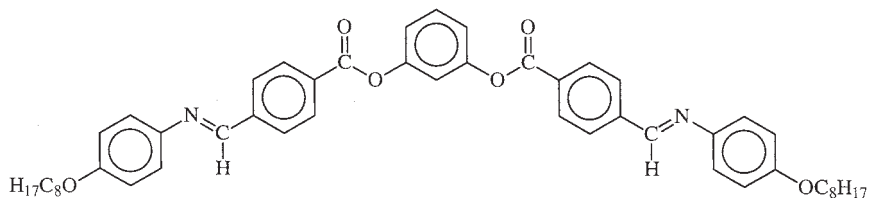


A.19 "761"

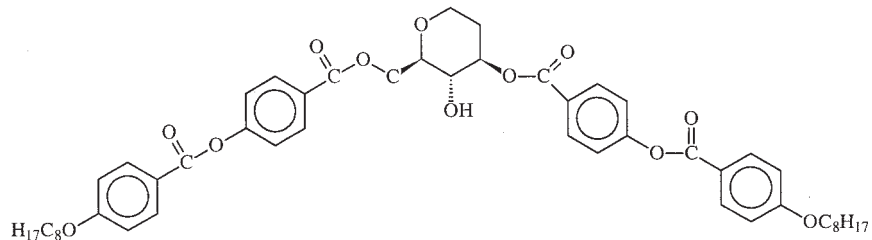
Textures of the B₁ banana phase depicted in Plates 108 and 109 were taken on compound "761"

**A.20 "700"**

Textures of the banana phases B₂, B₃, and B₄, which are shown in Plates 110, 111, and 113, were obtained from compound "700"

**A.21 GU-1**

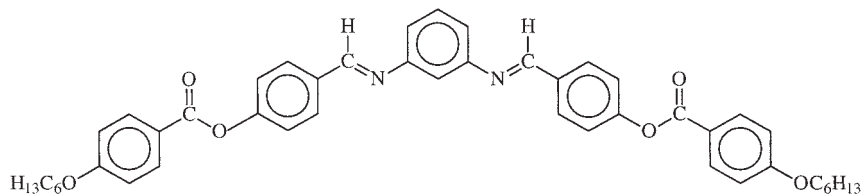
The (chiral) banana mesogene GU-1



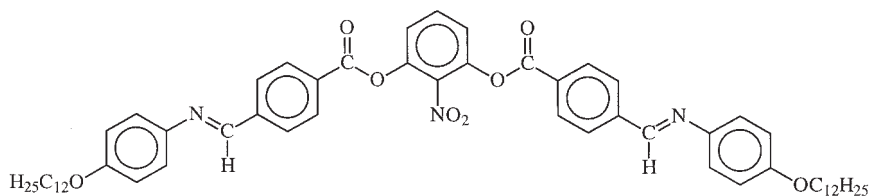
for which the switching of the Maltese cross is demonstrated, is shown in Plate 112.

A.22 “764”

The texture photograph of the B₆ banana phase of Plate 114 was taken on compound “764”

**A.23 BPHASE7**

The banana B₇ phase textures depicted in Plates 115–117 were obtained from the mesogen BPHASE 7



Appendix B: Summary of the most commonly observed natural textures of different liquid crystal phases (numbers indicate respective Plates)

B.1 Calamitic mesogens

BPI*	platelet texture	5, 6
BPII*	platelet texture	4
BPIII*	amorphous texture	3
SmQ*	grayish platelet texture	105
N	Schlieren texture	8–12
	marble texture	15
	thread-like texture	13
	pseudo-isotropic texture	
N*	oily streaks texture	16–18, 40
	Grandjean texture	22–29, 35
	fingerprint texture	21, 30–32, 35
	fan-like texture	19, 20
TGBA*	blurred oily streaks texture	37
	Grandjean texture	43–45
	filament texture	46–48, 50
	fingerprint texture	41, 48, 49
	blurred fan-shaped texture	36, 38
TGBC*	Grandjean texture	
	square grid texture	57–59
TGBC _A *	Grandjean texture	

SmA/SmA*	fan-shaped texture	39, 42, 61, 68, 75, 82(a), 83(a), 87, 91(a)
	homogeneous texture	64
	focal conic texture	62
	polygonal texture	63
SmC _α *	fan-shaped texture	82(b), 83(b)
SmC	broken fan-shaped texture	69
	domain texture	72
	focal conic texture	70
	Schlieren texture	71
SmC*	fingerprint texture	73, 76, 77
	broken fan-shaped texture	76, 91(b)
	domain texture	78
	Schlieren texture	
SmC _{1/3} *	fan-shaped texture	84(b), 85(b), 86(a)
	Schlieren-like texture	86(a)
SmC _{1/4} *	fan-shaped texture	
	Schlieren-like texture	
SmC _A *	fan-shaped texture with striations	82(e)
	pseudo-isotropic texture	86(b)
SmB/SmB*	fan-shaped texture	88
	mosaic texture	89
	pseudo-isotropic texture	
	dendritic growth	90
	Schlieren texture	
SmI	broken fan-shaped texture	
	Schlieren texture	
	mosaic texture	

SmI*	broken fan-shaped texture	91(c)
	remains of fingerprints	91(c)
	Schlieren texture	93(c)
	mosaic texture	
SmF	broken fan-shaped texture	
	Schlieren-like texture	
	mosaic texture	
SmF*	broken fan-shaped texture	91(d)
	Schlieren-like texture	
	mosaic texture	93(d)
B/B*	fan-shaped texture	88
	mosaic texture	89
	dendritic growth	90
J/J*	mosaic texture	
G/G*	mosaic texture	99, 101(a)
E/E*	fan-shaped texture with striations	96
	pseudo-isotropic texture	98
	mosaic texture	
K/K*	mosaic texture	
H/H*	mosaic texture	101(b)
CubD	pseudo-isotropic texture	Fig. 11.1

B.2 Discotic mesogens

N_D	Schlieren texture	
columnar	pseudo focal conic, fan-like texture	107
	dendritic growth	106

B.3 Bent-core mesogens

B ₁	mosaic texture	108, 109(b)
	dendritic growth	109(a)
B ₂	focal-conic-like texture	110
	fan-like texture with striations	111(a)
	fractal growth aggregates	Fig. 11.4
	quite often disordered texture appearance	
B ₃	fan-like texture	111(b)
	quite often disordered texture appearance	
B ₄	bluish domain texture	113
B ₅	often quite disordered texture appearance	
B ₆	fan-shaped texture	114
B ₇	growth of single and double spirals	115
	domain texture with line patterns	116, 117
	two-dimensional patterns (chiral domains)	116, 117
	domain texture without structure (achiral domains)	116, 117

Color Plates

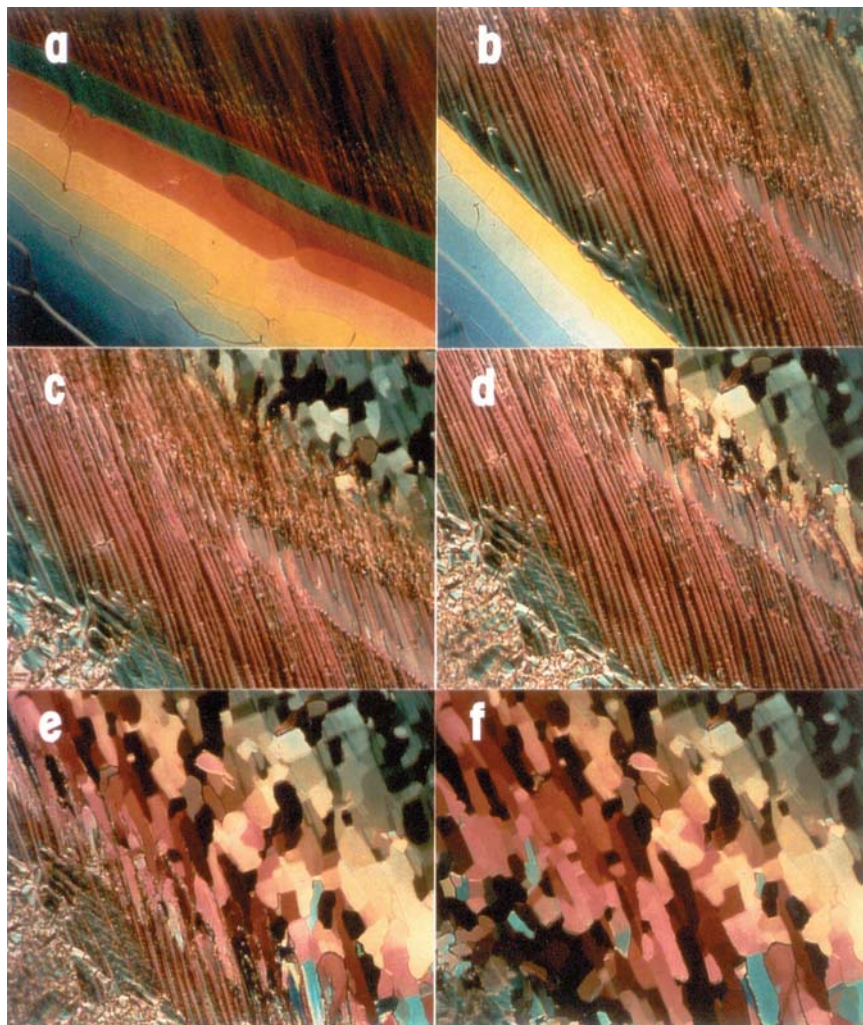


Plate 1. Demonstration of the miscibility rule to identify a higher ordered phase by means of a contact preparation of the reference compound TBAA4 (top right) and a (chiral) compound to be identified (bottom left). Textures (a)–(f) across the contact region were taken on cooling. (a) The phase boundary between SmA (top) and N* (bottom) is clearly visible. (b) On cooling, this boundary shifts to higher concentrations of the unidentified compound until (c) several phase boundaries are detected with (d)

the higher ordered phase coming in, observable by a characteristic mosaic texture. In (e), still at temperatures above the phase to be identified, there is still a clear phase boundary visible.

Photograph (f) shows the contact preparation at a temperature where both phases are in the region of their higher ordered phase, with no phase boundary being visible. In this case we can conclude that the higher ordered phase of the unidentified compound is the same as that of TBAA4, a SmG^(*) phase.

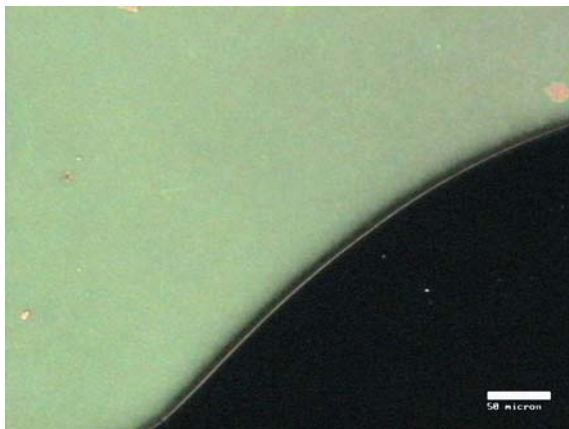


Plate 2. Demonstration of flow induced planar orientation (top left) on a substrate with homeotropic boundary conditions, prepared by deposition of a Langmuir–Blodgett film. Only after considerable time has elapsed do homeotropic domains nucleate and grow (bottom right). (Courtesy of V.S. U. Fazio.)

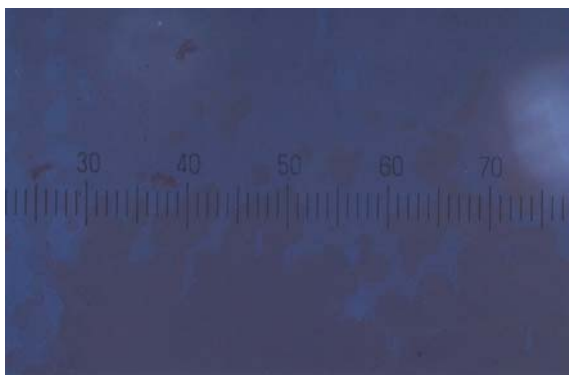


Plate 3. Texture photograph of the amorphous BP III* phase.

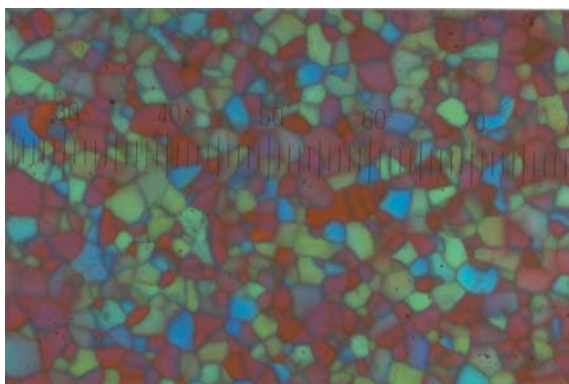
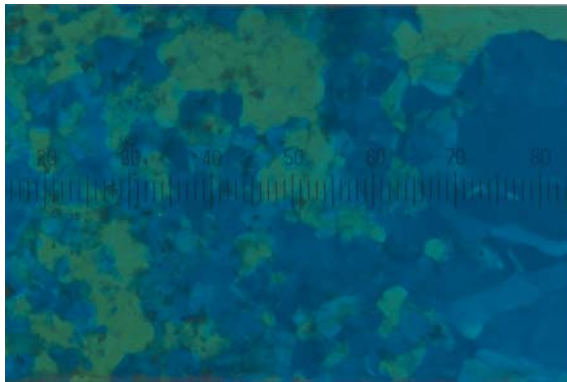
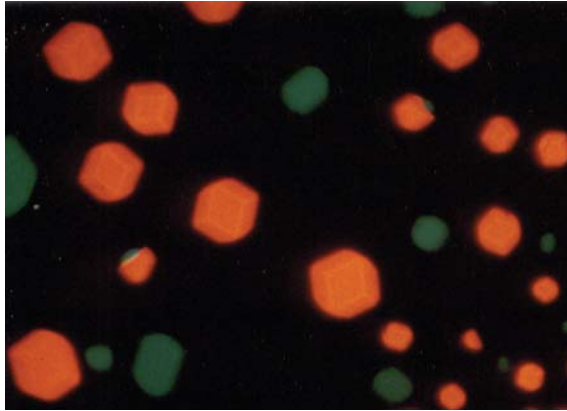
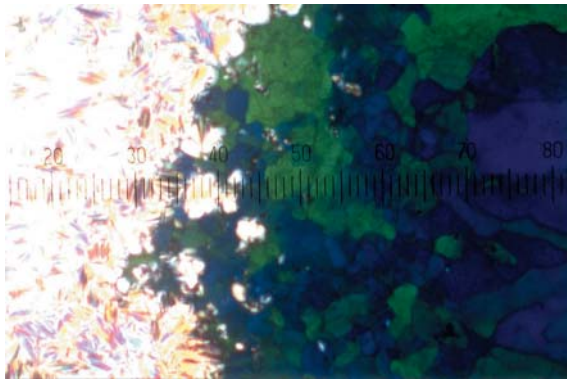


Plate 4. Platelet texture of a cubic Blue Phase. The different colors observed correspond to different lattice planes.

Plate 5. Texture with three dimensional single BPI* crystals (red) growing from the isotropic melt (black). (Courtesy of H. Stegemeyer, reproduced by permission of Taylor & Francis, H. Stegemeyer et al., *Liq. Cryst.*, **1**, (1986), 3 (<http://www.tandf.co.uk/journals>).)



A



B

Plate 6. (a) Platelet texture of a cubic BPI* phase and (b) the cholesteric phase (left) growing into BPI* (right) at slightly lower temperature.



Plate 7. Typical texture of a smectic blue phase. (Courtesy of E. Grelet, B. Pansu, M. H. Li and H. T. Nguyen.)

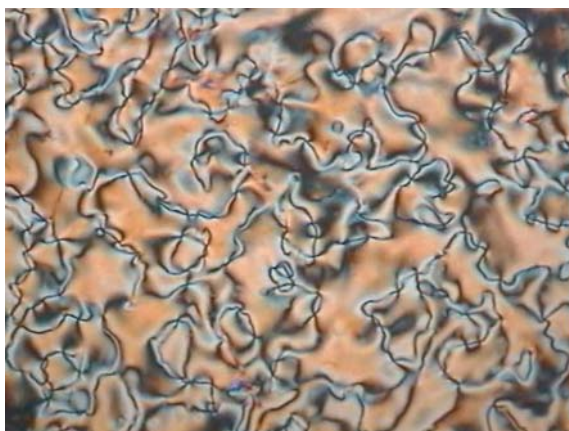


Plate 8. Schlieren texture of a nematic phase under planar anchoring conditions, at low magnification.

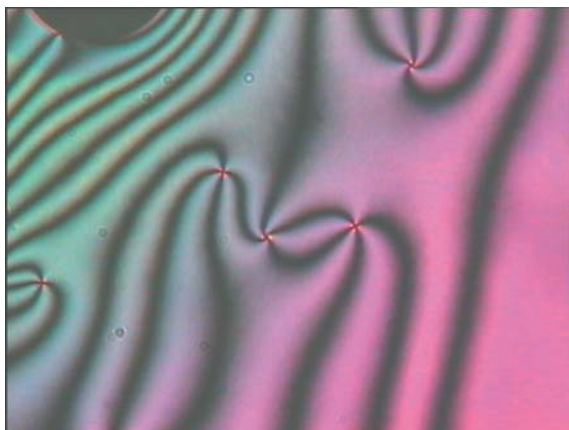


Plate 9. Schlieren texture of a nematic phase under planar anchoring conditions, at higher magnification. Note that the curved brushes converge into singular point defects and that brushes connect different defects, which have the same strength but opposite sign.

Plate 10. Texture of a Schlieren defect with twofold brushes of strength $s = \pm\frac{1}{2}$.

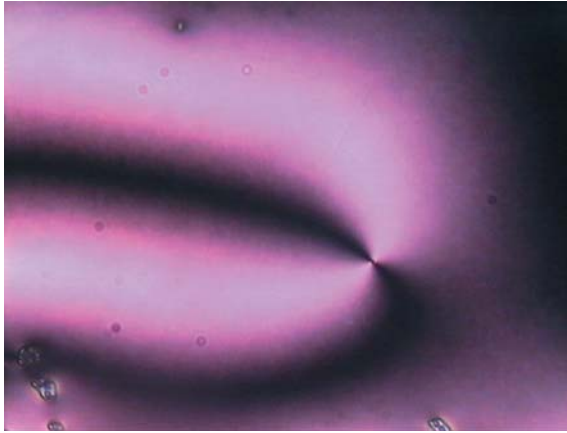


Plate 11. Texture of a Schlieren defect with fourfold brushes of strength $s = \pm 1$.

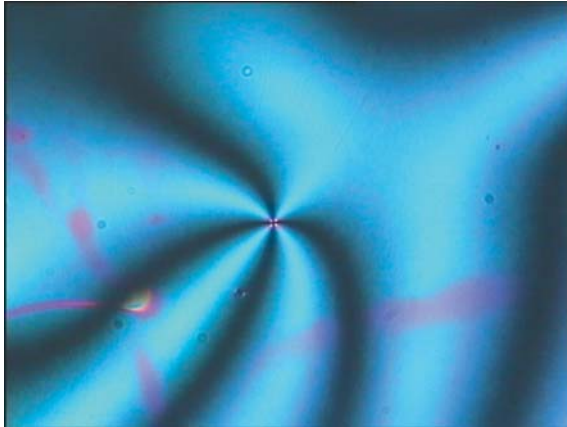
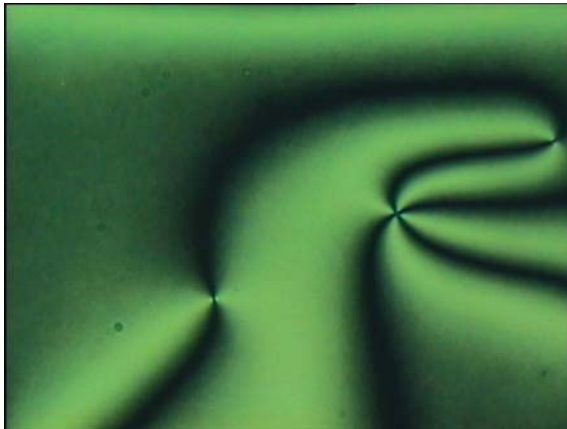


Plate 12. In the Schlieren texture of the nematic phase twofold and fourfold brushes are exhibited simultaneously within the same sample.



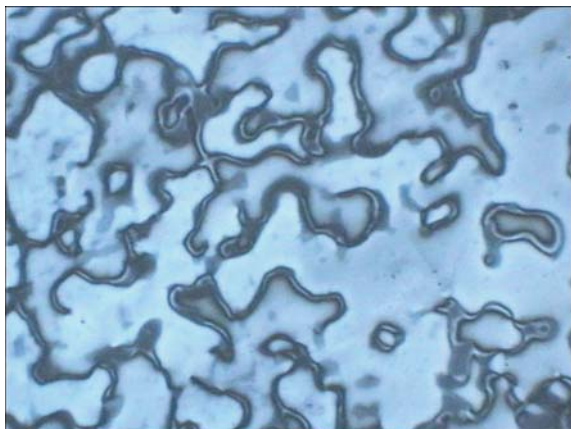


Plate 13. Nematic thread-like texture.

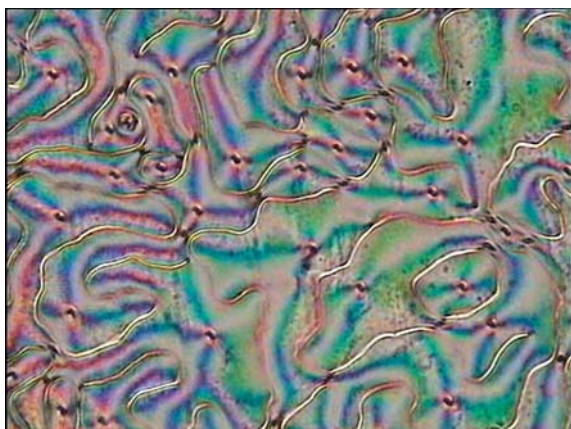


Plate 14. Nematic texture with surface disclination lines.

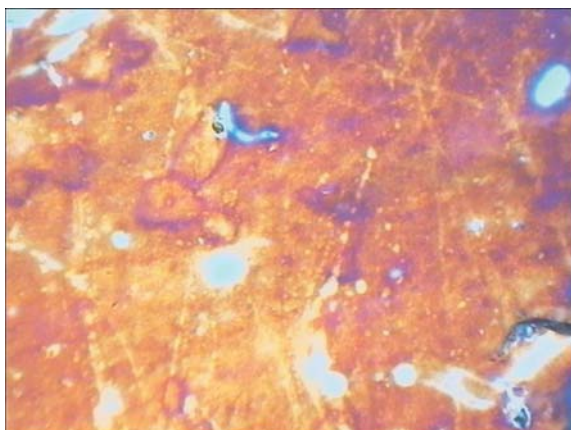


Plate 15. The marble texture is probably the most commonly obtained natural texture of a nematic liquid crystal.

Plate 16. Oily streaks texture of a cholesteric sample under planar anchoring conditions. The sample displays a N^* phase with a pitch of $P \approx 2 \mu\text{m}$, such that the color observed is not due to selective reflection. (Reproduced by permission of Taylor & Francis, I. Dierking et al., *Liq. Cryst.*, **13**, (1993), 45 (<http://www.tandf.co.uk/journals>).)

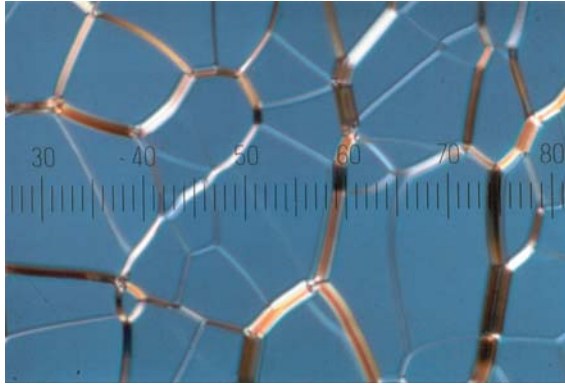


Plate 17. Oily streaks texture of a cholesteric phase with the wavelength of selective reflection in the visible region of the spectrum ($P \approx 450 \text{ nm}$). Different colors correspond to different twist states, due to hysteresis in temperature variation.

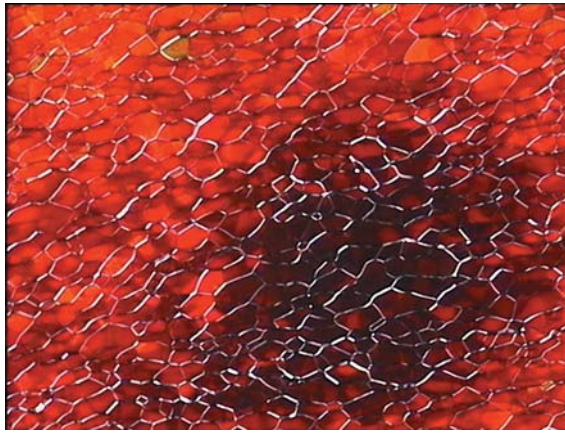
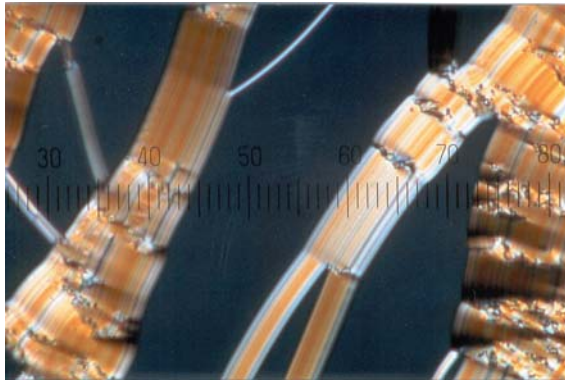


Plate 18. Close-up polarizing micrograph of a bundle of oily streaks of a cholesteric liquid crystal. (Reproduced by permission of Taylor & Francis, I. Dierking et al., *Liq. Cryst.*, **13**, (1993), 45 (<http://www.tandf.co.uk/journals>).)



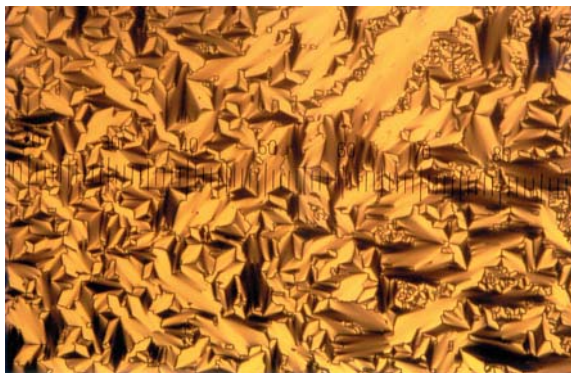


Plate 19. Fan-like texture of a short pitch cholesteric phase. Within individual fans the helix axis (equivalent to the optic axis) is oriented uniformly.

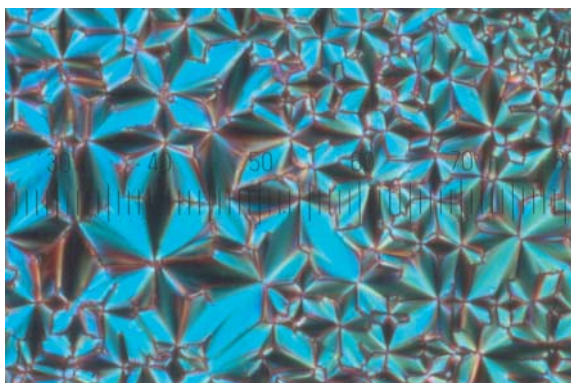


Plate 20. Fan-shaped focal conic texture of a short pitch cholesteric phase. (Reproduced by permission of Taylor & Francis, I. Dierking et al., *Liq. Cryst.*, **13**, (1993), 45 (<http://www.tandf.co.uk/journals>).)

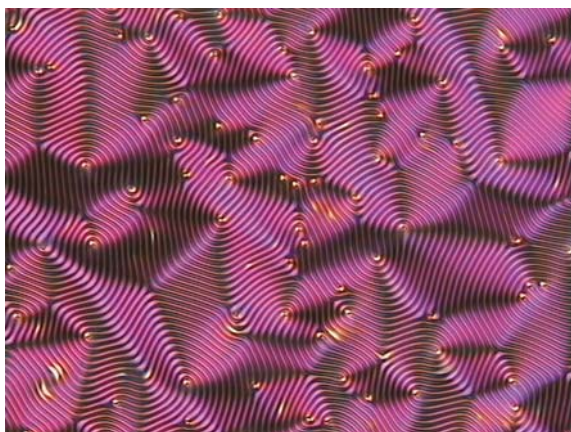


Plate 21. Cholesteric polygonal (fingerprint) texture of a sample with a relatively long pitch, such that the helical N^* superstructure can be resolved by polarizing microscopy.

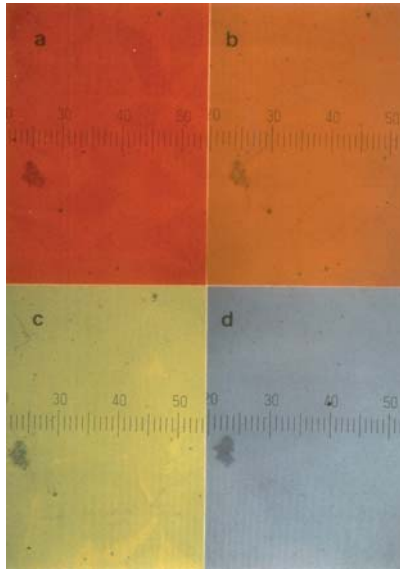


Plate 22. Texture photographs of a short pitch cholesteric sample under planar anchoring conditions (Grandjean orientation) taken in reflection microscopy on heating. Varying colors of the wavelength of selective reflection clearly illustrate a decreasing pitch from red to blue for increasing temperature from (a) to (d).

(Reproduced by permission of Taylor & Francis, I. Dierking et al., *Liq. Cryst.*, **18**, (1995), 443 (<http://www.tandf.co.uk/journals>).

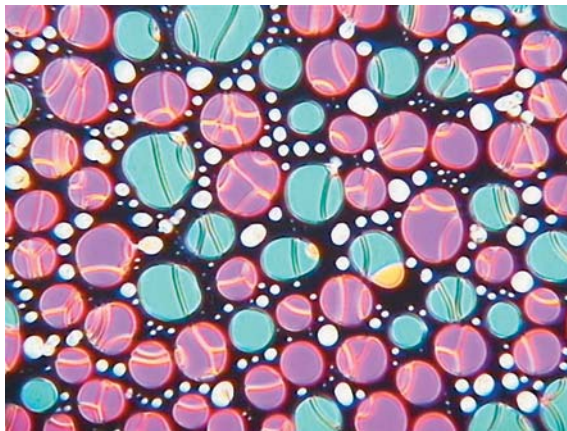


Plate 23. Cholesteric droplets of a long pitch N^* phase separating from the isotropic melt. Different colors correspond to different twist states.



Plate 24. Same sample as Plate 23 at a slightly lower temperature, showing coalescence of the cholesteric droplets during the phase ordering process.

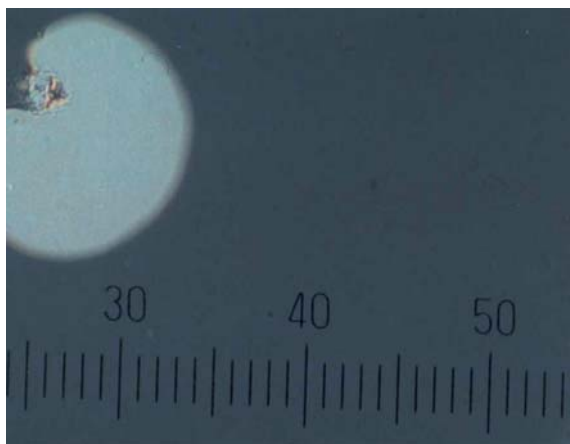


Plate 25. Two twist states of a long pitch cholesteric phase between substrates with planar boundary conditions, differing by a π turn of the helical superstructure. The discontinuous pitch jumps can be observed as domains of a different color nucleating and growing from a uniform N^* twist state. The different colors are not related to selective reflection.

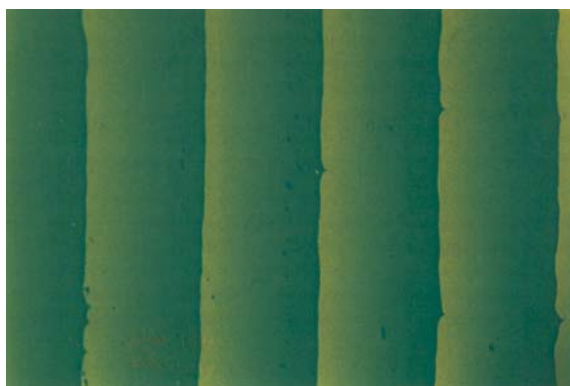


Plate 26. Preparation of a cholesteric sample in a wedge cell geometry, showing the typical Grandjean steps, which can be used to determine the value of the cholesteric pitch for known cell geometry. (Courtesy of P. Rudquist.)



Plate 27. Preparation of a cholesteric sample in the Cano geometry between a planar substrate and a lens with the N^* helix axis being parallel to the direction of light propagation. The pattern of concentric rings can be used to determine the value of the cholesteric pitch. (Courtesy of W. Kuczynski.)

Plate 28. Cholesteric pitch divergence at the transition to the SmA* phase. The photograph shows a contact preparation of a cholesteric (bottom) with a SmA (top) phase. As the pitch increases on approaching the SmA phase, Grandjean steps are seen between different twist states.

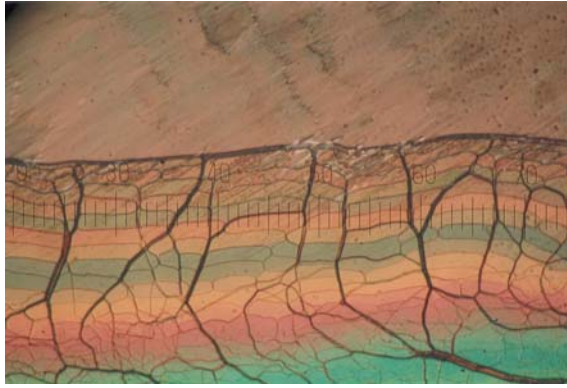


Plate 29. Cholesteric twist inversion compound at the inversion temperature. The N_{∞}^* state (black), which exhibits a quasi-nematic director configuration, nucleates in the middle of the texture photograph and can be brought into an extinction position. The surrounding twisted N^* state always appears bright when rotating the sample between crossed polarizers. (Reproduced by permission of Taylor & Francis, I. Dierking et al., *Liq. Cryst.*, **13**, (1993), 45 (<http://www.tandf.co.uk/journals>).)

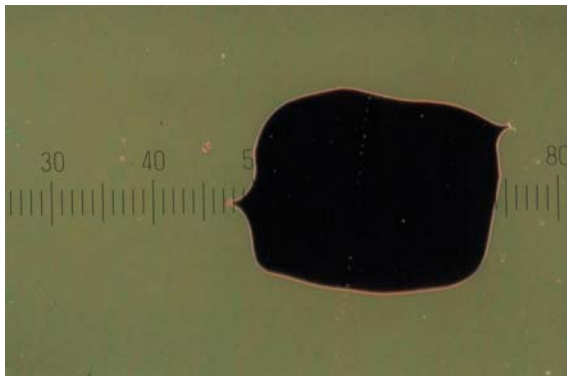


Plate 30. Fingerprint texture of a cholesteric phase under homeotropic anchoring conditions. Owing to the identity period $L = P/2$ of the cholesteric phase, the pitch can be determined as twice the distance between two dark lines.

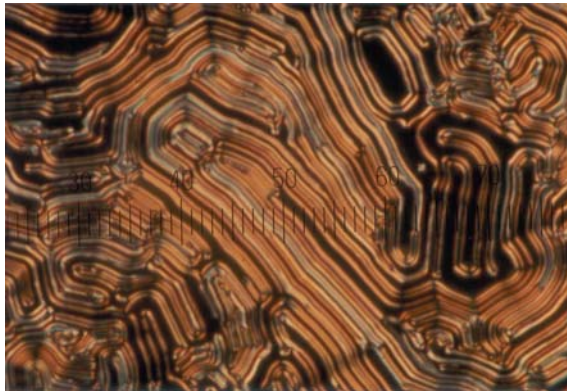




Plate 31. Fingerprint texture of a cholesteric phase under homeotropic anchoring conditions, for the pitch P approaching the cellgap d .



Plate 32. Coexistence of a cholesteric fingerprint texture with so-called cholesteric fingers (bright lines in the center) and a pseudo-isotropic region with a homeotropic nematic director configuration (black).



Plate 33. Sample with a diverging cholesteric pitch under homeotropic anchoring conditions, exhibiting so-called cholesteric fingers. In the strongly distorted director configuration, the dark areas represent a pseudo-isotropic, homeotropically aligned nematic.

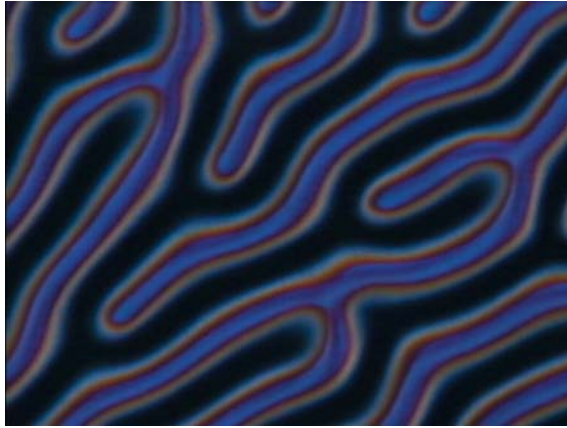


Plate 34. Close-up of a texture with cholesteric fingers.

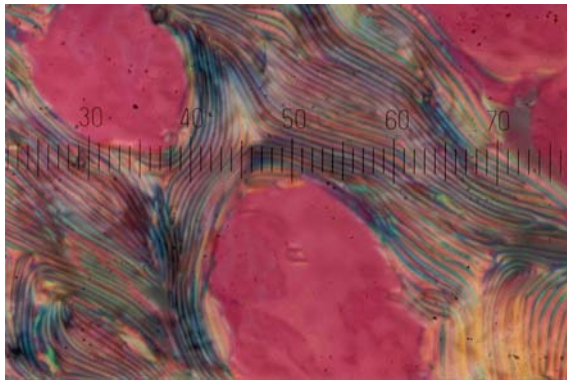
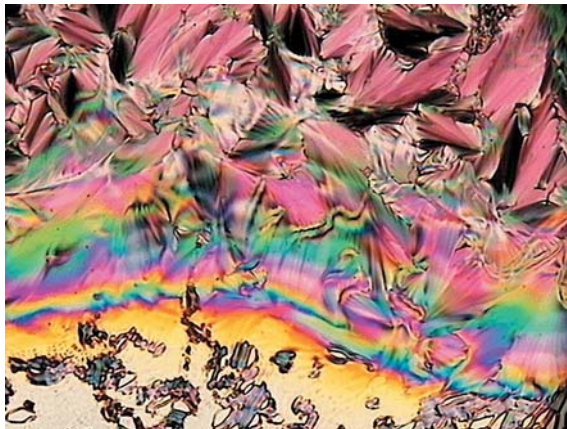


Plate 35. Coexistence of Grandjean-like and fingerprint areas of a cholesteric phase.

Plate 36. Photograph of natural textures of a sample with a N^* – $TGBA^*$ – SmA^* phase sequence under a temperature gradient. The top part of the photograph at lower temperature shows the fan-shaped SmA^* texture, while the bottom part depicts a cholesteric oily streaks texture at higher temperatures. The narrow $TGBA^*$ phase mediating the cholesteric and smectic phases can clearly be detected by the presence of the phase boundaries. (Reproduced by permission of Taylor & Francis, I. Dierking, S. T. Lagerwall, *Liq. Cryst.*, **26**, (1999), 83 (<http://www.tandf.co.uk/journals>).)



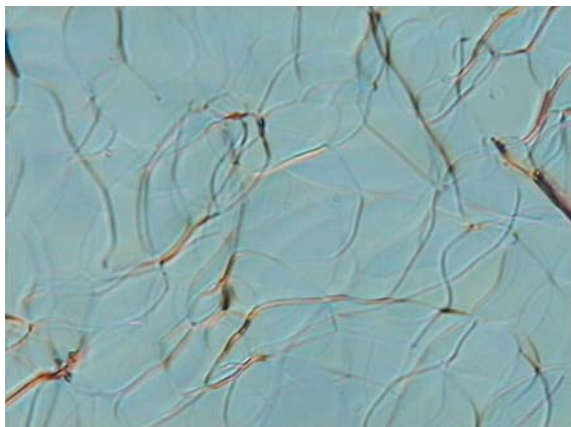


Plate 37. On passing through the transition from the oily streaks texture of the cholesteric N^* phase into $TGBA^*$ the oily streaks defects are retained but often become blurred and cannot be focused any more, as depicted in this texture photograph.

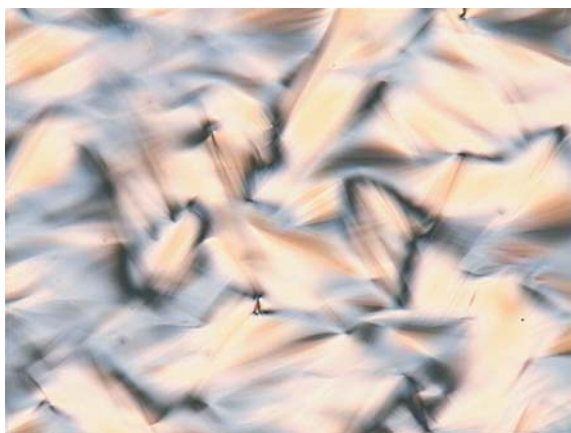


Plate 38. Textures of twist grain boundary phases often appear blurred and are hard to focus, like the fan-like texture of the $TGBA^*$ phase depicted in this texture photograph.

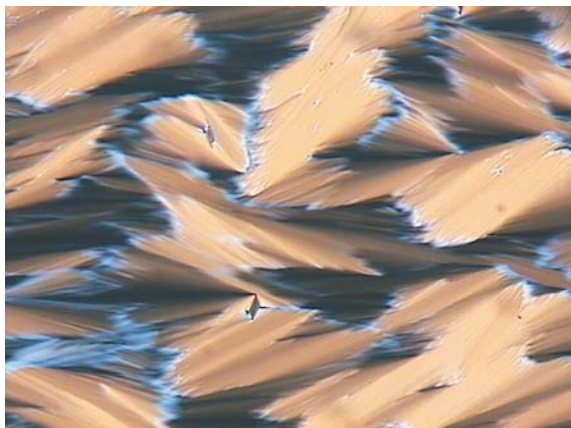


Plate 39. Same sample area as Plate 38, showing the fan-shaped texture of the SmA^* phase at lower temperatures.

Plate 40. Natural oily streaks texture of the cholesteric phase. (Reproduced by permission of Taylor & Francis, I. Dierking et al., *Liq. Cryst.*, **17**, (1994), 243 (<http://www.tandf.co.uk/journals>).)

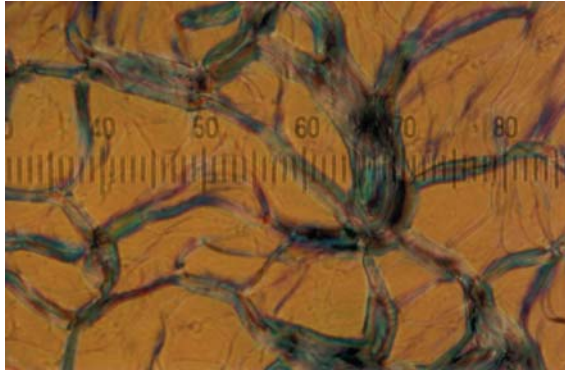


Plate 41. Same sample area as Plate 40 showing the unoriented TGBA* phase at slightly lower temperature. (Reproduced by permission of Taylor & Francis, I. Dierking et al., *Liq. Cryst.*, **17**, (1994), 243 (<http://www.tandf.co.uk/journals>).)

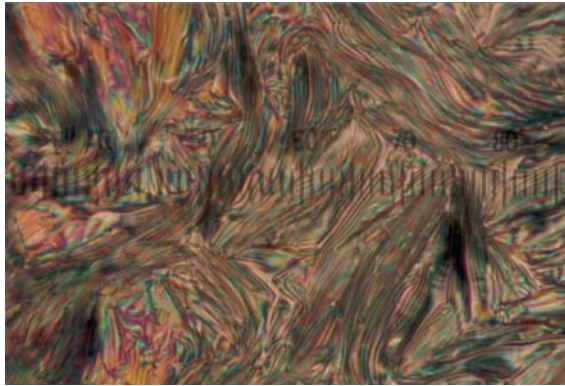


Plate 42. Same sample area as Plates 40 and 41 showing the fan-shaped texture of the SmA* phase at still lower temperature. (Reproduced by permission of Taylor & Francis, I. Dierking et al., *Liq. Cryst.*, **17**, (1994), 243 (<http://www.tandf.co.uk/journals>).)

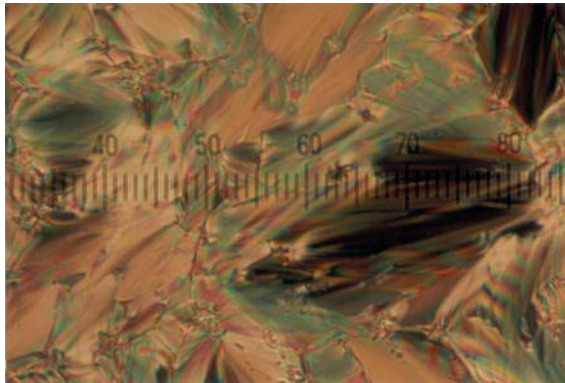




Plate 43. ATGBA* phase with relatively long pitch at planar anchoring conditions in the Grandjean orientation. The helix axis is parallel to the direction of light propagation and different colors are due to different twist states developing during cooling.

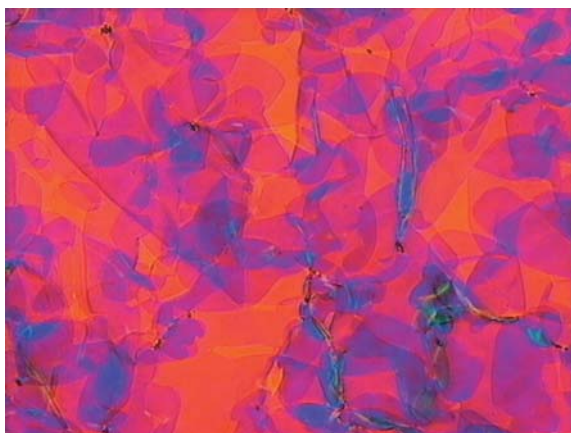


Plate 44. A short pitch TGBA* phase in Grandjean orientation due to planar anchoring conditions. Different twist states are observed on cooling with the helix axis perpendicular to the boundary plates and parallel to the direction of light propagation.

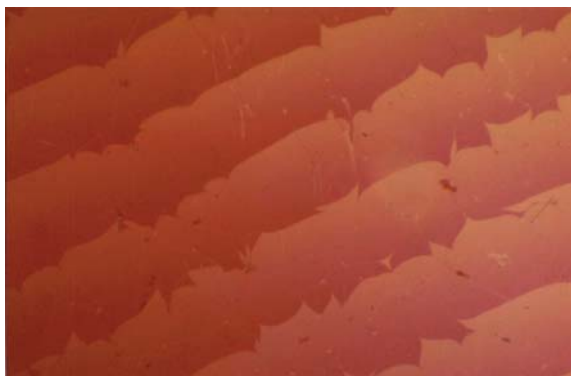


Plate 45. TGBA* phase under planar anchoring conditions in a wedge cell preparation. The helical superstructure with twist axis parallel to the direction of light propagation can clearly be observed by the formation of Grandjean-like steps. (Courtesy of W. Kuczynski.)

Plate 46. Sample on cooling under homeotropic boundary conditions at the transition from N^* (fingerprint texture at the right) to $TGBA^*$ (filament texture at the left).

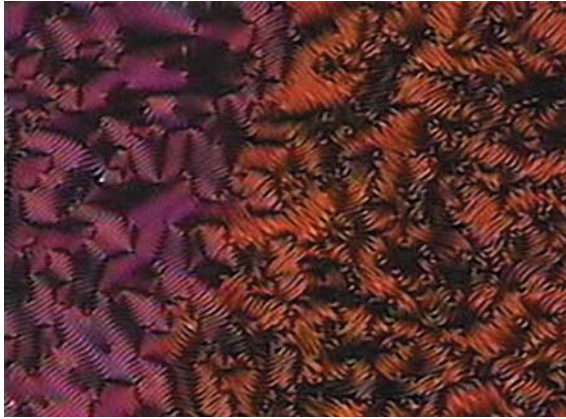


Plate 47. Sample on heating under homeotropic boundary conditions at the transition from SmA^* (black pseudoisotropic texture) to $TGBA^*$ (filament texture).

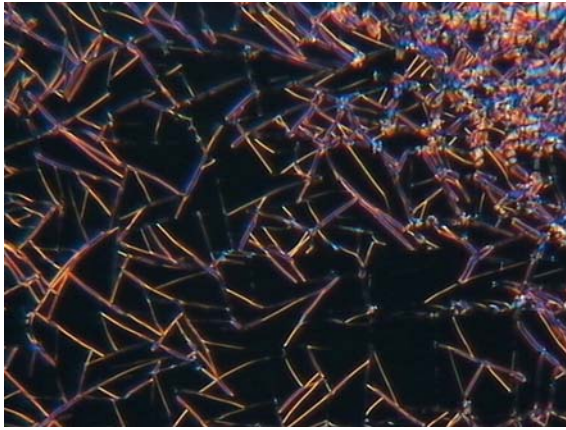
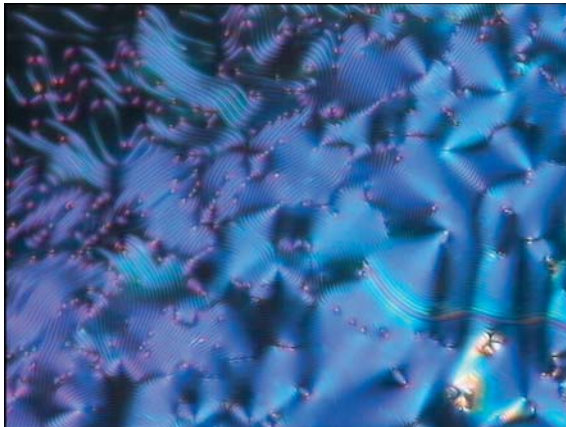


Plate 48. Fingerprint texture of the $TGBA^*$ phase under homeotropic anchoring conditions. The pitch of the helical superstructure can be estimated from twice the distance between adjacent dark lines, due to the identity period of $L = P/2$ for the $TGBA^*$ helix.



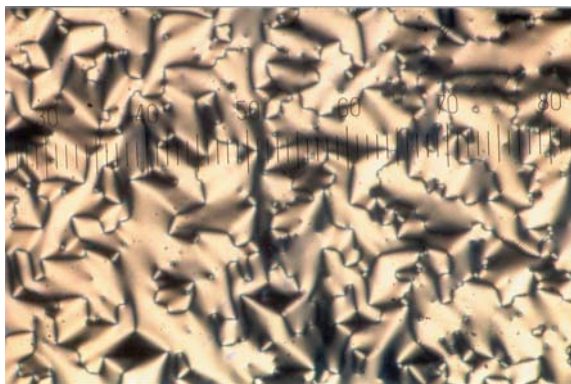


Plate 49. Fingerprint texture of the TGBA* phase subjected to homeotropic boundary conditions. (Reproduced by permission of Taylor & Francis, I. Dierking et al., *Liq. Cryst.*, **17**, (1994), 17 (<http://www.tandf.co.uk/journals>).)

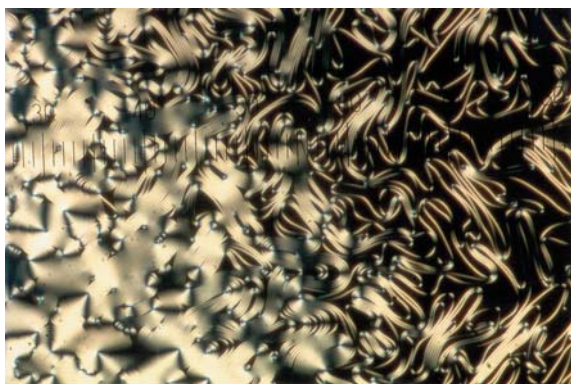


Plate 50. Same sample area as in Plate 49 at a slightly lower temperature. The TGBA* phase can be observed by its typical filament texture, while the pseudo-isotropic texture of the SmA* phase is seen as black areas, because here the optic axis is oriented along the direction of light propagation. (Reproduced by permission of Taylor & Francis, I. Dierking et al., *Liq. Cryst.*, **17**, (1994), 17 (<http://www.tandf.co.uk/journals>).)

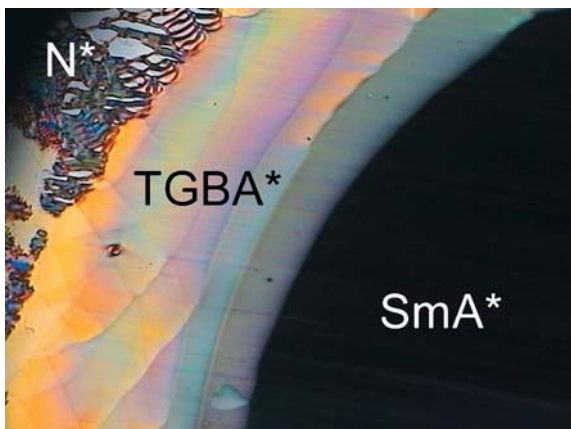
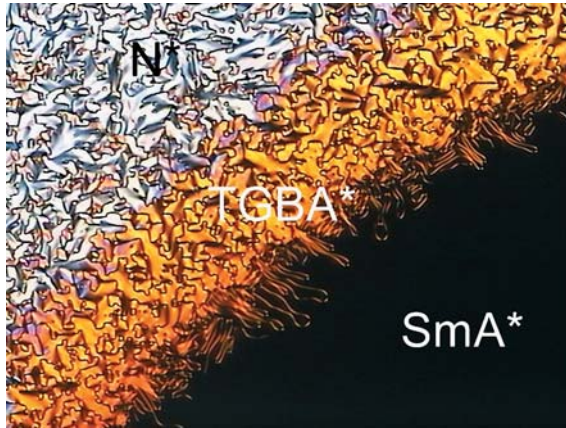


Plate 51. Planar wedge cell preparation of a N*–TGBA*–SmA* sample under a temperature gradient. In the right part of the photograph, at lower temperatures, the texture of the uniform planar SmA* phase can be brought into an extinction position. The TGBA* phase exhibits a texture with Grandjean steps and cannot be brought to extinction by rotation of the sample between crossed polarizers, due its helical superstructure. The cholesteric N* phase at higher temperatures can be seen at the top left of the photograph with an oily streaks texture. (Reproduced by permission of Taylor & Francis, I. Dierking, S. T. Lagerwall, *Liq. Cryst.*, **26**, (1999), 83 (<http://www.tandf.co.uk/journals>).)

Plate 52. Homeotropic wedge cell preparation of the same N^* -TGBA*-SmA* sample as depicted in Plate 51, also subjected to a temperature gradient. In the right part of the photograph the pseudo-isotropic SmA* texture can be observed, which appears black for all orientations of the sample between crossed polarizers. The TGBA* phase exhibits a typical filament texture at the SmA*-TGBA* transition area and a fan-like texture at slightly higher temperatures.



At still higher temperatures a cholesteric fan-like texture is observed in the left top part of the photograph, which can clearly be distinguished from TGBA* by a change in birefringence. (Reproduced by permission of Taylor & Francis, I. Dierking, S. T. Lagerwall, *Liq. Cryst.*, **26**, (1999), 83 (<http://www.tandf.co.uk/journals>).

Plate 53. Droplet preparation of the cholesteric phase, which shows a fingerprint-like texture at elevated temperatures. The cholesteric helix axis exhibits no preferred direction in the substrate plane. (Reproduced by permission of Taylor & Francis, I. Dierking et al., *Liq. Cryst.*, **17**, (1994), 17 (<http://www.tandf.co.uk/journals>).

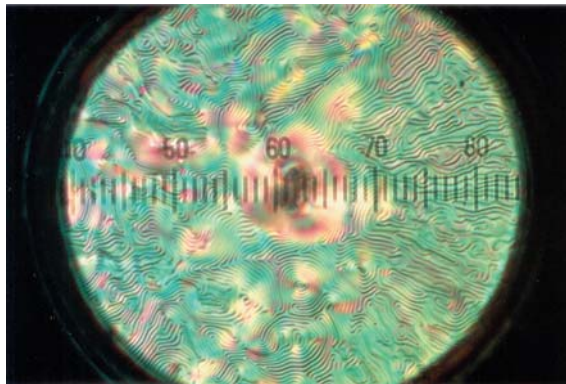
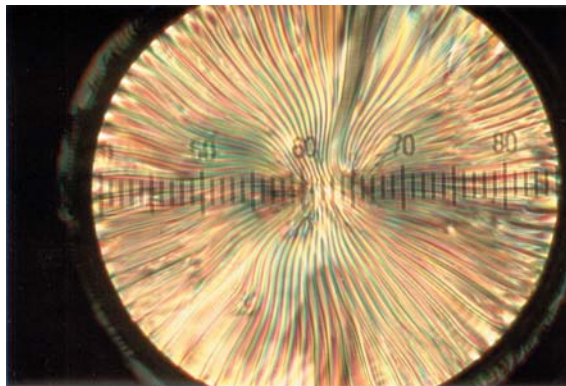


Plate 54. Same droplet preparation as Plate 53 at a slightly lower temperature, showing the TGBA* phase. The smectic layers are oriented in concentric circles with the TGBA* helix axis oriented along the smectic layer plane. This leads to a radial symmetric line pattern. (Reproduced by permission of Taylor & Francis, I. Dierking et al., *Liq. Cryst.*, **17**, (1994), 17 (<http://www.tandf.co.uk/journals>).



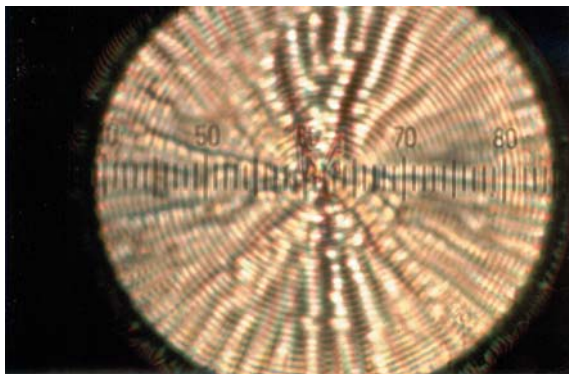


Plate 55. Same droplet preparation as Plates 53 and 54 at still lower temperature in the SmC^* phase. The smectic layers are still oriented in a concentric fashion, but the helix axis orientation is now radially symmetric. This results in a concentric line pattern, because the SmC^* helix lines are observed parallel to the smectic layer plane. (Reproduced by permission of Taylor & Francis, I. Dierking et al., *Liq. Cryst.*, **17**, (1994), 17 (<http://www.tandf.co.uk/journals>).)

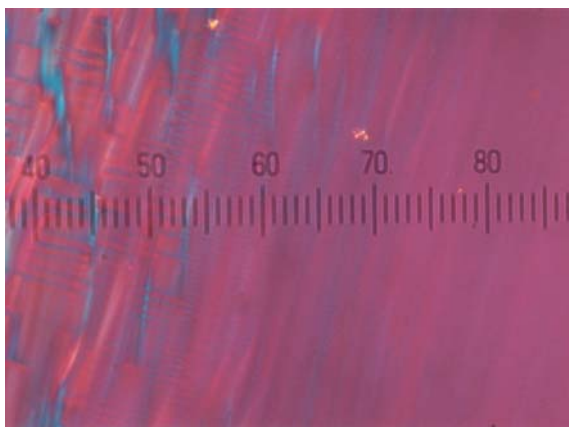


Plate 56. In thin cells with planar boundary conditions, the appearance of the helical TGBA^* phase can be suppressed by surface induced unwinding of the helical superstructure. The texture photograph shows the same sample as Plates 53–55 with a bulk phase sequence $\text{N}^*-\text{TGBA}^*-\text{SmC}^*$. In thin cells with planar anchoring conditions, the bulk TGBA^* phase is now observed as a

narrow uniform planar SmA^* phase (right), mediating the N^* and the SmC^* phase (left), which can be identified by the partial development of helix lines along the smectic layer planes. (Reproduced by permission of Taylor & Francis, I. Dierking, S. T. Lagerwall, *Liq. Cryst.*, **26**, (1999), 83 (<http://www.tandf.co.uk/journals>).)



Plate 57. Square grid texture of the TGBC^* phase under planar boundary conditions. The TGB helix is oriented perpendicular to the bounding plates, i.e. parallel to the direction of light propagation. The square grid pattern is presumed to be due to a helical director configuration within the individual SmC^* blocks, with the helix axis being in the plane of the substrate and mutually perpendicular in adjacent smectic blocks. Another model of the square grid texture is that of the undulated twist grain boundary C^* phase.

(Reproduced by permission of Taylor & Francis, I. Dierking, *Liq. Cryst.*, **28**, (2001), 165 (<http://www.tandf.co.uk/journals>).)

Plate 58. TGBC_#* phase (square grid texture at the right) at the transition to the common surface stabilized SmC* phase (left), which exhibits a ferroelectric domain texture (see also Chapter 7). (Reproduced by permission of Taylor & Francis, I. Dierking, *Liq. Cryst.*, **28**, (2001), 165 (<http://www.tandf.co.uk/journals>).)

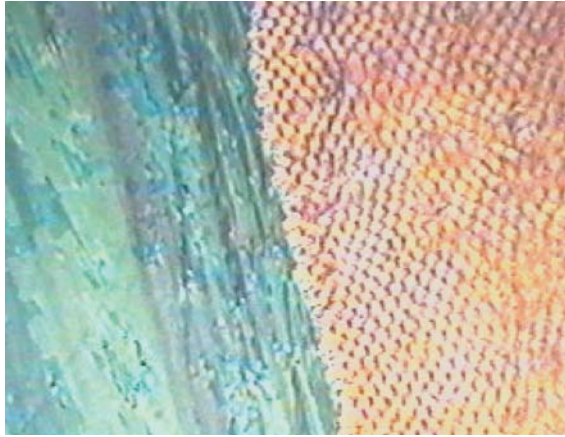
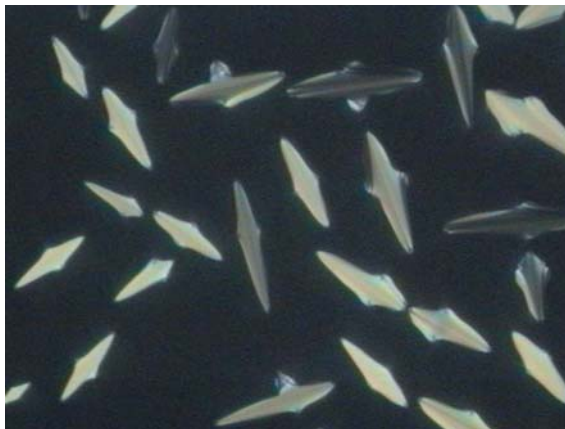


Plate 59. The TGBC_#* phase prepared in a wedge cell with planar boundary conditions. (Courtesy of S. K. Prasad.) The twist grain boundary helix axis is oriented perpendicular to the substrate plates and thus parallel to the direction of light propagation, leading to the observed Grandjean steps. The additional square grid pattern corresponds to a two dimensional director modulation in the plane of the substrate. This is due to either a SmC* helix within local smectic blocks, exhibiting a helix axis that is perpendicular in adjacent slabs, or a director configuration as proposed for the UTGBC* phase.



Plate 60. Growth of SmA^(*) *bâtonnets* (bright) from the isotropic melt (black). Note the pronounced growth anisotropy.



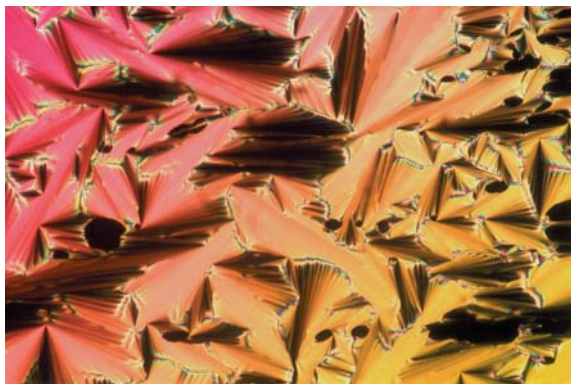


Plate 61. Typical fan-shaped texture of a SmA phase. The director basically lies in the plane of the substrate and the smectic layers are curved across the fans.

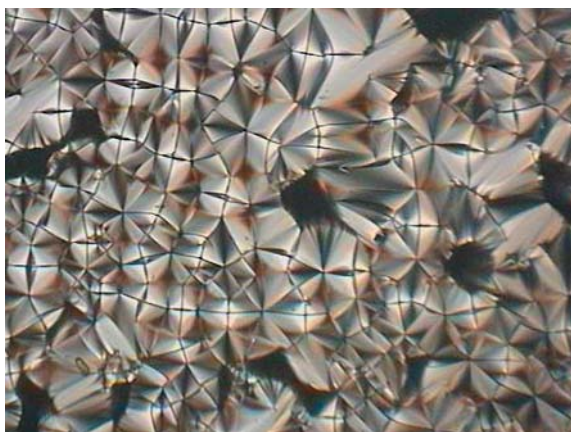


Plate 62. Typical focal conic texture of a SmA phase.



Plate 63. Polygonal texture of the SmA phase. (Courtesy of D. Demus and G. Pelzl.)

Plate 64. Example of a homogeneously oriented SmA phase by subjection to planar boundary conditions. The director is turned out of the polarizer direction by approximately 30° .

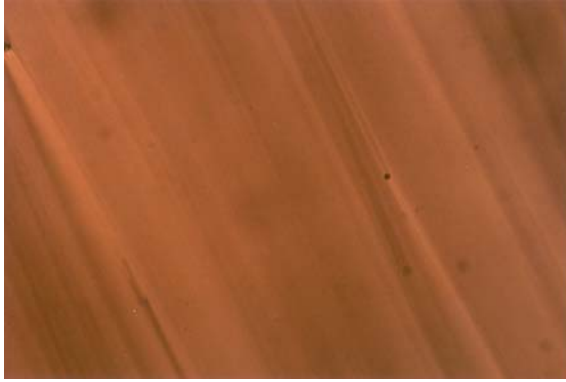


Plate 65. An example of the more rarely observed oily streaks appearance of a SmA phase, where birefringent bands are observed across a pseudo-isotropic background.

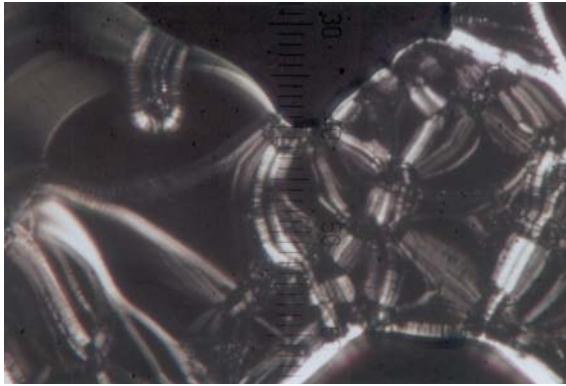
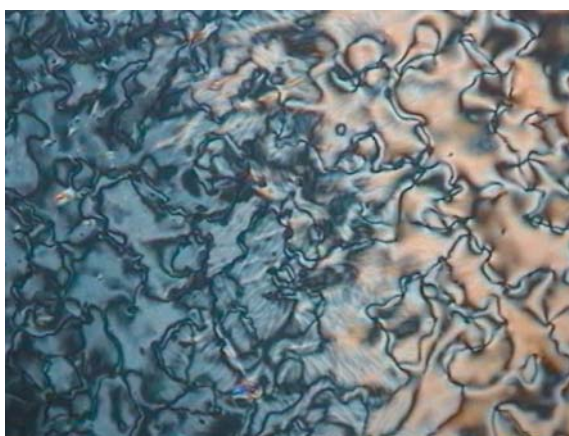


Plate 66. Electric field induced striped texture of a SmA* phase. The width of the stripes is approximately equal to the cell gap, in the present case approximately $6\ \mu\text{m}$.





A



B

Plate 67. (a) Transition bars observed at the transition from a uniform aligned nematic to smectic C phase. On further cooling, the transition bars will quickly disappear. (b) Transition from a nematic Schlieren texture (right, same sample region as Plate 8) to a SmC Schlieren texture (left).

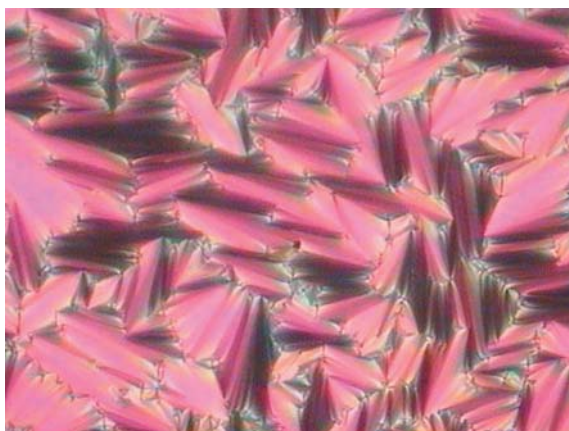


Plate 68. The fan-shaped texture of the SmA phase.

Plate 69. Same sample area as Plate 68, showing the transition to the broken fan-shaped texture of SmC on cooling.

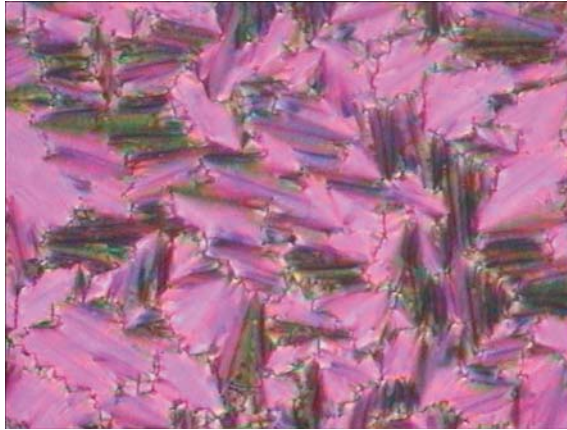


Plate 70. Focal conic texture of a SmC phase.

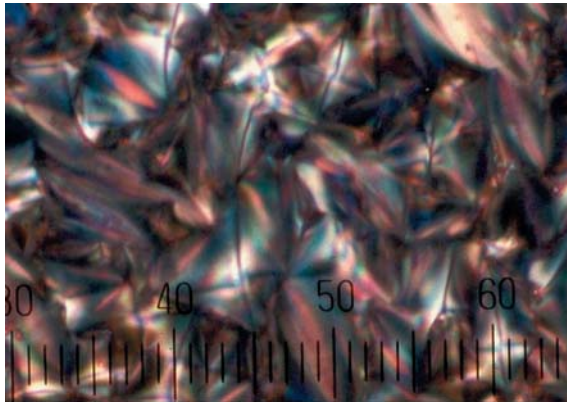
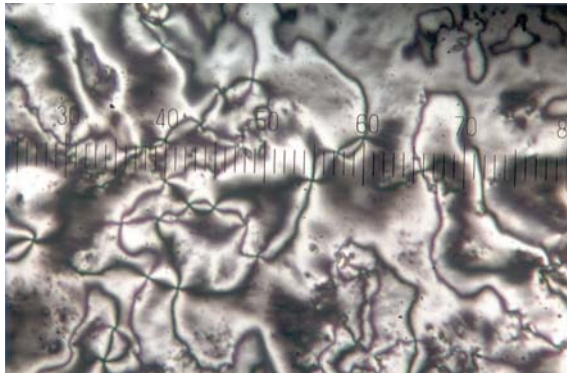


Plate 71. Schlieren texture of a SmC phase prepared under homeotropic boundary conditions. Note that the SmC phase only exhibits fourfold singularities, defects of strength $s = \pm 1$. (Reproduced by permission of Taylor & Francis, J. Schacht et al., *Liq. Cryst.*, **19**, (1995), 151 (<http://www.tandf.co.uk/journals>).)



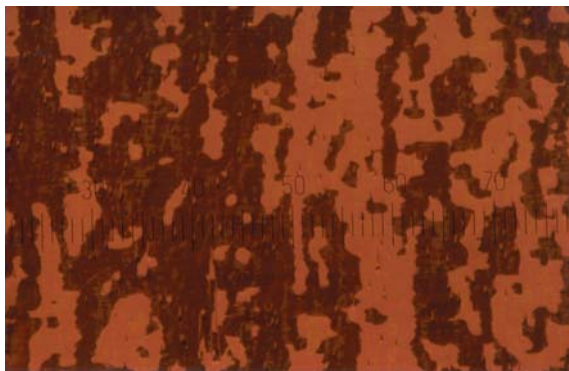


Plate 72. Domain texture of a SmC phase subjected to planar boundary conditions in a thin sandwich cell. The two types of domains result from the tilt of the director to either side of the smectic layer normal.

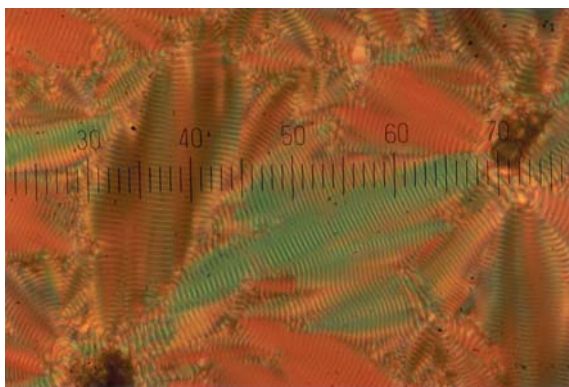


Plate 73. Fan-shaped texture of a chiral SmC* phase with an equidistant line pattern, due to the helical superstructure. The lines are parallel to the smectic layer planes and the distance between two adjacent dark lines gives the pitch of the helix. The helix axis is perpendicular to the lines.

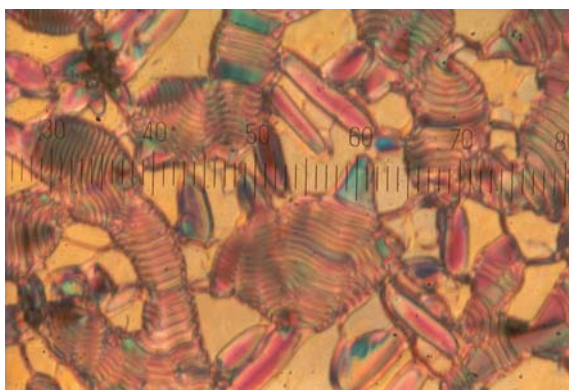


Plate 74. Transition from the cholesteric Grandjean texture (yellow background) to the helical SmC* phase (domains with equidistant line pattern). (Reproduced by permission of Taylor & Francis, J. Schacht et al., *Liq. Cryst.*, **19**, (1995), 151 (<http://www.tandf.co.uk/journals>).)

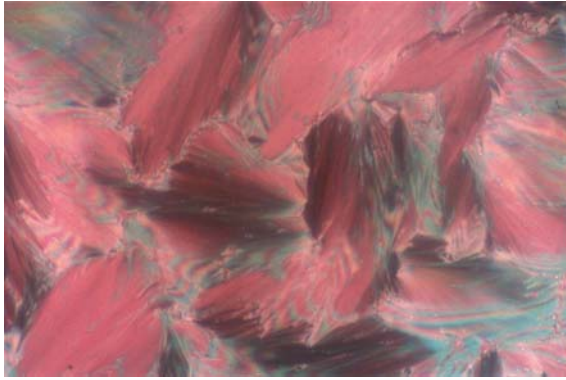


Plate 75. The fan-shaped SmA* texture.

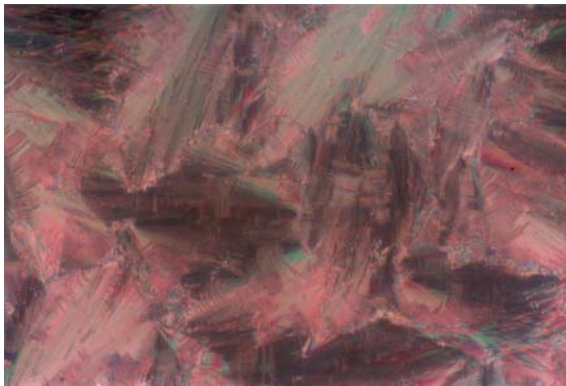
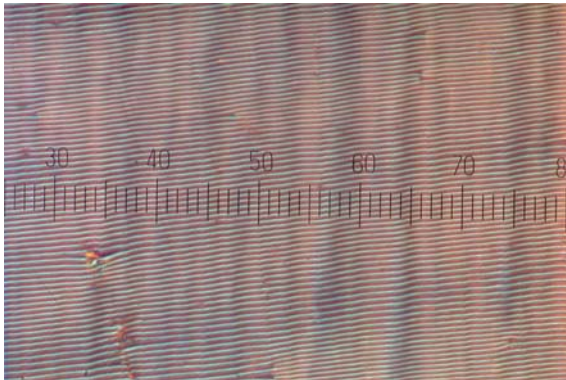


Plate 76. Same sample area as Plate 75, showing the transition to the broken fan-shaped texture with helix lines of the SmC* phase.

Plate 77. Subjecting a helical SmC* phase to homogeneous planar boundary conditions leads to a uniform equidistant line pattern. The helix lines are parallel to the smectic layer planes and the helix axis is perpendicular to the lines, i. e. the smectic layer plane. (Reproduced by permission of Taylor & Francis, I. Dierking et al., *Liq. Cryst.*, **13**, (1993), 45 (<http://www.tandf.co.uk/journals>).)



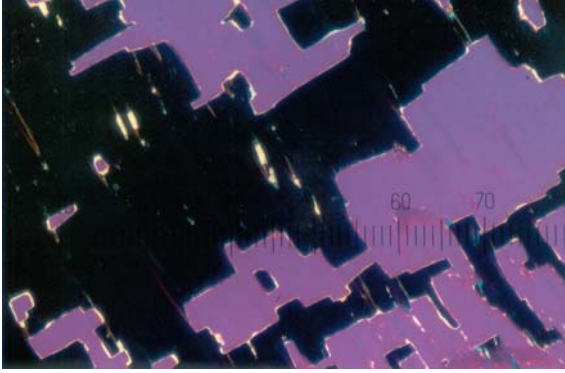


Plate 78. Reducing the gap of a SmC^* sandwich cell with homogeneous planar boundary conditions to values smaller than the helix pitch results in the *surface stabilized geometry*. The helix is unwound by elastic interactions between the liquid crystal and the substrates, and two types of domains are obtained, due to the tilt of the director. If these domains can be brought to extinction, we speak of the *bookshelf* orientation, where the smectic layers are perpendicular to the substrate plane.

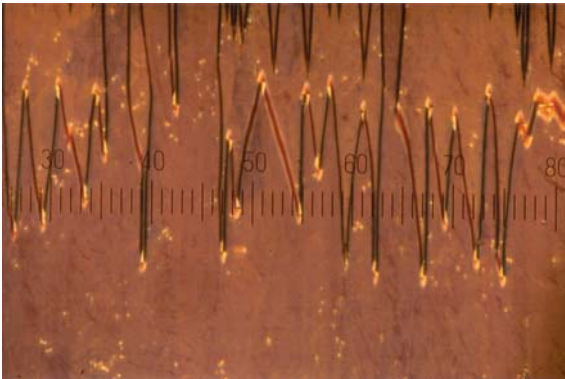


Plate 79. Typical zigzag defects of a surface stabilized SmC^* ferroelectric liquid crystal in the (vertical) *chevron* geometry. At the zigzag lines, domains of opposite layer inclination meet.

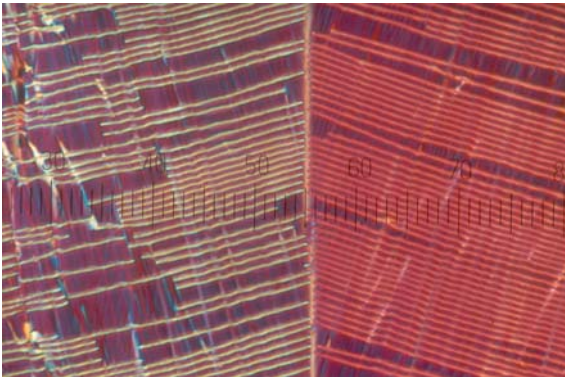


Plate 80. Texture of a field induced *horizontal chevron* structure. The helix lines clearly indicate the direction of the smectic layer planes, and in the region where two domains of opposite layer tilt meet, a vertical chevron defect forms the domain boundary.

Plate 81. The smectic layer rotation under applied asymmetric electric fields can lead to spiral smectic layer instabilities, shown here for a SmA^* phase close to the transition to SmC^* . (Courtesy of G. Andersson.)

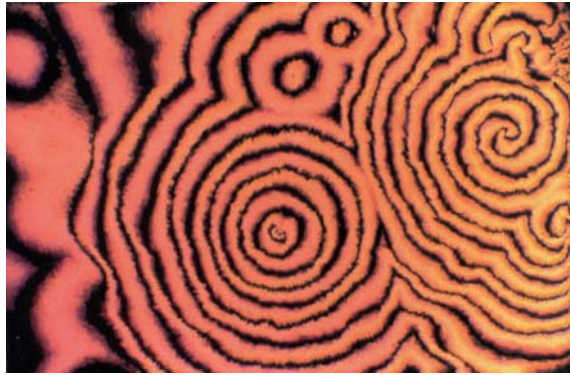
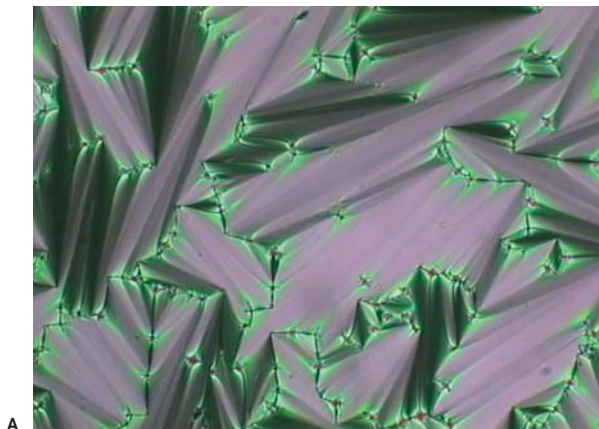
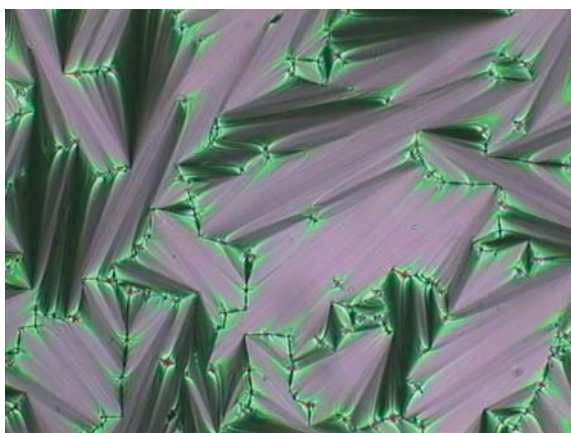


Plate 82. Texture series of MHPOBC showing the transitions through a number of different fluid smectic phases at the same sample region. Texture changes between (a) SmA^* , (b) SmC_α^* and

(c) SmC^* are very subtle, while the transition into (d) $\text{SmC}_{1/3}^*$ and especially the (e) antiferroelectric SmC_A^* phase can be detected more easily. Part (f) of the series shows the SmI_A^* phase.

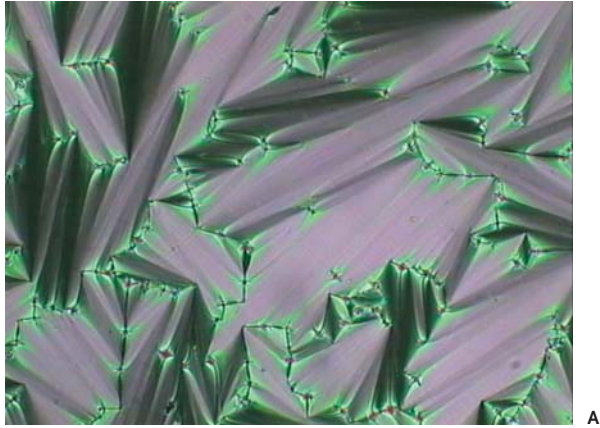


A

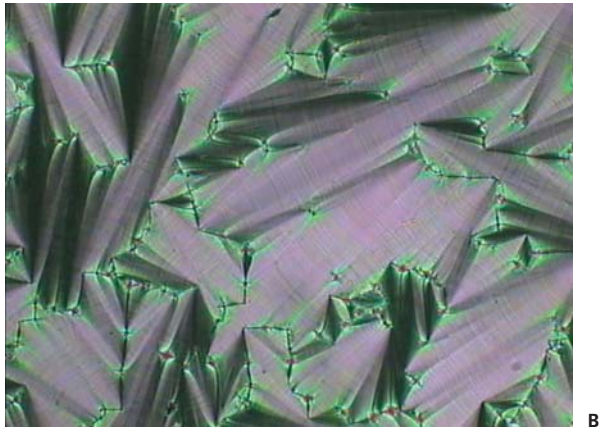


B

Plate 83. Fan-shaped textures of (a) the SmA* and (b) the SmC_α* phase, illustrating the very subtle appearance of a slight striation *along* the fans for SmC_α*.



A



B

Plate 84. Fan-shaped textures of (a) the SmC^* and (b) the $\text{SmC}_{1/3}^*$ phase, illustrating the appearance of a striation across the fans, when the transition into $\text{SmC}_{1/3}^*$ is passed. (Same sample area as Plate 83).

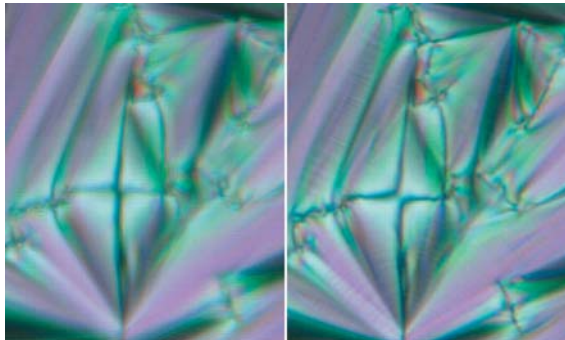


Plate 85. Break-up of focal conic defects at the transition from SmC^* (left) to $\text{SmC}_{1/3}^*$ (right).



A



B

Plate 86. Planar and homeotropic regions at the transition from (a) $\text{SmC}_{1/3}^*$ to (b) SmC_A^* . The so-called “ferri-electric” phase can easily be identified in the homeotropic sample area, due to a strongly fluctuating texture. Note that, in contrast to the grayish homeotropic SmC^* phase, the SmC_A^* appears black (pseudo-isotropic).

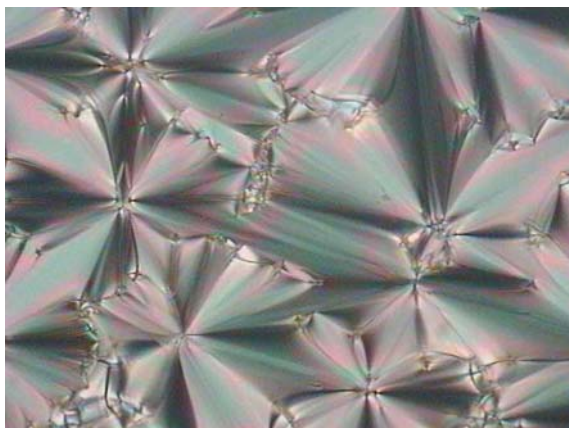


Plate 87. Fan-shaped texture of the SmA phase.

Plate 88. Same sample area as Plate 87, showing the fan-shaped texture of the SmB phase. The texture changes at the transition are rather subtle and sometimes hard to observe.

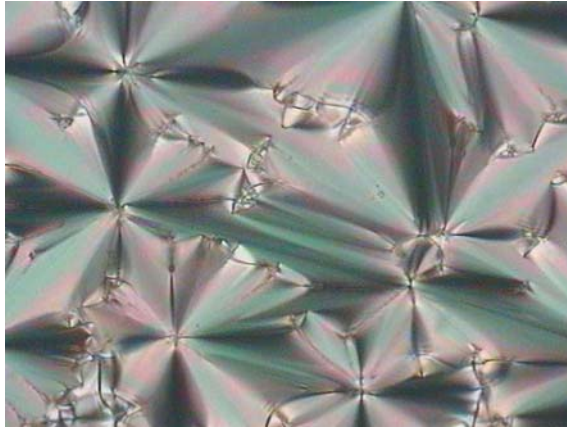
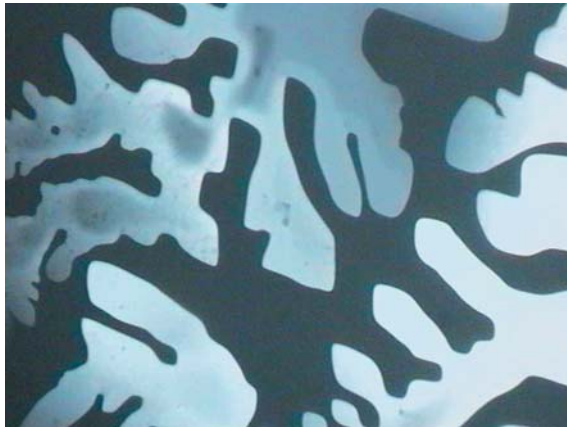
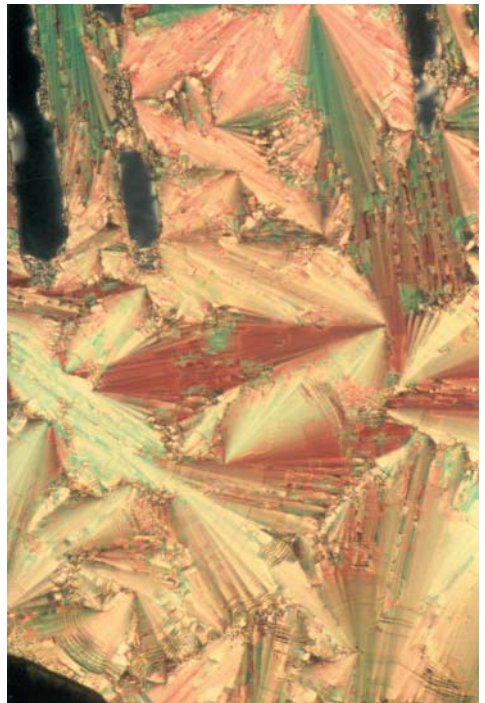
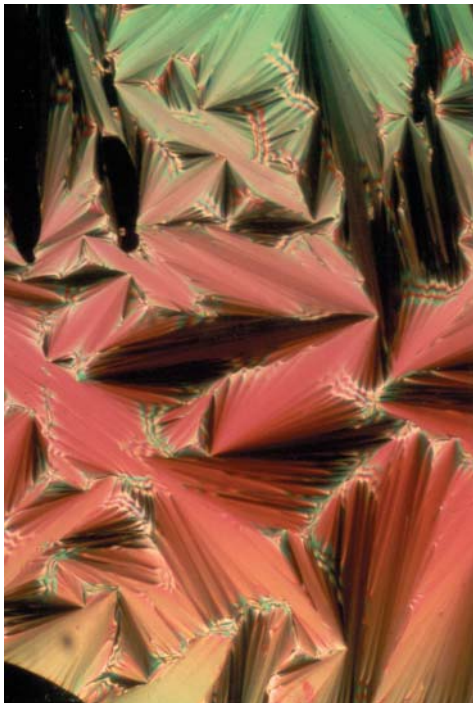
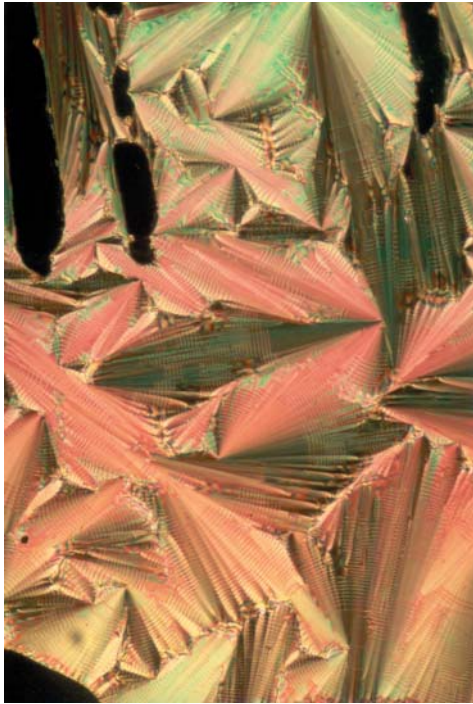


Plate 89. The *mosaic* texture is a common appearance of the SmB phase.



Plate 90. At the direct formation of the SmB phase (bright) from the isotropic melt (black), dendritic growth aggregates are often observed.





B

D

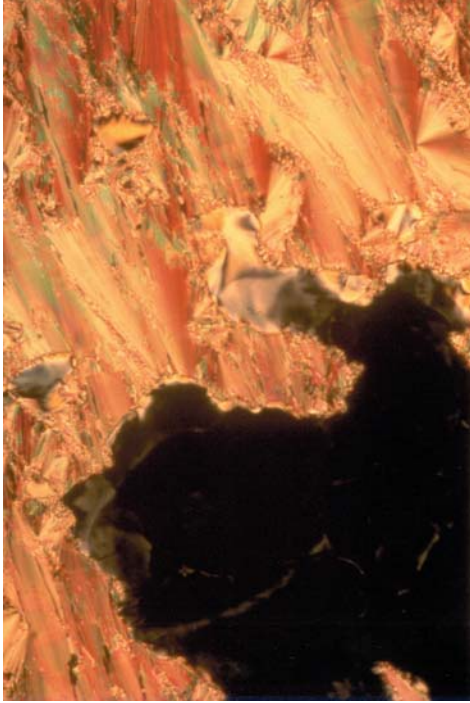
A

C

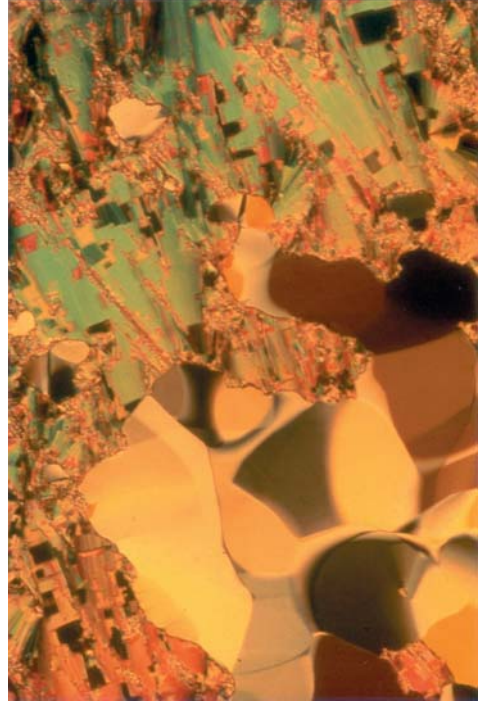
◀ **Plate 91.** Texture series of the same compound and sample area, illustrating the texture changes through the $\text{SmA}^*-\text{SmC}^*-\text{SmI}^*-\text{SmF}^*$ phase sequence. (a) The SmA^* phase shows the common fan-shaped texture, which is (b) superimposed by an equidistant line pattern due to the helical superstructure when passing into SmC^* . (c) In SmI^* only slight remnants of the helix are retained and we observe a broken fan-shaped texture, which (d) becomes much more pronounced as the transition into SmF^* is passed.

Plate 92. Texture of the surface stabilized SmI^* phase subjected to homogeneous planar boundary conditions in a thin sandwich cell. In contrast to SmC^* , the SmI^* phase exhibits four domain types, two of which are mutually quite similar in birefringence.





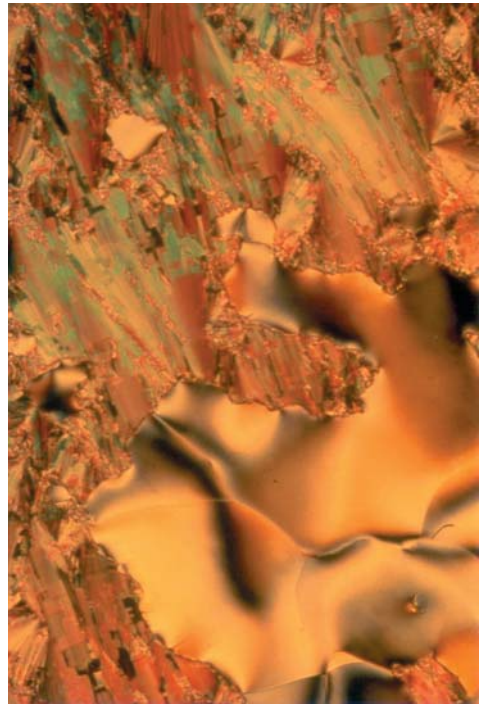
B



D



A



C

◀ **Plate 93.** Texture series through the SmA^* – SmC^* – SmI^* – SmF^* phase sequence for the same compound and sample area, showing coexisting planar and homeotropic regions. (a) In the homeotropic areas the SmA^* phase

exhibits the pseudo-isotropic texture, which (b) changes to a grayish appearance and later into a Schlieren texture for SmC^* . (c) The Schlieren texture is retained in SmI^* and (d) eventually changes to a mosaic texture for the SmF^* phase.

Plate 94. Homeotropic preparation of a chiral SmI^* phase.

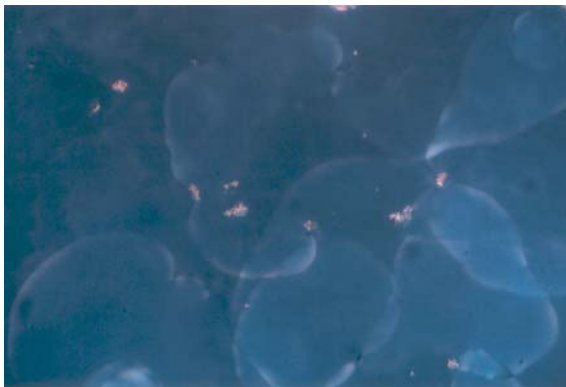
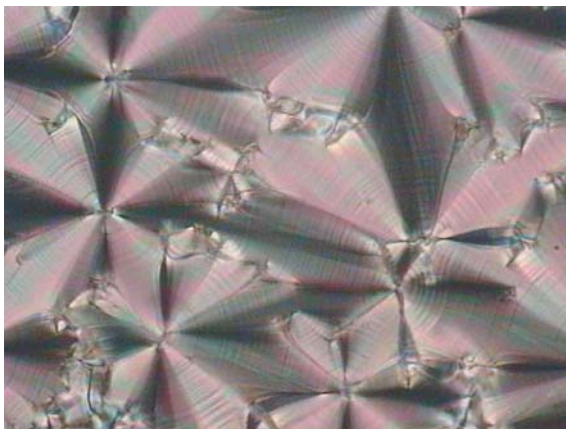


Plate 95. Same compound and sample area as Plate 94, showing the homeotropic preparation of a chiral SmF^* phase.



Plate 96. Striated fan-shaped texture of the soft crystal E phase (compare to Plates 87 and 88, showing the same compound and sample area). Note that this is an *achiral* compound.



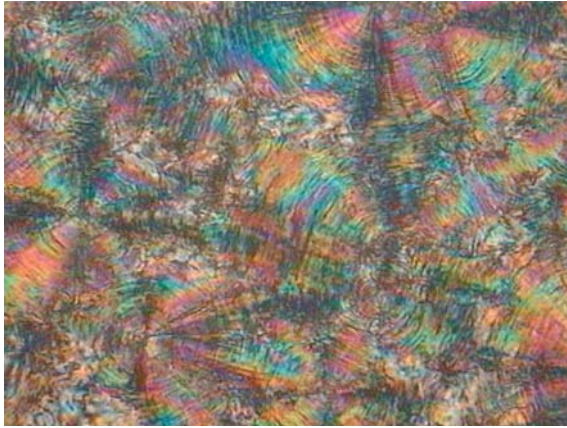


Plate 97. Same as Plate 96, after crystallization.



Plate 98. Coexisting planar and homeotropic regions of a soft crystal E phase.

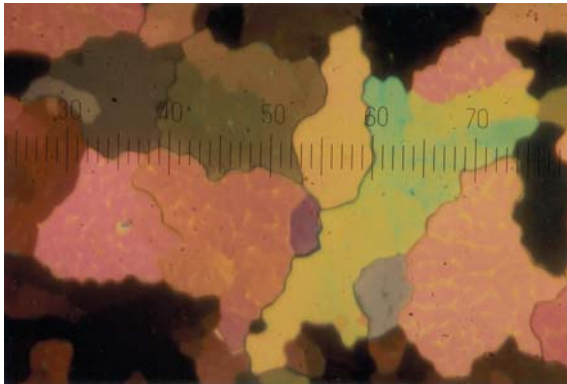
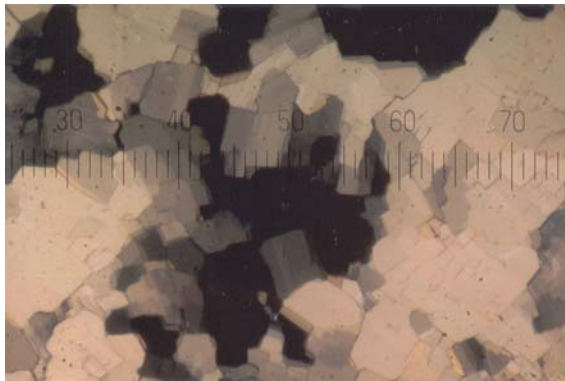
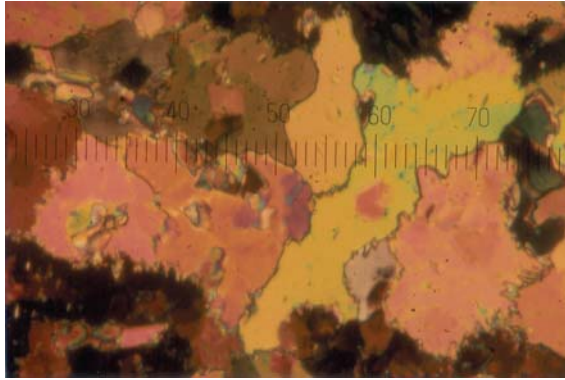
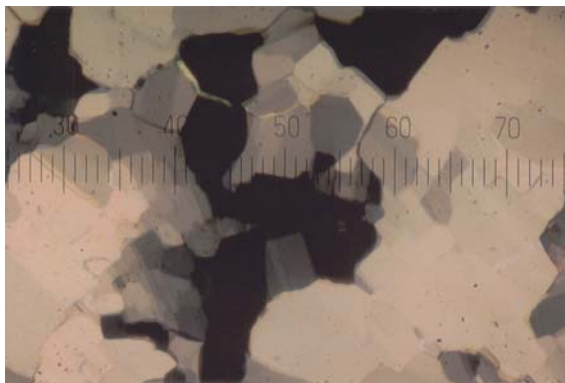


Plate 99. Mosaic texture of the soft crystal G* phase.

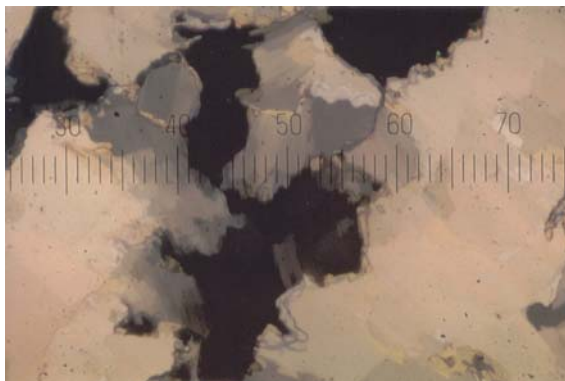
Plate 100. Same sample area as Plate 99, showing the appearance after crystallization. Remnants of the mosaic texture can be seen.



A



B



C

Plate 101. Texture series of the mosaic texture through the transitions of the soft crystal phases (a) G and (b) H until (c) final crystallization. The texture changes are very subtle.

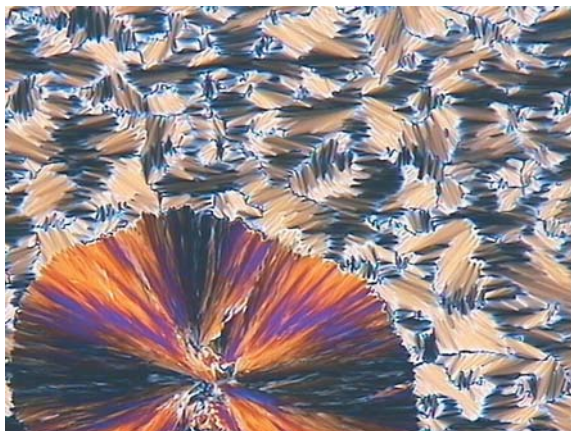


Plate 102. Crystalline spherulite growing from a SmA* phase.



Plate 103. A crystalline phase after completed spherulite growth.



Plate 104. Needle growth during direct crystallization from the isotropic melt, without mesogenic behavior.

Plate 105. Platelet texture of the SmQ* phase. (Courtesy of J. G. Meier.)

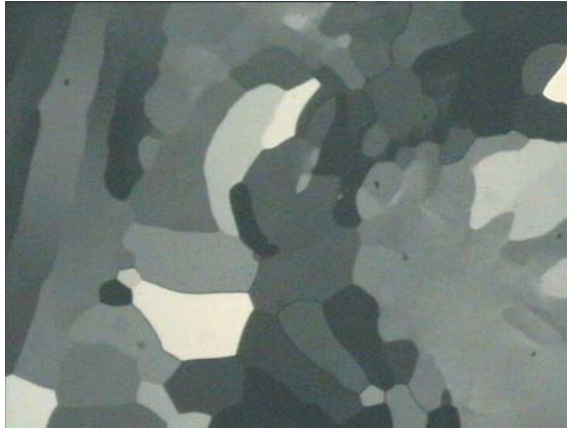


Plate 106. Dendritic growth aggregate of a discotic columnar phase (bright) from the isotropic melt (dark).

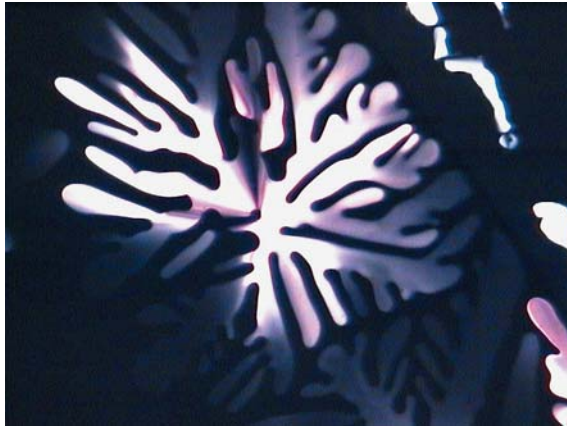
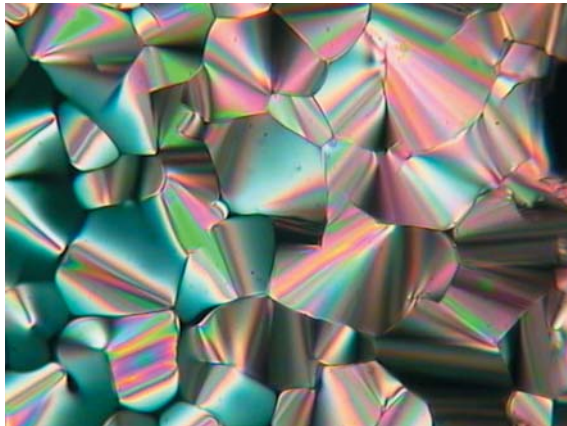


Plate 107. Pseudo focal conic fan-shaped texture of a discotic columnar phase.



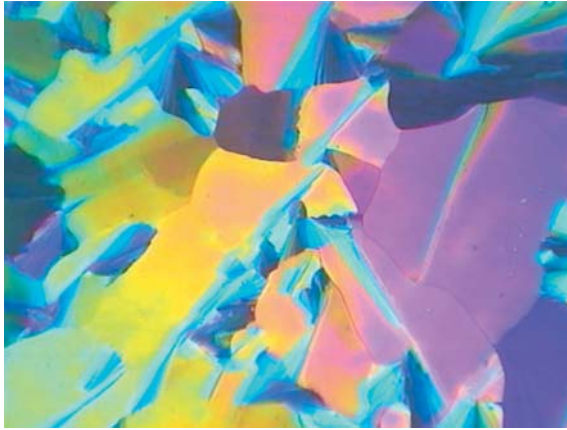
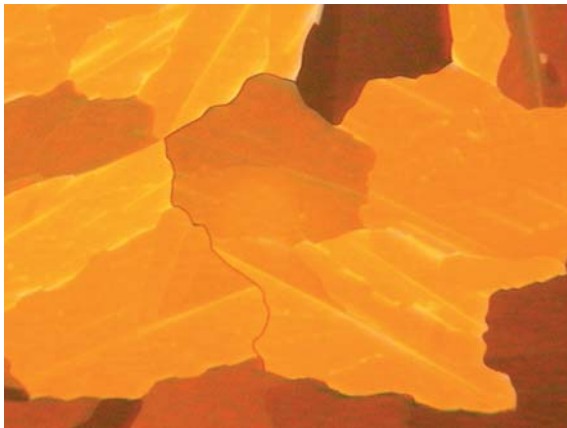


Plate 108. Mosaic texture of the banana B₁ phase.



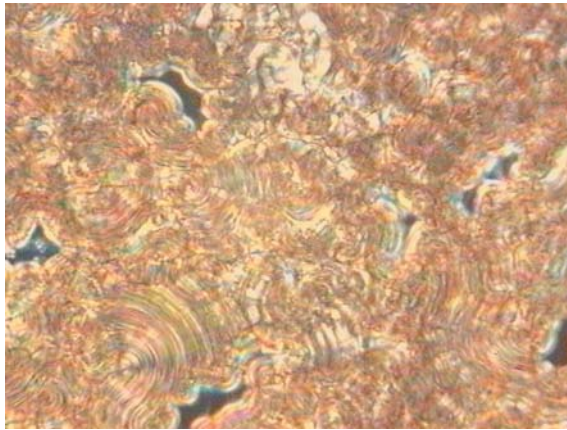
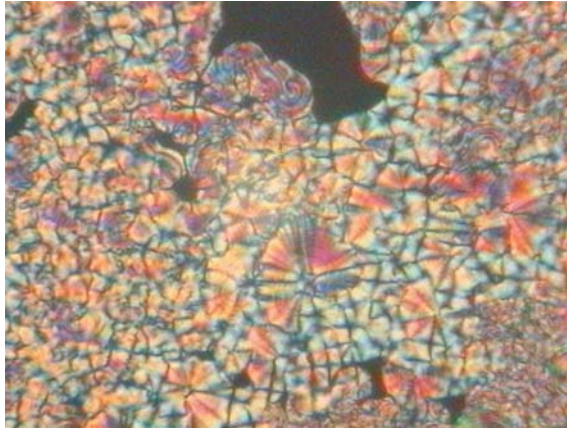
A



B

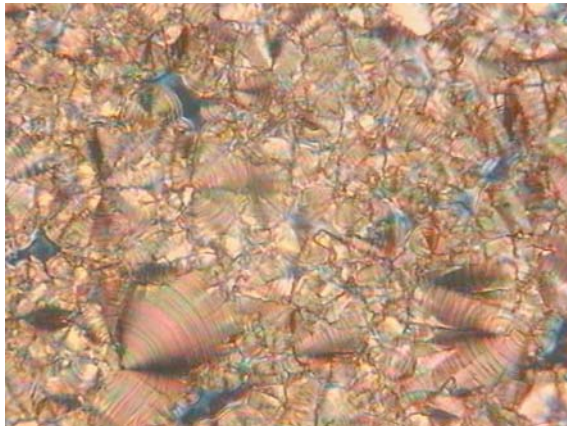
Plate 109. (a) Dendritic growth of the banana B₁ phase separating from the isotropic melt. (b) On further cooling the dendritic aggregates transform into a mosaic texture.

Plate 110. Focal-conic-like texture of the banana B_2 phase.



A

Plate 111. (a) Poorly developed fan-like texture of the banana B_2 phase, with striation across individual fans (see bottom left). (b) Same sample region after cooling into the B_3 phase.



B

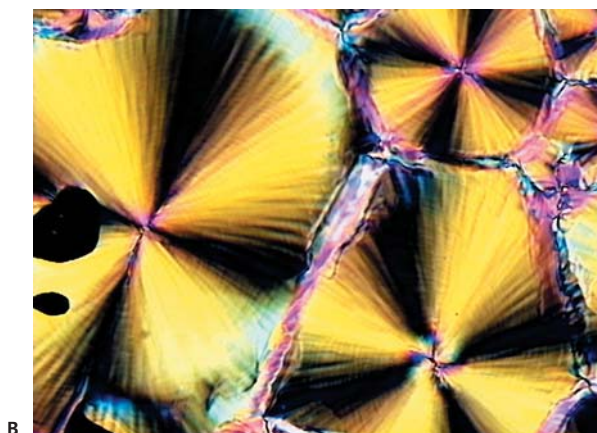
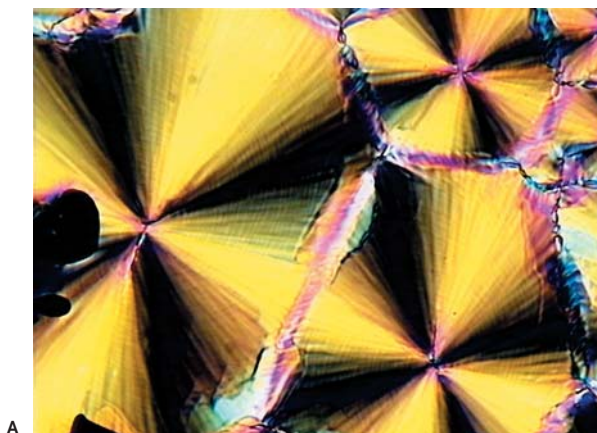


Plate 112. Switching of the extinction cross of a B₂ phase arranged in concentric smectic layers under applied electric fields: (a) positive applied voltage and (b) negative applied voltage.

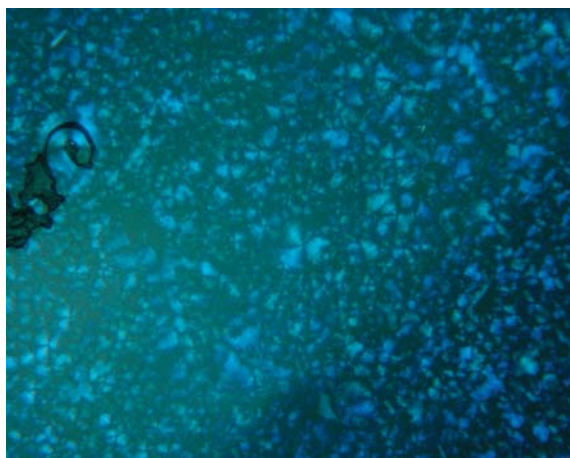


Plate 113. Bluish domain texture of the banana B₄ phase.

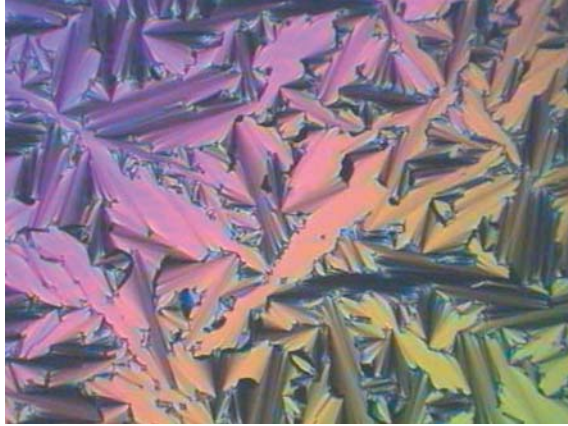


Plate 114. Fan-shaped texture of a banana B_6 phase.

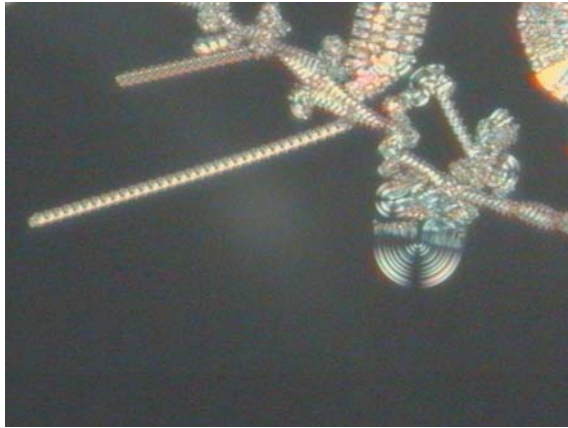


Plate 115. The banana B_7 phase shows a very characteristic growth behavior, which has no counterpart among the calamitic phases. Often the growth of complex single and/or double spirals is observed, separating from the isotropic melt.

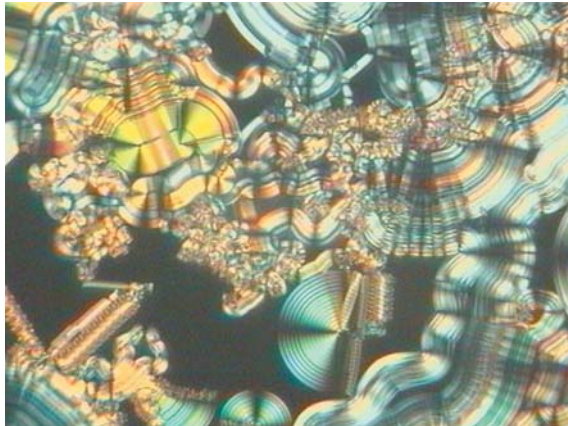


Plate 116. Example of the complexity and uniqueness of textures exhibited by the banana B_7 phase. Often circular, but also elongated, domains are formed in a spiral fashion, which exhibit an equidistant line pattern.

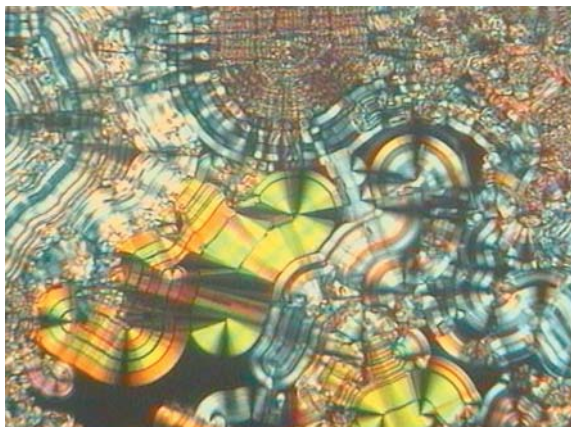


Plate 117. At lower temperatures the domains of the B_7 phase may exhibit a two dimensional pattern. Highly birefringent domains with no apparent structure are attributed to racemic regions within the sample.

Phase sequences in same texture region

TGBA*—SmA*	plates 38, 39 and 49, 50
N*—TGBA*—SmA*	plates 40—42 and 53—55
SmA—SmC	plates 68 and 69
SmA*—SmC*	plates 75 and 76
SmA*—SmC _{α} *—SmC*—SmC _{1/3} *—SmC _A *—SmI _A *	plate 82
SmA—SmB—E—Cryst	plates 87, 88 and 96, 97
SmA*—SmC*—SmI*—SmF*	plates 91 and 93
G—Cryst	plates 99 and 100
G—H—Cryst	plate 101

Index

a

Abrikosov phase 75f
achiral 16
– bent-core mesogens 149
AFLC 123ff
alignment techniques 21ff
amphiphilic 24, 145
anchoring length 110, 113
antiferroelectric 123ff
– TGBC_A* 87f
– model structure 125ff
antiferroelectricity 123ff
– banana phases 149
arc pattern 142
atomic force microscopy 22

b

B phase 14f, 141f
banana phases 148ff, 208ff
bâtonnets
– SmA 91, 187
– SmC 98
– SmC* 102
bend deformation 27ff
bent-core mesogens 148ff, 160f
biaxiality 38, 40, 97
birefringence dispersion 65f
birefringence 35ff, 43, 100
– lack of in cubic D 145
bistability 106
blue fog 44
Blue Phases 43ff, 168ff
bond orientational order 13, 135
bookshelf geometry 105ff, 137, 194, 201
boundary conditions 21f
bow-shaped mesogens 148ff, 160f
BP*, calorimetry 44
BP*, selective reflection 43f
BPI* 44ff, 169
BPII* 44ff
BPIII* 44, 168

Bragg scattering 44, 46
broken fan-shaped texture 98f
– SmC 191
– SmC* 102, 193
– SmF* 137, 200
– SmI* 137, 200
Brownian motion 54
brushes
– fourfold nematic 51f, 171
– fourfold SmC 99, 191
– twofold nematic 51f, 171

c

calamitic 2
calamitic mesogens 3
Cano pitch method 67f, 137, 176
capacitance 106
capacitive current 106
c-director 30
chevron 110ff
– folding 112f
– geometry 110ff
– horizontal 113ff, 194
– interface 110f
– vertical 110ff,
chiral 16f
– axis 17f
– center 17f
– elements 16f
– nematic 54ff
– plane 17f
chirality 16f
– banana phases 149
cholesteric 54ff
– fingers 71, 178f
– helical structure 55
– phase 54ff
– long pitch 64ff
– short pitch 57ff
cholesteryl benzoate 3, 155f

- cholesteryl pelargonate 156
 - Clark-Lagerwall effect 100, 105ff
 - clearing point 8
 - clock model 128
 - coalescence 64, 149, 175
 - columnar, discotic 147f, 207
 - commensurate structure 78ff
 - condensor 34
 - confinement, effects on SmC*
 - sub-phases 129ff
 - conoscopy 39ff
 - contact preparation 4, 68, 167
 - continuum theory 27ff
 - contrast 95
 - chevron geometry 111
 - DHF 103
 - horizontal chevrons 116
 - critical slowing down 96
 - crystallization 141ff, 205f
 - CubD 145f
 - cubic D phase 16, 145f
 - cubic defect structure 44ff
 - Curie-Weiss behaviour 110
 - cybotactic clusters 68
- d**
- DC balanced addressing 95
 - defect strength 51f
 - sign 52
 - defect wall
 - in horizontal chevrons 115, 194
 - in vertical chevrons 113, 194
 - deformed helix ferroelectrics 103
 - dendritic growth
 - banana B₁ 149, 208
 - discotic 148, 207
 - SmB 136, 199
 - DHF effect 103
 - diamagnetic susceptibility 24
 - diastereomer 17
 - dielectric anisotropy 24
 - differential scanning calorimetry 131, 141
 - dipole moment 101
 - disclinations 52, 67
 - discontinuous color changes 65f, 176
 - discotic 2, 207
 - mesogen 3, 159
 - phases 147f
 - disk-like mesogens 147, 159
 - distorted clock model 129f
 - distorted helix, SmC* 104
 - DOBAMBC 3, 157
 - domain boundary 106
 - domains, SmC* 106ff
- double layers 10f
 - double swallow-tailed 145
 - double twist cylinder 44f
 - droplet preparations 83f, 185f
 - Dupin cyclides 91f
- e**
- E phase 14f, 142, 203f
 - edge dislocations 57
 - elastic constant 27ff
 - elasticity 27ff
 - electroclinic coefficient 95f
 - electroclinic effect 5, 93ff
 - N* 69f
 - electroclinic viscosity 96
 - electrostrictive 93
 - enantiomer 17
 - enantiomeric excess 94
 - evaporation 23
 - extinction cross 149, 210
 - extra-ordinary ray 36f
- f**
- fan-like texture
 - B₂ 149, 209
 - N* 56f, 174
 - fan-shaped texture
 - B₁ 149
 - B₆ 150, 211
 - E 142, 203
 - SmA 91ff, 188, 190, 198
 - SmA* 102, 193, 195f, 200
 - SmB 135, 199
 - SmC 98
 - SmC* 192
 - soft crystal phases 141, 199
 - ferrielectric phases 126ff, 195, 197
 - ferrielectricity 126ff
 - ferroelectric domains 106ff, 194
 - ferroelectricity 100ff
 - banana phases 149
 - filament texture 80ff, 183ff
 - fingerprint texture 70
 - N* 177f
 - SmC* 192f
 - TGBA* 183f
 - FLC 100ff
 - flexoelectric
 - deformations 62
 - polarisation 62
 - flexoelectricity 61ff
 - flexoelectro-optic effect 61ff
 - flow alignment 24, 168
 - fluctuating textures 132, 198

fluid smectic phases 91ff
 fluorescence confocal polarizing microscopy 51
 flux lattice phase 75
 focal conics 91
 – line splitting at SmC^* - $\text{SmC}_{1/3}$ 131f, 197
 focal conic texture
 – B_2 149
 – SmA 92, 188
 – SmC 99, 191
 focal domains 91f
 fog phase 44
 four-fold singularities 51f, 171, 191
 fractal growth 150
 fracture 142
 free energy density
 – of elastic deformations 27ff
 – of N^* 28f
 – of SmA 29f
 – of SmC 30f
 – of SmC^* 31
 – at SmA - SmC 10
 free standing films 132
 Freedericksz transition 23f
 frustrated phases
 – BP^* 43, 168ff
 – TGB 75ff, 179ff
 full pitch band, SmC^* 104f

g
 G phase 14f, 142, 204f
 Grandjean orientation 59ff, 175
 Grandjean pitch method 66f
 Grandjean steps 66, 176f, 182
 gray-scales
 – DHF effect 103
 – electroclinic effect 95

h
 H phase 14f, 142, 205
 half pitch band, N^* 104
 hard deformations 29
 head-tail symmetry 100
 helical superstructure
 – B_2 150f
 – cholesteric 54ff
 – SmC^* 100ff
 – SmC_α^* 125ff
 – SmF^* 137
 – SmI^* 137
 helielectric 85f, 100, 126
 helix handedness, cholesteric 56ff, 61
 helix unwinding 102, 105f, 186

herringbone structure 15
 hexagonal order 135f
 hexagonal, discotic 148
 hexapentyloxytriphenylene 159, 207
 hexatic phases 13f, 135ff
 – tilted, chiral 100
 homeotropic alignment 24ff
 horizontal chevrons 112ff, 194
 hysteresis
 – antiferroelectric 124, 127
 – ferroelectric 127
 – ferroelectric 109, 127
 – SmC^* 109
 – SmC_A^* 124

i
 identity period, N^* , SmC^* 102
 incommensurate
 – TGB structure 78ff
 – SmC_α^* 126
 indicatrix 35ff
 induced chirality 18
 induced tilt angle 95
 intercalated structure 150
 interlayer correlation 135
 inversion symmetry 101
 ionic impurities 106
 Ising model 128

j
 J phase 14f, 145

k
 K phase 14f, 145
 Kossel diagram 44, 47ff

l
 Landau theory 10f, 128
 Langmuir-Blodgett technique 24f, 168
 layer inclination 97
 layer reorientation
 – asymmetric fields 117f
 – SmC^* , irreversible 112, 115
 layer rotation 117f, 195
 layer rotational instabilities 117f, 195
 layer shrinkage 93
 layer straightening, SmC^* , reversible 112
 layer tilt angle 110ff
 layer tilted geometry 110
 Legendre polynomial 8
 line pattern 101ff
 – SmC^* - $\text{SmC}_{1/3}^*$ or $\text{SmC}_{1/4}^*$ 131
 linear electro-optic effect, electroclinic 94ff
 lyotropic 1f, 145

m

Maier-Saupe theory 8
 Maltese cross 39f, 160, 210
 marble texture 53, 172
 MBBA 155
 Meissner effect 75
 Meissner phase 75f
 MHPOBC 123f, 158, 195
 micellar aggregates 145
 miscibility rule 4, 167
 molecular configuration 17
 mosaic texture
 – soft crystal phases 141
 – B 141
 – B₁ 149, 208
 – G 142, 204f
 – H 142, 205
 – SmB 135f, 199
 – smectic Q* 146, 207
 – smectic F* 138, 202
 myelinic texture 98

n

near field microscopy 51
 nematic 7
 nematic phase 51ff
 nematic, discotic 147f
 nomenclature 6
 – banana phases 149
 nonlinear electro-optic response, SmC*
 106ff
 nucleation 64, 143

o

objective 34
 ocular 35
 ohmic current 106
 oily-streaks texture
 – N* 56, 173
 – SmA 96, 189
 one-constant approximation 28
 optic axis dispersion 98
 optical activity 38f, 40, 149
 optical rotation 58f
 optically
 – isotropic 145
 – negative 35, 40
 – positive 35f, 40
 order
 – distribution function 8
 – long range positional 14f
 – orientational 7f
 – positional 9f
 – short range positional 13f

ordered lattice 143
 order parameter
 – nematic 7f
 – smectic 9f
 ordinary ray 36f
 orthogonal soft crystal phases 141f
 oval texture, SmB 136

p

paraelectric 110
 phase transition
 – first order 12, 109f
 – second order 12, 109f
 photolithography 23
 piezoelectric effect 93
 pinches 57
 pitch divergence 68
 – SmC*-SmC_{1/3}* or SmC_{1/4}* 132
 pitch jumps 65, 176
 pitch
 – cholesteric 55f
 – SmC* 103f
 planar alignment 22ff
 plate capacitor 106
 platelet texture
 – BP* 45f, 168f
 – smectic Q* 146, 207
 point defects
 – nematic 51f, 170f
 – SmC 99, 191
 polar order, banana phases 149
 polarization peaks
 – SmC* 108f
 – SmC_A* 124
 – B₂ 149
 polarization reversal current 106ff,
 131, 149
 polarizing microscope 33f
 polarizing microscopy 33ff
 polygonal texture
 – N* 57, 174
 – SmA 92, 188
 power consumption 106
 pseudo-isotropic 38, 178, 183, 185
 pseudo-isotropic texture 96
 – B 141
 – E 142, 204
 – smectic B 135
 – N* 178
 – nematic 54
 – smectic A(*) 105, 183, 185, 189, 203
 – smectic C(*) 100, 105, 203
 pseudo-morphology 143
 pyroelectricity 100

r

- racemic 151
- rectangular, discotic 148
- re-entrant phases 16
- reflected light microscopy 35, 175
- refractive index 35ff
- reorientation
 - of director 106ff
 - of spontaneous polarization 106ff
- resistivity 106
- response time
 - electroclinic 95f
 - ferroelectric 95f
- reversal current
 - contributions 106ff
 - horizontal chevron structure 117

s

- sanidic 2
- SAXS 10, 12
- Schlieren mosaic texture, SmF* 138, 202f
- Schlieren texture
 - nematic 51f, 170f
 - B₆ 149
 - discotic nematic 148
 - N-SmC 98, 190
 - SmC 99, 191
 - SmI* 138, 202
- second harmonic generation 149f
- selective reflection
 - cholesteric 57ff, 173, 175
 - SmC* 104f
- self-healing 96
- shape-polar molecules 61f
- shear alignment 26
- single BP* crystals 46, 169
- single crystal, cubic D 146
- singularities 51, 171
- smectic A 9, 135f, 188f
- smectic B 13f, 199
- smectic B* 94
- smectic Blue Phase 46f, 170
- smectic C 10, 191f
- smectic C_α* 125ff, 195f
- smectic C_β* 126
- smectic C_γ* 126
- smectic C* sub-phases 123ff, 195ff
- smectic C_{1/2}* 127
- smectic C_{1/3}* 126ff, 195, 197
- smectic C_{1/4}* 126ff
- smectic C_A* 124ff, 195, 198
- smectic C_{F11}* 126
- smectic C_{F12}* 126
- smectic F 13f, 136ff
- smectic F* 100, 200, 202f
- smectic I 13f, 136ff
- smectic I* 100, 200ff
- smectic layer instabilities 112ff, 195
- smectic M 14
- smectic Q* 47, 146, 207
- soft crystal B₄ phase 150, 210
- soft crystal phases 14f, 141ff
- soft-mode viscosity 96
- space group 145f
- spectroscopy, N* 65f
- spherulites 143, 206
- spiral instabilities 117, 195
- spiral lancets 150f, 211
- splay deformation 27ff
- splay-bend deformations 62f
- spontaneous polarisation 85, 100ff
 - as secondary SmC* order parameter 109f
 - SmC*-N* transition 109f
 - SmC*-SmA* transition 109f
- square-grid TGBC* texture 86f, 186f
- SSFLC
 - smectic C* 100f, 194
 - smectic I* 137, 201
- stereoisomer 17
- steric packing 149
- striated texture, SmC 98
- striation bands 142, 203
- striation
 - B₂ 149, 209
 - B₃ 150, 209
- stripe pattern 96f
- striped domains 96f
- striped texture 97, 114, 189
- sub-phases 123ff, 195ff
 - clock model 128
 - distorted clock model 129f
 - Ising models 128
 - Landau models 128
- superconductor 75f
- suppression
 - of sub-phases 129f
 - of TGB 84, 186
- surface anchoring 21f
- surface inversion walls 53, 172
- surface stabilized ferroelectric liquid
 - crystal 100f, 105ff, 194, 201
- surfactant 24
- swallow-tailed 145
- symmetry, SmC* 100f

t

- temperature-chirality diagram 44f
- TGB phases 75ff, 179ff

TGB structure
 – TGBA* 77ff
 – TGBC* 84ff
 TGBC* texture 86f, 186f
 thermal contraction 142
 thermotropic 1f
 thick wall
 – horizontal chevron 114
 – vertical chevron 111
 thin wall
 – horizontal chevron 114
 – vertical chevron 111
 thread-like texture 52f, 172
 threshold field
 – SmC* 128
 – SmC_A* 128
 tilt angle 10
 – optical 97f
 – wavelength dependence 98
 – x-ray 97f
 tilt cone 99ff, 137
 tilted
 – columnar, discotic 147
 – soft crystal phases 142
 tilt-polarization coupling 101
 tip splitting 136
 topological defects
 – BP* 44
 – N 51
 transition bars 98, 190
 – SmA-SmB 135
 – SmC_{1/3}*-SmC_A* 132, 198
 transition
 – first order 109f
 – N-SmC 98, 190
 – N*-SmC* 192
 – second order 98, 109f
 – SmA-SmC 190f
 – SmA*-SmC* 93ff, 102, 193, 200ff
 twist deformation 27ff

twist expulsion 75f
 twist grain boundary phases
 75ff, 179ff
 twist inversion
 – cholesteric 69ff, 177
 – between SmC* and SmC_A* 129, 132
 two-fold singularities 51f, 171
 type I superconductor 75f
 type II superconductor 75f

u

ultraviolet absorption 65
 undulated TGBC* 87
 uniaxial approximation 97
 uniaxiality 35ff, 39
 uniform planar
 – alignment 21
 – nematic 53f
 – SmA(*) 93f, 189
 – TGBA* 79f
 unit cell, cubic D 145
 UV absorption 65

v

vertical chevrons 110ff, 194
 vortex state 75

w

wedge cell preparation
 – N* 66f, 176
 – TGBA* 81ff, 182, 184f
 Williams domains 97

x

x-ray scattering 141
 x-ray, banana phases 149f

z

zigzag defects 110ff, 194
 zigzag loops 111f